THE UNIVERSITY *of* EDINBURGH

Systematic development of predictive molecular models of high surface area activated carbons for the simulation of multi-component adsorption processes related to carbon capture

Emanuela Di Biase

Institute for Materials and Processes

School of Engineering

A thesis submitted for the degree of Doctor of Philosophy

The University of Edinburgh

October 2015

Abstract

Adsorption in porous materials is a promising technology for CO_2 capture and storage. Particularly important applications are adsorption separation of streams associated with the fossil fuel power plants operation, as well as natural gas sweetening. High surface area activated carbons are a promising family of materials for these applications, especially in the high pressure regimes. As the streams under consideration are generally multi-component mixtures, development and optimization of adsorption processes for their separation would substantially benefit from predictive simulation models.

In this project we combine experimental data and molecular simulations to systematically develop a model for a high surface area carbon material, taking activated carbon Maxsorb MSC-30 as a reference.

Our study starts from the application of the well-established slit pore model, and then evolves through the development of a more realistic model, based on a random packing of small graphitic fragments.

In the construction of the model, we introduce a number of constraints, such as the value of the accessible surface area, concentration of the surface groups and pore volume, to bring the properties of the model structure close to the reference porous material.

Once a plausible model is developed, its properties are further tuned through comparison between simulated and experimental results for carbon dioxide and methane. The model is then validated by predictions for the same species at different conditions and by prediction of other species involved in the carbon capture processes.

The model is applied to simulate the separations involved in pre and post combustion capture processes and sweetening of sour natural gas, using realistic conditions and compositions for the multicomponent mixtures. Finally, it is used to explore the effect of water in pre and post combustion separations.

Declaration

The work presented in this thesis was carried out in the School of Engineering, the University of Edinburgh, and is a result of the original work of the author, except where acknowledged in the text. The thesis was composed by the author and was not submitted to any other degree or professional qualification.

Emanuela Di Biase

October 2015

Acknowledgements

First of all I would like to thank Dr. Lev Sarkisov for the great opportunity he has given me, for his endless support and encouragement, for his patience, for his kindness and for being such a friendly and precious advisor. Lev, no words are enough to express how much I have learnt! I have really understood that patience and humility are invaluable for a scientist and that it is not possible to arrive to good quality results without a lot of effort. Times can be hard, but we must never give up!

Thank you to Prof. Stefano Brandani for coordinating such an interesting and stimulating project; I really feel honoured for having been part of it! And thank you to Leigh, for her great organization and kindness, whatever the circumstances.

I also gratefully acknowledge EPSRC for sponsoring me.

Thank you to Alex for being such a nice deskmate, for making me laugh and for listening with so much patience to all the stories I came up with every morning. And thank you for all you precious help Alex; I will never be able to find enough Marmite to repay you for it!

I would also like to say thank you very much to David for all his support and encouragement, especially at the beginning of this adventure. A big thank you also to Ana, Enzo, Chiara, Zoe, Ares, Davide, Danié, Pedro, Matt, Linjang, Alex (the Greek), Gabriel, Evi, Eduardo, Dursun, Mike, Apostolos, Esme for creating such a nice, friendly and supportive environment. I will never forget you guys and, as I always said, I wish I could have spent much more time with you!

Thank you to all the great people in the workshop, especially George and Bobby and thank you to David, for all his help with the IT issues!

The IMP has really been a great environment to work in, always with a positive and relaxed atmosphere. Thank you also to Avril and Sue for contributing so much to it!

This adventure would have not been possible without the incredible help of all the friends I have met in Edinburgh. Thank you so much to Simon, Kat and Ewan: it has been great to share good and hard times with you guys and to know that, one way or another, we have always been there for each other.

Thank you to all the community in Leith, to Yan and Roger, Judith and James, Birte, Dietmar and Helena, Beata and Ella, Chriss, Iain and to everyone in Boda and Victoria: things have been much easier and pleasant with you guys around!

Thank you so much to Clara and Lluna and to all the people who run the playgroups and crèches in Leith: definitely I would have not been able to do this without your support. And a big thank you to Unitots, for the great quality of the childcare and for the flexibility of the management: you have been just what I needed. Now I really hope that the opening of the new nursery in the King's Buildings represents the beginning of a new era even for student parents.

Thank you to my family, for always being a rock behind my shoulders: thank you to my Mum Angela, to my Dad Giuseppe, to my Brother Gabri and to my Sister Elia. Thank you to Nonna Peppa, Zia Gina and Zia Rita. The presence of all of you has always been a comfortable and secure support, and without you I would have not been able to see the end of this.

I also have to thank Patsy, Jethro and Carol, Ffion, Tony, Lottie and Hannah. And thank you to my supportive friends in Sardinia: Stefania, Giovanna and Domenico, Laura, Chiara, Manuela, Jack, Emiliano and Maria Giovanna with Andrea, Alba with Laura and Sara, Tamara and Daniele with Gaia and Francesco.

And of course the biggest thank you is for Mal and Amélie. This has been a great adventure, it has been hard but we have made it! This goal is not only mine but it is ours. Thank you so much for all your patience, commitment and support Mal, and thank you for making my life always so rich! Definitely without you I wouldn't have even started! There is so much more I should say to you, but you know I am a bit shy about writing it here..! Thank you Amelie for being such a good girl, it has been great to wear big Wellies, jump in muddy puddles and run around in the Scottish rain with you! It is to you that this work is dedicated, to you and to all the other children in the World. I really hope that everything I have learnt can help to make sure that this Planet becomes a place better tailored for the children than it is now!

Contents

List of figures

List of tables

Chapter 1

Introduction

1.1. Background: the problem of global warming

"*Warming of the climate system is unequivocal, as is now evident from observations of increases in global average air and ocean temperatures, widespread melting of snow and ice and rising global average sea level.*" (1)

"*Most of the observed increase in global average temperatures since the mid-20th century is very likely due to the observed increase in anthropogenic GHG [greenhouse gases] concentrations.*" (2)

"*The observed widespread warming of the atmosphere and ocean, together with ice mass loss, support the conclusion that it is extremely unlikely that global climate change of the past 50 years can be explained without external forcing and very likely that it is not due to known natural causes alone.*" (3)

"*No coupled global climate model that has used natural forcing only has reproduced the continental mean warming trends in individual continents (except Antarctica) over the second half of the 20th century.*" (3)

The above quotations are taken from the Fourth Assessment Report (4) prepared by the Intergovernmental Panel for Climate Change (IPCC) in 2007. This report outlined the problem of global warming and officially recognized the link between climate change and human activities.

The most evident effects of global warming are the continuing retreat of glaciers, permafrost and sea ice, which have been well documented, especially in the last few years. Figure 1.1 shows one of the photos taken by Jan Ioughin, from the Polar Science Centre at the University of Washington, in the context of his studies on the mass balance of the Greenland and Antarctic Ice Sheets in response to climate change. The photo shows a Greenland ice canyon filled with melt water in summer 2010.

Figure 1.1. Greenland Meltstream. Photo: Jan Ioughin (Polar Science Centre, Applied Physics Lab, University of Washington.

A recent study (5), led by the University of Leeds, has combined the data from the different satellite missions which, using different technologies, have been monitoring Earth's biggest ice shields on Greenland and in the Antarctic for the last 20 years. Thanks to the accuracy of

the data sets presented in the study, it is now possible to conclude with confidence that Antarctica has been losing ice for the whole of the past 20 years; this fact has been long disputed, due to the past uncoordinated publication of individual one-off measurements which had led to some confusion in the field.

Direct consequences of the melting of ice masses are the rise in the sea levels (5) and the Arctic methane release, as exemplified by figure 1.2 (6), which shows bubbles of methane emerging from sediments below a frozen Alaskan lake.

Other likely effects of global warming include a change in the amount and pattern of precipitation and a more frequent occurrence of extreme weather events, including heat waves, droughts, heavy rainfall and possibly even extreme and unexpected low temperatures, which are caused by intense cold fronts resulting from melting polar ice. Averaged over all land and ocean surfaces, the increase in the global temperature between 1880 and 2012 has been reported to be roughly 0.85 °C (7). Since the 1990s limiting this increase within 2°C by 2100 has been commonly regarded as an adequate means of avoiding dangerous climate change (8). However, it has been recently shown (9) that the impacts of 2°C rise could be much greater than the earlier science indicated, and that the impact for a 1°C rise is now expected to be as great as that previously assumed for a 2°C rise. It has been speculated that in the absence of proper action the rise of the average global temperature will lead to irreversible, drastic and most likely adverse changes in the global climate, with the consequences including loss of agricultural land, population resettlement and species extinction. This scenario, and the temperature condition associated with it, is often referred as the point of no return.

To avoid this scenario, the international community has been urged to take commit to the control of the greenhouse gases emissions, which are considered to be directly related to the global warming.

Figure 1.2. Bubbles of methane emerging from sediments below a frozen Alaskan lake (6).

The greenhouse gas with the largest impact on climate change as a result of human activities is carbon dioxide, with annual global emissions having escalated by approximately 80% between 1970 and 2004 (10). Figure 1.3 shows data for the global GHG emissions referred to 2004 and presented in the IPCC Fourth Assessment Report. Graph (a) compares contributions of different GHGs to the total emission, while graph (b) compares different sources of GHG emission.

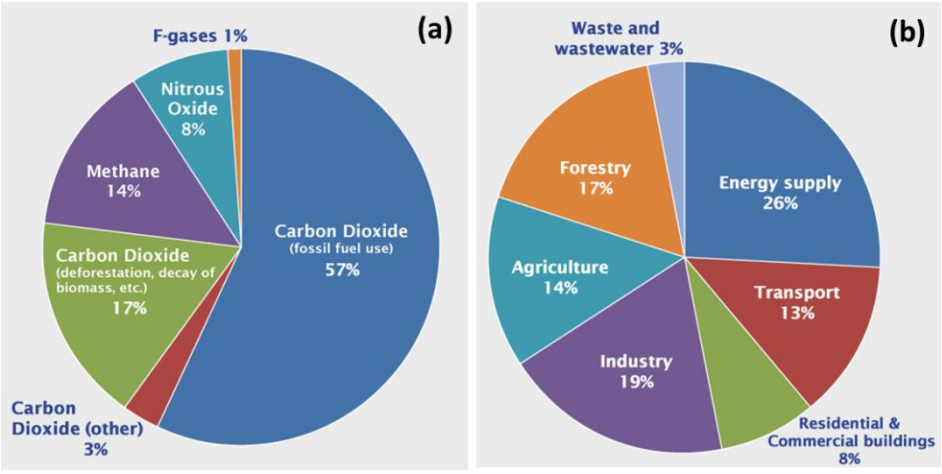

Figure 1.3. Global GHG emissions based on the data published in the IPCC Fourth Assessment Report (4). Graph (a) (11) shows emissions by gas and graph (b) (11) shows emissions by source. The graphs correspond to the data collected for 2004.

From figure 1.3, carbon dioxide is a dominating greenhouse gas, while energy supply (in other words power plants) is the main source of carbon dioxide emissions.

Despite growing concerns about global warming and international agreements (12) aiming to take proper action to control it, the global emissions of carbon dioxide have not diminished in the last few years. Actually, in 2011 they have reached 34 billion tonnes (3% up compared to 2010 and the highest level on record up to the same year) (13), with an average annual increase of 2.7% over the past decade. The report published in November 2013 by the Global Carbon Project (14) has shown an estimate of 36 billion metric tonnes of carbon dioxide emitted for 2013, 2.1% higher than the emissions registered for 2012.

With this rate it is unlikely that the current targets to cut carbon dioxide emissions will be met. It is therefore important to identify some strategies to reduce the emissions of carbon dioxide. Because the most significant contributor to anthropogenic carbon dioxide is electricity generation (15), a technology capable of capturing carbon dioxide directly from power plants would be particularly effective. Hence the importance of Carbon Capture and Storage technologies, to which the next section will be dedicated.

1.2. Carbon Capture and Storage

Carbon dioxide capture and storage (CCS) refers to a number of technologies consisting of separation of carbon dioxide from industrial and energy-related sources, transport of carbon dioxide to a storage location and its long-term isolation from the atmosphere (15, 16).

The IPCC Special Report on Carbon Dioxide Capture and Storage (15) considers CCS as an option in the portfolio of mitigation actions for the stabilization of atmospheric greenhouse gas concentrations. CCS has the potential to reduce carbon dioxide emissions while allowing the continued use of fossil fuelled power stations (16).

Capture of CO_2 can be applied to large point sources, such as large fossil fuel or biomass energy facilities, major CO_2-emitting industries, natural gas production, synthetic fuel plants and fossil fuel-based hydrogen production plants. The CO_2 would then be compressed and

transported for storage in geological formations, in the ocean, in mineral carbonates, or for use in industrial processes.

Figure 1.4 (15) is a schematic representation of the proposed CCS systems. The figure shows various point sources for which CCS may be relevant, as well as possible storage solutions.

The key challenge in carbon capture and storage is to reduce the energy cost associated with this process. For example, a power plant equipped with a CCS system (with access to geological or ocean storage) will need to produce roughly 10–40% more energy than a plant of equivalent output without CCS. This additional energy will be required for separation and compression of carbon dioxide (15).

In general, the net reduction of emissions to the atmosphere through CCS (CO_2 avoided) can be evaluated as the difference between the CO_2 captured, the increased CO_2 production due to the additional energy required for capture, transport and storage, any leakage from transport and the fraction of CO_2 retained in storage over the long term.

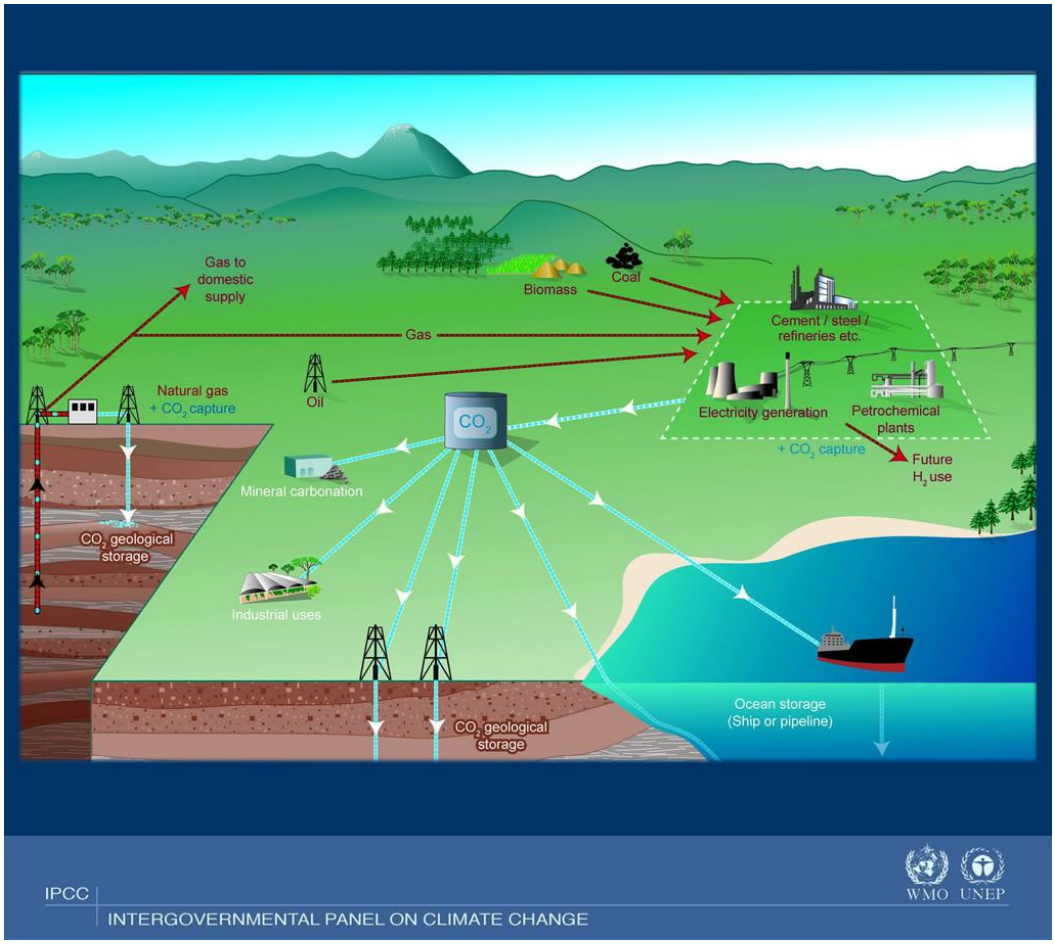

Figure 1.4. Schematic diagram of possible CCS systems (Courtesy of CO2CRC) (15). Red lines connect the sources of fossil fuels with the industrial and energy-related sources of carbon dioxide, while blue lines show possible routes for carbon dioxide, according to different storage solutions.

According to the IPCC, CO_2 emissions could be reduced by 80–90% for a modern conventional power plant equipped with carbon capture and storage technology. Also, it has been argued that Carbon Capture and Storage from power plants has the potential to reduce future CO_2 global emissions from energy generation by at least 20% (17, 18). Below we describe several different categories of processes available for this application.

Broadly, there are three different types of CO_2 capture processes that could possibly be applied to power plants. They are post combustion capture, pre combustion capture and oxyfuel combustion processes. The concentration of CO_2 in the gas stream, the pressure of the gas stream and the fuel type (solid or gas) are important factors in selecting the capture

system. Although not directly related to power plant operation, another process that involves CCS is the sweetening of sour natural gas.

The features, conditions, energy requirements, stream compositions, advantages and disadvantages of all of these techniques have been exhaustively presented in the literature (15, 16, 19-28); here we will simply recollect the main general aspects, dedicating more attention to the processes on which the present work will focus. In this project we will focus on pre and post combustion capture and we will also explore the process of sweetening of sour natural gas.

Figure 1.5 contains a schematic representation of the CCS processes applicable to power plants. The picture points out how, in the different technologies, the CO_2 separation happens at a different stage of the process.

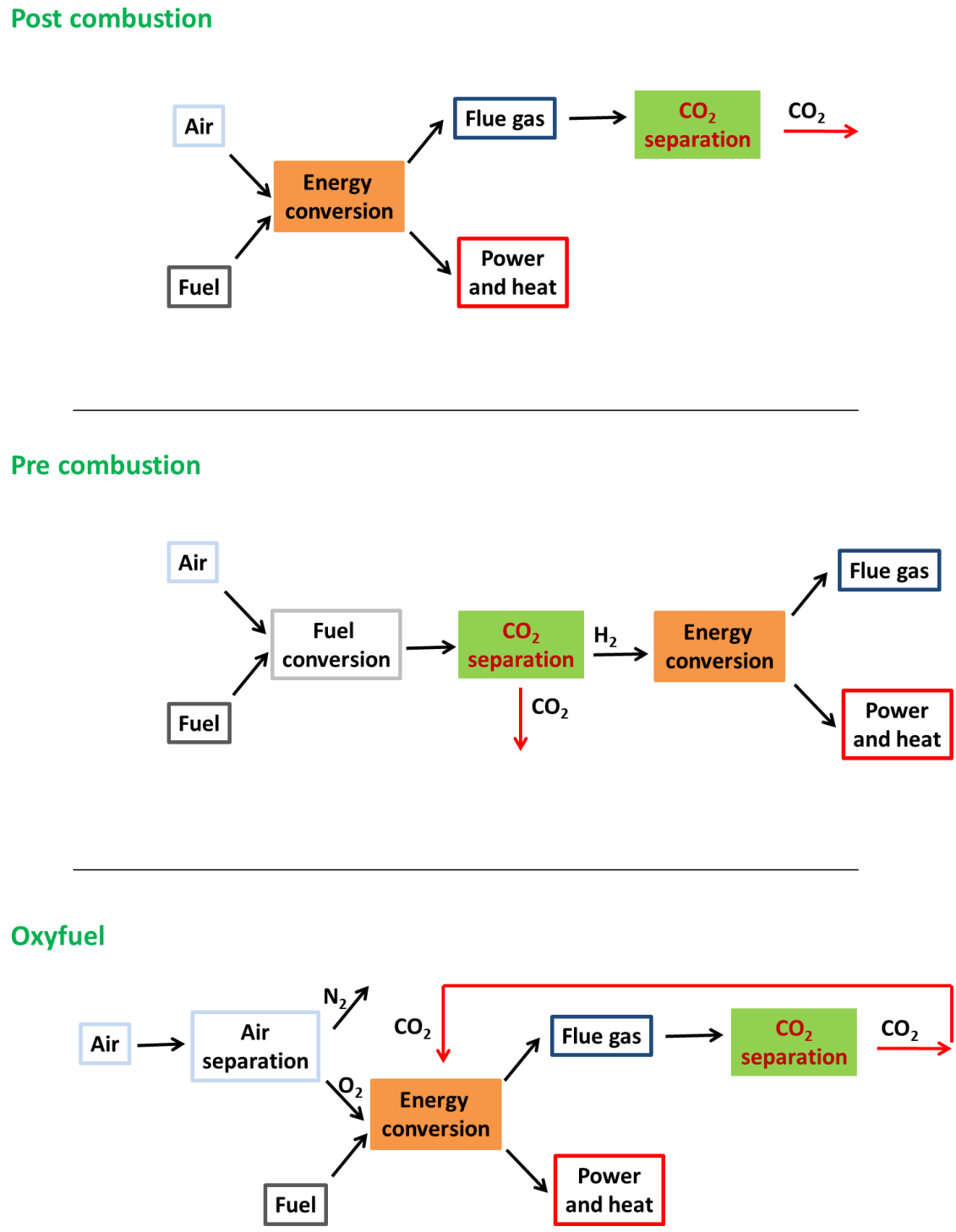

Figure 1.5. Schematic representation of CCS processes applicable to power plants.

As shown in figure 1.5 in the case of post combustion process (16, 20, 23), the CO_2 has to be removed from the flue gas generated after the combustion of the fuel. Here, the stream is mainly composed by nitrogen (~70-75%), while the molar percentage of carbon dioxide is quite low (~15%). Water vapour and oxygen are also present in percentages of about 5-7 and

3-4% respectively, together with very small amounts (order of magnitude of ppm) of nitrogen oxides (NO_x) sulphur oxides (SO_x) and carbon monoxide. The total pressure of the mixture is around 1 Bar and the temperatures are generally between 40-50 and 100°C, although the objective is to make the operational temperature as low as possible (therefore around 40°C). The biggest advantage of post combustion capture is that this process can be retrofitted onto the existing power plants; also, post combustion is the most developed of all the carbon capture technologies.

In the pre combustion processes (22, 23, 28) the CO_2 needs to be captured before the energy conversion stage. An example of the pre combustion process is the Integrated Gasification Combined Cycle (IGCC). This process is described as follows. First, fossil fuel stream (natural gas in this case) is brought to high pressure and temperature and partially oxidized to form synthesis gas (syngas), mainly composed of carbon monoxide and hydrogen. The second stage, which precedes the energy conversion, involves the transformation of carbon monoxide and water into carbon dioxide and hydrogen using a water-gas shift reactor.
The stream leaving the water-shift reactor is mainly composed of hydrogen (~55-60%) and carbon dioxide (~35-40%). Other components, all present in small amounts, are carbon monoxide (~1.1-1.2%), hydrogen sulphide (~0.5-1%), water vapour (~0.2-1%) and nitrogen (~0.25-0.75%). The total pressure in the stream is generally between 30 and 55 Bar and the temperature is around 40°C.

The significant advantages of the pre combustion capture are the higher CO_2 concentrations and the higher pressures (compared to post combustion process) of the stream to be treated, which reduce the energy penalty of the process to roughly half of that for post combustion (29). A further advantage is that the pre-combustion technology generates a hydrogen-rich fuel, which can be used in several applications, related to the development of the hydrogen economy.

Oxyfuel combustion (23, 28), in general, is the process of burning a fuel using pure oxygen instead of air as the primary oxidant. This implies lower fuel consumption and higher flame temperature, given that the nitrogen component of air is not heated. Historically, due to the high flame temperatures, the primary use of oxyfuel combustion has been in welding and cutting of metals, especially steel. In the context of fossil fuel power plants, firing with pure oxygen would result in too high of a flame temperature. To moderate the flame temperature,

the idea is to start combustion with an oxygen enriched gas mixture (95% of oxygen), and then switch to the stream diluted with recycled flue gas.

Oxyfuel combustion produces approximately 75% less of flue gas than air fuelled combustion and produces exhaust consisting primarily of CO_2 and H_2O. This results in high CO_2 concentrations in the outlet gas stream and, hence, in an easier separation of CO_2. However, there are increased energy requirements in the initial separation of oxygen from air. Oxyfuel combustion is still in the demonstration phase.

In sweetening of sour natural gas the composition of the mixture and properties of the stream can vary substantially depending on the source of the fossil fuel. As a typical example we can consider a stream with molar percentage of CO_2 around 10-15% at temperatures between 10 and 40ºC and pressures of about 68-75 Bar (24, 25).

Table I.1 shows the average compositions of the streams and conditions we will use as a benchmark for the processes object of this study. With a darker green we have indicated the main components of each mixture, which will also be the components of the binary mixtures we will consider as a starting point for each separation. The lighter green marks the minor components we will progressively add in each case.

Table I.1. Typical conditions and compositions (molar percentages) of the streams in the CCS processes, investigated in this study. Dark green indicates the main components of each mixture, while lighter green indicates the minor components that will be considered in this project.

Component	Post combustion	Pre combustion	Natural gas sweetening
CO_2	~15%	35 - 40%	10-15%
N_2	70-75%	0.25 - 0.75%	
H_2		55-60%	
CH_4			80-85%
O_2	3-4%		
CO	20 ppm	1.1-1.2%	
H_2S		0.5 - 1.1%	
SO_X	<800 ppm		
NO_X	500 ppm		
H_2O	5-7%	0.2 - 1%	
Temperature	40/50-100 ºC	40 ºC	10-40°C
Pressure	1 Bar	30 - 55 Bar	68-75 Bar

In all the processes we have briefly described the carbon capture phase consists in the separation of carbon dioxide from a multi-component gas mixture. Several techniques can be considered for this purpose and over the last few years a significant effort has been made in the research of innovative, efficient and cost effective strategies.

The conventional state-of-art method for post combustion capture is based on chemical absorption of carbon dioxide in amine solutions (15) (30), which provide high adsorption capacity and reasonably high adsorption rate, even when the partial pressure of carbon dioxide is low (which is the case for post combustion). The most widely used amine is monoethanolamine (MEA); its performance in the context of CO_2 capture is taken as a benchmark for the assessment of performances of all other types of materials considered for the purpose.

The use of amine solutions as absorbents suffers from a number of drawbacks, starting with the energy penalty associated with the regeneration. This is due to the high CO_2-alkanolamines bonding energies (up to ~100 kJ/mol) and to the high content of water (70%) in the solutions. It has actually been calculated that the regeneration of amine solutions

constitutes approximately 60% of the total CCS cost (31). Because of this and because of the additional costs which include amine degradation and corrosiveness (amine based solvents are in fact prone to thermal and oxidative degradation due to the presence in the stream of common flue gas components such as O_2, SO_x and NO_x), it has been estimated that CCS processes can cause an increase in the cost of electricity between 60 and 80% in a coal combustion plant. (31).

Initial studies in the feasibility of carbon capture using the state-of-art absorption technologies highlighted the need for the development of new, alternative approaches, tailored for the power sector (27). In particular, it would be important to meet specific targets for carbon capture in terms of capture efficiency and added cost of electricity (COE) (32, 33).

In a recent review Espinal and co-workers (34) have highlighted the urgent necessity for an international consensus in terms of standards for the evaluation of promising processes for CCS. In fact, US Environmental Protection Agency (EPA) has been in the process of establishing suitable standards.

Apart from the studies aiming to improve the solvent formulations in absorption (35-37) technologies, a growing interest and research effort have been directed towards alternative separation technologies. The main options include physical adsorption, membrane separation, cryogenic distillation, gas hydrates formation and chemical looping.

Despite the lack of a general consensus on the experimental parameters to be used for the evaluation of sorbent properties, physical adsorption with porous materials has been considered as one of the most energy efficient approaches (19, 21, 23, 38).

For the choice of suitable materials it is always important to bear in mind that adsorption separation processes are cycling in nature, as the adsorption step must always be followed by adsorbent regeneration step. Several techniques are available for the regeneration of the adsorbent, and the choice of a particular approach depends on the separation process at hand and other design requirements (such as the desired purity of the product or time of a complete cycle).

According to the chosen regeneration technique it is possible to make a distinction between Pressure Swing Adsorption, or PSA, (which includes also Vacuum Swing Adsorption, VSA)

and Temperature Swing Adsorption (TSA). A brief description of these technologies is given below, while a more detailed description can be found in the literature (39, 40).

Pressure swing adsorption (PSA) consists in the selective adsorption of certain components of a gas mixture at a relatively high pressure through contact between the gas and the solid adsorbent. This produces a gas stream enriched in the less strongly adsorbed components of the feed gas. The adsorbed components are then desorbed from the solid by lowering their bulk gas-phase partial pressures inside the column, so that the adsorbent can be reused. The desorbed gases are enriched in the more strongly adsorbed components of the feed gas. No external heat is generally used for desorption. A PSA process carries out the adsorption step at a superambient pressure, and the desorption is achieved at a near-ambient pressure level.

Vacuum Swing Adsorption (VSA) is a particular type of PSA. In this case the adsorption step takes place at a near-ambient pressure level, while the desorption is achieved under vacuum.

Whereas PSA techniques use changes in pressure to release the adsorbed gas, Temperature Swing Adsorption (TSA) achieves the same effect by increasing the temperature. Generally TSA involves a longer cycle time, as longer time is required for heating and cooling of the bed to exchange thermal energy.

Apart from the shorter cycle time, PSA shows other advantages, such as the lower energy costs (due to the lower operating temperatures) and the simplicity of the process, which make it possible to downsize the units.

In the context of CO_2 capture from power plants TSA appears to be particularly promising, in a sense that it gives the possibility to use low grade heat coming from the plants themselves (41, 42). As PSA requires the inlet gas to be at high pressure it is considered most appropriate for pre combustion separations, because it would be difficult to compress the large volumes of gas involved in post combustion, which happens at ambient pressure.
We will now give a brief overview of the materials that at the moment are considered as possible candidates for CCS processes.

1.3. Application of adsorption process to carbon capture and sequestration

At the heart of any adsorption process is the adsorbent. Naturally, development of an adsorption process for carbon capture should start with the identification of porous materials suitable for this application. This is however a challenging task. For example, a candidate adsorbent should exhibit affinity towards CO_2, however if the binding is very strong, this will lead to higher energy consumption during the regeneration cycle. Another essential characteristic is the selectivity of the material with respect to carbon dioxide, which needs to be efficiently separated from the industrial stream mixture.

Further important general requirements for a good capture material include high capacity for CO_2, ease in regeneration, affordable cost, stability in the presence of common flue gas components and contaminants such as H_2O, Hg, SO_x, and NO_x, fast adsorption and desorption kinetics and long term stability under cyclic pressure and temperature conditions involved in adsorption carbon capture processes (21, 23, 38).

A variety of solid physical adsorbents have been considered for CO_2 capture, including microporous and mesoporous materials (such as carbon-based sorbents, zeolites and metal-organic frameworks). In table I.2 we briefly review some of the most significant groups of materials explored in the context of carbon capture, also showing, for comparison, the properties of some of the most common chemisorbents (like metal oxides, and hydrotalcites, a class of anionic and basic clays), including alkanolamines.

Table I.2. Properties of some of the most common classes of sorbents considered in the context of CO_2 capture. S.A.: surface area, ΔH: heat of physi/chemisorption (at zero coverage for the physisorbents), C_p: specific heat capacity, S: adsorption selectivity. References are as follows. Zeolites: (23, 28, 43-47), activated carbons: (23, 28, 45, 47-50), MOFs: (23, 26, 28, 45, 47, 51, 52), oxydes: (23, 28) (45, 53-58), hydrotalcites: (23, 28, 45, 54, 56, 59-61), alkanolamines: (23, 26, 28, 45, 62).

Material	S.A. (m^2/g)	Adsorption capacity (mmol/g)	-ΔH (kJ/mol)	C_p ($J \cdot K^{-1} \cdot g^{-1}$)	Regenerability	Effect of water	S	Cost
SOLID PHYSISORBENTS								
Zeolites	Up to 1500	**13X**: 3.3 (323 K, 1 atm) 6.9 (295 K, 15 bar) 7.4 (298 K, 32 bar)	**13X**: 49	**4A**: 0.95 at 310 K	TSA and PSA; T from 135 to over 300°C	Substantial decrease of adsorption capacity	**Na-X**: CO_2/N_2=310 (313 K, 1 Bar, 15% CO_2 **13X**: CO_2/H_2 ~ 200 CO_2/CH_4 ~ 18.9 (298 K, 5 Bar, 10% of CO_2)	**Linde, Type A**: £ 94.5 for 10 g
Activated carbons	400-1000 **Maxsorb**: up to ~3400	**BPL**: 0.4 (301 K, 1 atm) 4 (323 K, 10 atm) **Maxsorb**: 0.5 (301 K, 1 atm) 25 (298 K, 1 bar)	**BPL**: 24.3 **Maxsorb**: 16.2	0.84-1.5 (T< 423 K)	Excellent reversibility of adsorption; Regeneration much easier than for zeolites	Hydrophobic in general; high % of water can decrease CO_2 capacity	**AX21**: CO_2/N_2 ~ 7 (293 K, 1 Bar) **BPL**: CO_2/H_2 ~ 20 **JX101**: CO_2/H_2 ~ 60 **Norit R1 Extra**: CO_2/CH_4 ~ 4.75 (298 K, 5 Bar, 10% in mol of CO_2)	**Norit CA1**: £ 92.2 for 1 kg
MOFs	Up to 6240	**MIL-101(Cr)**: 0.49 (298 K, 0.1 atm) **Mg/DOBDC**: 5.68 (298 K, 0.1 Bar) **MOF-177**: 33.5 (298K, 32 Bar) **MOF-210**: 74.2 wt% (298 K, 50 Bar)	From ~10 to ~96	**MOF-177**: 0.5-1-5 at 25-200°C	Low thermal stability; MIL-101(Cr) shows higher stability: Regenerable through TSA-N_2 stripping at 30°C or VTSA at 50°C	Rapid loss of cristallinity and surface area	**Zn_2(bttb)(py-CF_3)$_2$**: CO_2/N_2=41 (298 K, 17.5 Bar) **Mg_2(dobdc)**: CO_2/H_2 ~ 400 **Co(BDP)**: CO_2/H_2 ~ 10 **Zn_2(bpdc)$_2$(dpni)**: CO_2/CH_4 ~ 30 (296 K, 18 Bar) **Zn_2(bttb)**: CO_2/CH_4 ~ 4.8 (298 K, 17.5 Bar)	**Cu-BTC**: £ 238 for 10 g
CHEMISORBENTS								
Oxides	**ZnO**: 12-56	Theoretically 17.8	**CaO**: 182 at 298 K	**CaO**: 42 at 300 K	Calcination at T ≈ 900°C; Degradation of CC capability	CC enhanced or reduced according to H_2O partial pressure		**CaO, reagent grade**: £ 55 for 500 g
Hydrotalcites	15-250	0.25-0.5 (573 K, 1 bar)	**PURAL MG30-K**: 40 (phys); -130.8 (chem) (676 K)		N_2 purge stream; T = 400°C; Decrease of CC capability followed by stabilization after a few cycles	Steam enhances CO_2 sorption capacity and stability		**Hydrotal. Synthetic** (Aldrich): £ 47.50 for 1 kg
Alkanolamine Aqueous Solutions		3-6 (post combustion conditions)	50-100	3.1-3.5	T ≈ 100-140°C			**MEA**, ≥98%: £ 32.30 for 1 l

Among the properties included in table I.2 the thermal capacities are significant especially in the context of regeneration in TSA processes, given that the higher their values the higher the energy consumption for the heating of the materials. In particular, one of the main problems connected to CO_2 capture using alkanolamines is their high thermal capacity, due to their high content in water.

Another important property for an adsorbent is the heat of adsorption, which is related to the adsorption affinity. As mentioned at the beginning of this subsection the adsorption affinity should be high enough to ensure appreciable selectivity and high adsorption capacity, but at the same time it should be low enough to guarantee easiness of regeneration. One may wonder if an optimal heat of adsorption can be determined in order to establish a balance between the two requirements.

This problem has been studied by Bhatia and Myers (63) who, following the work by Matranga et al.(64), proposed a method to analyse the entire adsorption-desorption cycle and determine an optimum value of the heat of adsorption, based on the Langmuir isotherm. The use of the Langmuir model is an approximation, but for light gases it provides sufficient accuracy over a wide range of pressures and provides the simplest yet sufficiently accurate isotherm for the supercritical region. For full details on the simple procedure that was followed the reader is referred to the original publication (63); here we will limit ourselves to report the equation derived by Bhatia and Myers for the heat of adsorption that maximises the delivery of the adsorbate species at a given temperature *T*:

$$\Delta H_{opt}^{0} = T \cdot \Delta S^{0} + \frac{RT}{2} ln\left(\frac{p_1 \cdot p_2}{p_0^2}\right) \qquad \text{(I.1)}$$

where

ΔH_{opt}^{0}= optimum enthalpy change of adsorption

ΔS^{0}= entropy change relative to p_0

p_0 = standard pressure = 1 Bar

p_1 = storage pressure

p_2 = exhaustion pressure

In reality the differential enthalpy of adsorption is a quantity that generally varies with coverage, and it should be noted that in the Langmuir approximation on which equation (I.1) is based, the constant value of ΔH_{opt}^{0} represents the average of the enthalpy change between p_1 and p_2.

Equation (I.1) was applied by the authors to the cases of methane and hydrogen storage, and the optimum values of 18.8 and 15.1 kJ/mol were obtained for the two cases respectively.
The case of carbon dioxide storage has been later considered by Simmons and co-workers (65), who calculated that for pressures between 1 and 6 Bar at 298 K the optimum differential enthalpy of adsorption should be about -22 kJ/mol for the pure component case, or about -26 kJ/mol for a mixture containing 20% of CO_2.

The same equation can be applied for the pre-combustion conditions, using the typical values of p_1 = 55 Bar, p_2 = 1 Bar (total pressures of the stream), T = 313 K and considering a stream of molar composition CO_2/H_2 = 40/60. Taking for CO_2 the average value of ΔS^0 = -80 J/(k·mol) used by Simmons and co-workers (65), it is possible to calculate a value of ΔH_{opt}^{0} = -19.4 kJ/mol.

As mentioned at the beginning of the paragraph, not only the equilibrium adsorption properties have to be considered when screening materials for CO_2 capture, because even the kinetic properties play a crucial role. In general it is desirable to choose materials in which fast CO_2 adsorption is possible, and it is important to bear in mind that when operating with a gas mixture the differences in the diffusion rates of the components have an influence on the selectivity.

The review on adsorbents for CO_2 capture recently published by Choi et al. (38) compares the characteristics of several materials, taking into account even the kinetics. Physisorbents, for which kinetics are typically mass transfer controlled, generally show faster adsorption than chemisorbents, for which the kinetics are also controlled by the rate of the chemical reactions involved.

The authors refer to the work of several groups (66-68) to point out how the kinetics of zeolites needs to be studied through models that take into account both micropore and macropore diffusion, together with the effect of temperature and pressure, which in general make the process faster. According to the review zeolites have been ranked among the materials with the fastest adsorption rates, given the experimental studies which have shown how they can approach their adsorption capacities in times of the order of minutes (68-70).

In the case of activated carbons the authors cite the work of the most important groups (71-75) which contributed to the development of the most reliable models, which need to take into account not only micro and macropore diffusion, but also surface diffusion, together with nonisothermal effects (due to the released heat of adsorption) and the effect of change in surface coverage. The CO_2 adsorption rates of activated carbons are considered comparable to the adsorption rates on zeolites (38).

As for MOFs, a relatively low number of experimental studies have focussed on the kinetics, and in this sense there is the need for a more systematic approach to the issue (38) (23).

As an example of chemisorbent we can cite calcium oxide, for which the kinetics of CO_2 adsorption is governed by the rate of the carbonation process; this can be limited by the rate of the chemical reaction and by the rate of the CO_2 transport to the unreacted adsorption sites. Experimental studies have reported that the kinetics of adsorption on calcium oxide is much slower than the kinetics on zeolites and activated carbons (38), sometimes requiring several hours to achieve 70% of the total capacity (76).

In the case of alkanolamine solutions it has been reported that the tertiary amines (for which the reaction with CO_2 forms bicarbonate, as opposed to the carbamate formed by primary and secondary amines) show the slowest kinetics, followed in the order by secondary and primary amines (77). Moreover, some sterically hindered amines (2,piperidineethanol, for example) have shown faster kinetics in comparison to conventional amines, due to the lower stability of the carbamate they form (23).

To further emphasize the importance of both kinetics and thermodynamic properties, we would like to cite a recent American Physical Society (APS) report (78), according to which

the cost of CO_2 capture can be divided into two components: the capital cost and the operating cost; the capital cost depends on the size of the operation unit, which is inversely correlated with the kinetic rate constant of adsorption, while the operating cost depends on the enthalpy of adsorption/absorption. As a consequence, the report also underlines how the current challenge is not only to decrease the reaction enthalpies for CO_2 adsorption/absorption on the capture materials, but also to achieve faster adsorption and desorption kinetics.

From the data presented in table I.2 it is clear that no single material is likely to meet all the requirements specified at the beginning of this section. For example, MOFs, which show the great advantage of exceptional tuneability, are particularly promising in terms of surface areas and adsorption capacity both at high and low pressures, but their sensitivity to water, often low thermal and chemical stability and low mechanical resistance, together with their high costs still represent significant challenges.

On the other hand materials such as zeolites, which in general show higher adsorption capacities than MOFs at low pressures, are much more resistant and much cheaper than MOFs, but require relatively high energies for their regeneration and also are typically very hydroscopic.

Most likely the choice of the optimal material will depend on the specifics of the separation process, as the best material for post combustion carbon capture does have different requirements and optimal combination of properties from a material for pre combustion process. Therefore, the strengths and weaknesses of each adsorbent must be considered in the context of a specific adsorption process for effective CO_2 separation (38).

Recently several approaches have been proposed for the quick evaluation of adsorbents for CO_2 capture. Some of them are based on the comparison with the performance of MEA in terms of energy penalty, however there is no yet a clear consensus on what the appropriate, consistent metrics of evaluation of porous materials should be (34).

Here we provide several examples of attempts to develop these metrics. In particular, a recent study by Chu et al. (79) presents a correlation between the rate constants and the enthalpies of CO_2 adsorption for current and ideal sorbent materials. Another interesting example is given

in the work by Bae and Snurr (80), who consider five fundamental criteria for the evaluation of CC adsorbents: CO_2 uptake under adsorption conditions, working CO_2 capacity, regenerability, selectivity under adsorption conditions and sorbent selection parameter. For the definition and detailed description of all the parameters the reader is referred to the original publication.

Beyond the aspects presented above the identification of sustainable and industrially feasible materials with a good capture performance should also be based on a comprehensive life-cycle analysis approach, which should take into account the environmental impact associated with their extraction, manufacture, use, and disposal. Unfortunately, very little data is available at the moment from this point of view.

Among the materials considered for CO_2 applications, activated carbons are not the ones with the highest affinity or selectivity for CO_2; this aspect becomes particularly important in the case of post combustion capture, which involves a low partial pressure of carbon dioxide in the stream.

Several publications, more or less specifically, present advantages and disadvantages associated to the use of activated carbons as opposed to different other materials in the context of carbon dioxide adsorption (23, 38, 81-84).

Despite the relatively low selectivity for carbon dioxide activated carbons present several advantages. Indeed, they are a very versatile and diverse family of materials, they are commercially available and relatively inexpensive, and they are stable under a broad range of conditions, with highly reproducible and consistent adsorption behaviour (85). Also, the relatively low affinity towards CO_2 implies easiness of regeneration, given that the carbon dioxide is not as strongly adsorbed as in other materials (86), and the CO_2 adsorption kinetics is generally fast.

In particular, because of their high adsorption capacity, activated carbons with very high surface area and porosity could represent excellent candidates for storage applications or in the separations involving high pressures (such as pre combustion capture and natural gas sweetening) (48, 63, 87-90). Moreover, they could constitute a platform for the development

of more complex materials (44, 89, 91, 92) tuned to show higher affinity and selectivity for CO_2 even at low pressures, and hence suitable even for post combustion capture.

It is precisely on high surface area activated carbons in application to CCS that our project focuses; as a representative of the category we have chosen Maxsorb MSC-30, which has been commercially produced by the Kansai Coke and Chemicals since 1990s and shows surface area in excess of 3000 m^2/g (87, 93).

Maxsorb is produced from dehydration followed by activation between 600 and 900ºC of a mixture of various kinds of petroleum coke with an excess amount of KOH. The main characteristics on Maxsorb, MSC30 are summarized in Table I.3, which also presents a comparison with the properties of BPL carbon, chosen here as a representative of the conventional activated carbons.

Table I.3. Comparison of structural and zero loading adsorption characteristics of Maxsorb MSC-30 and BPL activated carbons (48, 87-89, 91).

Adsorption properties	**Maxsorb MSC-30**	**BPL**
BET surface area [m^2/g]	3000 -3400	1150
Micropore volume [cm^3/g]	1.3 – 1.7	0.43
Maximum CO_2 adsorption capacity at 298 K [mmol/g]	≈ 25	<8
Henry's constant of adsorption for CO_2 at 298 K [mol/(kg·Bar)]	2.44	4.59
Limiting heat of ads. at zero coverage for CO_2 [kJ/mol]	16.2	25.7

Apart from the high surface area and pore volume, on which we have already commented, table I.3 shows lower Henry's constant and lower differential enthalpy of adsorption at zero coverage for CO_2 adsorption compared to BPL. This means that Maxsorb at low pressure shows lower affinity for carbon dioxide than BPL, or other similar activated carbons (which does not make it the favourite candidate for the post combustion capture), but it also implies

less energy consumption in the regeneration process, which, as mentioned before, is an advantage.

Comparing the differential enthalpy of adsorption at zero coverage reported in table I.3 with the optimum value of -19.4 kJ/mol calculated for CO_2 using equation (I.1) it is possible to say that Maxsorb is promising from this point of view, especially because in the work by Himeno et al. (48) the isosteric heat of adsorption of CO_2 on this material is shown to grow with coverage.

It is also worth noticing that the C/O ratio in Maxsorb is lower than what on average is found for typical activated carbons (C/O ~ 12.6 (94)), which means that the amount of oxygen in Maxsorb is higher. Oxygenated functional groups may therefore play an important role in adsorption processes.
Another important characteristic of Maxsorb is its disordered structure, revealed by the very broad band shown by this material in the small angle X-ray diffraction pattern (95).

Having described the challenges that come with the choice of suitable adsorbents for CCS separations, we will now describe how molecular simulations can represent an invaluable tool for the routine assessment of candidate materials.

1.4. Importance of molecular modelling in CC studies

Development and optimization of pre and post combustion capture and natural gas sweetening adsorption separation processes require data on adsorption equilibrium and diffusion in candidate porous materials. However, it is generally difficult to measure multi-component adsorption isotherms, and even more so at high pressures and elevated temperatures (or both), which is the case for the processes of interest here. This motivates the development of accurate predictive molecular models, which are not constrained in the number of species or conditions under consideration. These models can also be used to gain molecular level insights on the details of adsorption processes in carbon materials and guide the development of new processes and applications.

In particular, molecular simulations could possibly be applied for a rapid screening and assessment of candidate materials and processes. Only a smaller group of the most promising candidates could then be eventually the subject of subsequent experimental testing.

A number of recent studies have applied molecular simulations as a method for the design and screening of CO_2 capture materials.

Some examples are given by the work by Cluson and Scaife (96), who designed carbonaceous hypothetical microstructures for the selective separation of CO_2 from gaseous mixtures, and by the works by Bae and Snurr, which we mentioned above, or Smit and co-workers (97), who have developed a method for the rapid screening of capture materials, which they applied to the evaluation of hundreds of thousands of zeolite and zeolitic imidazolate framework structures. A method for the quick screening of candidate capture materials based on the calculation of the adsorption properties in zero-loading regime has also been recently proposed (98).

Despite the increasing activity in molecular simulations applied to CO_2 capture, it has been recently highlighted that a more systematic approach to computational design of porous materials is needed (34). Furthermore, hierarchical, multi-scale modelling tools are needed to incorporate information about microscopic behaviour of candidate porous materials into simulation of the actual adsorption processes and process design. The development of suitable force fields capable of covering large number of material chemistries and pore networks is also required (34).

The most important feature of an adsorbent that needs to be modelled is the porous space, the shape and characteristics of which are a direct consequence of the structure of the material.
Although there has been a substantial progress in the application of the computational screening protocols to crystalline materials, in the case of disordered structures such as activated carbons these efforts have been hindered by the lack of accurate predictive models for these adsorbents. This provides the motivation for this thesis.

1.5. Objectives of the thesis

The objectives of this thesis stem for the following propositions:

1) Our project intends to be part of the research efforts aiming to identify and efficiently characterize promising materials to be applied to carbon dioxide separation processes using adsorption;
2) We believe that activated carbons, particularly the ones with high surface area and porosity, can play a substantial role in this context. This is because they are stable under a broad range of conditions, commercially available and relatively inexpensive, they show high adsorption capacity and highly reproducible adsorption behaviour, and they are relatively easy to regenerate. Their high adsorption capacity could make them excellent candidates for storage applications or separations involving high pressure and, despite their relatively low affinity for CO_2, activated carbons could serve as a starting platform for the development of more complex systems, tuned to show higher affinity and selectivity for CO_2 even at low pressure;
3) Current development of the processes based on activated carbons and assessing of their potential is hindered by poor understanding of their structure and lack of predictive models for adsorption;
4) To the best of our knowledge not many studies explore the efficiency of candidate capture materials using multicomponent mixtures under realistic conditions and, in particular, only a few publications deal with the impact of humidity, which is actually crucial in the context of CCS processes, especially in terms of added cost.

Hence the objectives of this thesis are:

1) To develop a model for high surface area activated carbons which correctly reflects its essential features, such morphology and surface chemistry;
2) To explore its properties in the context of CCS processes: for the purpose we apply it to the simulation of the separations involved in pre and post combustion capture and sweetening of sour natural gas, using realistic conditions and compositions for the multicomponent mixtures;
3) Explore the effect of water in pre and post combustion separations.

1.6. Structure of the thesis

The structure of this thesis is as follows:

After introducing the background and setting the problem (Chapter 1), and after introducing the main technical elements and tools we use and refer to for the achievement of our objectives (Chapter 2), we develop the project as follows:

Our initial approach was to build a model for high surface area activated carbons, here represented by Maxsorb MSC-30, starting with a well-established slit pore model. These efforts are summarized in Chapter 3. Interestingly, despite its simplifications, the slit-pore model applied to carbon dioxide and methane adsorption is quite accurate over a range of conditions; nonetheless for the study of CCS processes under realistic conditions, which also involve presence of water, it is not possible to neglect the presence of oxygenated functional groups on the surface of the porous material. This is particularly important for Maxsorb activated carbon as the composition of this material features a relatively high concentration of oxygen, including oxygen in the form of various surface groups. We therefore proceed to study two alternative, more realistic variants of the slit pore model, called respectively the single-layer model and single-layer model with groups and defects. The first model features pore walls made of one graphene layer, and the second model, also based on a single layer constituting the walls, also features functional groups and structural defects. We show that these additional elements of realism, surprisingly, do not cause any improvement in the predictive ability of the model, but even deterioration in the case of the single-layer model with groups and defects. For this reason, and also based on the experimental evidence on the disordered structure of Maxsorb, we decided to shift our efforts towards the development of a realistic, disordered model of high surface area activated carbons. Later on, the results from the following chapters (4 and 5) prompted us to revisit some of the aspects of the models based on slit pore geometry. In particular, we found that some improvement of the model can be achieved by tuning the solid-fluid interaction parameters, similarly to the approached adopted for disordered models. This constituted an additional section of this chapter.

Chapter 4 shows the systematic development of a disordered model for Maxsorb, based on a random packing of small graphitic fragments. Before proposing a possible model we used

Grand Canonical Monte Carlo simulations of adsorption of methane and carbon dioxide to study the effects of various parameters of the structural elements, such as their dimension, presence of functional groups, type of functional groups, curvature, method adopted to calculate partial charges, surface area of the system. Once a plausible model was developed its properties were further tuned through comparison between simulated and experimental results for methane and carbon dioxide. The model was then further validated by predicting adsorption of carbon dioxide and methane at other conditions and by predicting adsorption of other species involved in the CC processes.

In Chapter 5 we employ this model to study adsorption of mixtures with compositions and conditions representative of the pre and post combustion capture, and we also examine the CO_2/CH_4 separation, corresponding to the natural gas sweetening. In the case of pre and post combustion we start from the binary mixtures and we progressively add components up to quaternary and eventually quinary mixtures. For the binary mixtures we also make a comparison with the results obtained from the Ideal Adsorbed Solution Theory (IAST). Water is one of the components present in multi-component mixtures we consider. Adsorption of water in activated carbons is important in the context of carbon capture and separations, but also from a number of more fundamental perspectives. Hence this is the aspect of the studies where the analysis went into substantial depth. Chapter 6 contains some general conclusions inferred through the development of our project.

Finally, the thesis spans across a number of very different models and computational approaches. For clarity, parameters of the models and necessary simulation details will be introduced as needed in relevant chapters.

References

1. IPCC Fourth Assessment Report: Climate Change 2007. Synthesis report, Section 1.1: Observations of climate change. 2007.
2. IPCC Fourth Assessment Report: Climate Change 2007. Working Group I: The Physical Science Basis. 2007.
3. IPCC Fourth Assessment Report: Cimate Change 2007. Synthesis report, Section 2.4: Attribution of climate change. 2007.
4. IPCC. UN Intergovernmental Panel on Climate Change, Fourth Assessment Report: Climate change 2007.

5. Shepherd A, Ivins ER, A G, Barletta VR, Bentley MJ, Bettadpur S, et al. A Reconciled Estimate of Ice-Sheet Mass Balance. Science. 2012;338(6111):1183-9.
6. Whiteman G, Hope C, Wadhams P. Climate science: Vast costs of Arctic change. Nature. 2013;499:401-3.
7. Unit IWGITS. Climate Change 2013 - The Physical Science Basis - Working Group I Contribution to the Fifth Assessment Report of the Intergovernmental Panel on Climate Change. 2013.
8. den Elzen M, Meinshausen M. Meeting the EU 2°C climate target: global and regional emission implications. Netherlands Env. Assessment Agency., 2005.
9. Smith JB, Schneider SH, Oppenheimer M, Yohe GW, Hare W, Mastandrea MD, et al. Assessing dangerous climate change through an update of the Intergovernmental Panel on Climate Change (IPCC) "reasons for concern. Proceedings of the National Academy of Sciences 2009;106(11).
10. Stern N. Stern Review on the Economics of Climate Change. Cambridge: Cambridge University Press; 2006.
11. Agency E-USEP. Global Greenhouse Gas Emissions Data [updated 9/9/2013]. Available from: http://www.epa.gov/climatechange/ghgemissions/global.html.
12. (COP) UCotP. Report of the Conference of the Parties on its fifteenth session, held in Copenhagen from 7 to 19 December 2009. Addendum. Part Two: Action taken by the Conference of the Parties at its fifteenth session. Copenhagen: 2009.
13. Olivier JGJ, Janssens-Maenhout G, Peters JAHW. Trends in Global CO_2 Emissions 2012 Report. The Hague/Bilthoven: PBL Netherlands Environmental Assessment Agency, 2012.
14. Le Quéré C, Peters GP, Andres RJ, Andrew RM, Boden T, Ciais P, et al. Global carbon budget 2013. Earth Syst Sci Data Discuss. 2013;6(2):689-760.
15. Metz B, Davidson O, de Coninck H, Loos M, Meyer L. IPCC special report on carbon dioxide capture and storage. 2005.
16. Boot-Handford ME, Abanades JC, Anthony EJ, Blunt MJ, Brandani S, Mac Dowell N, et al. Carbon capture and storage update. Energy & Environmental Science. 2013.
17. Energy technology perspectives [Internet]. 2008. Available from: www.iea.org.
18. Haszeldine RS. Carbon Capture and Storage: How Green Can Black Be? Science. 2009;325(5948):1647-52.
19. Aaron D, Tsouris C. Separation of CO_2 from Flue Gas: A Review. Separation Science and Technology. 2005;40(1-3):321-48.
20. Grande CA, Cavenati S, Rodrigues AE, editors. Pressure swing adsorption for carbon dioxide sequestration. 2nd Mercosur Congress on chemical Engineering; 4th Mercosur Congress on Process systems Engineering; 2005; Costa Verde Do Brasil.
21. Chaffee AL, Knowles GP, Liang Z, Zhang J, Xiao P, Webley PA. CO_2 capture by adsorption: Materials and process development. International Journal of Greenhouse Gas Control. 2007;1(1):11-8.
22. DOE/NETL-2007/1281. Cost and Performance Baseline for Fossil Energy Plants Volume 1: bituminous Coal and Natural Gas to Electricity Rev.12007.

23. D'Alessandro DM, Smit B, Long JR. Carbon Dioxide Capture: Prospects for New Materials. Angewandte Chemie International Edition. 2010;49(35):6058-82.
24. Alonso TV, editor High efficiency on CO_2 removal in natural gas with UCARSOL^{TM} solvents Rio Oil & Gas Expo and Conference; 2010; Rio de Janeiro, Brazil.
25. Gudmundsson JSN, A.; Ismailpour, A.; Saleem, F.; Idrees, M.U., Zaidy, S.A.H. Natural Gas Sweetening & Effect of Declining Pressure. Department of Petroleum Engineering & Applied Geophysics - Norwegian University of Science & Technology, Trondheim, Norway, 2011.
26. Sumida K, Rogow DL, Mason JA, McDonald TM, Bloch ED, Herm ZR, et al. Carbon Dioxide Capture in Metal–Organic Frameworks. Chemical Reviews. 2012;112(2):724-81.
27. Gomez-Briceño D, Jong MD, Drage T, Falzetti M, Hedin N, Snijkers F. Scientific Assessment in Support of the Materials Roadmap Enabling Low Carbon Energy Technologies; Fossil Fuel Energies Sector, Including Carbon Capture and Storage. European Commission, Joint Research Centre, Institute for Energy and Transport, 2011.
28. Espinal L, Morreale BD. Materials challenges in carbon-mitigation technologies. MRS Bulletin. 2012;37(04):431-8.
29. Eide LI, Bailey DW. Precombustion Decarbonisation Processes. Oil & Gas Science and Technology – Rev IFP. 2005;60(3):475-84.
30. Rochelle GT. Amine Scrubbing for CO_2 Capture. Science. 2009;325(5948):1652-4.
31. Rubin ES, Mantripragada H, Marks A, Versteeg P, Kitchin J. The outlook for improved carbon capture technology. Progress in Energy and Combustion Science. 2012;38(5):630-71.
32. DOE/NETL. Carbon Dioxide Capture and Storage RD&D Roadmap. Department of Energy: 2010.
33. DOE/NETL. Advanced Carbon Dioxide Capture R&D Program: Technology Update. National Energy Technology Laboratory: 2011.
34. Espinal L, Poster DL, Wong-Ng W, Allen AJ, Green ML. Measurement, Standards, and Data Needs for CO2 Capture Materials: A Critical Review. Environmental Science & Technology. 2013;47(21):11960-75.
35. Aroonwilas A, Veawab A. Characterization and Comparison of the CO_2 Absorption Performance into Single and Blended Alkanolamines in a Packed Column. Industrial & Engineering Chemistry Research. 2004;43(9):2228-37.
36. Vaidya PD, Kenig EY. CO_2-Alkanolamine Reaction Kinetics: A Review of Recent Studies. Chemical Engineering & Technology. 2007;30(11):1467-74.
37. Bougie F, Iliuta MC. Analysis of regeneration of sterically hindered alkanolamines aqueous solutions with and without activator. Chemical Engineering Science. 2010;65(16):4746-50.
38. Choi S, Drese JH, Jones CW. Adsorbent Materials for Carbon Dioxide Capture from Large Anthropogenic Point Sources. ChemSusChem. 2009;2(9):796-854.
39. Sircar S. Pressure Swing Adsorption. Industrial & Engineering Chemistry Research. 2002;41(6):1389-92.
40. Knaebel KS. For your next separation, consider Adsorption. Chem Engin. 1995;102(11):92-102.
41. Merel J, Clausse M, Meunier F. Experimental Investigation on CO2 Post−Combustion Capture by Indirect Thermal Swing Adsorption Using 13X and 5A Zeolites. Industrial & Engineering Chemistry Research. 2007;47(1):209-15.
42. Berger AH, Bhown AS. Comparing physisorption and chemisorption solid sorbents for use separating CO2 from flue gas using temperature swing adsorption. Energy Procedia. 2011;4(0):562-7.
43. Qiu L, Murashov V, White MA. Zeolite 4A: heat capacity and thermodynamic properties. Solid State Sciences. 2000;2(8):841-6.
44. Sweatman M. Improving the equilibrium performance of active carbons for separation processes by co-adsorption with low pressure solvent: application to carbon capture. Adsorption. 2011;17(4):723-37.

45. . Nature. 1995;378(6555):366.
46. Bae T-H, Hudson MR, Mason JA, Queen WL, Dutton JJ, Sumida K, et al. Evaluation of cation-exchanged zeolite adsorbents for post-combustion carbon dioxide capture. Energy & Environmental Science. 2013;6(1):128-38.
47. Herm ZR, Swisher JA, Smit B, Krishna R, Long JR. Metal–Organic Frameworks as Adsorbents for Hydrogen Purification and Precombustion Carbon Dioxide Capture. Journal of the American Chemical Society. 2011;133(15):5664-7.
48. Himeno S, Komatsu T, Fujita S. High-Pressure Adsorption Equilibria of Methane and Carbon Dioxide on Several Activated Carbons. Journal of Chemical & Engineering Data. 2005;50(2):369-76.
49. Buonicore AJ, Davis WT, Air, Association WM. Air pollution engineering manual: Van Nostrand Reinhold; 1992.
50. Lee KB, Beaver MG, Caram HS, Sircar S. Reversible Chemisorbents for Carbon Dioxide and Their Potential Applications. Industrial & Engineering Chemistry Research. 2008;47(21):8048-62.
51. Liu Q, Ning L, Zheng S, Tao M, Shi Y, He Y. Adsorption of Carbon Dioxide by MIL-101(Cr): Regeneration Conditions and Influence of Flue Gas Contaminants. Sci Rep. 2013;3:1-6.
52. Yazaydın AÖ, Snurr RQ, Park T-H, Koh K, Liu J, LeVan MD, et al. Screening of Metal–Organic Frameworks for Carbon Dioxide Capture from Flue Gas Using a Combined Experimental and Modeling Approach. Journal of the American Chemical Society. 2009;131(51):18198-9.
53. Chase MW, Jr. NIST-JANAF Themochemical Tables, Fourth Edition. J Phys Chem Ref Data, Monograph 9. 1998:1-1951.
54. Halabi MH, de Croon MHJM, van der Schaaf J, Cobden PD, Schouten JC. High capacity potassium-promoted hydrotalcite for CO2 capture in H2 production. International Journal of Hydrogen Energy. 2012;37(5):4516-25.
55. Park N-K, Lee JD, Lee TJ, Ryu SO, Chang CH. The preparation of a high surface area metal oxide prepared by a matrix-assisted method for hot gas desulphurization. Fuel. 2005;84(17):2165-71.
56. Hutson N, Attwood B. High temperature adsorption of CO_2 on various hydrotalcite-like compounds. Adsorption. 2008;14(6):781-9.
57. Florin NH, Harris AT. Enhanced hydrogen production from biomass with in situ carbon dioxide capture using calcium oxide sorbents. Chemical Engineering Science. 2008;63(2):287-316.
58. Lin S, Harada M, Suzuki Y, Hatano H. Continuous experiment regarding hydrogen production by Coal/CaO reaction with steam (II) solid formation. Fuel. 2006;85(7–8):1143-50.
59. Ding Y, Alpay E. High temperature recovery of CO_2 from flue gases using hydrotalcite adsorbent. Trans IChemE. 2001;79-B1:45-51.
60. Fetter G, Olguín MT, Bosch P, Bulbulian S. Surface Areas of Nitrated Hydrotalcites. Journal of Porous Materials. 2000;7(4):469-73.
61. Oliveira ELG, Grande CA, Rodrigues AE. CO_2 sorption on hydrotalcite and alkali-modified (K and Cs) hydrotalcites at high temperatures. Separation and Purification Technology. 2008;62(1):137-47.
62. Puxty G, Rowland R, Allport A, Yang Q, Bown M, Burns R, et al. Carbon Dioxide Postcombustion Capture: A Novel Screening Study of the Carbon Dioxide Absorption Performance of 76 Amines. Environmental Science & Technology. 2009;43(16):6427-33.
63. Bhatia SK, Myers AL. Optimum Conditions for Adsorptive Storage. Langmuir. 2006;22(4):1688-700.
64. Matranga KR, Myers AL, Glandt ED. Storage of natural gas by adsorption on activated carbon. Chemical Engineering Science. 1992;47(7):1569-79.
65. Simmons JM, Wu H, Zhou W, Yildirim T. Carbon capture in metal-organic frameworks-a comparative study. Energy & Environmental Science. 2011;4(6):2177-85.
66. Yucel H, Ruthven DM. Diffusion of CO2 in 4A and 5A zeolite crystals. Journal of Colloid and Interface Science. 1980;74(1):186-95.
67. Ruthven DM, Lee L-K, Yucel H. Kinetics of non-isothermal sorption in molecular sieve crystals. AIChE Journal. 1980;26(1):16-23.

68. Zhao Z, Cui X, Ma J, Li R. Adsorption of carbon dioxide on alkali-modified zeolite 13X adsorbents. International Journal of Greenhouse Gas Control. 2007;1(3):355-9.
69. Hernández-Huesca R, Díaz L, Aguilar-Armenta G. Adsorption equilibria and kinetics of CO2, CH4 and N2 in natural zeolites. Separation and Purification Technology. 1999;15(2):163-73.
70. Khodakov AY, Rees LVC. Effect of propane on the kinetics of carbon dioxide adsorption in NaA zeolites. Gas Separation & Purification. 1995;9(4):253-7.
71. Andrieu J, Smith JM. Rate parameters for adsorption of CO2 in beds of carbon particles. AIChE Journal. 1980;26(6):944-8.
72. Sircar S. Sorption of carbon dioxide on activated carbons: Effect of the heat of sorption during kinetic measurements. Carbon. 1981;19(3):153-60.
73. Doong SJ, Yang RT. Bulk separation of multicomponent gas mixtures by pressure swing adsorption: Pore/surface diffusion and equilibrium models. AIChE Journal. 1986;32(3):397-410.
74. Gray PG, Do DD. Dynamics of carbon dioxide sorption on activated-carbon particles. AIChE Journal. 1991;37(7):1027-34.
75. Ding LP, Bhatia SK, Liu F. Kinetics of adsorption on activated carbon: application of heterogeneous vacancy solution theory. Chemical Engineering Science. 2002;57(18):3909-28.
76. Mess D, Sarofim AF, Longwell JP. Product Layer Diffusion during the Reaction of Calcium Oxide with Carbon Dioxide. Energy & Fuels. 1999;13(5):999-1005.
77. Yu C, Huang C, Tan C. A review of CO_2 capture by absorption and adsorption. Aerosol and Air Quality Research. 2012;12(5):745 - 69.
78. Socolow R, Desmond M, Aines R, Blackstock J, Bolland O, Kaarsberg T, et al. Direct Air Capture of CO_2 with Chemicals: A Technology Assessment for the APS Panel on Public Affairs. American Physical Society, 2011.
79. Chu S, Majumdar A. Opportunities and challenges for a sustainable energy future. Nature. 2012;488:294-303.
80. Bae Y-S, Snurr RQ. Development and Evaluation of Porous Materials for Carbon Dioxide Separation and Capture. Angewandte Chemie International Edition. 2011;50(49):11586-96.
81. Chue KT, Kim JN, Yoo YJ, Cho SH, Yang RT. Comparison of Activated Carbon and Zeolite 13X for CO2 Recovery from Flue Gas by Pressure Swing Adsorption. Industrial & Engineering Chemistry Research. 1995;34(2):591-8.
82. Sircar S, Golden TC, Rao MB. Activated carbon for gas separation and storage. Carbon. 1996;34(1):1-12.
83. Siriwardane RV, Shen M-S, Fisher EP, Poston JA. Adsorption of CO2 on Molecular Sieves and Activated Carbon. Energy & Fuels. 2001;15(2):279-84.
84. Drage TC, Blackman JM, Pevida C, Snape CE. Evaluation of Activated Carbon Adsorbents for CO2 Capture in Gasification. Energy & Fuels. 2009;23(5):2790-6.
85. Marsh H, Rodríguez-Reinoso F. Activated Carbon: Elsevier; 2006.
86. Xu D, Xiao P, Zhang J, Li G, Xiao G, Webley PA, et al. Effects of water vapour on CO2 capture with vacuum swing adsorption using activated carbon. Chemical Engineering Journal. 2013;230(0):64-72.
87. Otowa T, Tanibata R, Itoh M. Production and adsorption characteristics of MAXSORB: High-surface-area active carbon. Gas Separation & Purification. 1993;7(4):241-5.
88. Lozano-Castelló D, Cazorla-Amorós D, Linares-Solano A. Powdered Activated Carbons and Activated Carbon Fibers for Methane Storage: A Comparative Study. Energy & Fuels. 2002;16(5):1321-8.
89. Jordá-Beneyto M, Suárez-García F, Lozano-Castelló D, Cazorla-Amorós D, Linares-Solano A. Hydrogen storage on chemically activated carbons and carbon nanomaterials at high pressures. Carbon. 2007;45(2):293-303.
90. Xu WC, Takahashi K, Matsuo Y, Hattori Y, Kumagai M, Ishiyama S, et al. Investigation of hydrogen storage capacity of various carbon materials. International Journal of Hydrogen Energy. 2007;32(13):2504-12.

91. Yong Z, Mata V, Rodrigues A. Adsorption of Carbon Dioxide on Chemically Modified High Surface Area Carbon-Based Adsorbents at High Temperature. Adsorption. 2001;7(1):41-50.
92. Plaza MG, Pevida C, Arenillas A, Rubiera F, Pis JJ. CO_2 capture by adsorption with nitrogen enriched carbons. Fuel. 2007;86(14):2204-12.
93. Otowa T, Nojima Y, Miyazaki T. Development of KOH activated high surface area carbon and its application to drinking water purification. Carbon. 1997;35(9):1315-9.
94. Bansal RC, Goyal M. Activated Carbon Adsorption: CRC Press; 2005.
95. Xing W, Qiao SZ, Ding RG, Li F, Lu GQ, Yan ZF, et al. Superior electric double layer capacitors using ordered mesoporous carbons. Carbon. 2006;44(2):216-24.
96. Kluson P, Scaife SJ. Microporous Adsorbents for a Selective Separation of Carbon Dioxide from Mixtures with Methane and Nitrogen. Chem Biochem Eng Q. 2002;16(3):97-103.
97. Lin LC, Berger AH, Marrtin RL, Kim J, Swisher JA, Jariwala K, et al. In silico screening of carbon-capture materials. Nature Materials. 2012;11:633-41.
98. Sarkisov L. Toward Rational Design of Metal-Organic Frameworks for Sensing Applications: Efficient Calculation of Adsorption Characteristics in Zero Loading Regime. The Journal of Physical Chemistry C. 2012;116(4):3025-33.

Chapter 2

Adsorption: fundamentals, molecular simulations and experiments

As explained in Chapter 1, the overall objective of this thesis is to develop realistic, predictive models of high surface area activated carbons (specifically, Maxsorb) and explore adsorption behaviour of these models in the context of carbon capture process. The development, validation and application of these models require both experimental adsorption measurements and a variety of molecular simulation techniques. It is therefore useful to briefly describe these techniques, which are presented in this chapter as follows: in Section 2.1 we will introduce the fundamental concepts associated with adsorption phenomena and adsorption as a characterization technique, in Section 2.2 we will describe the main aspects of statistical mechanics and molecular simulation of adsorption, while in Section 2.3 we will briefly overview experimental adsorption measurements in general and describe in more detail the procedures adopted in the present work. The concepts presented in this chapter are common for the whole thesis. Additional methods, actual simulation parameters and details of the models will be introduced as needed in relevant chapters.

2.1. Adsorption: fundamentals and application as a characterization technique

2.1.1. Fundamentals

Adsorption is defined by the International Union of Pure and Applied Chemistry (IUPAC) as an increase in the concentration of a substance at the interface of a condensed phase and a liquid or gaseous layer forming as a result of surface forces.

In other words adsorption occurs whenever the surface of a material (the adsorbent) is exposed to a fluid (the adsorptive), because of the attractive interaction between the molecules of the fluid and the atoms of the solid surface. The molecules of adsorptive in the adsorbed phase are then called adsorbate.

According to the nature of the surface interactions it is possible to distinguish two broad classes of adsorption phenomena: physical adsorption (physisorption) and chemisorption. Physical adsorption involves the van der Waals and electrostatic interactions, which can be important or even dominant for polar adsorbents. Chemisorption implies formation of chemical bonds between the adsorbing molecules and the surface.

The energy of physisorption (which is always an exothermic process) is therefore lower than the energy of chemisorption, and is generally not much larger than the energy of condensation of the adsorptive. While physisorption is a phenomenon with a relatively low degree of specificity, chemisorption depends on the reactivity of the adsorbent and adsorptive. Another important difference is that physisorbed molecules keep their chemical identity, while chemisorbed molecules do not. This means that while physisorbed molecules can be recovered in their original chemical form via desorption (either by heating adsorbent, by lowering bulk pressure of the adsorbate or by reducing the bulk concentration of the adsorbate using purge gas), chemisorption is an irreversible process. Given the exothermic nature of physisorption lower temperatures promote adsorption. Chemisorption, being essentially a chemical reaction, is a process governed by activation energy, with the kinetics of the process increased at higher temperatures.

Adsorption is an equilibrium process, for which the overall effect is dependent on the extent of the interfacial area. Therefore all industrial adsorbents are porous and have large specific surface areas.

Given the importance of porosity in the context of adsorption, we will now introduce some essential terms and definitions.

The IUPAC classification of the porosity (1) (based on the classification first proposed by Dubinin) (2), is based on the pore width, which represents the distance between the walls of a slit-shaped pore or the diameter of a cylindrical pore. According to this classification the pores are divided into three groups: micropores, mesopores and macropores.

Micropores have internal width lower than 2 nm. Nitrogen adsorption at 77 K in these pores occurs through volume filling, and there is no capillary condensation taking place. The adsorption energy in these pores is much larger compared to larger pores, because of the overlapping of adsorption forces from the opposite walls of the micropores. The extent to which micropores are present depends on the material. In activated carbons, for example, specific surface area associated with micropores constitutes in general about 95% of the total surface area (3).

Mesopores (transitional pores) have effective width between 2 and 50 nm. In activated carbons the surface area of these pores in general does not exceed 5% of the specific surface area (3). Besides contributing significantly to the overall adsorption process, mesopores are generally considered as conduits leading the adsorbate molecules to the micropores. Macropores have dimension that exceeds 50 nm. They are not of considerable importance to the process of adsorption in activated carbons, because their contribution to the surface area is very low (3).

Adsorption is generally described through isotherms, which represent the relationship between the amount of fluid adsorbed by unit mass or unit volume of adsorbent and the equilibrium pressure p or concentration of adsorbate at a temperature T. The amount of fluid adsorbed obviously depends on the nature of the adsorbent-adsorptive system.

Experimental adsorption isotherms are usually presented in graphical form. The majority of experimental isotherms reported in literature can be grouped into six classes according to the IUPAC classification (1), as shown in figure 2.1, where the x axis represents the relative pressures p/p^0 (with p^0 being the saturation pressure of the adsorbate at the temperature of interest) and the y axis represents the specific amounts adsorbed.

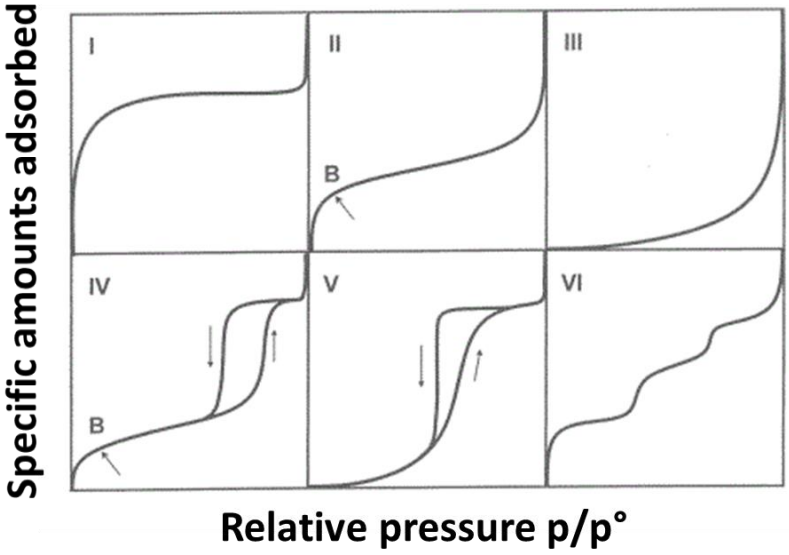

Figure 2.1. The six types of adsorption isotherms in the IUPAC classification (1).

Let us briefly describe the types of isotherms above. Type I isotherm is typical of microporous solids: it shows a steep increase at low relative pressure (corresponding to the process of micropore filling), followed by a plateau at higher pressure (corresponding to the adsorbent reaching its adsorption capacity). Type II indicates the formation of an adsorbed layer the thickness of which increases proportionally to the pressure up to $p/p^0 = 1$, at which condensation occurs. If the knee of the isotherm is sharp, the uptake at point B is usually considered to correspond to the completion of a monolayer and to the beginning of a multilayer formation. Type III is indicative of weak adsorbent-adsorbate interactions. Type IV isotherm is closely related to type II, but tends to level off at high pressures. It shows a hysteresis loop, in which the lower branch represents the progressive addition of gas to the adsorbent (adsorption), while the upper branch represents the progressing withdrawal (desorption). The existence of a hysteresis loop is generally associated with the filling and emptying of the mesopores via capillary condensation mechanism. The exact shape of the hysteresis loop can vary substantially from system to system. Type V, as type III, is indicative of low adsorbent-adsorbate interactions and it also shows hysteresis. Both type III

and type V isotherms are quite rare. Type VI isotherm, or stepped isotherm, is associated with layer by layer adsorption on a highly uniform surface. The classification above, applicable only to pure-component adsorption, is obviously a simplification, while in many cases experimental adsorption isotherms exhibit a more complex behaviour to be singularly classified according to figure 2.1.

Despite the differences all the isotherms in figure 2.1 show a linear portion in the very low pressure range. This region is linear in any adsorption isotherm and gives an indication of the strength of the adsorbent-adsorbate interaction. In this region any isotherm is characterized by the Henry's constant k_H of adsorption, which is defined as the slope of the adsorption isotherm in the limit of low pressures.

In general, it is important to be able to correlate adsorption data using appropriate analytical equations to describe the isotherms. In the most general form, the amount adsorbed N_a and the mass of adsorbent m_s are related to the bulk pressure of adsorbate at a constant temperature:

$$\frac{N_a}{m_s} = f(p)_T \tag{II.1}$$

and if the gas is below its critical temperature it is possible to write:

$$\frac{N_a}{m_s} = f(p/p^0)_T \tag{II.2}$$

where p^0 is the saturation pressure of the adsorbate at temperature T. The amount adsorbed per gram of porous material is commonly defined as adsorbed density ρ:

$$\rho = \frac{N_a}{m_s} \tag{II.3}$$

Having defined the concept of adsorbed density we can now define Henry's law adsorption constant more rigorously as:

$$k_H = \lim_{p \to 0} \frac{d\rho}{dp} \qquad \text{(II.4)}$$

and we can also write the equation for the adsorption isotherm in the Henry's law regime, which is the simplest case of adsorption isotherm and, as expected, is the following:

$$\rho = k_H \cdot p \qquad \text{(II.5)}$$

Over the years a number of different approaches have been developed for the purpose of describing adsorption isotherms; before introducing further examples of simple equations relevant to our research we will show an example of adsorption isotherms on activated carbon: figure 2.2 (4) presents the isotherms measured for carbon dioxide at 273, 283, 298 and 323 K on a sample of Norit R1 by Himeno et al. (4) and by Dreisbach et al. (5):

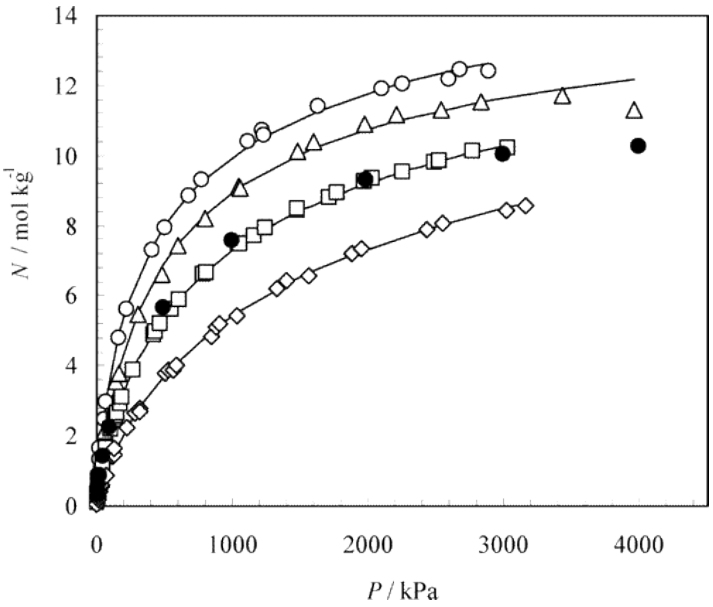

Figure 2.2. CO_2 adsorption isotherms measured on a sample of activated carbon Norit R1 at 273 K (empty circles), 283 K (empty triangles), 298 K (empty squares) and 323 K (empty diamonds) by Himeno et al. (4) and at 298 K (filled circles) by Dreisbach et al. (5).

The isotherms in Figure 2.2 all resemble type 1, as generally is the case for carbon dioxide adsorption on activated carbons, for instance.

A simple equation describing type 1 adsorption isotherm is the Langmuir equation (6), which will be briefly explained and derived below. It constitutes a platform for the derivation of more complex equations, such as the Brunauer-Emmet-Teller (BET) isotherm (7).

The Langmuir theory represents one of the earliest attempts to analytically describe adsorption, and it was originally developed by treating the adsorption process as a pseudochemical reaction between adsorbate molecules and available adsorption sites on the surface of the material. Within this theory adsorption is described as an equilibrium between adsorptive molecules in the gas phase at a pressure p and the adsorbed molecules in the surface layer:

$$A_g + S \leftrightharpoons AS \tag{II.6}$$

where A_g is a molecule of adsorptive in the gas phase, S is one adsorption site and AS is the molecule A adsorbed on the site S.

The derivation of the Langmuir isotherm is based on the following four assumptions:

1) all the adsorption sites are equivalent and each site can only accommodate one molecule
2) the surface is energetically homogeneous and adsorbed molecules do not interact with one another
3) no phase transitions are involved
4) at the maximum adsorption, only a monolayer is formed.

The fraction of the sites covered during the adsorption process is defined as θ, while the number of molecules impinging on the adsorbent surface per unit area in unit time is proportional to the pressure. The rate of adsorption is therefore proportional to $p(1-\theta)$, and the rate of desorption is proportional to θ only. At equilibrium, these two rates are equal, so that:

$$k_1 p(1-\theta) = k_{-1}\theta \tag{II.7}$$

where k_1 and k_{-1} are the rate constants of adsorption and desorption respectively.

Following from equation (II.7) it is possible to derive the Langmuir isotherm expression for the surface coverage:

$$\theta = \frac{K_L p}{1+K_L p} \tag{II.8}$$

where θ is the fraction of the adsorption sites which are occupied, p is the partial pressure of the gas and $K_L = \frac{k_1}{k_{-1}}$ is the Langmuir constant.

If θ is expressed as the ratio between the amount adsorbed at the pressure p and the saturated amount adsorbed, Langmuir equation becomes:

$$N = N_{sat} \cdot \frac{K_L p}{1+K_L p} \tag{II.9}$$

where N is the amount adsorbed at pressure p and N_{sat} is the saturated amount adsorbed.

The assumptions on which the Langmuir isotherm is based are in general quite strong, and they are not satisfied in real adsorption processes. Therefore, starting from assumptions which differ more or less substantially from the postulates introduced by Langmuir, several other isotherms have been derived. Two examples relevant to this project are Toth (8, 9) and BET (7) isotherms.

Toth model represents a development from Langmuir model and it accounts for the heterogeneity of the adsorbent. It is commonly used for heterogeneous adsorbents such as activated carbons, especially because of its simplicity and because of its accuracy both at low and high pressure. The equation is the following:

$$N = \frac{N_{sat} \cdot p}{(K_T + p^t)^{1/t}} \quad \text{(II.10)}$$

where K_T is a constant and t is a parameter that accounts for the heterogeneity of the adsorbent

It is clear that when t =1 Toth equation reduces to the Langmuir equation, so it is generally assumed that the more t deviates from unity, the more heterogeneous the adsorbent is. In this project Toth equation is applied for the fitting of the high pressure pure component simulated adsorption isotherms whenever they are used as an input for the application of the Ideal Adsorbed Solution Theory (IAST) (10). Details on the IAST, which is used to provide a comparison for the results of the direct simulation of mixtures, will be introduced in Chapter 5.

BET theory builds on the Langmuir ideas and extends the approach to describe formation of a multilayer. Both theories were also redeveloped later on the proper statistical mechanical grounds. The BET theory was derived by Brunauer, Emmet and Teller (7), who modified Langmuir mechanism as follows:

1) $A_g + S \leftrightharpoons AS$ (II.11)

2) $A_g + AS \leftrightharpoons A_2S$ (II.12)

.
.
.

n+1) $A_g + A_nS \leftrightharpoons A_{n+1}S$ (II.13)

The equations above describe the formation of multiple layers of adsorbate: equation (II.11), identical to equation (II.6), corresponds to the formation of a monolayer as in the Langmuir theory, equation (II.12) corresponds to the formation of a bilayer, with the molecules of adsorptive interacting with the adsorbate molecules forming the monolayer, and so on until the formation of layer n+1, the molecules of which interact with molecules on layer n.

The key assumption used in deriving the BET equation is that the successive heats of adsorption for all layers except for the first one are equal to the heat of condensation of the adsorbate. Other assumptions involved in the BET theory can be summarized as follows:

1) adsorption takes place on a uniform surface and the energies of adsorption of all molecules in the first layer are identical;
2) each molecule adsorbed in a layer is itself a potential adsorption site for the next layer;
3) there is no steric limitation to the thickness of the multilayer;
4) it is only for the first layer that the heat of adsorption is higher than the energy of condensation;
5) interactions between molecules adsorbed in the same layer do not play any part in the adsorption equation;
6) the second and further layers start to build up before the completion of the first one.

We will discuss the accuracy and realism of some of these assumptions later in the context of the surface areas derived based on BET theory. The resulting BET equation is as following:

$$\frac{1}{W\left(\left({p^0}/{p}\right)-1\right)} = \frac{1}{W_m C} + \frac{C-1}{W_m C}\left({p}/{p^0}\right) \qquad \text{(II.14)}$$

where W is the weight of gas adsorbed at a relative pressure ${p}/{p^0}$, W_m is the weight of adsorbate constituting a monolayer of surface coverage and C is the BET constant.

The BET C constant is related to the energy of adsorption in the first layer and consequently is an indication of the magnitude of the adsorbent-adsorbate interaction.

Both Langmuir and BET equations can be applied to obtain the surface areas of porous solids using adsorption of gases such as argon and nitrogen at cryogenic conditions. Determination of the specific surface area represents one of the applications of adsorption as a characterization technique. It is precisely to this topic that the next section will be dedicated: besides the determination of the specific surface area we will also describe a method to derive

the micropore volume of porous materials. As will be shown in later chapters, our strategy developed to construct realistic models of disordered carbons is based on capturing the key morphological features of the materials, such as the surface area and micropore volume. Hence, we place a particular emphasis on how these characteristics are obtained in physical adsorption experiments.

2.1.2. Adsorption as a characterization technique

Determination of the specific surface area: the BET method

The BET method is the most widely used procedure for the determination of the surface area of solid materials. In general, the Langmuir equation is considered more suitable to determine the surface area of microporous materials, while BET equation is considered more accurate for mesoporous materials; it has been however shown that, provided that certain consistency criteria are respected, the BET equation can be also applied to microporous materials (11). This aspect will be examined more in depth in the Section A9.4.1 of the Appendix.

The derivation of the surface area using the BET method requires a linear plot of

$\frac{1}{W\left(\left(p^0/p\right)-1\right)}$ against $\left(p/p^0\right)$, as in equation (II.14) and in figure 2.3:

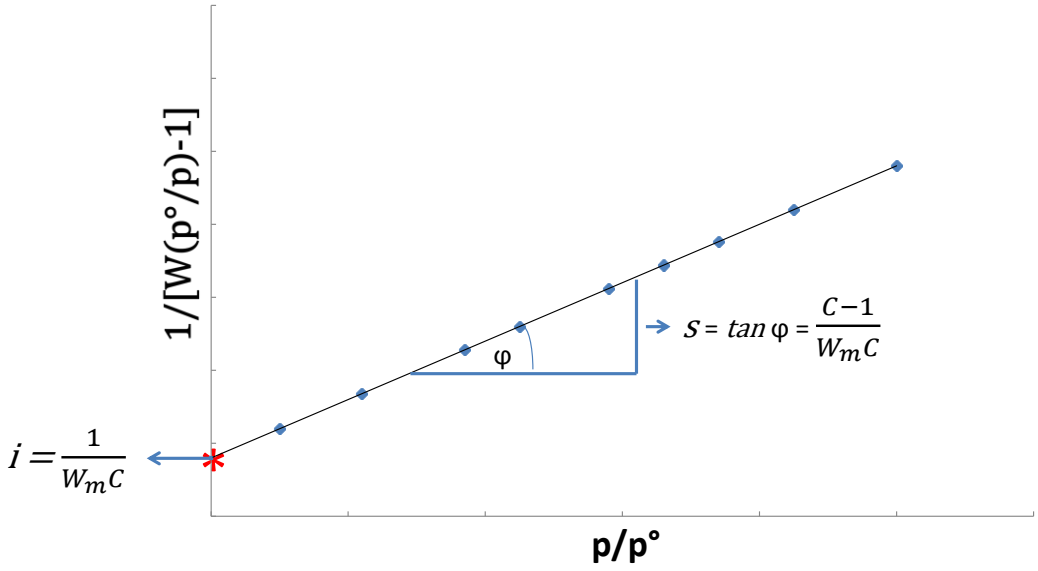

Figure 2.3. Typical BET plot, with intercept i and slope s expressed as a function of the quantities W_m and C, defined in Section 2.1.1. Angle φ is indicated simply to define the slope of the straight line.

It is clear that the slope s and intercept i of the graph are:

$$s = \frac{C-1}{W_m C} \tag{II.15}$$

and

$$i = \frac{1}{W_m C} \tag{II.16}$$

In this way the weight W_m of a monolayer can be derived from equations (II.15) and (II.16) as:

$$W_m = \frac{1}{s+i} \tag{II.17}$$

Once W_m has been determined the total surface area of the sample can be calculated as

$$S_t = \frac{W_m N_A A_{CS}}{M} \tag{II.18}$$

where S_t is the total surface area of the sample, N_A is Avogadro's number, A_{CS} is the molecular cross-sectional area of the adsorbate and M is molar mass of the adsorbate.

As mentioned before, nitrogen is the most widely used gas for the surface area determination since it exhibits intermediate values for the C constant (50–250) on most solid surfaces. For the hexagonal close-packed nitrogen monolayer at 77 K, the cross-sectional area A_{CS} for nitrogen is 16.2 $Å^2$.

The specific surface area S of the solid can be calculated from the total surface area S_t and the sample weight m_s, according to equation

$$S = \frac{S_t}{m_s} \tag{II.19}$$

As introduced before, the BET theory has been developed to account for multi-layer physisorption, and the BET method can essentially be considered as a mathematical procedure to analyse the adsorption isotherm and derive a monolayer capacity, which is then used to calculate a surface area.

In order to understand the limitations of this approach it is important to revisit the realism of the assumptions, involved in the BET theory. Specifically, of the assumptions above only number 6) is usually correct (except for ultramicropores which cannot accommodate more than two molecules) and number 4) can be considered as an acceptable approximation.

Assumption 1) is rarely fulfilled (and in fact many adsorbents are heterogeneous from the point of view of adsorption energy), assumption 2) is exceptionally fulfilled either, assumption 3) does not hold for porous adsorbents and assumption 5) is in general incorrect.

Moreover, as described before, when a surface area for the adsorbent is derived from the monolayer capacity, each molecule of adsorbate in the monolayer (assumed to be arranged as a hexagonal close-packing) is considered to cover the same area, equal to the molecular cross-sectional area A_{CS} and derived from the density of the adsorptive in the bulk liquid state.

All the assumptions above raise a number of questions, including the reproducibility of the BET monolayer capacity and the meaning of the concept of “BET surface area”, especially

for microporous adsorbents, for which even assumption 6) does not hold and the premises for the derivation of the surface area from the monolayer capacity are not valid.

A useful way to ensure the reproducibility of the results is to systematically choose an interval of applicability for the equation; that is the interval on which the equation II.14 is indeed linear. The relative pressure range between 0.05 and 0.35 (1) is well suited for type II and type IV isotherms and in any case the BET model (not applicable for type III and type V isotherms) generally fails for relative pressures higher than 0.5, which is considered as the onset for capillary condensation.

For microporous materials the interval of linearity of BET equation becomes narrower, and an appropriate choice of the pressure range depends on the application of certain consistency criteria. This aspect, mentioned at the beginning of this section, has been presented (11) and explored (12, 13) in the literature and will be more deeply discussed in Section A9.4.1 of the Appendix, in which the BET equation is applied to experimental and simulated data for nitrogen at 77.35 K on Maxsorb MSC-30.

We conclude this discussion pointing out that for microporous materials the concept of "BET monolayer content", actually misleading (because the idea of monolayer in this case has no clear physical or theoretical meaning), could be replaced by that of "BET strong retention capacity", as introduced by Rouquerol, Llewellyn and Rouquerol based on their results from calorimetric experiments (11).

Gas adsorption can also be applied for the characterization of the porosity of powders and other porous solids. Below we will describe Dubinin-Radushkevich method (14) for the determination of microporosity.

Characterization of the microporosity: Dubinin-Radushkevich method

Similarly to the determination of the surface area, characterization of the porosity generally relies on the adsorption of nitrogen at 77 K.

Here we will limit ourselves to the characterization of microporosity, given its relevance for activated carbons. In particular, we will concentrate on the method proposed by Dubinin and Radushkevich (14), and therefore called the DR method. This method is currently used to determine the micropore volume of activated carbons, by means of the homonymous equation.

Based on Polanyi potential theory of adsorption (15), DR equation has a semi-empirical origin and gives a macroscopic description of the behaviour of the adsorption loading for a given pressure. It is based on a picture of adsorption process happening by micropore filling, as opposed to layer-by-layer adsorption on the pore walls.

The assumptions on which Polanyi potential theory (actually derived to describe multilayer adsorption on non-porous sorbents) is based are the following:

1) the adsorption volume is filled by liquid adsorbate only;
2) the liquid adsorbed phase is incompressible;
3) the gas phase vapour in equilibrium with the adsorbed liquid exhibits ideal behaviour;
4) creating a liquid surface involves negligible work

Polany theory defines an adsorption potential, *A*, which represents the decrease in the Gibbs' free energy of the system upon adsorption of one mole of adsorbate (Gibbs' free energy of adsorption) and can be expressed as:

$$A = RTln\left({p^0}/{p}\right) \qquad \text{(II.20)}$$

In the DR "theory of adsorption in the micropores" a further assumption is that the fraction of the adsorption volume V occupied by liquid adsorbate can be expressed as a Gaussian function, which depends on the free energy of adsorption:

$$V = V_0 exp\left[-\left(\frac{A}{\beta E_0}\right)^2\right] \quad \text{(II.21)}$$

where V_0 is the micropore volume of the adsorbent, A is the free energy of adsorption, E_0 is the characteristic energy of adsorption, which is related to the adsorbent (particularly, to the distribution of the volume of the pores according to their size) and β is the so called affinity coefficient.

Equation (II.21) gives an expression of what in literature is referred to as "characteristic curve" for a particular adsorbate on a particular adsorbent. In the work by Dubinin (2, 16) this curve is shown not to be dependent on temperature, in the sense that if for a given material and for a given adsorbate the volume adsorbed at different temperatures is plotted as a function of the square of the free energy of adsorption, all the data points fall into one curve. Equation (II.21) can obviously be used in its linear form, calculating the logarithms at both sides. The affinity coefficient β enables comparison of characteristic curves for various adsorbates with a standard reference, which Dubinin chose to be benzene. β can be approximated by a ratio of the liquid molar volumes of the adsorbate and benzene.

Despite the temperature invariance of the characteristic curves the free energy of adsorption is actually related to this variable according to equation (II.20).

Therefore equation (II.21) can be written in the linear form:

$$log_{10}(V) = log_{10}(V_0) - 2.303\left(\frac{RT}{\beta E_0}\right)^2 \cdot \left[log_{10}\left(p^0/p\right)\right]^2 \quad \text{(II.22)}$$

which implies that the micropore volume V_0 can be calculated from the intercept of the plot of the isotherm data as $log_{10}(V)$ vs. $log_{10}\left(p^0/p\right)^2$.

Dubinin et al. have presented experimental data to show that equation (II.22) adequately describes the adsorption data of many adsorbates onto a wide variety of microporous carbons over a wide pressure range (16-19).

However, deviations from linearity can occur. First of all the equation cannot be applied in the region of zero coverage, because it does not reduce to Henry's law. Further deviations from linearity have also been widely discussed (20-22). For the purpose it is important to bear in mind that one of the assumptions on which DR theory is based is that the pore size distribution of the material is Gaussian. Marsh et al. (21) have proposed that a completely linear plot may be obtained only when this assumption reflects the real structure of the material, while deviations from linearity could give an indication of how much the pore size distribution deviates from a Gaussian function.

Actually, Marsh and Rand (21) have applied DR equation to several microporous carbons and the results have shown that in no case the plot is linear over the entire range of pressures; nonetheless, if a limited range of pressures is considered, the linearity is preserved. And this also suggests that this is the pressure range in which the micropore filling can really be described as a Gaussian function of the free energy of adsorption.

Another aspect is the fact that the temperature invariance of the characteristic curves can be considered as realistic concept only if the adsorption is governed by dispersion forces: this is because when a polar adsorbate is adsorbed onto a surface containing polar sites the thermal motion has an effect on the orientation on the dipoles or quadrupoles in the molecules involved. Therefore for adsorbents with highly polar sites and highly polar adsorbates the DR model should not be applicable. In the case of carbons there is however sufficient evidence that dispersion forces in general dominate adsorption processes (21, 23).

Further deviations from linearity in the DR plot are associated to the assumptions made in Polany potential theory: first of capillary condensation is not predicted by the model, because the density of the adsorbate phase is considered to be equal to the density of the bulk liquid (which, actually, is a satisfactory approximation only at temperatures well below the boiling point of the bulk liquid at atmospheric pressure); moreover, given that creating a liquid surface is assumed to involve negligible work, the DR method cannot predict phenomena such as wetting.

As we mentioned before, DR equation has semi-empirical origin; nonetheless several attempts to derive it using a theoretical approach and, in particular, statistical thermodynamics, have been made (24-26). In all these cases what has been derived are actually more general equations that, for moderate pore fillings, can be reduced to DR equation.

Having introduced the fundamental aspects of physical adsorption, including its application as a characterization technique for porous materials, next we will present statistical mechanical treatment of these phenomena and link it to the molecular simulation techniques available to study adsorption.

2.2. Statistical mechanics and molecular simulation of adsorption

As we mentioned in Chapter 1 molecular simulations and experimental measurements of adsorption are the main tools which have been applied to pursue the objectives of this thesis. Now, the properties considered in the context of experiments (adsorbed density, bulk pressure, temperature, etc.) belong to the macroscopic realm, while molecular simulations act on the microscopic level, simulating the positions and motion of atoms and molecules. It is therefore important to create a correspondence between the macroscopic and microscopic levels of description. The framework to relate microscopic and macroscopic properties is provided by statistical mechanics and thermodynamics.

At the foundation of statistical mechanics is the concept of an ensemble. An ensemble is a collection of all possible microscopic states (microstates) of a system, subject to a set of extensive constraints, such as fixed energy E of the system, volume V, and number of molecules, N.

The ensemble approach implies that the system under consideration obeys the ergodicity criteria. A closed system in equilibrium is ergodic if in infinite time it goes through all possible microstates. This implies that if we wish to compute macroscopic properties of a system, we can either consider averaging properties of the system as it evolves in time (via,

for example, molecular dynamics) or, equivalently, averaging over microstates generated in a stochastic algorithm (i.e. Monte Carlo) as long as both approaches generate microstates with the Boltzmann distribution.

Different types of ensembles correspond to different sets of properties of the system that are kept fixed. Commonly encountered types of ensemble are the Microcanonical (NVE), Canonical (NVT) and Isothermal-Isobaric (NPT) ensembles. In an adsorption process, molecules from the bulk phase diffuse into the porous material until the equivalence of the chemical potential between the bulk and adsorbed phases is reached. Hence, in this process the porous material is an open system and the Grand Canonical ensemble provides an appropriate framework to describe this system. Therefore, Grand Canonical ensemble is discussed in more detail below.

A Grand Canonical ensemble can be defined as a distribution of microstates for an open system, which is being maintained in thermodynamic equilibrium (thermal and chemical) with a reservoir. The system is open in the sense that it is allowed to fluctuate between various microstates with different energies and different numbers of particles, by exchanging them with the reservoir. Formally, this ensemble is described by fixed chemical potential μ, volume V, and temperature T, or μVT in the abbreviated form.

Within the statistical mechanical formulation, the Grand Canonical ensemble is characterized by a probability distribution π describing the likelihood of observing each microstate. π is proportional to the Boltzmann factor and is normalized through a physically meaningful constant, called the partition function. Both the Boltzmann factor and the partition function are described more in detail below.

The Boltzmann factor is a weighting factor that determines the probability of observing the system of interest in a particular microstate, corresponding to a specific current number of particles N, each with mass m, position $\boldsymbol{r}$ and momentum $\boldsymbol{p}$. In the canonical ensemble (NVT) this probability density is defined as following:

$$\pi = \frac{1}{Q(NVT)} e^{\frac{-H(\boldsymbol{r}^N, \boldsymbol{p}^N)}{k_B T}} \tag{II.23}$$

where $H(\boldsymbol{r}^N, \boldsymbol{p}^N)$ is the Hamiltonian of the N particles, the Boltzmann factor is $e^{\frac{-H(\boldsymbol{r}^N,\boldsymbol{p}^N)}{k_BT}}$ and $Q(NVT)$ is the canonical partition function. For compactness of notation, the quantity $1/k_BT$ is often expressed as β. k_B is the well-known Boltzmann constant, equal to $1.3807 \cdot 10^{-23}$ J/K. Here canonical partition function Q plays a normalization factor role. However, it is also the most fundamental property in the statistical mechanics as it contains in the embedded form the complete information about thermodynamics properties of a particular system under consideration. Specifically, thermodynamic equilibrium of a system under constant NVT condition is described by the minimum of the Helmholtz free energy and this property is linked to the canonical partition function through the expression $A=-kTlnQ(NVT)$.

The partition function for the Grand Canonical ensemble is given as a weighted sum of canonical partition functions, each corresponding to a fixed number of particles N:

$$\Xi(\mu, V, T) = \sum_{N=0}^{\infty} \frac{e^{\frac{\mu N}{k_BT}}}{h^{3N} N!} \cdot Q_N \qquad \text{(II.24)}$$

where Q_N is a canonical partition function for N particles, h^{3N} accounts for the phase space volume of each energetic state and $N!$ accounts for the indistinguishability of the particles and μ is the chemical potential.

Inserting the classical mechanical expression for the canonical partition function Q_N in equation (II.24) we obtain:

$$\Xi(\mu, V, T) = \sum_{N=0}^{\infty} \frac{e^{\frac{\mu N}{k_BT}}}{h^{3N} N!} \int \cdots \int e^{-\beta H(\boldsymbol{r}^N, \boldsymbol{p}^N)} d\boldsymbol{r}^N d\boldsymbol{p}^N \qquad \text{(II.25)}$$

The Hamiltonian $H(\boldsymbol{r}^N, \boldsymbol{p}^N)$ is given by the sum of the potential energy U (accounting for the fluid-fluid and the solid-fluid interactions) and the kinetic energy K (depending on the momenta and the masses of the particles) of the system.

Since the Hamiltonian consists of two contributions, each depending either on the momenta or positions, the partition function above can be factorized into a product of the two contributions:

$$\Xi(\mu,V,T) = \sum_{N=0}^{\infty} \frac{e^{\frac{\mu N}{k_B T}}}{h^{3N} N!} \int e^{\frac{-\boldsymbol{p}^2}{2mk_B T}} d\boldsymbol{p}^N \cdot \int \cdots \int e^{-\beta U(\boldsymbol{r}^N)} d\boldsymbol{r}^N \qquad \text{(II.26)}$$

The integral

$$Z = \int \ldots \int e^{-\beta U(\boldsymbol{r}^N)} d\boldsymbol{r}^N \qquad \text{(II.27)}$$

is called the *configurational integral*, and contains all the information about the intermolecular interactions and, thus, fluid non-idealities. If Z can be solved for a real fluid, then the partition function Ξ can be calculated as well.

The integral associated with the momenta can be reduced to a simple analytical expression:

$$\int e^{\frac{-\boldsymbol{p}^2}{2mk_B T}} d\boldsymbol{p}^N = \int e^{\frac{-\beta \boldsymbol{p}^2}{2m}} d\boldsymbol{p}^N = \left(\frac{2\pi m}{\beta}\right)^{\frac{3N}{2}} \qquad \text{(II.28)}$$

which, in turn, leads to a more compact expression for the partition function:

$$\Xi(\mu,V,T) = \sum_{N=0}^{\infty} \frac{e^{\frac{\mu N}{k_B T}}}{\Lambda^3 N!} \int \cdots \int e^{-\beta U(\boldsymbol{r}^N)} d\boldsymbol{r}^N \qquad \text{(II.29)}$$

where Λ is the de Broglie wavelength, $\Lambda = \frac{h}{\sqrt{2\pi m \cdot k_B T}}$. In a broader physical sense the de Broglie wavelength is way to characterize wave-like behaviour (and wave-particle duality) of non-zero mass particles.

If the partition function is known, all other thermodynamic properties of the system can be derived. In particular, the Grand Potential $\Phi = -pV$, which is a macroscopic property of the system, is linked to the Grand Canonical partition function through:

$$\Phi = -k_B \mathrm{T} \cdot \ln \Xi(\mu, V, T) \qquad \text{(II.30)}$$

Thus, the link between the microscopic world and macroscopic properties is established. However, with an exception for very idealized or simplified systems, it is impossible to directly evaluate expressions such as the one provided above for the Grand Canonical partition function. To circumvent the problem the approach that we adopt in this project is the numerical Monte Carlo procedure in the Grand Canonical ensemble.

The Monte Carlo method is now well established and well documented (27, 28). The main idea of the Monte Carlo approach to the calculation of the properties of a system as statistical averages is to generate a sufficiently large sample M of microstates of the system with appropriate probability distribution density, so that the macroscopic properties can be calculated simply from the averages over the generated microstates. For example, the macroscopic adsorbed density can be calculated as an average of the adsorbed densities for all the generated microstates:

$$< \rho(T, V, \mu) > \approx \frac{1}{M} \cdot \sum_{i=1}^{M} \rho_i \qquad \text{(II.31)}$$

This approach offers an alternative to the calculation of the partition function which, as mentioned before, is a numerically intractable task, except for very simple systems.

A very important practical aspect of molecular simulations is that sampling of the microstates must be efficient, which means that the probability of their existence needs to be non-negligible. This leads to the concept of "importance sampling", which consists of re-distributing the sampling of the configuration space towards the regions where the Boltzmann factor is non-vanishing. An efficient way of generating this target set of microstates is the Metropolis algorithm.

The main idea is to generate states in the configuration space with a relative probability proportional to the Boltzmann factor. The general approach is to first prepare the system in a certain configuration that corresponds to a non-vanishing Boltzmann factor, and then to attempt a perturbation of the system. In general, an attempt to create a perturbation in an old configuration is called a trial move. The nature of the perturbation will depend on the type of

the ensemble under consideration. The Boltzmann factor corresponding to the new trial configuration will be different from the preceding one. The problem is then to decide whether the trial configuration will be accepted or rejected. For simplicity we will now consider the Metropolis algorithm using the canonical ensemble. The number of particles and the volume is fixed in this ensemble, while different microstates in the ensemble correspond to different locations (and momenta) of particles. Therefore to perturb the system and create a new microstate it is sufficient to change the position of one of the particles (here we still adhere to the simple system and do not consider orientational or conformational degrees of freedom for simplicity).

Let us denote the old configuration with *o* and the new configuration with *n*. The old configuration is characterized by Boltzmann factor $e^{-\beta U(o)}$ and probability $\pi(o)$, while for the new configuration the same quantities are $e^{-\beta U(n)}$ and $\pi(n)$. $U(o)$ and $U(n)$ represent the potential energies of the old and new configurations respectively.

The main features of the Metropolis scheme are the following:

1) The outcome of each trial depends only on the outcome of the trial that immediately precedes it (the system has no memory);
2) Every point in the configuration space can be reached within a finite number of trials, which means that the system satisfies the hypothesis of ergodicity;
3) The system must fulfil microscopic reversibility: at equilibrium the average number of accepted trials from the old configuration *o* to any other new configuration *n* must be exactly the same as the number of the accepted reverse moves.

The last condition can be mathematically formulated as follows. If $\Pr(o \rightarrow n)$ is the probability of going from state *o* to state *n* and $\Pr(n \rightarrow o)$ is the probability for a change in the opposite direction, then the following must be true, according to the principle of microscopic reversibility:

$$\pi(o)Pr(o \rightarrow n) = \pi(n)Pr(n \rightarrow o) \qquad \text{(II.32)}$$

which implies that

$$\frac{Pr(o\to n)}{Pr(n\to o)} = \frac{\pi(n)}{\pi(o)} \tag{II.33}$$

The probability $Pr(o\to n)$ is composed of two contributions, $\alpha(o \to n)$ and $\mathrm{acc}(o \to n)$, which respectively represent the probability of *creating* the new configuration *n* starting from the old configuration *o* and the probability of *accepting* the new configuration. In the original Metropolis scheme $\alpha(o \to n) = \alpha(n \to o)$; at the same time, as has been already established, the probabilities π are proportional to the Boltzmann factors. Therefore it is possible to write:

$$\frac{acc(o\to n)}{acc(n\to o)} = \frac{\pi(n)}{\pi(o)} = e^{-\beta(U(n)-U(o))} \tag{II.34}$$

The condition above is particularly significant because it shows that the Monte Carlo simulation alleviates the need to calculate the full partition function or explicit probabilities of each microstate (as these would also involve the partition function). Generation of new microstates is based on the *ratio* of probabilities, and this ratio can be calculated using only the Boltzmann factors.

The condition above will be preserved if the new configuration is accepted with probability:

$$\mathrm{acc}(o \to n) = \min(1, e^{-\beta\left(U(n)-U(o)\right)}). \tag{II.35}$$

In particular:

$$\begin{cases} \mathrm{acc}(o \to n) = 1 & U(n) < U(o) \\ \mathrm{acc}(o \to n) = e^{-\beta\left(U(n)-U(o)\right)} & U(n) > U(o) \end{cases} \tag{II.36}$$

The criteria above are easily explained: indeed, if $U(n) < U(o)$ then the exponent in the Boltzmann factor becomes positive and the Boltzmann factor becomes higher than 1; vice versa, if $U(n) > U(o)$ the exponent is negative and the Boltzmann factor is definitely lower than 1. Evaluating in this way the acceptance probability for the new configuration it will be possible to establish if it can be accepted or not. It can be shown that the ensemble

configurations generated according to this scheme do indeed follow the required Boltzmann distribution and therefore can be used to calculate the average properties of the system as in equation (II.29) (28).

So far we have considered the case of the canonical ensemble, in which new configurations are generated through random displacement of the particles. For monoatomic particles systems displacements are only represented by translations, but in the case of rigid, non-spherical particles, we should also consider rotations of these particles, as a variant of displacement moves.

In the Grand Canonical ensemble, given that the system is open, the number of particles can change, and therefore the perturbation of an old configuration can also happen through the insertion or deletion of the particles. For the Grand Canonical ensemble of rigid molecules four types of trial moves can be identified: translations and rotations, insertions and deletions. Since we have already discussed the translation move and the acceptance criteria associated with it (the formalism for rotational move will remain the same), we now proceed to consider insertion and deletion trial moves. For simplicity of expression we will adopt a notation suitable for simple spherical particles.

In a trial insertion a new particle or molecule is placed into the system in a random position; the acceptance criterion becomes:

$$acc_{INS}(o \to n) = \min(1, \frac{e^{\frac{\mu}{k_B T}}}{\Lambda^3} \frac{V}{N+1} e^{-\beta\left(U(n)-U(o)\right)}) \qquad \text{(II.37)}$$

A deletion trial attempts to remove one of the molecules, selected at random, from the system; in this case the acceptance probability becomes:

$$acc_{DEL}(o \to n) = \min(1, \frac{\Lambda^3}{e^{\frac{\mu}{k_B T}}} \frac{N}{V} e^{-\beta\left(U(n)-U(o)\right)}) \qquad \text{(II.38)}$$

In both cases the probabilities depend on the chemical potential μ, which is related to the fugacity of the bulk fluid in equilibrium with the adsorbed phase through the relation:

$$\frac{f}{k_B T} = \frac{e^{\frac{\mu}{k_B T}}}{\Lambda^3} \tag{II.39}$$

Considering that the fugacity can be easily calculated from the pressure of the bulk phase, which is what is directly measured during an adsorption experiment, the above expression is particularly useful.

In this project the conversion between fugacity and pressure has been implemented using the Peng-Robinson equation of state, known to be accurate for the species under consideration in this thesis.

As stated above, for clarity of notation in our discussion we have assumed simple spherical particles. Nonetheless, the project will also deal with more complex rigid molecules. In these cases the expression for the partition function also needs to include an additional term associated with rigid body rotation of molecules. Similarly to the the treatment of the canonical partition function of simple spherical particles, the Hamiltonian can be factorized into translational, rotational and intermolecular energy contributions, while the canonical partition function becomes a product of translational, rotational and configurational partition functions. Ultimately, it will lead to the appearance of the term representing a single molecule rotational partition function in the acceptance criteria for the Monte Carlo moves. In this way, calling this additional term q_{rot},the acceptance and deletion probabilities will become:

$$acc_{INS}(o \to n) = \min\left(1, \frac{q_{rot} e^{\frac{\mu}{k_B T}}}{\Lambda^3} \frac{V}{N+1} e^{-\beta\left(U(n)-U(o)\right)}\right) \tag{II.40}$$

and

$$acc_{DEL}(o \to n) = \min\left(1, \frac{q_{rot}\Lambda^3}{e^{\frac{\mu}{k_B T}}} \frac{N}{V} e^{-\beta\left(U(n)-U(o)\right)}\right) \tag{II.41}$$

We will now proceed with the description of the experimental measurements of adsorption, starting with the basic review of the techniques available and then focusing on the specific apparatus and the methodology employed in this work.

2.3. Adsorption experiments

As mentioned in the first part of this chapter the most common way to describe and quantify adsorption is the adsorption isotherm, which shows the relationship between the amount of fluid adsorbed by unit mass or unit volume of adsorbent and the equilibrium pressure *p* at a certain temperature *T*.

To obtain the adsorbed amount as a function of pressure and temperature different experimental methods can be used, each of them implying the measurement of a different variable. Broadly, these methods can be divided into four types: volumetric/manometric, gravimetric, carrier gas and calorimetric methods.

A comprehensive review of the existing methods has been written by Keller and Staudt (29). In the context of this work we limit ourselves to a brief description and comparison of the gravimetric and the volumetric methods, which have also been extensively discussed by Belmabkhout et al. (30). More detail will be put in the description of the volumetric method, which is the one adopted for this project.
In the case of gravimetric method, which is considered as a well-established and accurate technique, the variable to be measured as a function of pressure at a certain temperature is the adsorbed mass by means of a balance.

A well-known problem with this method is the buoyancy effect, which is due to the force exerted by the gas on the adsorbent, thus influencing the measurement of the mass. This becomes a particularly important issue in high pressure experiments.

The volumetric method gives an indirect measurement of the amount adsorbed. It consists in expanding a gas from a pressure cell (pre-adsorption cell) into an evacuated adsorption cell containing a clean adsorbent during an isothermal process. The volumes of both cells, respectively V_{pre} and V_{ads}, are known.

The total amount of gas initially introduced in the pre-adsorption cell (N_1) and the amount of gas remaining in the pre-adsorption and adsorption cells after the adsorption equilibrium is reached (N_2) are determined, using an appropriate equation of state, through the measurement

of pressure before and after adsorption, while the temperature *T* is kept constant for the whole experiment.

The calculation procedure is as follows:

$$N_1 = \frac{V_{pre}}{V_m(T,p_1)} \tag{II.42}$$

$$N_2 = \frac{V_{pre}+V_{ads}}{V_m(T,p_2)} \tag{II.43}$$

$$N_{ads} = \frac{N_1-N_2}{m_{sample}} \tag{II.44}$$

where $V_m(T,p_1)$ and $V_m(T,p_2)$ are the molar volumes of the adsorbate in the gas phase at temperature T and pressures respectively p_1 and p_2, m_{sample} is the mass of the outgassed adsorbent and N_{ads} is the adsorbed number of moles per unit mass of the outgassed adsorbent. $V_m(T,p_1)$ and $V_m(T,p_2)$ are calculated through the chosen equation of state.

Compared to the gravimetric method, volumetric method is easier to setup and use. It is particularly suitable for high pressure measurements, where buoyancy would cause substantial problems for the gravimetric analysis.

A significant disadvantage of the volumetric method is due to the errors arising from the indirect determination of the adsorbed quantities; in particular, the main sources of errors in this technique are associated with the determination of the pre-adsorption and adsorption cell volumes, the error in the pressure and temperature measurements, the error due to leakage at high pressure, the error in the sample mass and the error due to the inaccuracies of the equation of state.

The volumetric apparatus and the experimental procedure used for the adsorption measurements in the present project are described in the next sections.

2.3.1. Description of the adsorption apparatus

High pressure CO_2 and CH_4 adsorption isotherms have been measured on a sample of Maxsorb with the BET surface area of 3179.24 m^2/g and micropore volume of 1.63 cm^3/g using a static volumetric rig.

A schematic representation of the apparatus is shown in Figure 2.4. The rig can be used for static volumetric measurements of pure component isotherms and mixtures, at pressures up to 33 bar (with an accuracy of 0.05% of the usable measurement range) and temperatures between 263 and 370 K.

During the experimental measurements the temperature is kept constant (±0.02 K) using a bath provided with a refrigerating/heating circulator (Julabo type F25) for temperatures up to 300 K; if the temperature needs to be higher it is maintained using a jacket oven, which can also be used for the regeneration of the sample *in situ*. The regeneration of the sample always takes place under vacuum (generally less than $2 \cdot 10^{-3}$ Torr), using a rotary pump (Edward type RV5). The degree of vacuum is monitored with a vacuum gauge (Edward type Active Pirani Gauge). Different sections of the rig are connected through a system of Swagelok valves and can be isolated from each other as required by the experimental protocol.

The rig is also equipped with two mass flow controllers (Brooks type 5850), a back-pressure controller (Brooks type 5866), and a read out/control device (Brooks type 0154).

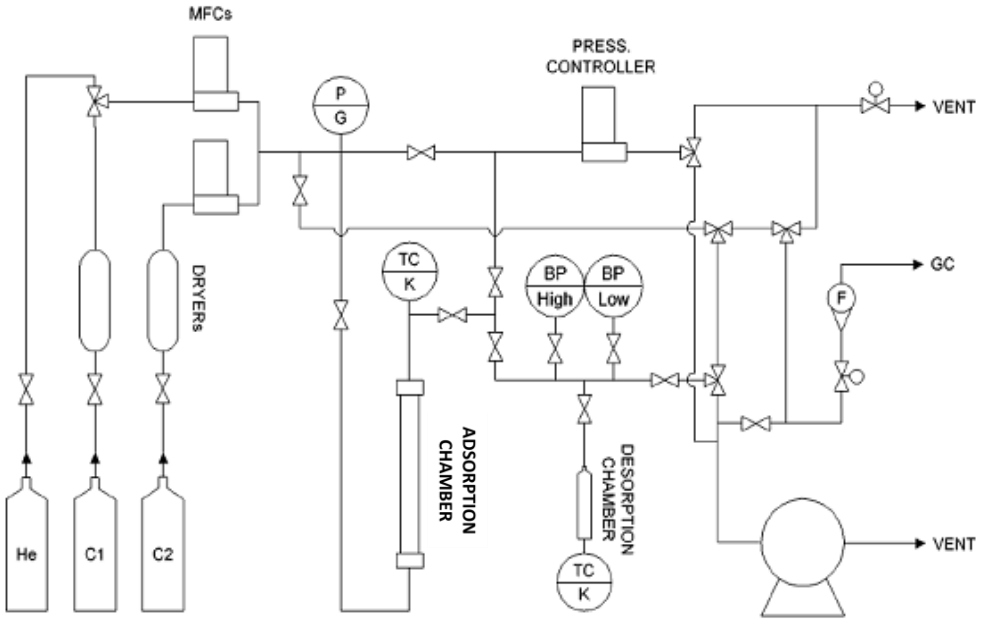

Figure 2.4. Schematic representation of the adsorption apparatus.

The apparatus is fitted with two Baratron absolute pressure transducers (MKS type 127A) with a two-channel readout/signal conditioner (MKS Type PR4000).

From Figure 2.4 it can be seen that the adsorbent is placed in a cell (adsorption chamber) which can be isolated from the rest of the apparatus. During the adsorption experiment a certain amount of adsorptive gas at a specified temperature and pressure is first introduced in the part of the apparatus that immediately precedes the adsorption chamber (pre-adsorption chamber). Once thermal equilibrium has been reached, the valve that separates the two chambers is opened and the adsorption process can start. Once the equilibrium is reached (this step can take from a few minutes to several days, depending on the species and conditions involved) temperature and pressure are recorded and the amount adsorbed is calculated according to the procedure described above for the volumetric measurements. The equation of state that has been employed for this work is Peng-Robinson.

Before each adsorption measurement the sample is regenerated by heating it up (with the jacket oven placed around the adsorption cell) and evacuating the adsorption cell. The dead volume of the system, required for the volumetric calculations, is measured using Helium expansion. This consists in introducing He at sub-atmospheric pressure (generally between 250 and 500 Torr) into the only part of the rig for which the volume is known (the desorption chamber in our case). Then, knowing volume, temperature and pressure, the number of moles

of gas is calculated using the Ideal Gas law. Once the number of moles is known the gas is allowed to expand into other parts of the rig (one at a time), and every time the volume that occupies each of them is calculated.

The apparatus is also equipped with a desorption chamber and a gas chromatograph Shimadzu GC-14B with a thermal conductivity detector, to be used when the experiment involves mixtures. A description of the rig and the experimental procedure can also be found in literature (31).

We will now describe the experimental procedure adopted specifically for this project.

2.3.2. Operating procedure and adsorption isotherms

Before each adsorption measurement in this study, the sample was regenerated for at least 5 hours at 433 K. Each point on the adsorption isotherm required between 45 min and 1 hour of equilibration time, while thermal equilibrium in the pre-adsorption chamber was considered to be achieved after 15 minutes.

Given that the sample of Maxsorb MSC-30 was in the form of fine powder, it was necessary to place it, before placing it in the adsorption chamber, in a membrane container (figure 2.5). This allowed for the equilibration of the sample with the gas phase in the chamber and prevented contamination of the system.

Figure 2.5. a) adsorption chamber b) membrane container filled with sample and sealed.

The container has a cylindrical design, composed by two stainless steel pieces placed on the extremes, with the same diameter as the inner adsorption chamber. The membrane is glued to the metal pieces forming a cylinder. The top piece has a hole that permits the introduction of the sample, which is then sealed through a screw; the bottom metal piece has an opening to fit a thermocouple to accurately measure the temperature of the sample during the experimental measurements. Figure 2.5 shows the pictures of the adsorption chamber (a) and the membrane container (b) used for the experimental measurements.

Methane and carbon dioxide adsorption isotherms were measured on 1.3707 g of dried sample at 273 and 298 K. Each experimental measurement has been followed by regeneration of the sample in order to prepare it for the following isotherm. To insure the reliability and the reproducibility of our measurements (for which the uncertainty has been estimated to be lower than 1%) the adsorption isotherms experimentally determined in our group have been compared with those reported in literature. The results of these comparisons are shown in figure 2.6.

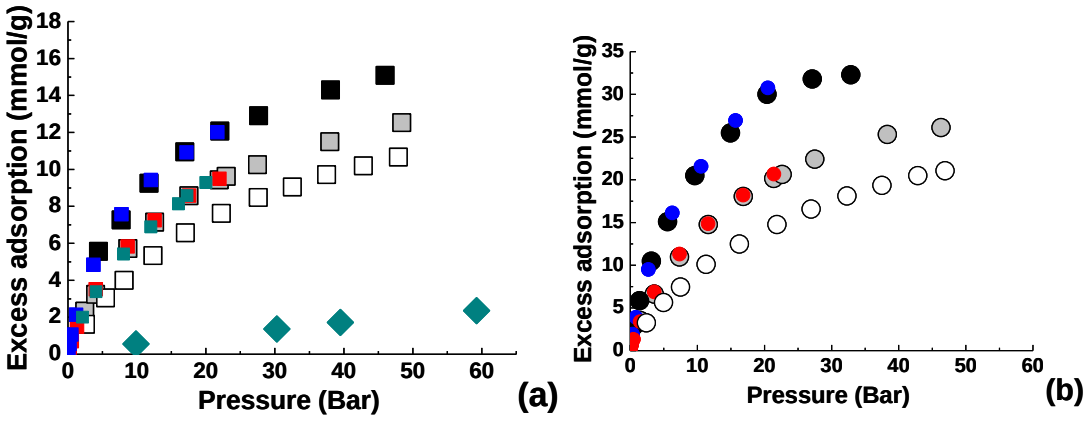

Figure 2.6. (a) Experimental adsorption isotherms measured by different groups on Maxsorb MSC-30. Black (4) and blue (present work) squares are for CH_4 at 273 K. Red squares (4), cyan squares (32) and grey squares (present work) are for CH_4 at 298 K. Open squares (4) are for CH_4 at 323 K. Cyan diamonds are for H_2 at 298 K (33). (b) Black circles (4) and blue circles (present work) are for CO_2 at 273 K. Grey circles (4) and red circles (present work) are for CO_2 at 298 K are for CO_2 at 298 K. Open circles are for CO_2 at 323 K (4).

An excellent agreement is observed at all temperatures for CO_2 and CH_4. The graph also shows the adsorption of H_2 at 298 K as measured by Linares-Solano and co-workers (33). The agreement between the literature data and our own results makes it possible to use all the isotherms shown in Figure 2.6 as reference in our model validation.

The sample of Maxsorb MSC-30 has been characterized through the measurement of nitrogen adsorption at 77.35 K (the isotherm is shown in Figure 2.7) performed on a Quantachrome Autosorb IQ apparatus coupled with the Quantachrome ASiQwin software for the automated acquisition and reduction of the data. In particular, the micropore volume has been determined using Dubinin-Radushkevich method (14), while the surface area has been determined using the BET method (7), following the consistency criteria described by Rouquerol, Llewellyn and Rouquerol (11) for the application of the BET equation to the microporous materials. Further details on the calculation of the accessible surface area will be presented in the Appendix (Section A9.4.1).

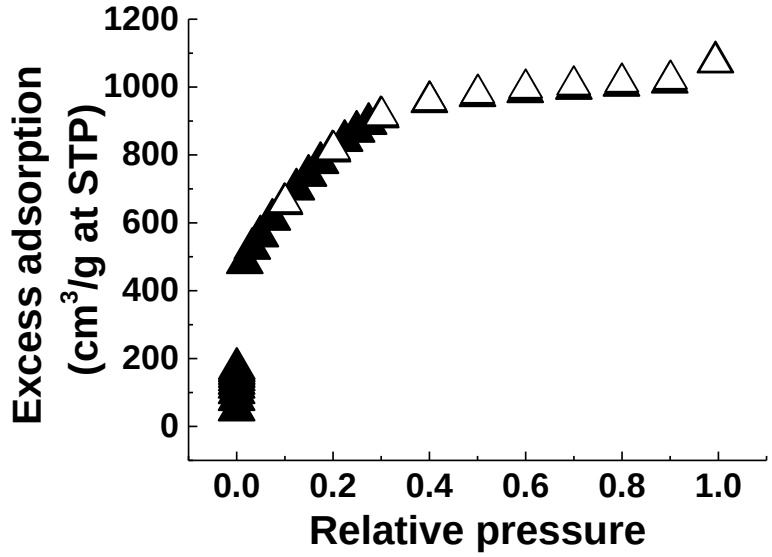

Figure 2.7. Nitrogen experimental adsorption isotherm measured on our sample of Maxsorb MSC-30 at 77.35 K. Black and white symbols represent respectively adsorption and desorption branches.

The isotherm in figure 2.7 shows perfect reversibility of the adsorption process.

So far we have described molecular simulation of adsorption process and the experimental procedures to measure adsorption. In both cases the outcome is an adsorption isotherm. However, it is important to compare isotherms from simulations and experiments on a consistent basis and this is briefly discussed in the next section

2.3.3. Calculation of excess adsorption

The outcome of the adsorption experiments is the so called excess adsorption. Provided that in all adsorption experiments the contact between the adsorbent and the adsorptive happens in a vessel called adsorption cell, excess adsorption is defined as the difference between the total amount of fluid present in the cell (absolute adsorption) and the amount of fluid that would be in the cell in the absence of the adsorbent. The results of molecular simulations, instead, are expressed in terms of absolute adsorption. It is therefore necessary to convert these results into excess adsorption. This is often achieved following the procedure proposed by Talu and Myers (34), which we also adopt in the present work:

$$N_{exc} = N_{abs} - \rho_{bulk} V \tag{II.45}$$

where N_{exc} is the excess adsorption density, N_{abs} is the absolute adsorption density per unit cell as calculated from simulation, V is the accessible pore volume and ρ_{bulk} is the density of the bulk adsorbate.

As explained in Section 2.3.2, during the experiments the dead volume has been determined through Helium expansion; for consistency with the experimental protocol the pore volume therefore has been calculated using Helium as a probe. According to Talu and Myers, volume accessible to Helium is related to its second adsorption virial coefficient:

$$V = B^a = \frac{1}{m_s} \int e^{\frac{-U_{sf}(\boldsymbol{r})}{k_B T}} d\boldsymbol{r} \tag{II.46}$$

where V is the volume accessible to Helium, B^a is the adsorption second virial coefficient for Helium from simulation, m_s is the mass of a representative sample of the solid adsorbent in the simulation and $U_{sf}(\boldsymbol{r})$ is the solid-fluid potential energy of a single gas molecule with position $\boldsymbol{r}$.

The second virial coefficient can be calculated using the Widom insertion method (35), where a probe Helium atom is placed in random positions within the system and the values of the corresponding Bolzmann factors are accumulated into an average. This average multiplied by the system volume provides an estimate of the integral constituting the second virial coefficient.

In this chapter we have introduced all the concepts and tools required for the development of the project described in this thesis. The next three chapters will show the results of our research, derived from application of the methods and techniques we have presented here. More advanced details concerning these methods and techniques will also be introduced in the next chapters when pertinent and necessary.

References

1. Sing KSW, Everett DH, Haul RAW, Moscou L, Pierotti RA, Rouquerol J, et al. REPORTING PHYSISORPTION DATA FOR GAS/SOLID SYSTEMS with Special Reference to the Determination of Surface Area and Porosity. Pure & Applied Chemistry. 1985;57(44):603-19.
2. Dubinin MM. The Potential Theory of Adsorption of Gases and Vapors for Adsorbents with Energetically Nonuniform Surfaces. Chemical Reviews. 1960;60(2):235-41.
3. Bansal RC, Goyal M. Activated Carbon Adsorption: CRC Press; 2005.
4. Himeno S, Komatsu T, Fujita S. High-Pressure Adsorption Equilibria of Methane and Carbon Dioxide on Several Activated Carbons. Journal of Chemical & Engineering Data. 2005;50(2):369-76.
5. Dreisbach F, Staudt R, Keller JU. High Pressure Adsorption Data of Methane, Nitrogen, Carbon Dioxide and their Binary and Ternary Mixtures on Activated Carbon. Adsorption. 1999;5(3):215-27.
6. Langmuir I. THE CONSTITUTION AND FUNDAMENTAL PROPERTIES OF SOLIDS AND LIQUIDS. PART I. SOLIDS. Journal of the American Chemical Society. 1916;38(11):2221-95.
7. Brunauer S, Emmett PH, Teller E. Adsorption of Gases in Multimolecular Layers. Journal of the American Chemical Society. 1938;60(2):309-19.
8. Tóth J. Uniform interpretation of gas/solid adsorption. Advances in Colloid and Interface Science. 1995;55(0):1-239.
9. Toth J. Adsorption. Theory, modeling, and analysis.: Taylor & Francis; 2002.
10. Myers AL, Prausnitz JM. Thermodynamics of mixed-gas adsorption. AIChE Journal. 1965;11(1):121-7.
11. Rouquerol J, Llewellyn P, Rouquerol F. Is the BET equation applicable to microporous adsorbents? In: Llewellyn PL, Rodriguez-Reinoso F, Rouquerol J, Seaton N, editors. Studies in SurfaceScience and Catalysis Elsevier; 2007. p. 49-56.
12. Coasne B, Gubbins KE, Pellenq RJM. A Grand Canonical Monte Carlo Study of Adsorption and Capillary Phenomena in Nanopores of Various Morphologies and Topologies: Testing the BET and BJH Characterization Methods. Particle & Particle Systems Characterization. 2004;21(2):149-60.
13. Bae Y-S, Yazaydın AÖ, Snurr RQ. Evaluation of the BET Method for Determining Surface Areas of MOFs and Zeolites that Contain Ultra-Micropores. Langmuir. 2010;26(8):5475-83.
14. Dubinin MM, Radushkevich LV. Equation of the characteristic curve of activated charcoal. Proceedings of the Academy of Sciences, Physical Chemistry Section, USSR 55. 1947:331-3.
15. Polanyi M. Section III.-Theories of the adsorption of gases. A general survey and some additional remarks. Introductory paper to section III. Transactions of the Faraday Society. 1932;28(0):316-33.
16. Dubinin MM. Adsorption in micropores. Journal of Colloid and Interface Science. 1967;23(4):487-99.
17. Dubinin AMM. A study of the porous structure of active carbons using a variety of methods. Quarterly Reviews, Chemical Society. 1955;9(2):101-14.
18. Bering BP, Dubinin MM, Serpinsky VV. Theory of volume filling for vapor adsorption. Journal of Colloid and Interface Science. 1966;21(4):378-93.
19. Dubinin MM. In: Walker, editor. Chemistry and Physics of Carbon. 2. London: Arnold; 1966. p. 51.
20. Marsh H. Adsorption methods to study microporosity in coals and carbons—a critique. Carbon. 1987;25(1):49-58.
21. Marsh H, Rand B. The characterization of microporous carbons by means of the dubinin-radushkevich equation. Journal of Colloid and Interface Science. 1970;33(1):101-16.
22. Porosity in Carbons: characterization and applications: John Wiley & Sons Inc; 1995.
23. Barrer RM. Specificity in physical sorption. Journal of Colloid and Interface Science. 1966;21(4):415-34.
24. Chen SG, Yang RT. Theoretical Basis for the Potential Theory Adsorption Isotherms. The Dubinin-Radushkevich and Dubinin-Astakhov Equations. Langmuir. 1994;10(11):4244-9.

25. Ustinov EA, Polyakov NS, Petukhova GA. Statistical interpretation of the Dubinin-Radushkevich equation. Russ Chem Bull. 1999;48(2):261-5.
26. Nguyen C, Do DD. The Dubinin–Radushkevich equation and the underlying microscopic adsorption description. Carbon. 2001;39(9):1327-36.
27. Allen MP, Tildesley DJ. Computer Simulation of Liquids. Bristol: J.W. Arrowsmith Ltd.; 1989.
28. Frenkel D, Smit B. Understanding Molecular Simulation: From Algorithms to Applications: Academic Press; 2002.
29. Keller JU, Staudt R. Gas Adsorption Equilibria: Experimental Methods and Adsorptive Isotherms: Springer; 2005.
30. Belmabkhout Y, Frère M, Weireld GD. High-pressure adsorption measurements. A comparative study of the volumetric and gravimetric methods. Measurement Science and Technology. 2004;15(5):848.
31. Heuchel M, Davies GM, Buss E, Seaton NA. Adsorption of Carbon Dioxide and Methane and Their Mixtures on an Activated Carbon: Simulation and Experiment. Langmuir. 1999;15(25):8695-705.
32. Lozano-Castelló D, Cazorla-Amorós D, Linares-Solano A. Powdered Activated Carbons and Activated Carbon Fibers for Methane Storage: A Comparative Study. Energy & Fuels. 2002;16(5):1321-8.
33. Jordá-Beneyto M, Suárez-García F, Lozano-Castelló D, Cazorla-Amorós D, Linares-Solano A. Hydrogen storage on chemically activated carbons and carbon nanomaterials at high pressures. Carbon. 2007;45(2):293-303.
34. Talu O, Myers AL. Molecular simulation of adsorption: Gibbs dividing surface and comparison with experiment. AIChE Journal. 2001;47(5):1160-8.
35. Widom B. Some Topics in the Theory of Fluids. The Journal of Chemical Physics. 1963;39(11):2808-12.

Chapter 3

Slit pore models in application to Maxsorb activated carbon

3.1. Introduction

As explained in Chapter 1, the main objective of this thesis is to develop a predictive model of adsorption in high surface area activated carbons and apply this to adsorption separation processes associated with carbon capture. This is not an easy task, because activated carbons are, structurally, among the most complex porous materials and this presents the most significant challenge in modelling their properties.

Figure 3.1 shows the High Resolution Transmission Electron Microscopy (HRTEM) images of two different types of activated carbons. This picture nicely illustrates structural diversity possible within this family of materials. Specifically, for a sample of Norit material (Figure 3.1 on the left) (1), it is possible to identify regions of lamellar structure and this may suggest a simple model reflecting this structural organization. On the other hand, activated carbon material shown on the right of Figure 3.1 (2) seems to lack any kind of order.

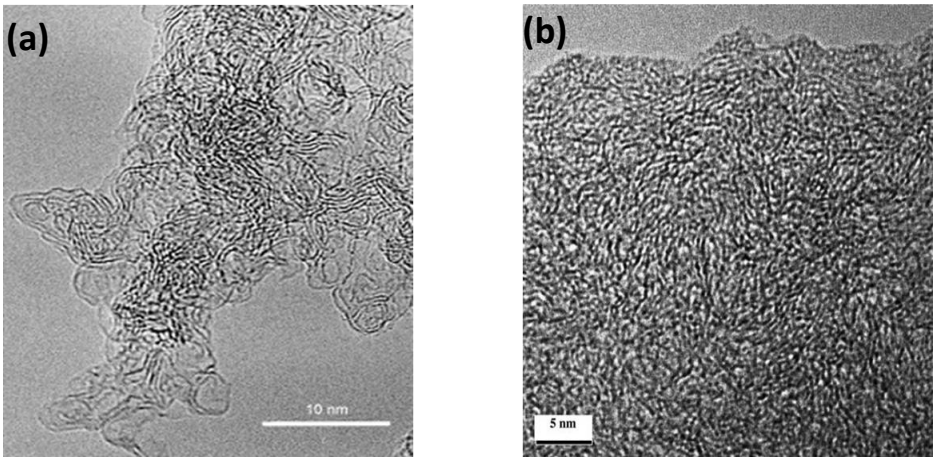

Figure 3.1. HRTEM images of activated carbons: a) activated carbon Norit GSX (1); b) activated carbon prepared by NaOH activation of anthracite (2).

Structural analysis of activated carbons has been important for many decades as these materials are extensively used in chemical engineering, and the first models (or hypotheses on the structural organization of porous carbons) actually predate the era of computers and molecular simulations.

The slit pore model is the most commonly used model to describe activated carbons (3). Based on the experimental evidence of the lamellar pore structure in many carbons, it treats porous space as a collection of independent slit pores, with the pore walls made of an infinite number of graphite sheets. From the fundamental perspective, a single slit pore is the simplest model of a porous structure and, not surprisingly, a substantial body of the early theoretical insights on the confined fluid properties had been obtained using this model.

Figure 3.2 shows a schematic representation of a finite element of graphitic slit pore. In this figure, *W* is the pore width and it is defined as the distance between the nuclei of the first layers of carbon atoms on opposing pore walls. Figure 3.2 also shows a molecule of CO_2 in the porous space: *z* is the distance between one site of the molecule (in this specific case the centre of mass) and a carbon atom in the adsorbent surface.

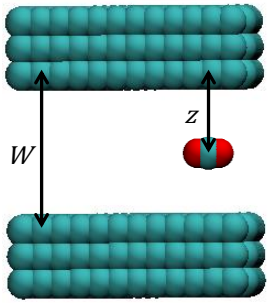

Figure 3.2. Schematic representation of a slit pore with the walls made of three graphene sheets and a CO_2 molecule in the porous space. Cyan: carbon, red: oxygen.

The slit pore model is clearly an oversimplification, as the porous space of a real carbon material features pores of different sizes and shapes, forming a complex network. One way to increase realism of the model based on the slit pore representation is to allow for a possibility of slit pores of different sizes within the structure (the pores however still remain independent). The pore size distribution (PSD) then characterizes the distribution of total pore volume over slit pores of different width.

The notion of PSD opens two important possibilities. On one hand, if the model is an accurate depiction of a porous material, an adsorption isotherm in this material must be a cumulative result of adsorption in different slit pores and therefore it should in principle be possible to obtain a PSD from this experimental measurement. On the other hand, if the true PSD for the material is known, it should be possible to predict adsorption properties of this material, by considering adsorption in individual slit pores and weighting the behaviour of individual pores with the PSD. These ideas have been the starting point in the development of characterization and predictive adsorption models for activated carbons. Below we describe the key steps and elements generally involved in this class of approaches.

The pore size distribution, ($f(W)$), is formally defined as:

$$f(W) = dV/dW \tag{III.1}$$

where V is the volume of the pores of width W per unit mass of the adsorbent.

The adsorption integral equation (AIE) establishes, for a certain pressure p and temperature T, a relationship between the amount of fluid adsorbed in the whole sample of the material ($N(T,p)$), the adsorption in single slit pores ($\rho(W,T,p)$) and the PSD ($f(W)$) (4):

$$N(T,p) = \int_0^\infty \rho(W,T,p) f(W) dW \qquad \text{(III.2)}$$

In the characterization mode, the amount adsorbed in the whole sample is measured experimentally. Adsorption in individual slit pores is generated using either grand canonical Monte Carlo or classical density functional methods. Solution of the AIE allows one to recover a PSD. In the predictive mode, AIE combines an already established PSD and simulated adsorption isotherms in individual pores, to obtain the adsorption behaviour of the material with respect to new species or under new conditions. Figure 3.3 shows a schematic representation of the AIE approach, summarizing the concepts which have just been explained.

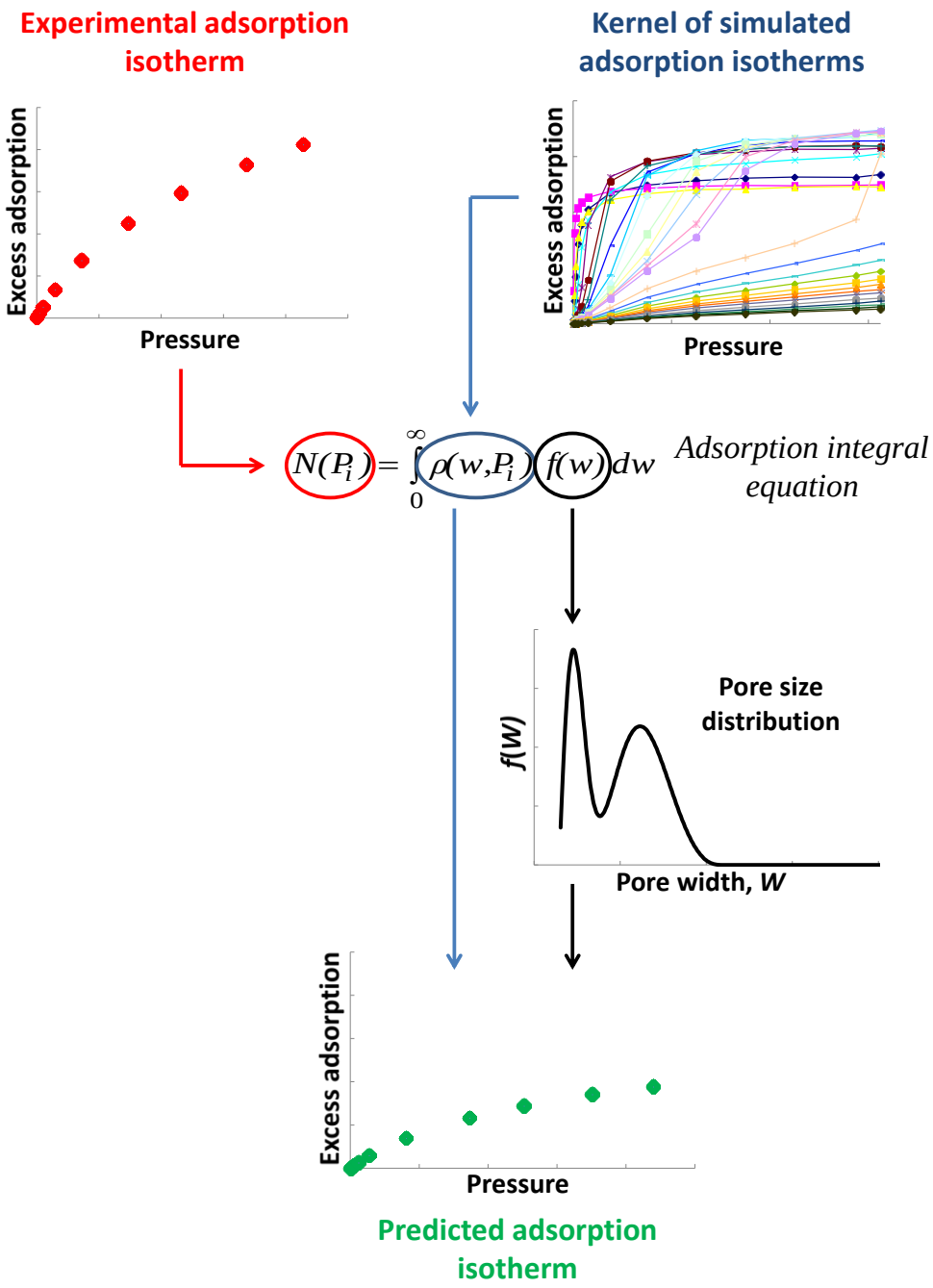

Figure 3.3. Schematic representation of the protocol involved in the AIE approach.

The difficulty with this approach lies in the fact that the AIE cannot be solved analytically, as this is a Fredholm integral equation of the first kind; therefore the determination of the PSD requires special numerical techniques. Several alternative approaches exist. For example, Sweatman and co-workers (5) employed a sum of log-normal functions, each with three free parameters, and used a simulated annealing scheme to converge to the most appropriate PSD by minimizing the errors between the fit isotherm and the experimental data. Similar methods

were used by Lastoskie et al. (6), Sosin and Quinn (7) and Scaife et al. (8) Here we adopt the numerical method developed by Davies and Seaton (9) (10), as it is well established in the literature and has been extensively applied to study adsorption of alkanes (methane, ethane) and carbon dioxide in various porous carbon materials (11-14). Similar methodology has been also used by Neimark and co-workers (15). An additional factor in choosing this methodology has been access to the required codes from the group of Prof. Seaton at the University of Edinburgh. It is important to emphasize, however, that further development of these methods or their comparison with other existing approaches to obtain PSD is out of scope of this thesis. On this note let us briefly recollect the main aspects of the procedure.

The protocol is based on a discretized representation of the PSD: the range of the pore widths which is taken into account (with the upper limit being an arbitrarily large pore size) is appropriately split into *m* quadrature intervals δW_j, each of average pore size W_j^*; in this way for all the data points, each corresponding to pressure p_i,the AIE can be written as:

$$N(T,p_i) = \sum_{j=1}^{m} \rho\left(W_j^*, T, p_i\right) f\left(W_j^*\right) \delta W_j \qquad \text{(III.3)}$$

where the values of W_j^* represent the widths of the *m* pores in the PSD.

Once the AIE has been discretized, it is possible to attempt the calculation of a representative PSD: the idea is to use a least square algorithm to minimize the difference between the right and the left side of equation (III.3) for a set of *n* data points, i.e. to minimize the following residual:

$$R = \sum_{i=1}^{n} \left[N(T,p_i) - \sum_{j=1}^{m} \rho\left(W_j^*, T, p_i\right) f\left(W_j^*\right) \delta W_j\right]^2 \qquad \text{(III.4)}$$

R is a quadratic function of $f\left(W_j^*\right)$, with positive coefficient for the quadratic term. This implies that *R* is a convex semi-definite positive function and therefore it has only one global minimum or several degenerate minima.

Equation (III.3) can be written more compactly in matrix notation:

$$N = AWf \tag{III.5a}$$

where

$$N = N(T, p_i)_{i=1\ldots n} \tag{III.5b}$$

$$A = (\rho(W_j^*, T, p_i))_{i=1\ldots n, j=1\ldots m} \tag{III.5c}$$

$$W = diag(\delta W_j)_{j=1\ldots m} \tag{III.5d}$$

$$f = (f(W_j^*))_{j=1\ldots m} \tag{III.5e}$$

A physically meaningful PSD must be strictly nonnegative, therefore $f \geq 0$.

$$R = (N - AWf)^T (N - AWf) \tag{III.6}$$

Special attention is required because the solution of the AIE is an ill-posed problem: if one PSD can be fitted to the data in principle an infinite number of PSDs can; also, small perturbations in the data can lead to very different PSDs, thus challenging their physical meaning. One way to make the calculations relatively insensitive to small perturbations in the data (in particular to the error associated with the experimental measurements) is to adopt a regularization procedure, which is to add additional constraints that can be based on the smoothness of the PSD.

For this purpose it is necessary to take into account a function which measures the smoothness of the PSD; in this case equation (III.6) becomes:

$$R_{Reg} = (N - AWf)^T (N - AWf) + \alpha S \tag{III.7}$$

where α is a strictly non-negative smoothing parameter and S is a discrete representation of a function suitable to measure the smoothness of the PSD. The most commonly adopted function for the purpose is the integral of the square of the second derivative of the pore size distribution (9). Therefore S can be written as:

$$S = \sum_{j=1}^{m} [f''(w_j^*)]^2 \delta w_j \qquad \text{(III.8)}$$

This implies that R_{Reg} is also a semi-definite positive convex function.

Once S has been chosen, equation (III.7) can be solved for a specific value of α using standard nonlinear minimization routines.

Davies and Seaton have adopted two methods to estimate the optimal value of the smoothing parameter: the approximation to the generalized cross-validation (GCV) score function, originally proposed by Wilson (16), and the so called "L-curve" (9, 10).

In the case of the GCV score function the main assumption is that a well-chosen smoothing parameter would make it possible to predict any of the n experimental data points from a PSD determined using the remaining n-1 data points. In the approximation proposed by Wilson (16), appropriate when calculating strictly non-negative PSDs, the optimal smoothing parameter is the one which minimizes the GCV function.

As for the "L-curve" this is a plot of the error of the fit to the data as a function of the smoothing parameter. Up to a certain value (taken as a threshold) of the smoothing parameter, the error usually remains more or less constant (or increases extremely slowly) with the increase of the smoothing parameter; after the threshold value the increase in the error is much faster. It is exactly this threshold value which is considered to be the best value of the smoothing parameter for the pore size distribution: the error is still reasonable and at the same time the PSD is smooth). Figure 3.4 shows examples of L-curve and GCV plot reported in literature (17):

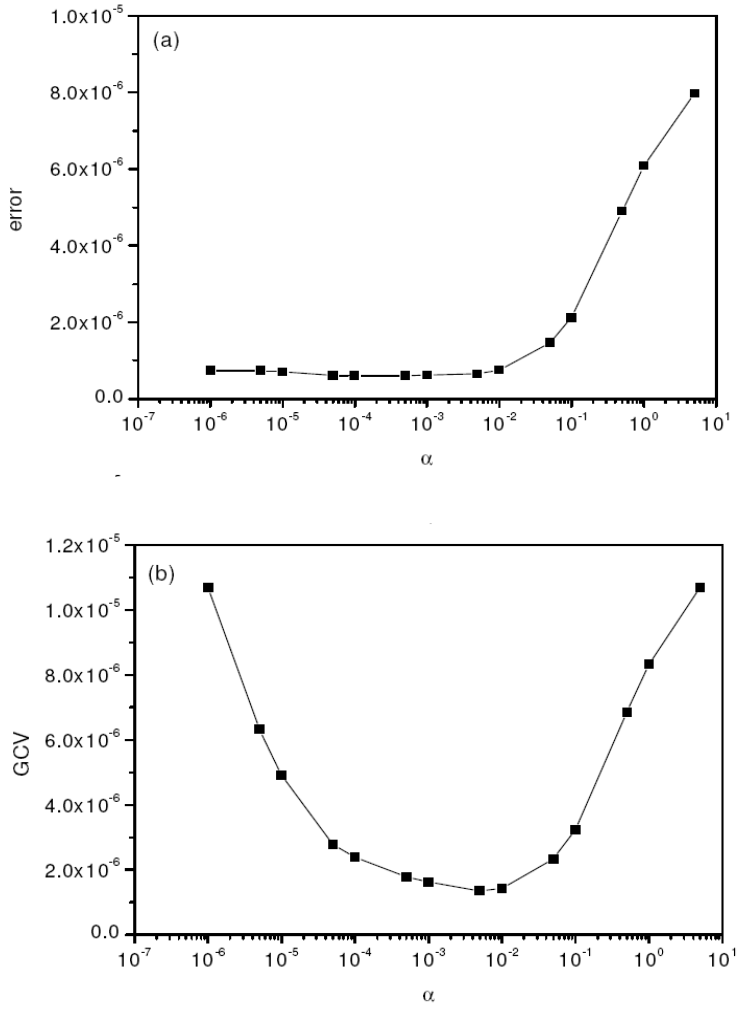

Figure 3.4. Examples of (a) L-curve and (b) GCV score function presented in literature (17).

A simple overview of the issues related to the extraction of a reliable PSD, different methods and regularization protocols is presented in the review by Vega (18).

The slit pore model has been applied to investigate adsorption of different light gases in activated carbons, including CO_2, N_2, CH_4 and H_2O (12, 19-29). In some cases not only single components but also binary and more complex mixtures have been considered (12, 21, 27). Applications of the slit pore model include the work by Nicholson (30), who was able to capture the variation of the isosteric heat of adsorption of methane and carbon dioxide, and the work by Lopéz-Ramón et al. (31), who were able to predict the adsorption properties of certain activated carbons for CH_4, SF_6 and CF_4 for a wide range of pressures and temperatures.

It has been also recognized that the slit pore model may be oversimplified to adequately describe the complex nature of real carbon materials. In particular, as pointed out by Jorge and Seaton (32), the model may not be sufficiently accurate for the prediction of the adsorption properties of highly polar species; in their work they needed to include polar surface groups to be able to successfully capture the adsorption properties of water/ethane mixture in BPL carbon. The capability of a model to correctly capture the behaviour of species such as water is particularly important for the study of CC processes, as water can have an effect on the efficiency, and therefore on the costs, of the separations.

Over the years different elements of heterogeneity have been added to the classical slit pore model, including structural defects, impurities, sheets of finite size, active sites, functional groups, effects of pore blocking and connectivity (29, 33-48). Nguyen and Bhatia have also introduced the concept of pore wall thickness distribution (PWTD), to be taken into account besides the PSD (49-51).

Similar approaches have been also applied to materials known a priory to be highly heterogeneous, such as the combustion-chamber deposits (CCDs) which tend to accumulate on the inner surfaces of internal combustion engines (14, 52). In this case, the procedure described above becomes an optimization problem to find a PSD, with all different types of structural heterogeneities effectively incorporated into this function. Although the generated function may still provide an optimal solution (in terms of the ability of the model, based on this function, to predict adsorption of different species under different conditions), the physical meaning of the peaks in this function and whether they really correspond to the existence of slit pores of that specific size becomes less certain.

Here we recognize that it is unlikely that the slit pore model is a realistic representation of the very heterogeneous high surface area materials such as Maxsorb. Nevertheless, in this chapter we attempt to follow the protocol described above to construct a predictive model of Maxsorb based on the slit pore representation. This will allow us to place our studies in the context of the previous substantial body of work based on this approach and rigorously establish its scope and applicability.

In figure 3.5 we show the PSD which has been reported in literature for Maxsorb, compared to the PSD of a steam activated carbon (AC) in the original publication by Otowa et al. (53). This distribution was obtained by the authors using data from nitrogen at 77 K with Cranston and Inkley analysis method (54), which is still based on a slit pore representation of the carbon; therefore it is to some extent subject of all the uncertainties described above.

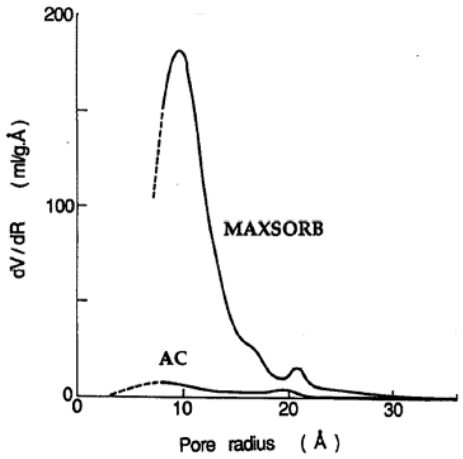

Figure 3.5. Pore size distribution typical of Maxsorb compared to the PSD of a steam activated carbon (AC), both determined starting from nitrogen adsorption data (53).

According to this figure, the PSD in Maxsorb is centred around the pore size of 20 Å (the very intense peak), while also a smaller peak at 40 Å of pore size can be observed (in the figure the sizes are shown as the radii of the pore). Here we will use this figure for comparison with the PSDs obtained from adsorption of species more relevant in the context of CC applications (carbon dioxide and methane at ambient temperatures).

Specifically, in all cases our work will be based on the experimental isotherms we have measured on methane and carbon dioxide at 273 and 298 K, which have been presented in Chapter 2.

We start from the study of the classic slit pore model applied to Maxsorb (Section 3.3). For this purpose we use grand canonical Monte Carlo method to simulate appropriate kernels of isotherms in pores of different widths for the same fluids and in the same conditions as for our reference experimental isotherms. Using the experimental and simulated data we derive possible pore size distributions for Maxsorb and use them to make predictions, which are

always compared with the reference adsorption isotherms. Parameters of the simulations, as well as other technical details of the methodology, such as calculation of the excess adsorption and the notion of the window of reliability, will be presented in the next section.

The same approach is then used for two slightly different variants of the classic slit pore model, in this work designated as "single layer model" (Section 3.4) and "single layer with groups and defects model" (Section 3.5). In the first case the slit pore walls are still constituted by graphene sheets, but each wall is made of only one layer; the second case is a development of the first, to which defects and functional groups are added, so that the C/O ratio is compatible with the one reported for Maxsorb MSC-30.

The latter modifications of the slit pore model are justified by the recent studies by Nguyen and Bhatia (49, 50), which have shown that the number of graphitic sheets constituting the pore walls should be inversely proportional to the surface area of the carbon material. Figure 3.6 summarizes the data calculated by Nguyen and Bhatia for several activated carbons (50).

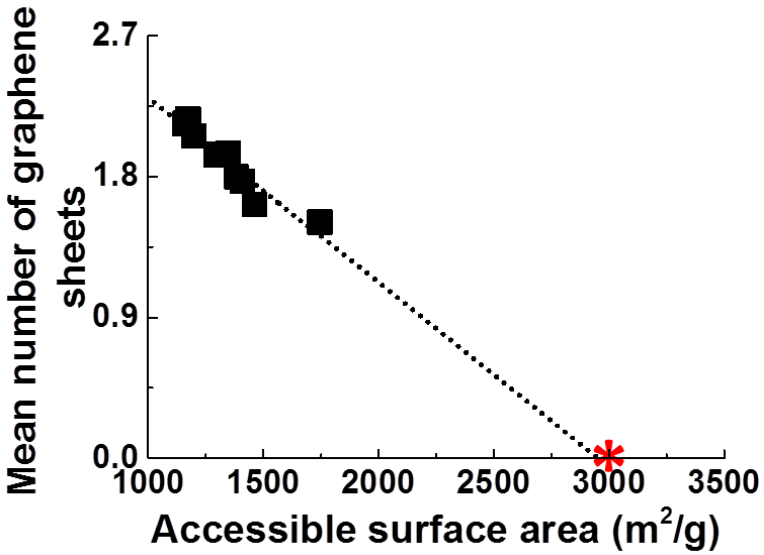

Figure 3.6. Plot of the mean number of graphene sheets as a function of accessible surface area for several types of activated carbon (50).

The graph above suggests that the surface area of Maxsorb MSC-30 (> 3000 m^2/g) is not really compatible with a classic slit pore representation, given that an extrapolation of the linear fit to the data seems to show that the average number of graphitic sheets should be lower than 1 (even lower than zero!); one may argue that a linear fit may not be the most

appropriate, but nevertheless the idea is reinforced by the fact that even a single layer graphitic "wall" has surface area lower than 3000 m^2/g (2622 m^2/g) (55).

The introduction of defects and groups is considered as a strategy that would possibly increase the surface area of the model and at the same time provide a more accurate description of the adsorption of polar species. Moreover, Jorge and Seaton (32) have shown that the distribution of polar sites on the surface of the carbon has almost no effect on the adsorption of water at high pressures, but it has a strong impact at low pressures. In the case of post-combustion capture the total pressure of the stream and the pressure of water are low, which suggests that a good level of accuracy on the distribution of the polar groups should be required. The inspiration to our approach comes from the work of Tenney and Lastoskie (42) and, while our work was in progress, a similar idea has been published by Liu and Wilcox (56). In these studies the slit pores are decorated with different types of oxygenated surface groups, eventually in the presence of structural defects (when the groups are not on the edges of the graphitic sheets). The structures and compositions of the models are different, especially because in our study we try to tailor the C/O ratio to the composition of Maxsorb MSC-30, and of course because the protocols adopted to build the models are different. Moreover, in both studies the oxygenated groups have been added on graphitic layers which are always part of a slab of sheets, and therefore never part of a structure of "single layers". In this project we saw vacancies (essentially holes) in a single layer of graphene as a simple way to increase the surface area of the material beyond the value for a single graphitic sheet cited above. Furthermore, in this approach the valence of four for the carbon atoms is preserved. On the hindsight we recognize that the model should have further taken into account accessibility of the surface groups and a more realistic model would possibly include both the vacancies decorated with surface groups and groups attached to the surface of the graphene layer, similarly to the work of Jorge and Seaton. This will be further discussed in the later sections. We note that in the projects mentioned above, which use GCMC simulations, no attempt to extract a pore size distribution or to make predictions based on a particular type of activated carbon is made. The studies focus on more fundamental aspects related to the presence of heterogeneities on the surface of the carbon slit pores. Further comments will be added in the conclusions of this chapter.

3.2. Methodology

3.2.1. Simulation parameters

The simulation of adsorption requires the choice of appropriate potentials and force-fields to describe the solid-fluid and fluid-fluid interactions. As explained in Chapter 2, the forces involved in physisorption are relatively weak, being represented by van der Waals and Coulombic interactions. Several methods can be applied for the calculation of the Coulombic contributions arising from the partial charges on the atoms of the molecules, while van der Waals, or dispersion interactions, are commonly described using the Lennard-Jones (LJ) potential:

$$E_{LJ}(r) = 4\varepsilon \cdot \left[\left(\frac{\sigma}{r}\right)^{12} - \left(\frac{\sigma}{r}\right)^{6}\right] \quad \text{(III.9)}$$

where ε represents the minimum of the potential energy curve, while σ is the distance at which the total LJ energy is equal to zero. When calculating LJ interactions between different species the cross interaction parameters are determined using the standard Lorentz-Berthelot mixing rules.

$$\sigma_{ij} = \frac{\sigma_i + \sigma_j}{2} \quad \text{(III.10)}$$

$$\varepsilon_{ij} = \sqrt{\varepsilon_i \varepsilon_j} \quad \text{(III.11)}$$

As for the Coulombic interactions between partial charges in the present work they are calculated using Ewald summation (57) in the case of the solid-fluid interaction and using the Fennell-Gezelter method based on a spherically truncated summation (58) in the case of the fluid-fluid interaction. The Fennel-Gezelter method in our preliminary studies has been shown to agree very well with the Ewald summation method, but at the same time it seems to

provide better computational efficiency. In all cases we adopt the principle of additivity of the pairwise interactions.

In the case of the classic slit pore model each wall is considered as a semi-infinite slab of stacked graphitic sheets. In this case, there are no partial charges and, consequently, no Coulombic interactions with the walls. In general, the interaction between an adsorbate site and a single semi-infinite pore wall of graphite should be determined adding all the Lennard-Jones interactions between the adsorbate site and each carbon atom in each graphitic sheet of the pore wall; an easy way to calculate this, avoiding to perform all the pair-wise calculations, is the use of the Steele's 10-4-3 potential (59). The well-known expression for the Steele potential is a result of an integration in three dimensions (x and y correspond to a plane of single graphitic sheet and z is the direction in which single sheets are stuck together) of the function representing the LJ interaction between an adsorbate site and one graphitic carbon atom:

$$U_{sf}(z) = 2\pi\varepsilon_{sf}\rho_{sf}\sigma_{sf}^2\Delta\left[\frac{2}{5}\left(\frac{\sigma_{sf}}{z}\right)^{10} - \left(\frac{\sigma_{sf}}{z}\right)^{4} - \frac{\sigma_{sf}^4}{3\Delta(z+0.61\Delta)^3}\right] \qquad \text{(III.12)}$$

where ρ_s is the number of carbon atoms per unit area in the graphite layer, Δ is the separation distance between the layers of graphitic carbon, σ_{sf} and ε_{sf} are the solid-fluid LJ parameters and z is the distance between the adsorbate site under consideration and the pore wall. Since slit-shaped pores have two pore walls, the combined potential is calculated by using:

$$U_{slit}(z) = U_{sf}(z) + U_{sf}(W - z) \qquad \text{(III.13)}$$

In the present work we have compared the results obtained using the Steele potential to the results obtained using an atomistic representation of the slit pores with walls made of at least three graphitic sheets (for layers beyond the third the LJ interaction tends to zero).

The comparison, presented in Section A5 of the Appendix (figure A2), has shown almost identical results; this has allowed us to adopt an atomistic representation which, despite being more computationally expensive, is required for the variants of the slit pore model developed later. This is particularly evident in the case of the slit pore model with groups and defects, because of the introduction of heteroatoms (oxygen and hydrogen) and partial charges.

We now provide some details on the parameters of the intermolecular interactions. In the cases of the classic and single-layer slit pore models the LJ parameters we have adopted are the same used in the derivation of the Steele potential (59). As for the single-layer model with groups and defects we have adopted the parameters proposed by Tenney and Lastoskie in their study on the effect of oxygenated functional groups on carbon dioxide adsorption in graphitic slit-pores (42). These parameters are in line with other parameters reported in the literature (60-63) and for graphitic carbon atoms which are not in the proximity of functional groups or defects they maintain the same LJ parameters we have adopted for the classic and single-layer model. A complete list of the parameters used for the adsorbent is provided in table A1 in the Appendix.

For methane we use the united atom model (64), while for carbon dioxide we use the three centre model from the TraPPE forcefield (65). A table with the LJ parameters and charges used for the fluids simulated in this part of the project and in the following chapters is reported in the Appendix (table A2).

All the species subject of the present study are modelled as rigid. For all our simulations we use the energy biased GCMC method, as implemented in the MuSiC simulation package (66). Further details of the GCMC simulations protocol adopted in this work are provided in Section A2 of the Appendix (table A4), which includes details of the potential cut-offs, number of Monte Carlo moves per adsorption point, type and weight of Monte Carlo moves and other parameters.

3.2.2. Excess adsorption

As we also explained in Chapter 2, once the isotherms have been simulated it is necessary to convert the results (absolute adsorption) into excess adsorption, according to equation (II.45). For this reason it is important to calculate the volume accessible to the molecules of adsorbate.

In the case of the slit pore model the calculation of the accessible volume V has to take into account for any fluid the smallest pore W_{spi} in which adsorption can happen. The dimension of W_{spi} depends on the dimensions of the adsorptive molecule. It is assumed that the accessible volume will be zero for pore widths lower than W_{spi}, while it will be non-zero for bigger pores.

To be precise, we adopt the definition by Davies and Seaton (9) which is the following:

$$V(W) = \begin{cases} 0 & W < W_{spi} \\ (W - W_{spi})A & W > W_{spi} \end{cases} \qquad \text{(III.14)}$$

where A is the area of the surface of the pore wall in a simulation cell.

For methane and carbon dioxide W_{spi} has been determined by Davies and Seaton (12) to be respectively 6.1 and 5.7 Å These values, which have been estimated by means of test simulations, are approximate and depend on the parameters of the solid-fluid interactions. A similar concept of a so-called chemical width (in the rest of the paragraph called w_c) has been also adopted in other studies. In particular, in the words of Sweatman and Quirke, "*the chemical width describes the width occupied by adsorbate molecules, which is typically about σ_{ss} less than the physical width, w, defined by the distance between and normal to carbon atom centers in the first layer of the opposing slit walls. Because the volume occupied by adsorbate molecules is not absolutely defined (it depends on the nature of the gas-surface interaction), w_c is not absolutely defined.*" (5). In their work they chose to "*arbitrarily set w_c = w - 0.24 nm*", for consistency with other similar studies.

Once the excess adsorption has been calculated it has to be expressed in terms of adsorbed density per unit of volume; for consistency with the definition of the pore width the volume considered in this case is the volume of the simulation cell (V_{SC} = AW) (9). The excess adsorbed density then becomes:

$$\rho_{exc} = \frac{N_{exc}}{V_{SC}} \tag{III.15}$$

3.2.3. Solution of the AIE, quadrature parameters and the window of reliability

For the solution of the AIE we have adopted 500 quadrature intervals together with 250 simulated and experimental data points (this high number of points has been obtained through interpolation between the actual data). The protocol by Davies and Seaton actually establishes that the data points should be at least as many as the quadrature intervals (9) (10); however, in a series of preliminary studies we have run several tests, which show that even when using more quadrature intervals than data points the effect on the results is negligible. This observation is particularly important for the cases in which not many experimental data points are available.

Once a possible PSD has been extracted another aspect to bear in mind is that not all the peaks (corresponding to different pore widths) reported in it may be reliable (i.e. physically meaningful). This happens because after a certain pore width all excess adsorption isotherms start to behave essentially in the same way; this means that two very different pores become indistinguishable from the adsorption isotherm perspective and may be exchanged one for another.

This can be explained also considering that all simulations are affected by a statistical error, and in order for the results to be meaningful, the simulated adsorbed densities must be sufficiently higher than the error itself: if the errors are comparable in magnitude to the adsorbed densities, the associated isotherms cannot be of course considered reliable.

To give an idea of the errors in our simulations, errors in adsorbed density for pure component isotherms in a 10 Å pore have been calculated for CO_2 to be between 17% at 0.02 Bar and 0.34% at 30 Bar at 298 K, while for methane at the same temperature they have been

calculated to be between 22.6% at 0.02 Bar and 0.74% at 30 Bar. When the temperature is as low as 273 K the errors for CO_2 span between 11.8% at 0.02 Bar and 0.37% at 30 Bar, while for CH_4 they span from 15.4 % at 0.02 Bar and 0.63% at 30 Bar.

If in general we define the errors as noise and the adsorbed densities as signal, we can state that the reliability of a simulated isotherm is strongly related to the signal to noise ratio, which must be sufficiently high. The intensity of the signal in general decreases with temperature and is strongly related to the adsorbed species: species which interact more strongly with the adsorbent will produce higher signals, if compared to species that interact more weakly. Also, the signal is amplified at lower temperatures as the average solid-fluid interaction is stronger at lower temperatures.

If we consider carbon dioxide and methane, for example, we can expect to have a higher signal to noise ratio in the case of carbon dioxide, which interacts with graphitic carbon more strongly than methane; if we also take the temperatures into account, for example 273 and 298 K, the higher signal to noise ratio is expected for carbon dioxide at 273 K. As a limiting case we can consider helium, which due to weak solid-fluid interactions is treated as non-adsorbing species, a property exploited in helium porosimetry to measure the accessible pore volume of the material.

Another element to take into account is of course the role of the adsorbent. In the case of the slit pore model, in general, the narrowest pores will exert stronger interaction onto the adsorptive species, given the overlap between the potentials emanating from the two pore walls; in the case of very wide pores there will be no overlap between the potentials and, eventually, there will be a pore width after which the molecules at the centre of the pore will not interact with the walls at all. Of course, there will still be the cooperative effect among different molecules of adsorptive which, after a certain pore width, will simply start to behave more and more similarly to the bulk phase. This will mean that the excess adsorption will start to decrease, and eventually tend to zero as the pore width increases.

We must not forget, also, that the signal to noise ratio also depends on the pressure: low pressures are generally associated to higher errors, especially in the case of GCMC simulations (given the low numbers of molecules involved), and lower adsorbed densities,

and therefore to lower signal to noise ratios; at higher pressures, instead, adsorbed densities, and therefore signal to noise ratios, tend to be higher.

To summarize, the most reliable simulations will be related to highly adsorbing species, low temperatures, high pressures and narrow pores. A good way to consider all the variables mentioned above at the same time is the concept of "window of reliability", which has been introduced by Gusev et al. (67): the window of reliability represents the range of pore widths in which the signal to noise ratio is high enough to be sure that the adsorption isotherms are reliable. In particular, within the window of reliability it is possible to appreciate the effect of different adsorptive species, temperatures, pressures and pore width, and therefore the excess adsorption isotherms are different from one pore to another. For this reason the window of reliability corresponds to the widths that can be considered reliable in the pore size distribution. As expected, the width of the window of reliability depends on the adsorbate used, the temperature, and the maximum pressure at which the adsorption is measured. For practical purposes, we use an operation definition of the pores beyond the window of reliability (67) as pores wide enough so that excess adsorption in these pores is the same as in an arbitrary large pore.

3.3. Classic slit pore model results

We now present the results of our studies on the classic slit pore model, starting from the simulation of the adsorption isotherms for carbon dioxide at 298 K (figure 3.7). As mentioned in section 3.1 the protocol we adopt to determine the pore size distribution and to make predictions has been developed by Davies and Seaton (9, 10, 68). This protocol was built following a number of previous developments in the field (16, 31, 67, 69, 70); as such, it is well established and well documented. In the PhD thesis by Davies (71), the protocol is validated by considering hypothetical systems made of a known number of pores, with known widths. Application of the protocol to prediction of adsorption of single component species and mixtures in activated carbons at various conditions asserts it practical accuracy (9, 15, 16).

We note that in this project for the simulation of the kernels we have chosen intervals in pressure that would cover at least the intervals covered during the experimental measurements, while for the resolution of the pore widths we have used the same protocol which has been previously employed in the group of Prof. Seaton.

In theory, the minimum resolution of the pores should be consistent with the smallest physical distance between the two carbon sheets in graphite equal to 3.35 Å. Nonetheless for pores up to 20 Å we use a resolution of 1 Å to have a better picture on variation of properties with the pore size in the most sensitive region of pore widths. Having said this, it has been shown by Davies and Seaton that for light gases the differences in resolution do not have a significant effect on the determined PSDs and that no difference is found in the predictions (68).

We also point out that, given that the regularization protocol by Davies and Seaton is adopted, the error on the experimental data (in our case estimated to be lower than 1% for single component isotherms) has only a small effect on the PSDs. This issue has been already addressed previously and there is no need to revisit it (68).

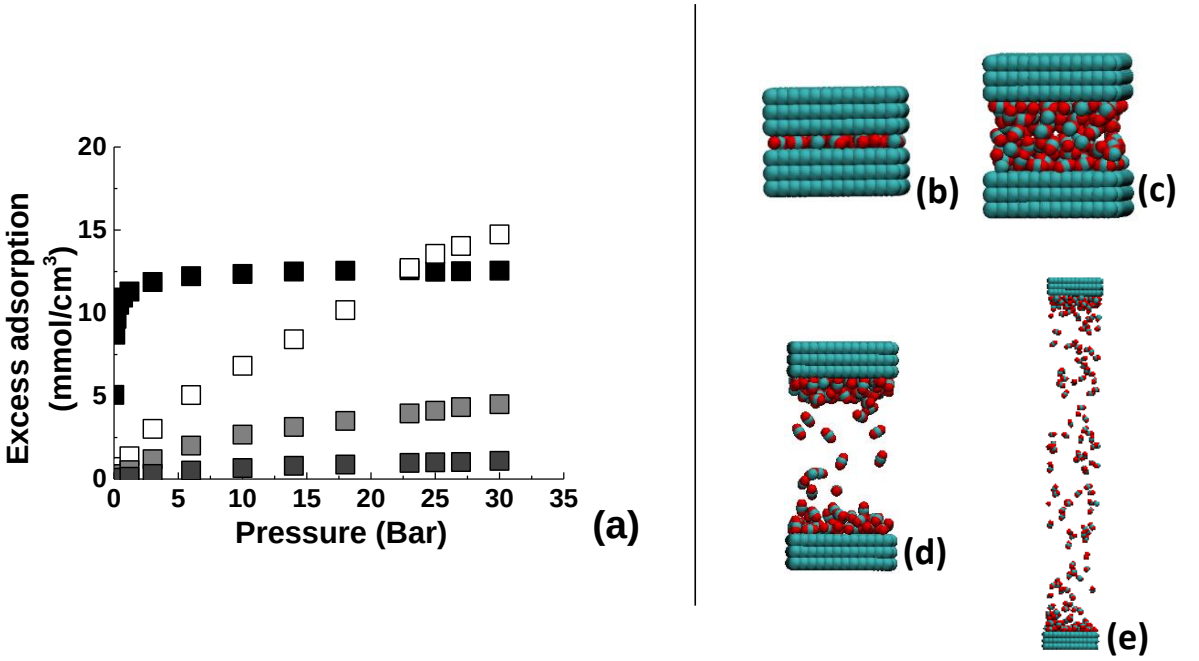

Figure 3.7. a) selected adsorption isotherms from the kernel of simulated isotherms for CO_2 at 298 K; black: 7 Å pore, white: 20 Å pore, grey: 50 Å pore; dark grey: 200 Å pore. (b), (c), (d), (e): configurations corresponding to a pressure of 30 Bar for CO_2 in pores of 7, 20, 50 and 200 Å in width, of respectively. Cyan: carbon, red: oxygen.

In figure 3.7 we show some of the adsorption isotherms simulated for CO_2 in pores of different widths (left side of the figure), together with the configurations corresponding to a pressure of 30 Bar for the same pores (right side). We can notice that for the 7 Å pore a plateau, corresponding to a completely filled pore, is reached at a relatively low pressure: this is because the space between the two pore walls is characterized by a deep potential well, due to the superposition of the potentials coming from the opposite walls. In the case of the 20 Å pore this effect is reduced due to the increased distance between the walls, and the pore filling happens at a higher pressure; moreover, the increase in volume between the walls determines an increase in the adsorption at high pressure. For the pores of 50 and 200 Å the distance between the walls is so large that in the space between them the fluid tends to behave like bulk. There is still adsorption in the proximity of the walls, but given that the excess is expressed in mmol/cm^3, its value tends to diminish (and eventually will become zero) as the pore width, and therefore the pore volume, increase.

The behaviour we have just described for carbon dioxide is also typical of methane and can also be observed in the modifications of the slit pore model we will examine later, therefore we will not further discuss it in the next sections.

We will now show some results concerning the solution of the AIE. Figure 3.8 shows the GCV plot and L-curve resulting from solution of the AIE for CO_2 at 298K; these curves derived from other sets of data show similar features.

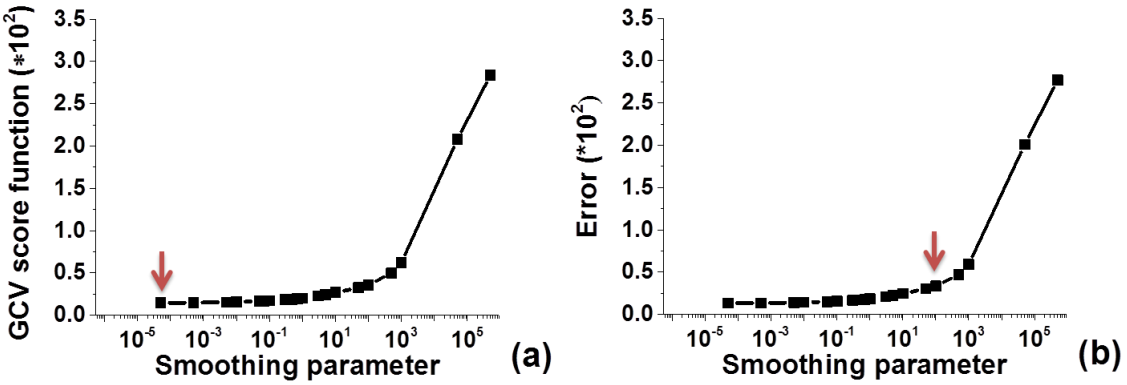

Figure 3.8. a) GCV plot and b) L-curve obtained for CO_2 at 298 K (classic slit pore model). The arrows indicate the values of the smoothing parameters we have chosen to generate two possible PSDs.

The GCV plot in figure 3.8 does not present a pronounced minimum, as the function simply tends to decrease slowly for low values of the smoothing parameter. Therefore for our analysis we choose the lowest value on the curve, which also corresponds to the lowest value of the smoothing parameter ($\alpha = 5*10^{-5}$). In the case of the L-curve we choose a value of α situated in the region in which the error starts to increase more rapidly; specifically we choose $\alpha = 1*10^{2}$. We now show (Figure 3.9) the PSDs corresponding to the two values of smoothing parameter we have chosen:

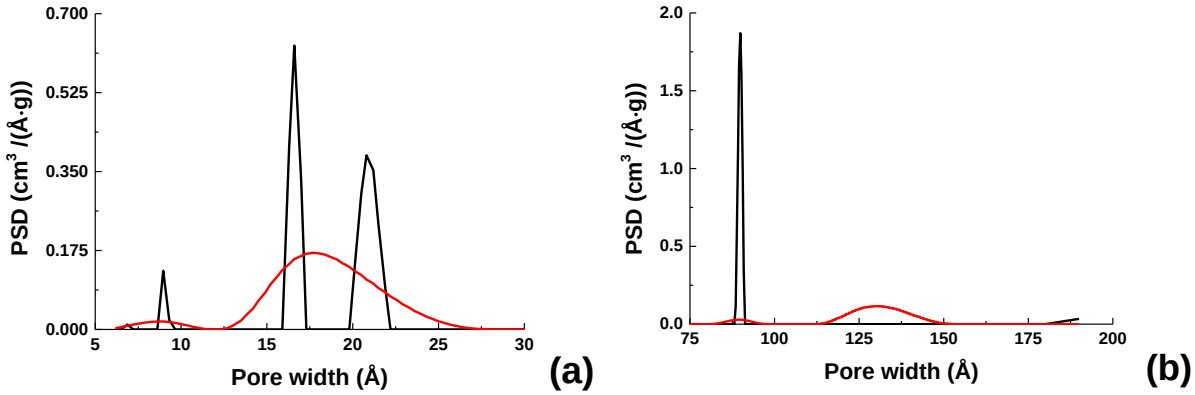

Figure 3.9. Pore size distributions corresponding to the smoothing parameter values chosen from analysis of the GCV plot (black line) and L-curve (red line) for CO_2 at 298 K (classic slit pore model). For clarity, graph (a) shows the range of pores in the PSDs up to 30 Å , while graph (b) focuses on the region between 75 and 200 Å. We note that none of the two PSDs present any pores in the interval 30 – 75 Å, which has therefore been omitted.

The black and red line PSDs correspond respectively to the smoothing parameter values chosen from the analysis of the GCV plot and L-curve. The left panel of the figure (a) focuses on the window of reliability, which for CO_2 at 298K includes pores up to 30 Å in width. It is quite clear that the two PSDs are different: first of all, as expected, the PSD corresponding to the higher value of α is much smoother than the other; also, it only shows one smooth peak, centred around a pore width of 17.8 Å, while the other shows three more intense peaks respectively at 8.96, 16.6 (the most intense) and 20.8 Å.

To understand which of the two PSDs would be the best to represent Maxsorb MSC-30 we have tried to make predictions using both. In figure 3.10 we show the predictions for CH_4 at 273 K. This system deviates from the conditions for which PSD was obtained both in terms of the adsorbing species and temperature, and we expect it to provide a sensitive test for the accuracy of the PSDs.

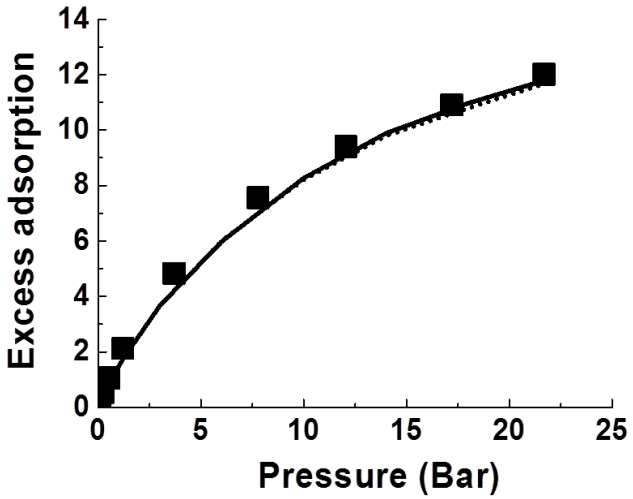

Figure 3.10. Predictions for methane adsorption on Maxsorb MSC-30 at 273 K, performed using PSDs extracted from CO_2 data at 298 K using two different values of the smoothing parameter: $\alpha = 5*10^{-5}$ (solid line) and $\alpha = 1*10^{2}$ (dotted line). Symbols represent the experimental results.

It is clear that both PSDs, despite being so different, give very good predictions, almost identical to each other. This insensitivity of the results to PSDs (whether determined with analysis of GCV plot or L-curve) has been previously observed and reported (71). This naturally implies a question: "If both PSDs give very good predictions, how can we choose the most accurate to represent Maxsorb?" Actually, none of the two pore size distributions is identical to the PSD reported in figure 3.5; nevertheless it may be possible to say that they both show some degree of similarity to it, as they both feature peaks in the vicinity of 20 Å. But how similar do two PSDs need to be in order to be considered consistent with each other?

Here, for a better understanding of the problem we continue with the analysis using all the different sets of data at our disposal. Figure 3.11 (panels a, b and c) shows the PSDs we have extracted starting from pure component data both for CO_2 and CH_4 at 298 and 273 K. In this case we also focus on the window of reliability for the different species.

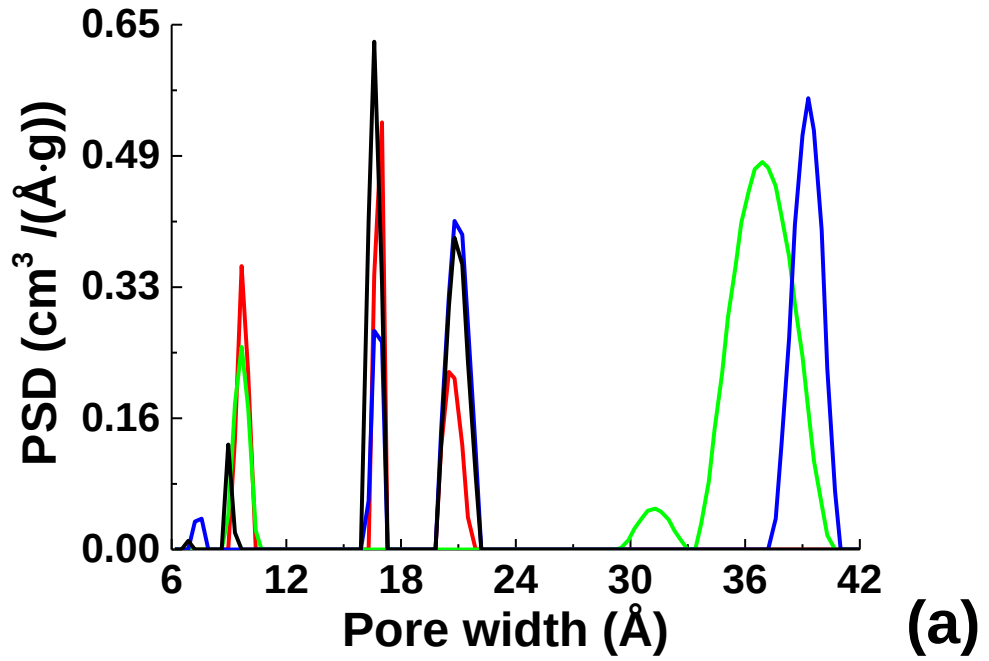
0.65
0.49
0.33
0.16
0.00
PSD (cm3 /(Å·g))
6
12
18
24
30
36
42
Pore width (Å)
(a)

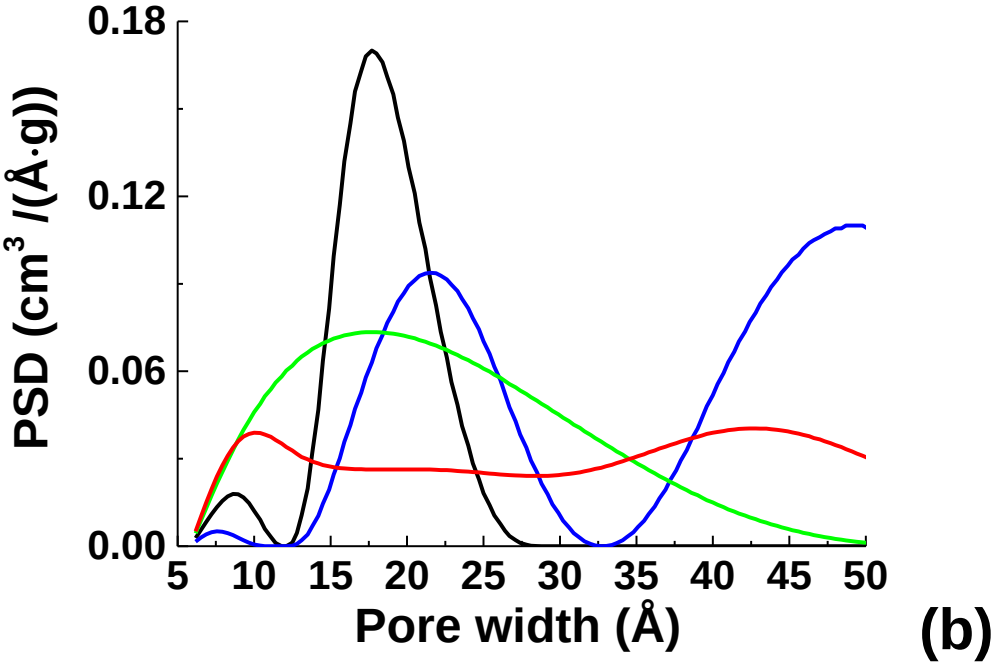
0.18
0.12
0.06
0.00
PSD (cm3 /(Å·g))
5
10
15
20
25
30
35
40
45
50
Pore width (Å)
(b)

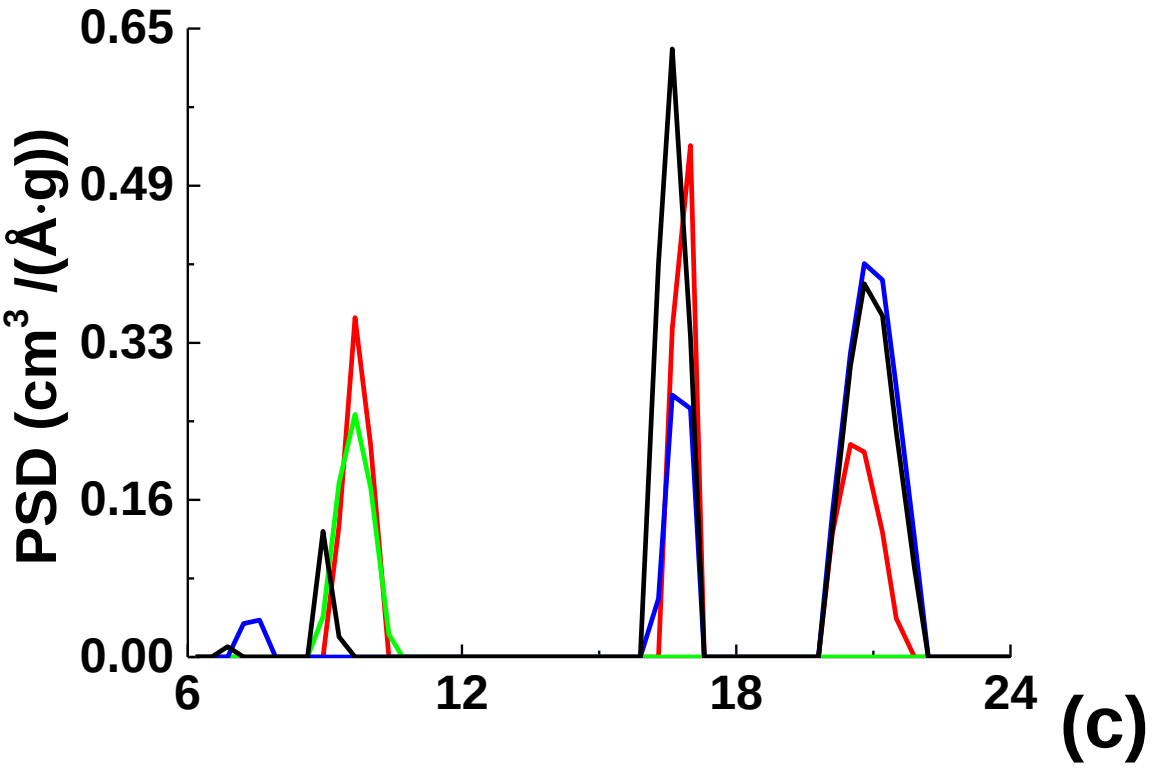

Figure 3.11. PSDs extracted from different sets of data: CO_2 at 273 K (blue line), CO_2 at 298 K (black line), CH_4 at 273 K (red line), CH_4 at 298 K (green line). The PSDs correspond to values of smoothing parameter chosen from analysis of the GCV plot (graph (a)) and L-curve (graph (b)). Graph (c) is an expanded version of graph (a) in the region up to 24 Å.

It is important to mention that for the different sets of data the examination of the excess adsorption isotherms has revealed different windows of reliability, depending on the adsorbing species and temperature: if for carbon dioxide at 298 K we consider the highest reliable pore width to be 30 Å, in the case of CO_2 at 273 K this threshold is moved to 50 Å. In the case of methane the identification of the window of the reliability is not as clear as for CO_2; nevertheless we believe that 19-20 Å for CH_4 at 298 K and 20-30 Å for CH_4 at 273 K are reasonable upper bounds. The windows of reliability have been determined through visual inspection of the isotherms (that is by identifying the pore widths at which the excess adsorption isotherms become indistinguishable) and up to a certain extent they are therefore subjective. The different sets of excess adsorption isotherms are reported in Section A6 of the Appendix.

If in figure 3.11 we compare different PSDs in the region of 0-20 Å, (within the window of reliability for all species and conditions) the agreement seems quite reasonable, at least for the results based on the smoothing parameter from the GCV plot. In figure 3.11 (c) all sets of data, apart from CH_4 at 298 K, have generated two peaks in the proximity of 20 Å, while the data coming from methane, together with the data for carbon dioxide at 298 K, have all generated a peak centred around 10 Å. The PSDs obtained from the L-curve smoothing parameter show less coherence. Nevertheless, in figure 3.11 (b) all PSDs, apart from the one extracted from data for CH_4 at 273 K, show a broad peak centred around ~ 20Å, while the data for carbon dioxide, together with the data for methane at 273 K, have generated small peaks centred around 10 Å.

All the differences and similarities observed for the PSDs we have extracted and a comparison with the PSD reported in figure 3.5 suggest that none of them may give precise description of the pore structure of Maxsorb MSC-30, but altogether they still give an indication of which pores play the most relevant role in adsorption phenomena.

Although a substantial number of predictions has been carried out, using a number of generated PSDs, here we show only a selected set of predictions. These predictions are based on the PSDs derived from CO_2 and CH_4 adsorption isotherms at 298 K. In general, PSDs derived from the CO_2 isotherm at 298 K (corresponding to different values of the smoothing parameter) gave the most accurate predictions, whereas PSDs from the methane isotherm at 298 K gave the least accurate predictions. This is consistent with the earlier discussion on the

signal-to-noise issues provided earlier. According to the same discussion we could have, in principle, decided to use for the predictions data for CO_2 at 273 K. In the kernel of simulated isotherms, anyway, some isotherms show capillary condensation, a phenomenon which for the reasons explained in detail in Section 3.7, we wish to avoid for the moment. As a result, although we do have some predictions based on PSD from CO_2 at 273 K, the results and discussion are largely based on the PSD from CO_2 at 298 K. Below we show data corresponding to the most accurate predictions, available within a set of PSDs obtained from a particular reference isotherm. In the case of CO_2 at 298 K this PSD corresponds to $\alpha = 5*10^{-5}$ (chosen from analysis of the GCV score function), while in the case of CH_4 at 298 K the PSD corresponds to $\alpha = 5*10^{4}$ (chosen from analysis of the L-curve).

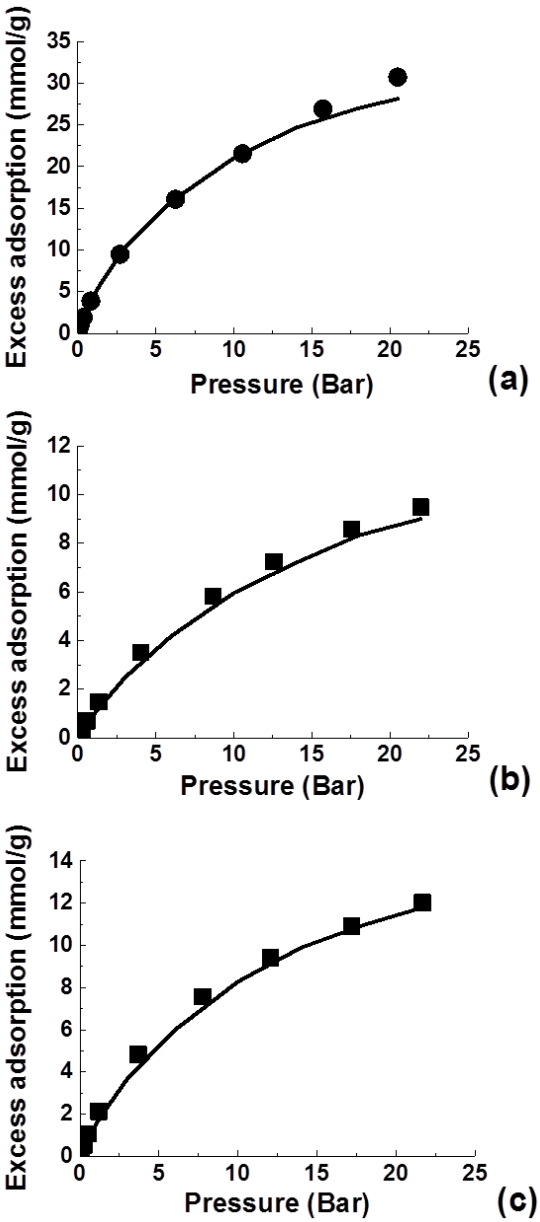

Figure 3.12. Isotherms predicted using the PSD obtained from CO_2 at 298 K. Symbols represent experimental data and solid lines represent predictions. a): CO_2 at 273 K, b): CH_4 at 298 K, c): CH_4 at 273 K.

The results presented in figure 3.12 show that the PSD calculated for CO_2 at 298 K allows quite accurate predictions; only carbon dioxide adsorption at 273 K is slightly underestimated at pressures over 15 Bar.

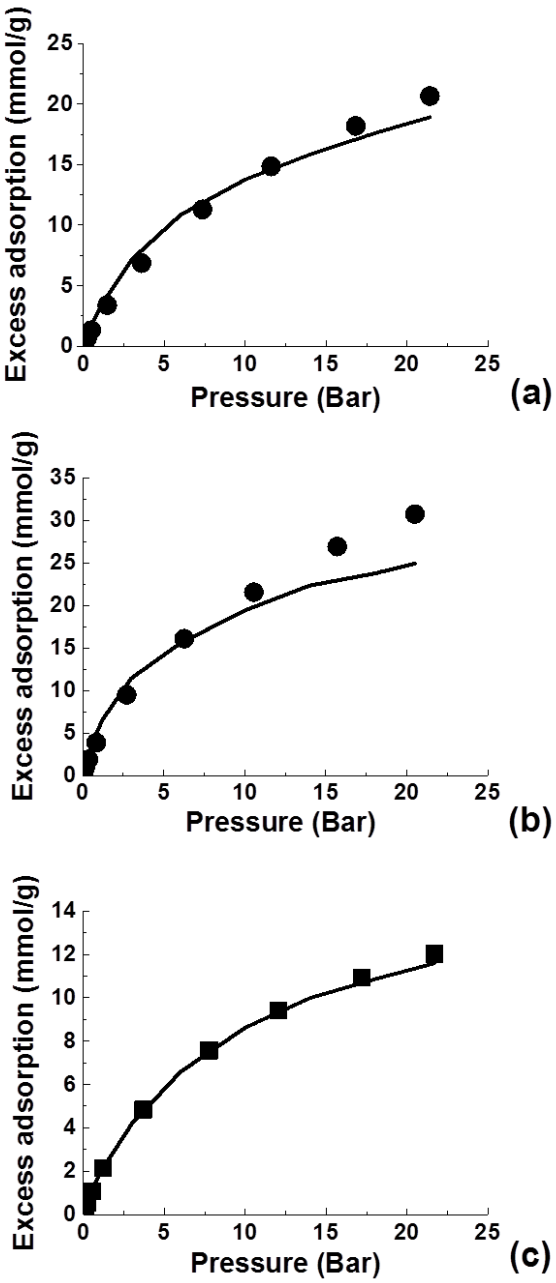

Figure 3.13. Isotherms predicted using the PSD obtained from CH_4 at 298 K. Symbols represent experimental data and solid lines represent predictions. a) CO_2 at 298 K, b) CO_2 at 273 K, c) CH_4 at 273 K.

Figure 3.13 shows that the PSD extracted from data for methane at 298 K give an accurate prediction for the same species at 273 K, but predictions for a different species (in this case CO_2) visibly lose accuracy, in particular at 273 K.

To better quantify this statement, we consider all the predictions performed starting both from data for CO_2 at 298 K and for CH_4 at 298 K, and in all cases we calculate the mean squared errors (MSE) considering the differences between all the experimental points in each isotherm and the predictions at the same pressures. At the end of Section 3.5 (figure 3.29) all the MSEs for the predictions of the same species but using different models will be compared, in order to have a quantitative indication of the accuracy of the different models, one relatively to another.

For the results presented in figure 3.12 the mean squared errors for the predicted adsorbed densities are 0.18, 0.17 and 0.81 for CH_4 at 298 K, CH_4 at 273 K and CO_2 at 273 K respectively, while in the case of figure 3.13 the mean squared errors are 0.81, 7.98 and 0.031 for CO_2 at 298 K, CO_2 at 273 K and CH_4 at 273 K, respectively.

From the results obtained for the classical slit pore model we can conclude that for Maxsorb MSC-30 several pore size distributions compatible with experimental and simulated data can be extracted; the pore size distributions, selected using the method by Davies and Seaton, are not identical to one another, but they do show some agreement, especially the PSDs extracted from carbon dioxide data, in the region close to 20 Å. The PSD derived using nitrogen data in the original publication by Otowa et al. (53) also shows an intense peak in this region. These elements suggest that in the case of Maxsorb a PSD calculated using the classical slit pore model may provide a reasonable picture about the dominant features of the pore structure. One may argue that the degree of uncertainty coming from the differences in the PSDs may still constitute a concern in terms of characterization of the material; anyway this does not constitute a problem at all for the sake of the predictions, which are definitely quite accurate when starting from data for CO_2 at 298 K. The only predictions for which it might be desirable to reach higher accuracy concern carbon dioxide at 273 K. Further development of the model could be pursued via using PSD from carbon dioxide at 273 K (thus increasing signal-to-noise ratio, as we mentioned earlier in the chapter) and calibrating solid-fluid interactions individually for each adsorbing species using available experimental data. We will further discuss these ideas in the conclusions of the chapter.

One of the fundamental questions we set to investigate was how the accuracy of these predictions would change as we start deviating from the classical slit pore model by considering only one layer of graphene and introducing different types of defects while

adhering to the original protocol by Davies and Seaton to obtain PSDs. Although the model of Nguyen and Bathia suggests that the number of layers per pore wall in Maxsorb should be fewer than 1, it seems natural to start from a model where the walls are made of just one graphitic sheet. The results in the two following sections follow the same scheme, logic and criteria followed in this section.

3.4. Single layer model results

As explained in the introduction the single layer model is based on one graphitic sheet per pore wall. Figure 3.14 shows as an example a snapshot from the simulation of methane at 273 K in a 15 Å pore in periodic boundary conditions.

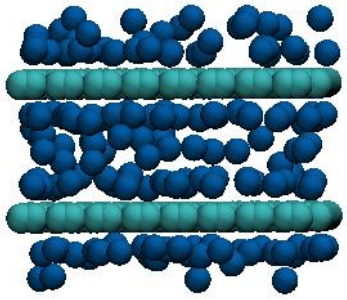

Figure 3.14. Computer visualization from the simulation of methane adsorption at 273 K in a pore of 15 Å in width in the periodic boundary conditions. Cyan: carbon, blue: methane.

In figure 3.15 as we did in the previous section we show the GCV plot and L-curve obtained from the solution of the AIE for carbon dioxide at 298 K.

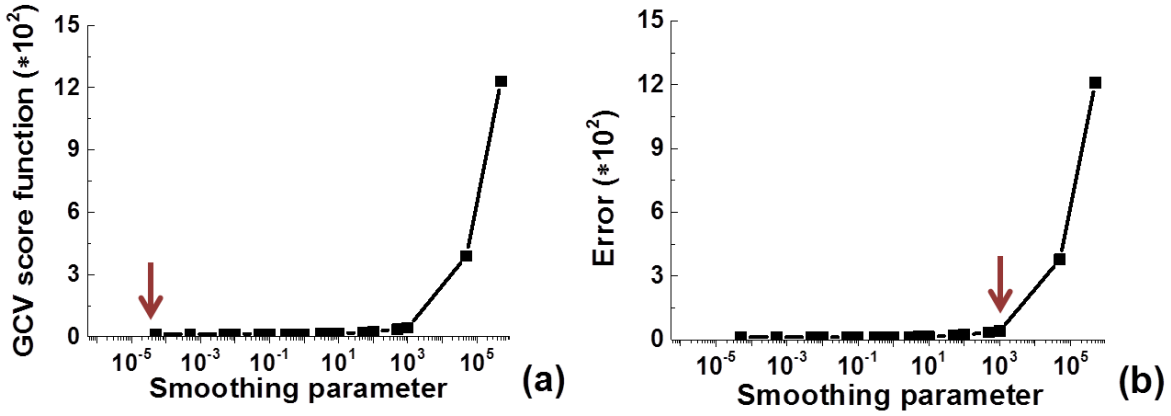

Figure 3.15. (a) GCV plot and (b) L-curve obtained for CO_2 at 298 K (single-layer model). The arrows indicate the values of the smoothing parameters we have chosen as corresponding to two possible PSDs.

A comparison between figure 3.15 and 3.8 shows that even in the case of the single-layer model the GCV curve does not feature any minima. The PSDs corresponding to the chosen values of the smoothing parameter ($\alpha = 5*10^{-5}$ and $\alpha = 1*10^{3}$) are presented in figure 3.16.

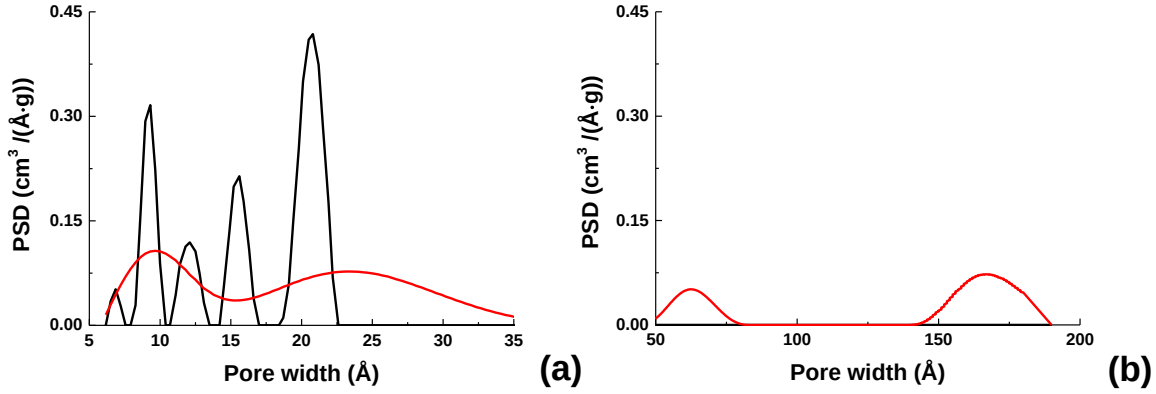

Figure 3.16. Pore size distributions corresponding to the values of the smoothing parameter chosen from analysis of the GCV plot (black line) and L-curve (red line) for CO_2 at 298 K (single-layer model). Graph a) shows the range of pores in the PSDs up to 35 Å, while graph (b) focuses on the region 50 – 200 Å. None of the PSDs feature any pores in the region 35 – 50 Å; in particular, as seen from graph (b), all the pores in the PSD extracted from the GCV plot are located in the region 5 – 25 Å.

In this case the two pore size distributions are very different, and none of them really resembles the reference PSD from the literature, even though they both feature a peak (very

pronounced in one case, very smooth in the other) around 20 Å. The window of reliability has now been identified as the region up to 20-30 Å.

As an example of predictions we show methane adsorption at 273 K in figure 3.17, and the results are almost identical.

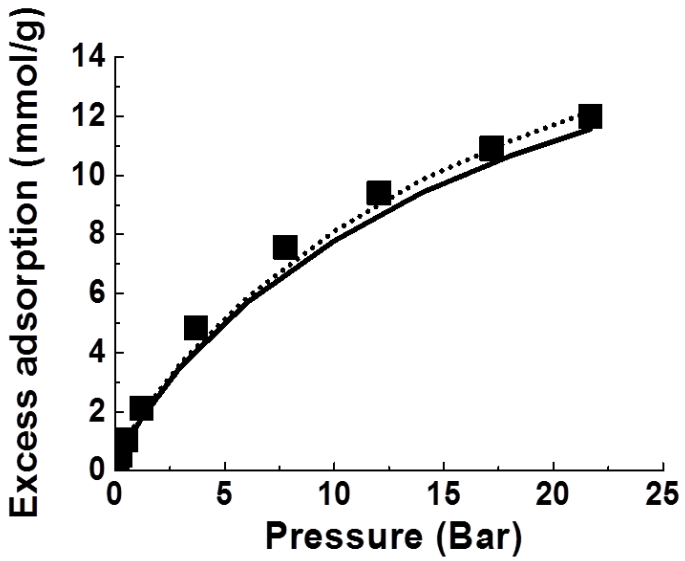

Figure 3.17. Predictions for methane adsorption on Maxsorb MSC-30 at 273 K (single-layer model), performed using PSDs corresponding to two different values of the smoothing parameter: $\alpha = 5*10^{-5}$ (solid line) and $\alpha = 1*10^{3}$ (dotted line). Symbols represent the experimental results.

The pore size distributions extracted starting from all different sets of data are presented in figure 3.18:

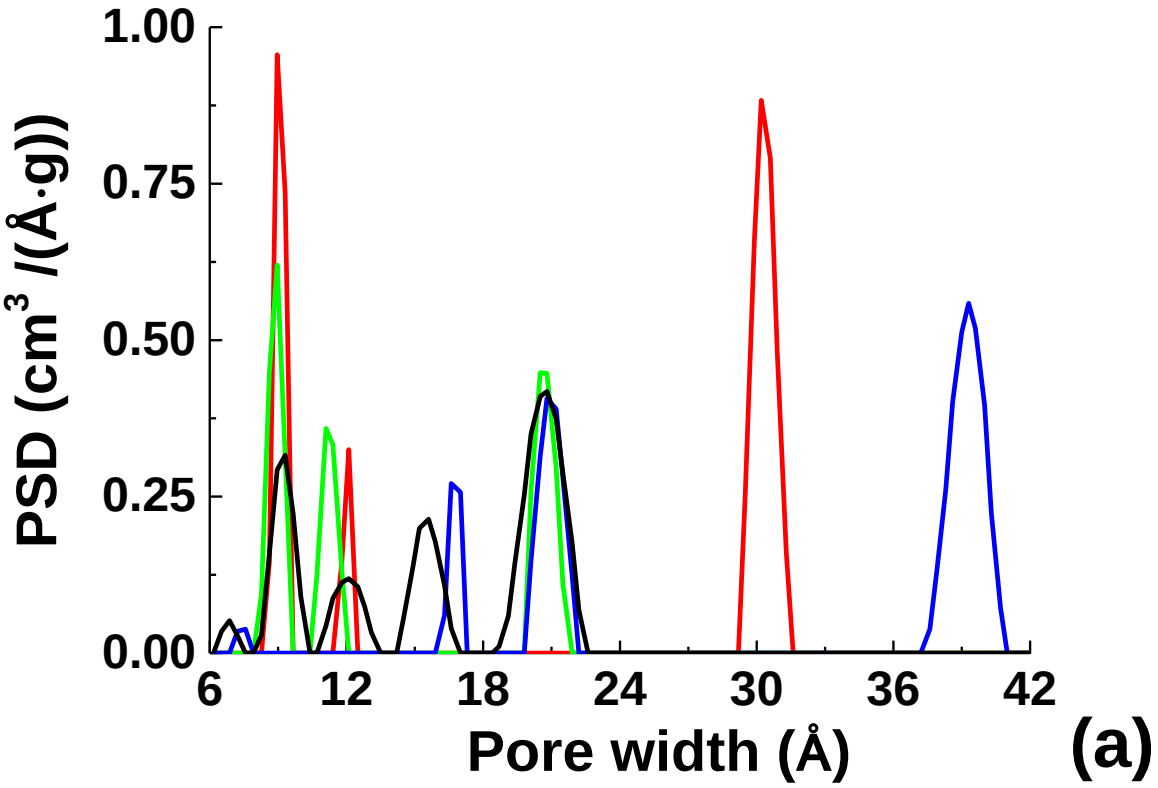
1.00
0.75
0.50
0.25
0.00
PSD (cm3 /(Å·g))
6
12
18
24
30
36
42
Pore width (Å)
(a)

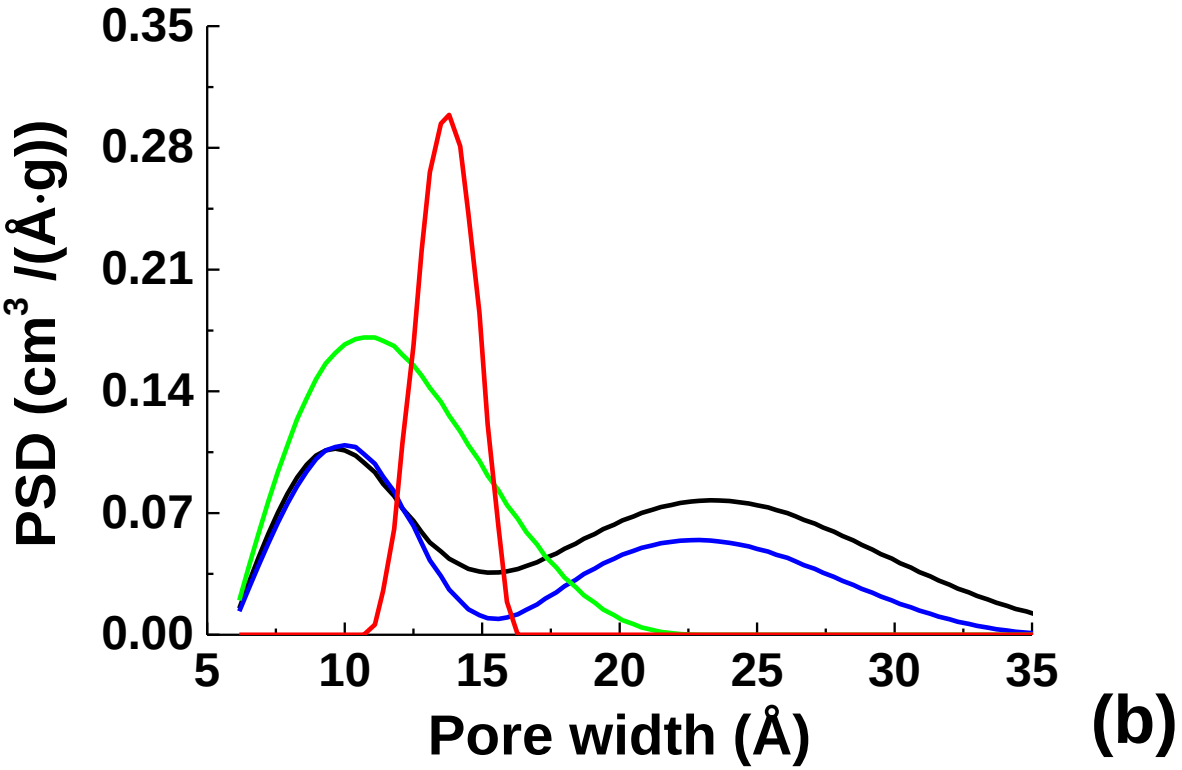
0.35
0.28
0.21
0.14
0.07
0.00
PSD (cm3 /(Å·g))
5
10
15
20
25
30
35
Pore width (Å)
(b)

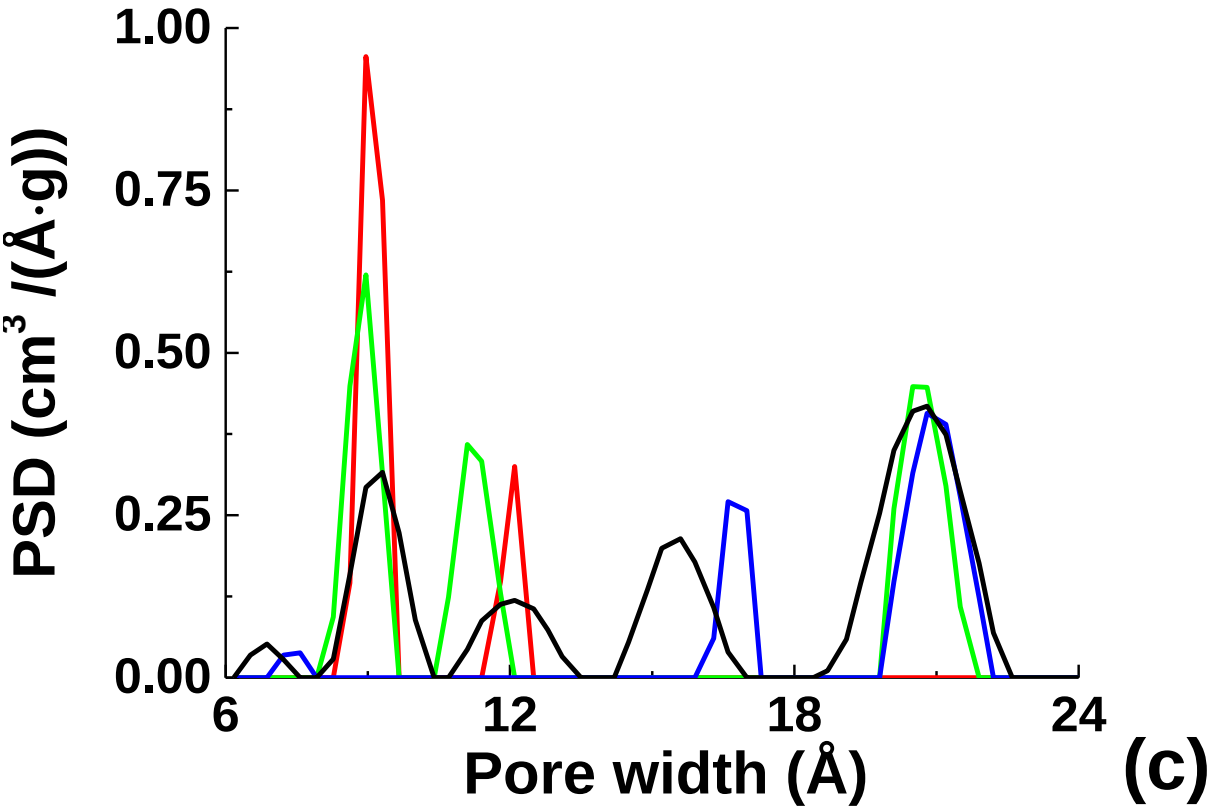

Figure 3.18. PSDs extracted from different sets of data (single-layer model): CO_2 at 273 K (blue line), CO_2 at 298 K (black line), CH_4 at 273 K (red line), CH_4 at 298 K (green line). The PSDs correspond to values of smoothing parameter chosen from analysis of the GCV plot (graph (a)) and L-curve (graph (b)). Graph (c) is an expanded version of graph (a).

The upper bounds for the windows of reliability have been identified at 20-30, 30-40, 13-15 and 19-20 Å for CO_2 at 298 K, CO_2 at 273 K, CH_4 at 298 K and CH_4 at 273 K, respectively (see complete kernels in Section A6 of the Appendix, figure A4). In general, we expect the window of reliability to move to lower values: pores with only one layer constituting the walls exert weaker interactions on the adsorbate and under the same conditions of temperature and pressure the signal-to-noise ratio is going to be lower.

Different PSDs extracted from carbon dioxide data seem to more or less agree in identifying peaks at 10 and 20 Å. Compared to the classical slit pore model, the peaks around 10 Å are much more pronounced, or, in other words, in this model the most relevant pore widths are shifted towards lower values. This aspect represents a deviation from the result by Otowa et al. (73). PSDs obtained from methane data show much greater variability and smoothness,

with the latter property attributed to a substantially higher value of the smoothing parameter used to extract these PSDs. Interestingly, the PSD extracted from the carbon dioxide data at 273 K still features an intense peak around 40 Å, in agreement with the result shown in Figure 3.11 for the classic slit pore model.

We now show predictions calculated from the PSDs for CO_2 at 298 K (figure 3.19) and CH_4 at 298 K (figure 3.20), respectively. In the case of CH_4 at 298 K the predictions have been performed using the PSD corresponding to $\alpha = 1*10^{3}$ (chosen from analysis of L-curve), while in the case of CO_2 at 298 K the value of $\alpha = 5*10^{-5}$ (chosen from analysis of the GCV score function) has been used.

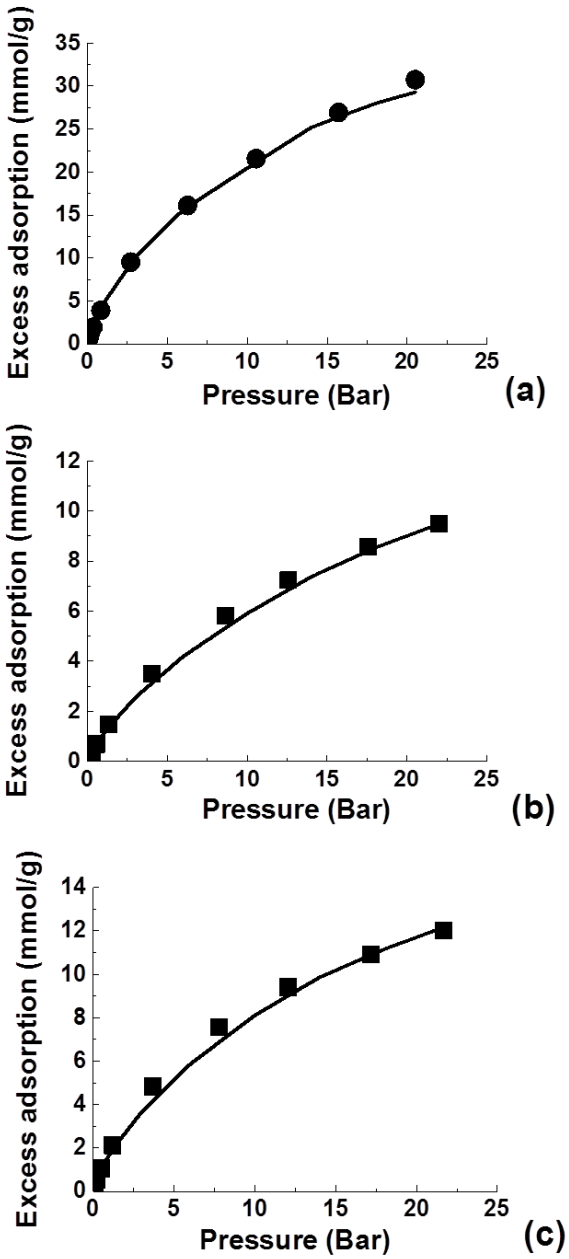

Figure 3.19. Isotherms predicted using the PSD obtained from CO_2 at 298 K (single-layer model). Symbols represent experimental data and solid lines represent predictions. a): CO_2 at 273 K, b): CH_4 at 298 K, c): CH_4 at 273 K.

The predictions in figure 3.19 appear to be accurate, also with an improvement in accuracy for the prediction for carbon dioxide at 273 K. The mean squared errors in this case are 0.11, 0.21 and 0.24 for CH_4 at 298 K, CH_4 at 273 K and CO_2 at 273 K respectively. This also shows a slight improvement even for the prediction of methane at 298 K.

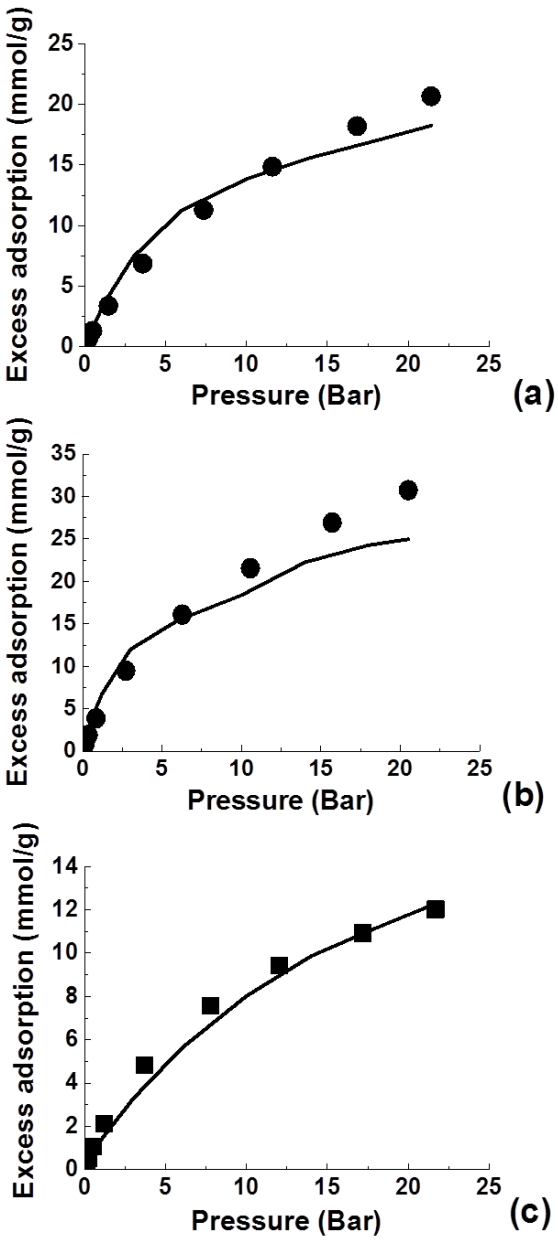

Figure 3.20. Isotherms predicted using the PSD obtained from CH_4 at 298 K (single-layer model). Symbols represent experimental data and solid lines represent predictions. a) CO_2 at 298 K, b) CO_2 at 273 K, c) CH_4 at 273 K.

The results in figure 3.20 point out that in the case of the PSD from CH_4 at 298 K the predictions deteriorate, showing a lower level of accuracy compared to the predictions in the classic slit pore model. This time the mean squared errors are 1.55, 8.27 and 0.4 for prediction of CO_2 at 298 K, CO_2 at 273 K and CH_4 at 273 K respectively. This is not surprising however if, as before, this result is understood in terms of the relation between the

strength of interaction, the signal-to-noise ratio and the window of reliability. On these grounds, the single layer model, featuring weaker solid-fluid interactions in general, must be less robust compared to the classical slit pore model. The only prediction that remains quite accurate is for methane at 273 K. Other choices of the smoothing parameter to extract PSDs from methane data do not improve this picture and, in fact, the data shown in figure 3.20 is the best prediction that could be obtained based on methane calibration isotherm at 298 K.

To summarize, a possible explanation for the worsening on the predictions starting from the methane data is the fact that the lower number of graphitic sheets per pore wall reduces the adsorption of methane so much that the PSDs become unreliable.

3.5. Single layer with groups and defects model results

In this section we attempt to add yet another degree of complexity to the model considered in the previous section by creating defects within the single graphitic layer walls and adding the functional groups.

The functional groups which have been identified in Maxsorb are of three types: hydroxylic, carboxylic and lactonic (73). We consider a simplified system, where all oxygen in the structure is present in the form of hydroxyl groups (the most abundant) only, so that the C/O ratio in Maxsorb, identified as 7.8 (73), is more or less respected (in the model we develop the C/O ratio is 8.1). This choice, which will be further discussed in Chapter 4, is supported by the previous studies which suggest that the adsorption behaviour of carbon materials is influenced mainly by the total amount of oxygen present rather than by the type of groups themselves (74) (32).

The construction of our model consists in placing the hydroxyl groups bonded to randomly selected carbon atoms on the graphitic sheets and the simultaneous removal of the atoms in the structure that would overlap with them. The hydroxylic groups are added so that the carbon-oxygen bonds lie on the same plane with the graphitic sheet and so that the C-C-O bond angles are 120°. This is done in order to preserve the sp^2 hybridization geometry of the carbon atoms. Carbon atoms in the proximity of vacancies are saturated through hydrogen

atoms; groups CH_2 and CH_3 are modelled using the OPLS united atom representation (61), with an additional partial charge on the CH_2 groups (bonded to the OH groups) to insure electroneutrality The reason for this choice is motivated because in the work by Tenney and Lastoskie (42) no parameters for the CH_3 groups are reported. Figure 3.21 (a) shows a computer visualization of a single graphitic layer, featuring defects and hydroxyl groups. This layer contains 274 carbon atoms (out of the 448 which were present in the pure carbon layer) and 25 hydroxyl groups. Figure 3.21 (b) shows a snapshot corresponding to CO_2 adsorption in a 10 Å pore at 298 K and 30 Bar.

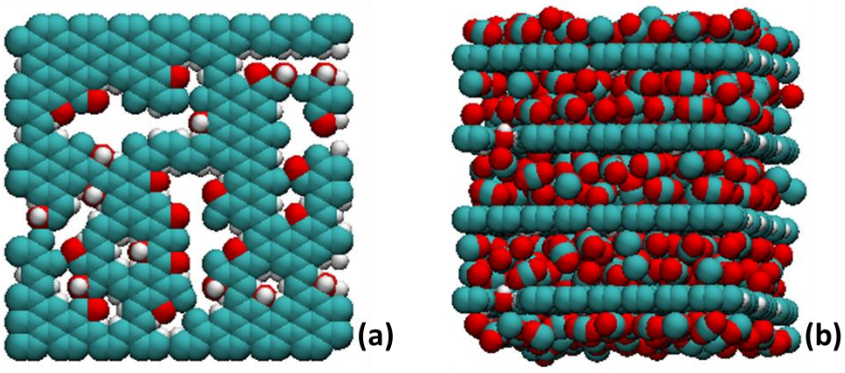

Figure 3.21. a) Top view of one wall of the single layer slit pore model with groups and defects; b) snapshot of CO_2 adsorption at 298 K and 30 Bar in 10 Å pores with groups and defects in periodic boundary conditions. Cyan: carbon, CH_2 and CH_3 groups; red: oxygen; white: hydrogen

In figure 3.22, as we did in the previous two sections, we show the GCV plot and L-curve for carbon dioxide at 298 K.

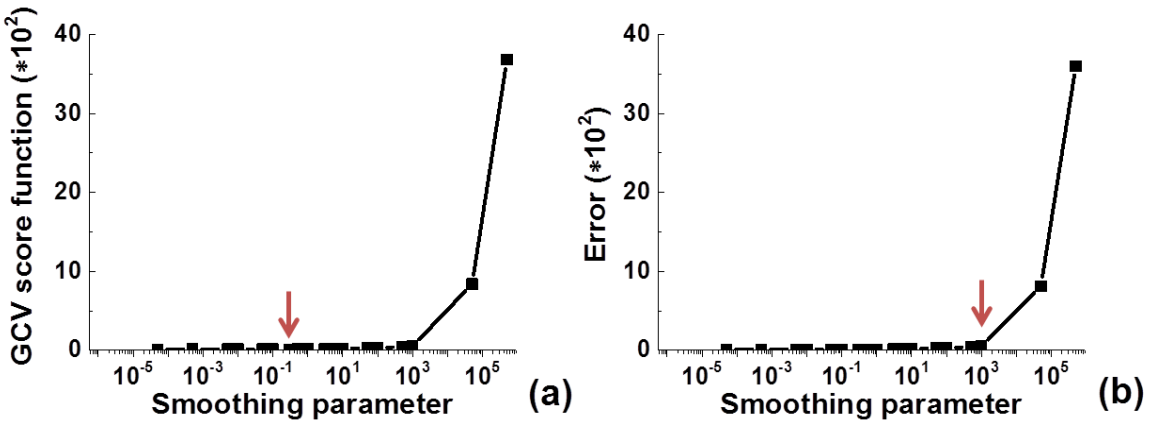

Figure 3.22. a) GCV plot and b) L-curve obtained for data for CO_2 at 298 K (single-layer model with groups and defects). The arrows indicate the values of the smoothing parameters we have chosen as corresponding to two possible PSDs.

In figure 3.23 we compare L-curves obtained for the single layer slit pore model with defects and functional groups, single layer model and classical slit pore model. It is noticeable that, for the higher values of smoothing parameter, the errors accumulate much faster in the single layer slit pore model with defects.

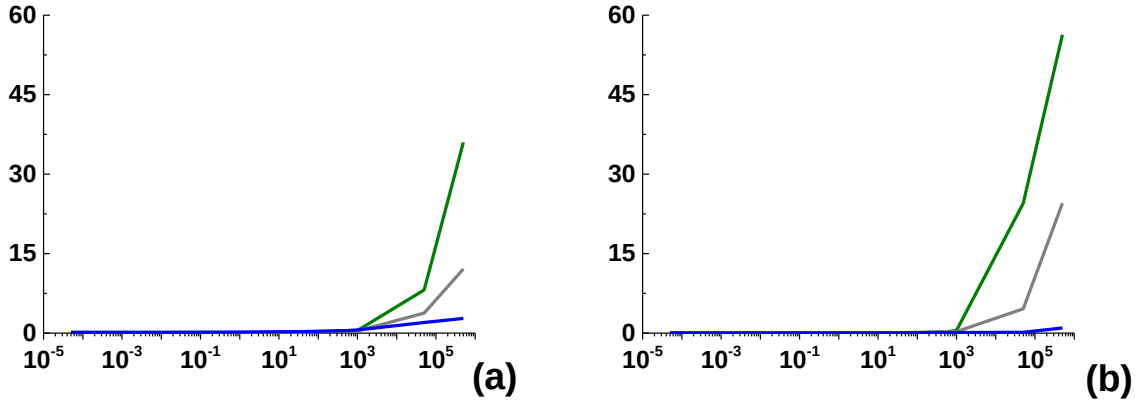

Figure 3.23. L-curves obtained for data from: a) CO_2 at 298 K and b) CH_4 at 298 K for the different types of the slit pore model. Blue lines: classic slit pore model, grey lines: single layer model, green lines: single layer with groups and defects model.

Going back to the case of the slit pore with groups and defects model (figure 3.22) the GCV plot presents a very slightly pronounced minimum for $\alpha = 3*10^{-1}$. This is therefore the value

we choose to use as associated to a possible PSD. In the case of the L-curve we choose $\alpha = 1*10^3$.

Figure 3.24 shows the possible PSDs corresponding to the selected smoothing parameters.

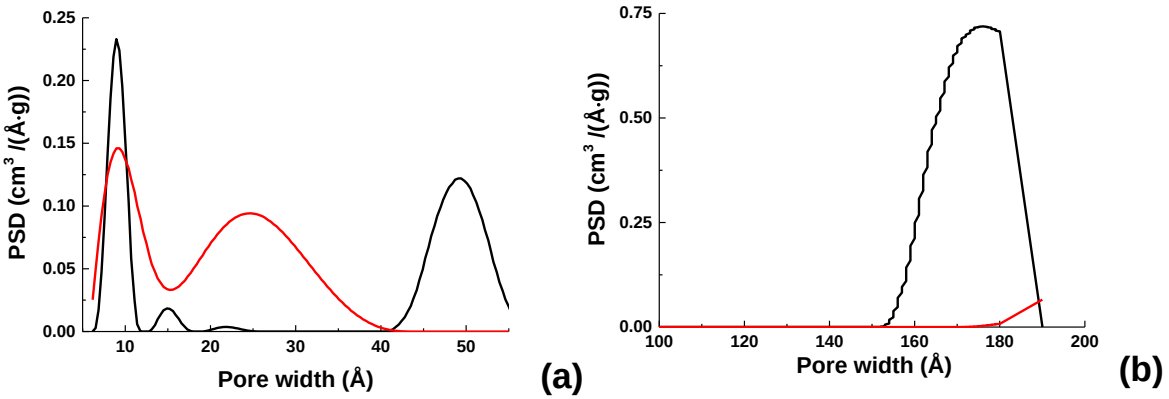

Figure 3.24. Pore size distributions corresponding to the values of smoothing parameter selected from the analysis of the GCV plot (black line) and L-curve (red line) for CO_2 at 298 K (single-layer model with groups and defects). Graph a) shows the range of pores up to 55 Å, while graph b) focuses on the region 100 – 200 Å. The PSDs do not feature any pores in the region 55 – 100 Å.

The pore size distributions are different from each other, even though they both show the most pronounced peak at 10 Å (within the window of reliability); this time any similarity with the PSD extracted from the nitrogen data (figure 3.5) has decreased even further. The PSDs confirm the trend, observed in the previous variant of the model, for which the most relevant pore widths are shifted towards lower values (about 10Å). In this case the window of reliability corresponds to pore widths between 0 and 20-30 Å.

Isotherms for methane at 273 K predicted using the PSDs above are presented in figure 3.25.

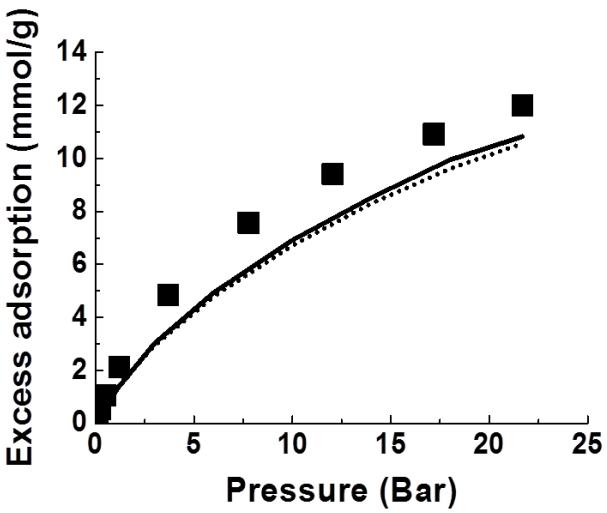

Figure 3.25. Predictions for methane adsorption on Maxsorb MSC-30 at 273 K (single-layer model with groups and defects), performed using the PSDs corresponding to two different values of the smoothing parameter: $\alpha = 3*10^{-1}$ (solid line) and $\alpha = 1*10^{3}$ (dotted line). Symbols represent the experimental results.

The predictions shown in figure 3.25 are still very similar to each other, but in this case the accuracy has deteriorated, as both predicted isotherms visibly underestimate the experimental adsorption. Before further commenting on this, we show the PSDs obtained from all available sources of data (figure 3.26).

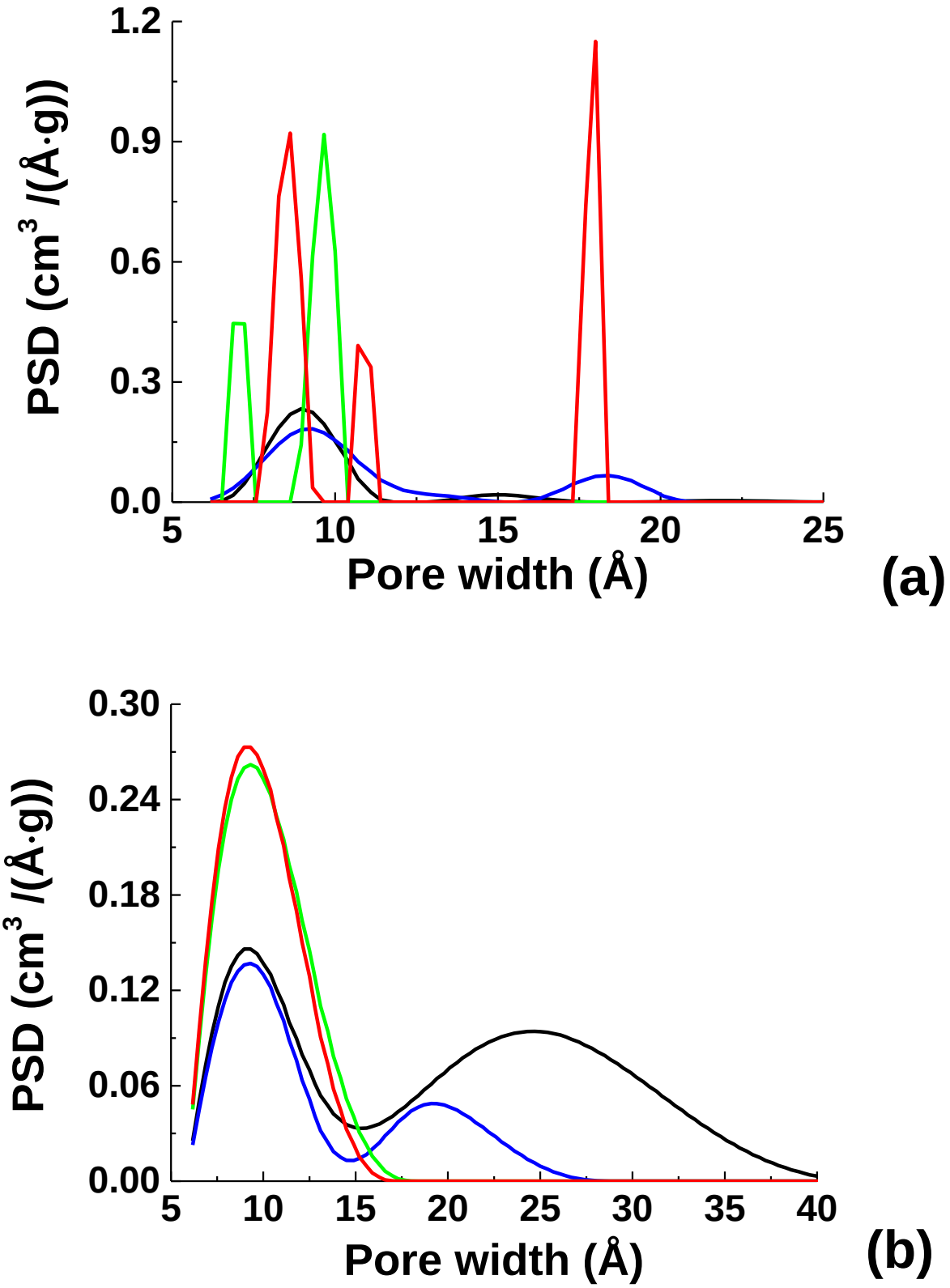

Figure 3.26. PSDs extracted from different sets of data (single-layer model with groups and defects): CO_2 at 273 K (blue line), CO_2 at 298 K (black line), CH_4 at 273 K (red line), CH_4 at 298 K (green

line). The PSDs correspond to values of smoothing parameter selected from the analysis of the GCV plot (graph (a)) and L-curve (graph (b)).

In this case the windows of reliability we have identified are the following: 0 to 20-30 Å for CO_2 at 298 K, 0 to 30-40 Å for CO_2 at 273 K, and 0 to 13-15 Å both for CH_4 at 298 K and 273 K.

Both in figure 3.26 (a) and (b) the PSDs extracted from the same species at different temperatures are very similar to each other. Moreover, in figure 3.26 a) all the PSDs show the most relevant of their peaks centred around 10 Å; only the data for methane at 273 K generate an intense peak at about 20 Å too. In figure 3.26 b) all PSDs feature the most pronounced peak at about 10 Å. Again, these results confirm that in the process of adding elements of complexity to the slit pore model the most pronounced peaks have been progressively shifted towards lower widths.

Given that in the region internal to a pore of 10 Å width a molecule of adsorptive is in general susceptible to higher potential than what happens in the region internal to a 20 Å pore, the shift towards lower pore widths could be an effect that compensates for the progressively lower number of atoms in each of the pore walls and hence weaker interaction emanating from the walls. The effect of lower number of atoms in the pore walls, due to the introduction of vacancies, prevails on the effect of the polar groups, which should increase the solid-fluid interaction at least for carbon dioxide.

The predictions performed using PSDs obtained from the data for CO_2 and CH_4 both at 298 K are shown in figures 3.27 and 3.28. The value of the smoothing parameter used for CO_2 at 298 K is $3*10^{-1}$, while for methane at 298 K the value of $\alpha = 5*10^{-5}$ has been selected. These values have been selected from the analysis of the GCV curve and they both correspond to the best predictions that could be obtained, starting from a particular set of the reference experimental data.

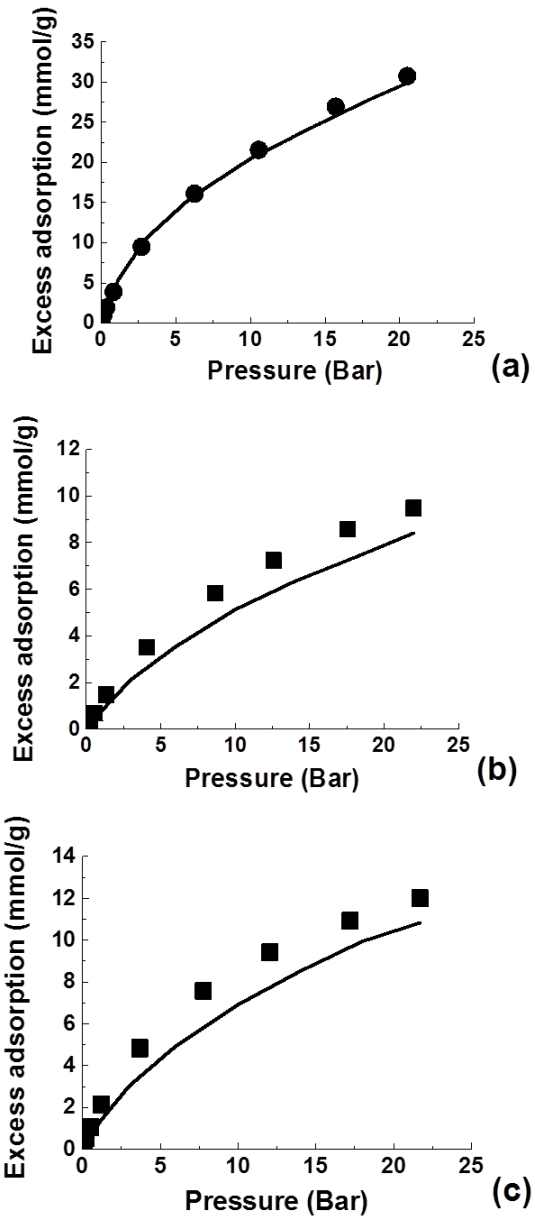

Figure 3.27. Isotherms predicted using the PSD from CO_2 adsorption data at 298 K (single-layer model with groups and defects). Symbols represent experimental data and solid lines represent predictions. a) CO_2 at 273 K, b) CH_4 at 298 K, c) CH_4 at 273 K.

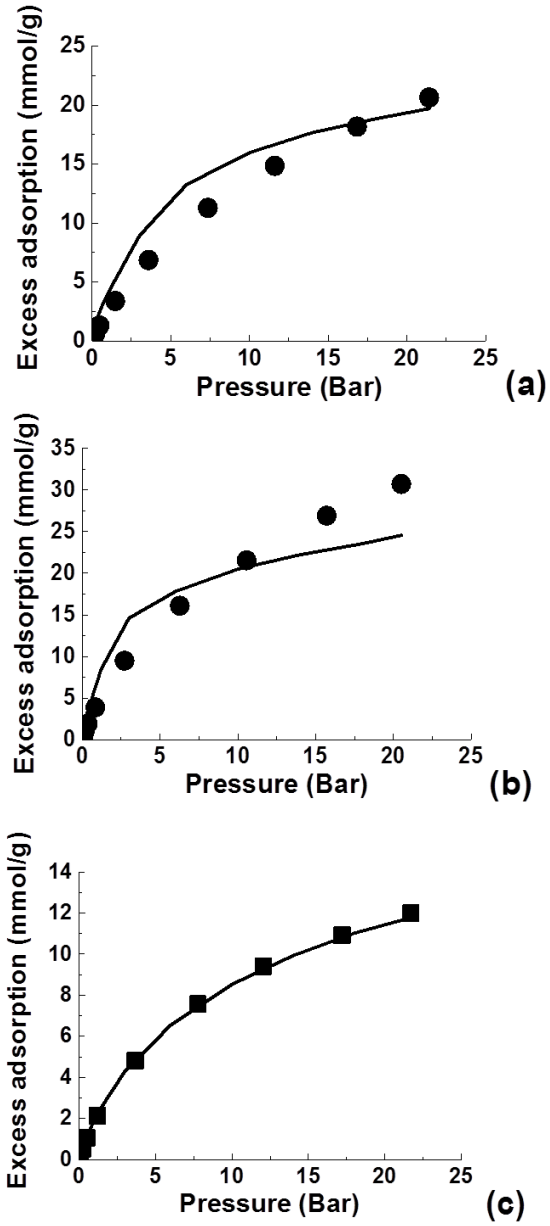

Figure 3.28. Isotherms predicted using the PSD from CH_4 adsorption data at 298 K (single-layer model with groups and defects). Symbols represent experimental data and solid lines represent predictions. a) CO_2 at 298 K, b) CO_2 at 273 K, c) CH_4 at 273 K.

Compared to the results for the single layer model, figure 3.27 still shows good performance in the prediction of CO_2 adsorption at 273 K, but also reveals some loss of accuracy in the case of methane at both the temperatures considered. The results in figure 3.28 show substantial loss of accuracy in the predicted CO_2 isotherms, although the predictions for methane are still good.

The general picture emerging from these results is that the introduction of the defects and surface groups in a single layer model leads to a deteriorated predictive capability of the model, despite it featuring elements of heterogeneity which should have made it more realistic.

To better quantify this statement, even for this variant of the slit pore model we calculate the mean squared errors (MSE) considering the differences between all the experimental points in each isotherm and the predictions at the same pressures. When starting from data for CO_2 at 298 K the errors are 1.31, 2.08 and 0.44 for CH_4 at 298 K, CH_4 at 273 K and CO_2 at 273 K respectively; if we start from data for CH_4 at 298 K the errors are 3.88, 10.94, and 0.02 for CO_2 at 298 K, CO_2 at 273 K and CH_4 at 273 K respectively. These results are presented in figure 3.29, which shows a comparison with the MSEs calculated for the other two variants of the slit pore model:

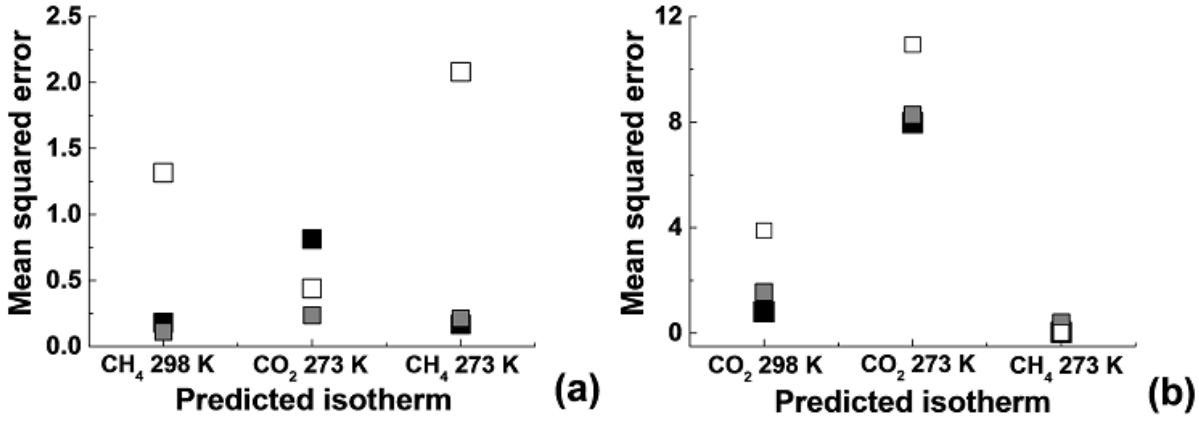

Figure 3.29. Mean squared error calculated for predictions starting from data for CO_2 at 298 K (graph a)) and from data for CH_4 at 298 K (graph b)). Black symbols: classical slit pore model, grey symbols: single layer model, white symbols: single layer with groups and defects model.

The results shown in figure 3.29 confirm the overall picture emerging from this analysis. The classical slit pore model gives accurate predictions in most of the cases, particularly when the predictions are based on the PSD from CO_2 isotherm at 298 K (graph a)). In this instance, the most significant error is observed for the predicted CO_2 isotherm at 273 K, and in fact in this specific case the overall error of the predictions exceeds those in the other two models.

Interestingly, the single layer model shows performance comparable with the classical slit pore model (being even more accurate when carbon dioxide adsorption at 273 K is predicted starting from carbon dioxide data at 298 K and showing a slight improvement even when the same data are used to predict methane at 298 K). Finally, despite appearing more realistic, the single layer model with defects and surface groups shows substantial errors, with this effect being more pronounced, as expected, when the predictions are made starting from data for methane adsorption.

As for the predictions performed using data for methane at 298 K (graph b)), first of all the values of the MSE are in general higher than the values shown in graph a) (as should be expected given all the discussion based on the signal to noise ratio issue), with the best predictions being the ones for CH_4 at 273 K. For the prediction of carbon dioxide adsorption at 298 and 273 K, again the single layer with groups and defects model shows values of MSE much higher than the other two models. At both temperatures the classical slit pore model performs slightly better than the single layer model.

The data presented in figure 3.29 are also coherent with the data presented in figure 3.23, in the sense that the highest values of MSE are generally associated to the model that show the highest values in the error of the fit.

Summarizing all the data, the models that on average show the best predictive capability are the classic slit pore model and single layer model, while the single layer with groups and defects model shows a good performance only when predicting the same species but at different temperatures. Throughout the section we have already alluded to the underlying reason of this result: as the slit-pore model was modified the solid-fluid interaction emanating from the pore walls became weaker from classical slit pore model to single layer model to single layer with defects and surface groups. This led to weaker adsorption in the pore of the same width under the same conditions, reduction of the signal-to-noise ratio and window of reliability and in general lower robustness of the model.

3.6. Calibration of single layer with groups and defects model

To understand the scope and relevance of the next two sections of results, it is important to provide a historical perspective on the thesis development. Our initial effort to build predictive models of adsorption in Maxsorb MSC-30 focused on the well-established slit pore model and its variants. As the project progressed it became apparent that the introduction of the elements, which we originally thought would make the model more realistic, actually led to worsening of the accuracy of predictions as has been explained in the previous section. On the conceptual level, the slit pore model was also difficult to reconcile with the morphological features of Maxsorb MSC-30 such as high surface area and degree of disorder. These factors promoted us to explore alternative models, based on disordered packings of structural elements. These models are covered in the next chapters of the thesis. Without pre-emptying the results of the chapters to come, here it suffices to say that the development of these models required adjustment of the solid-fluid interactions for individual classes of adsorbing species. Although this adjustment is properly justified in the upcoming chapters on the grounds of the chemistry of the involved structural elements, it nevertheless poses a question whether a similar strategy can be adopted for slit-pore based models. This would allow one to compare predictive power of two classes of models on the same basis. Furthermore, as has been shown by Sweatman and Quirke (5, 75, 76) accurate models of adsorption in activated carbons based on slit-pore approach do require solid-fluid interaction parameters for individual species to be optimized. Following the work by Sweatman and Quirke (5, 75, 76) we now proceed to re-calibrate the methane – adsorbent interaction for the single layer with groups and defects model (and noting that this set of studies has been carried *a posteriori*, after the disordered models of Maxsorb MSC-30 had been constructed and explored).

For this purpose the idea is to consider the pore size distribution which has given the best predictions so far and use it to predict methane at a certain temperature, this time starting from a kernel for which the methane-surface interaction has been scaled. Several scaling factors need to be tried, until agreement with the experimental methane isotherm at the same temperature is obtained. Once the appropriate scaling factor has been chosen the new model can be tested trying to predict methane at a different temperature or different species.

In our case the pore size distribution that has given the best prediction for the slit pore with groups and defects model has been extracted using data for carbon dioxide at 298 K and smoothing parameter $\alpha = 3*10^{-1}$. This PSD has already been presented in figure 3.24, but for clarity it is also reported below (figure 3.30) with focus on the window of reliability:

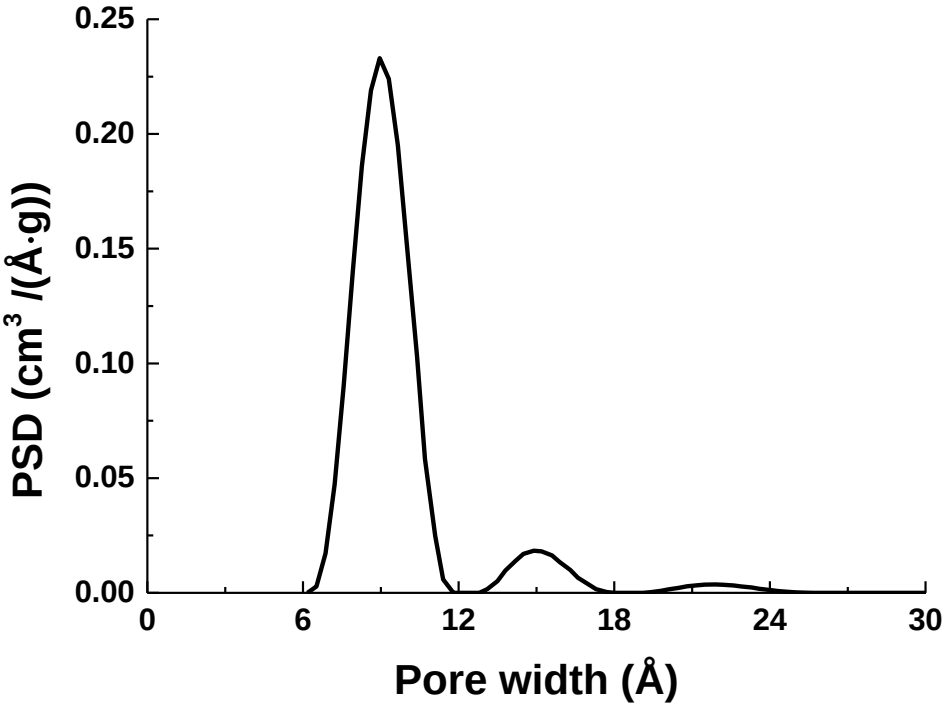

Figure 3.30. Pore size distribution corresponding to the value of smoothing parameter selected from the analysis of the GCV plot ($\alpha = 3*10^{-1}$) for CO_2 at 298 K (single-layer model with groups and defects).

Using the PSD above we have predicted methane adsorption at 298 K. Each prediction is based on a different value of the scaling parameter for the the methane – adsorbent interaction. The results are shown in figure 3.31.

The scaling factors which have been adopted are 1.1 and 1.2 and in both cases the predictions (red line and blue line respectively) are compared to the experimental isotherm (square symbols) and to the predictions made without using any scaling factor (black line).

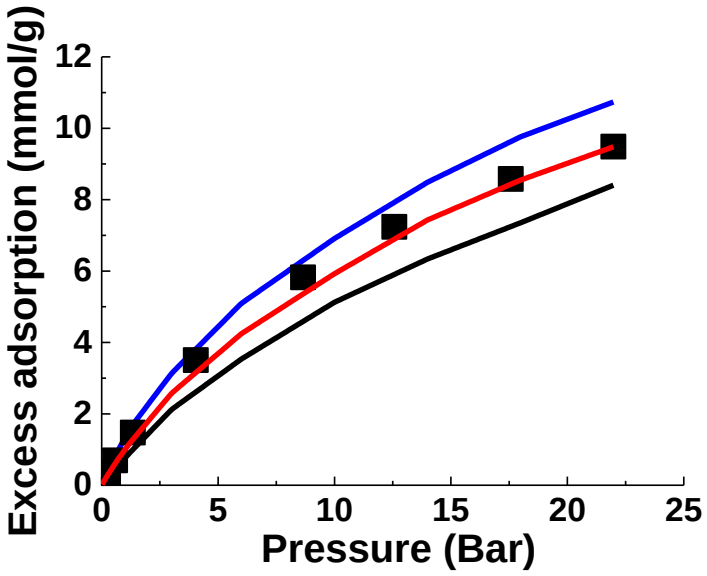

Figure 3.31. Predictions for methane adsorption at 298 K obtained using kernels simulated for the same species at the same temperature with scaling factor 1.1 (red line) and 1.2 (blue line) and the PSD reported in figure 3.30. Squared symbol represent the experimental data, while the black line represents the prediction obtained without using a scaling factor.

The graph above shows an improvement in the predictions for the scaling factor 1.1, while the predictions made using the scaling factor 1.2 overestimate the experimental data. In table III.1 we show the mean squared errors calculated in all cases (without any scaling, and with scaling factors 1.1 and 1.2) taking the experimental data as the reference.

Table III.1. Mean squared errors for the prediction of CH_4 adsorption at 298 K, made using the PSD reported in figure 3.30 and kernels simulated for CH_4 at 298 K with different values of scaling factor for the solid-fluid interaction.

SCALING FACTOR	MSE
1	1.32
1.1	0.09
1.2	0.56

The results in the table above confirm the improvement in the predictions when the scaling factor 1.1 is used; table III.2 also shows a comparison with the MSEs of the predictions obtained using the classic and single layer slit pore models:

Table III.2. Mean squared errors for the prediction of CH_4 adsorption at 298 K, made using PSDs extracted from CO_2 data at 298 K in different variants of the slit pore model (single layer with groups and defects model and scaling factor 1.1 for the methane-surface interaction, termed SL_GR_scaled_1.1 here, classic slit pore model (CLASSIC) and single layer model (SINGLE LAYER)).

MODEL	MSE
SL_GR _scaled_1.1	0.09
CLASSIC	0.17
SINGLE_LAYER	0.11

The data in table III.2 show that even if compared with the classic and single layer slit pore models the prediction performed using the scaling factor 1.1 in the single-layer with groups and defects model is the most accurate. However, we note that obviously the same scaling strategy applied to the classic slit pore model and single layer model would also substantially improve their accuracy. Therefore, for methane adsorption at 298 K we adopt the solid-fluid potential obtained using the scaling factor of 1.1 and we proceed to test this optimized model.

For the purpose we try to predict the adsorption of methane at 273 K using a kernel simulated for the same species and at the same temperature with the scaling factor of 1.1 and the pore size distribution presented in figure 3.30. The results are presented below.

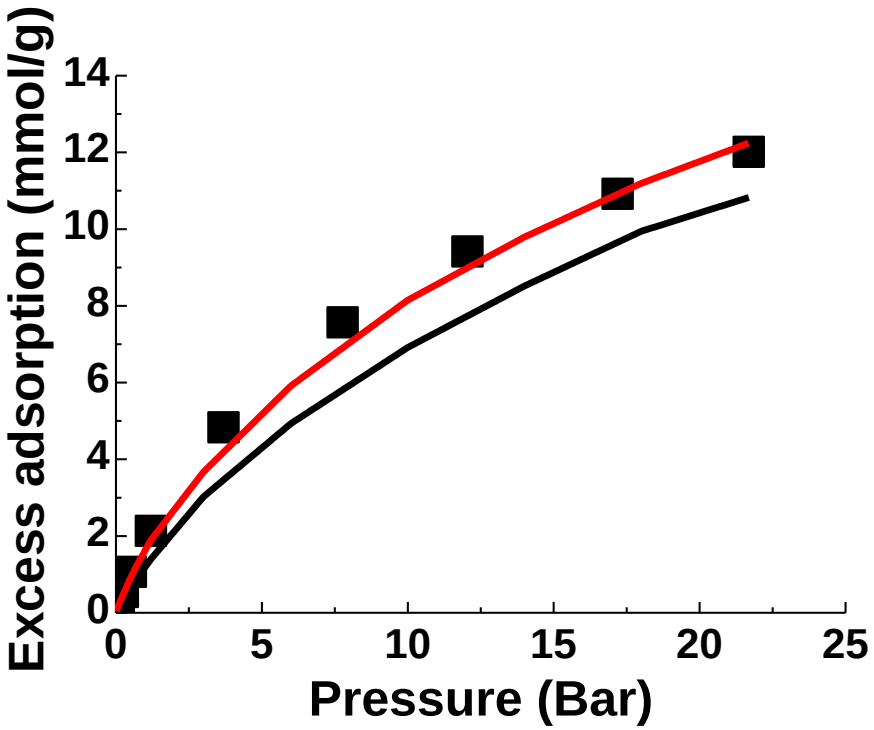

Figure 3.32. Prediction for methane adsorption at 273 K obtained using kernels simulated for the same species at the same temperature with scaling factor of 1.1 (red line) and the PSD reported in figure 3.30. Squared symbols represent the experimental data, while the black line represents the prediction obtained without using a scaling factor.

Figure 3.32 shows that the model with re-calibrated solid-fluid interactions leads to a substantial improvement in the predictions for methane. This is confirmed by the mean squared errors in table III.3, which also show a comparison with the performance of the classic and single layer slit pore models.

Table III.3. Mean squared errors for the prediction of CH_4 adsorption at 273 K, made using the PSD reported in figure 3.30 and kernels simulated for CH_4 at 273 K without and with the re-calibration of the solid-fluid interactions for methane (SL_GR not scaled and SL_GR scaled 1.1, respectively) compared with the MSEs for the classic slit pore model and the single layer model.

SCALING FACTOR	MSE
SL_GR not scaled	2.08
SL_GR scaled 1.1	0.21
CLASSIC	0.16
SINGLE LAYER	0.21

The results reported in table III.3 show that, even at 273 K, the accuracy of the predictions is now comparable to the accuracy of the classic and single layer slit pore models.

3.7. Simulation of water adsorption in the single layer with groups and defects model

One of the main reasons to move from the classic slit pore model towards models featuring defects and surface groups was the ambition to include water in the consideration of multicomponent adsorption in carbon capture related processes. Given that applying the scaling to the methane – adsorbent interaction the model has now acquired a good predictive capability we now attempt to simulate adsorption of water in the model based on the single layer with groups and defects. For water we use the tip4p model and we run simulations at 298 K using the same pore width resolution as for methane and carbon dioxide.

In figure 3.33 we report the results of our simulations for pore widths between 6 and 10 Å.

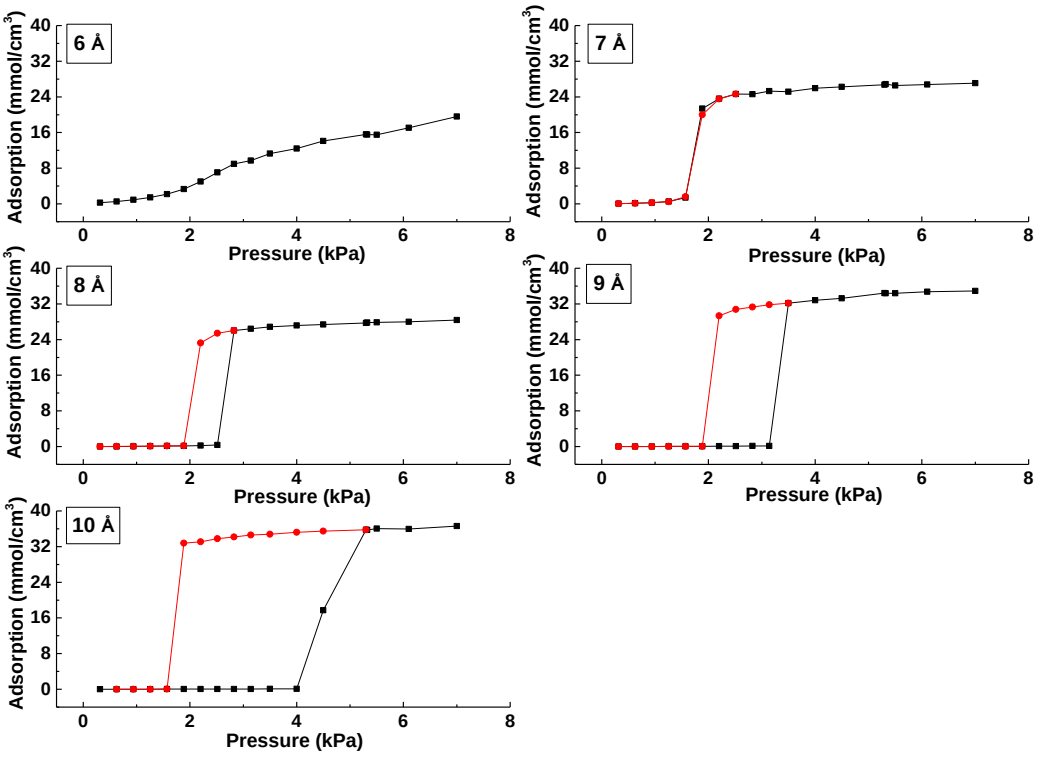

Figure 3.33. Simulation of water adsorption at 298 K (absolute adsorption) in pores of different widths (slit pore with groups and defects model). Red lines and symbols correspond to the desorption isotherm.

From the figure above we can notice that the model slit pores behave as hydrophobic structures, with the isotherms being similar in shape to those reported in many other studies on adsorption of water in carbon slit pores (77-79). The results are plotted in terms of absolute adsorption, because for 10 Å pore the complete filling of the material happens at pressures exceeding p^0 for the tip4p model (4.48 kPa). We also notice that as the pore width increases the pressure at which condensation occurs also increases, as expected due to the weakening of the potential well inside the pores.

The isotherm simulated in the 6 Å pore shows that the pore filling happens through a continuous process. This case is analogous to the process of micropore filling as described by Thommes (80). In the range of 7-10 Å all isotherms exhibit capillary condensation, that is a

sharp phase transition from a film on the surface of the pore to a pore with fluid in a liquid-like state.

We note that the pores exhibit hydrophobic properties despite the presence of the surface groups, with virtually no water adsorption prior to capillary condensation. In the same figure for the pores in which condensation occurs we also show desorption isotherms. These isotherms were obtained by starting from a higher pressure state with the isotherm fully filled with liquid. A range of decreasing pressure values were then considered with the starting configuration for each pressure point corresponding to the final configuration at the neighbour point with higher pressure. This process mimics experimental desorption procedure. The figure shows that isotherms in 8, 9, 10 Å pores feature distinct hysteresis loop. As the pore becomes smaller, the hysteresis loop also becomes smaller and finally disappears in 7 Å pore.

Before we reflect on the consequences of this behaviour for the implementation of the predictive model, it is important to (briefly) put these results in the context of the extensive existing studies on capillary condensation and phase behaviour under confinement and in particular slit pores.

The current body of knowledge can be briefly summarized as follows (81). Phase behaviour of a fluid confined in a slit pore can be described by a phase diagram similar in the appearance to the bulk vapour-liquid coexistence diagram. The density of the vapour-liquid state will be however higher compared to the bulk densities at the same temperature, whereas the densities of the liquid-like phase will be lower than the bulk liquid density at the same temperature. Hence, in the graph where bulk and confined diagrams are imposed onto each other, the confined diagram will look like a shrunk version of the bulk diagram (figure 3.34 (a)). The vapour-like state in the slit pore will comprise of a liquid film on the walls of the slit pore and lower density vapour in the centre; the liquid-like state corresponds to the pore completely filled with liquid. The reduced or shrunk form of the phase coexistence diagram also implies lower value of the critical point, compared to the bulk diagram. The greater degree of confinement is the smaller the confined phase envelop is, until it finally disappears in very small pores where no capillary condensation or phase coexistence is observed.

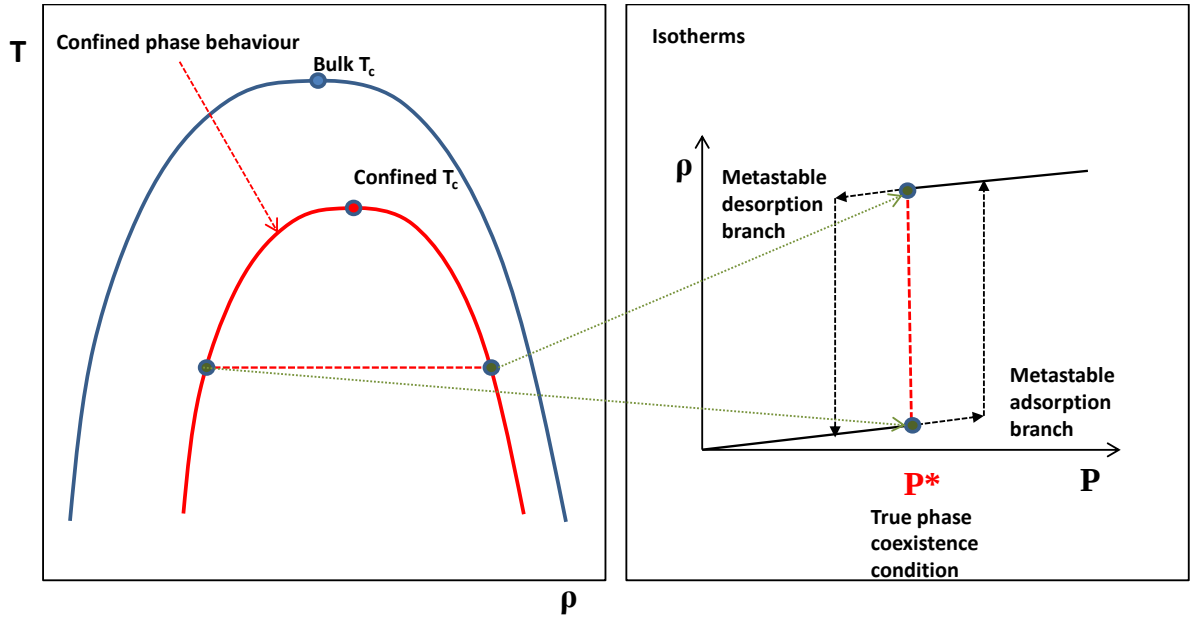

Figure 3.34 Schematic depiction of the relation between the bulk vapour-liquid phase diagram and the same diagram for the confined fluid (on the left); and the relation between the simulated capillary condensation adsorption isotherm and the location of the phases in coexistence on the confined diagram (on the right).

Consider now an adsorption isotherm as shown in figure 3.34 (on the right). As the pressure increases, a liquid film forms on the surface of the pore. At a certain pressure point a capillary condensation occurs. If we now reverse the process and consider desorption in a slit pore, two important scenarios must be considered.

First, let us imagine that the slit pore is open from two ends. In this case the starting configuration is a pore featuring liquid-vapour meniscus, which recedes once the pressure corresponding to the confined phase coexistence is reached on the desorption process. The adsorption and desorption mechanism clearly feature different pathways leading to an adsorption hysteresis in the slit pore. This consideration has long served as a plausible mechanism of adsorption hysteresis in real materials. The liquid film prior to condensation is in a metastable state; it is the jump on the desorption isotherm that is considered to be the true location of the phase coexistence (82).

A slightly different consideration is required when dealing with simulation of adsorption in slit pore models in periodic boundary conditions. In this case, there is no explicit vapour-liquid meniscus and both adsorption and desorption branches will enter the regions of

metastability, as shown in Figure 3.34. The pressure value corresponding to the true phase coexistence is located somewhere in between two pressure jumps and methods such as thermodynamic integration are required to obtain it (83).

As the confinement increases the hysteresis loop decreases and finally disappears together with the condensation. As the temperature increases the hysteresis loop decreases and finally disappears together with the phase coexistence at the critical point (80). This is schematically depicted in Figure 3.35.

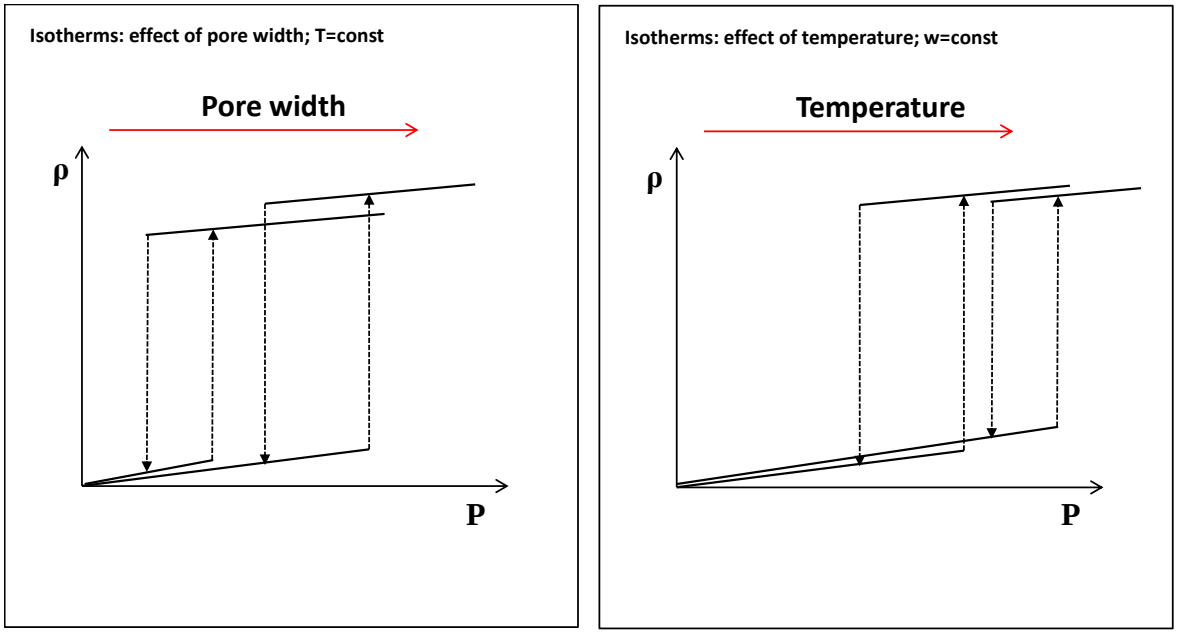

Figure 3.35. Hysteresis behaviour in simulated adsorption isotherms undergoing capillary condensation in a slit pore: larger pores feature broader hysteresis loop (on the left); higher temperature leads to smaller hysteresis loop and its ultimate disappearance.

In the context of water adsorption in slit pores the effects illustrated above have been extensively studied by Monson and co-workers (77) (84). Indeed, the results shown in figure 3.33 confirm this picture: the hysteresis loops increase with the pore width; the location of the transition is shifted to lower pressures as the pore width decreases.

For the predictive models based on AIE and PSD the presence of hysteresis in general presents a substantial technical challenge. The adsorption and desorption isotherms cannot be used within the AIE as the extent of the metastabilities of the branches is not a reflection of the properties of the real material, but to a significant extent an artefact of the model geometry (slit pore in PBC) and methodology (GCMC). A more appropriate protocol would

establish the location of the true phase coexistence for each pore. Indeed this is the approach implemented in structural characterization of porous solids using nitrogen and argon sorption at 77 and 87K. Within the DFT methods applied to these fluids the location of the phase coexistence can be obtained analytically. In the case of water adsorption in complex slit pore model, a thermodynamic integration approach would be required, which implies a substantial computational effort.

Thus we have reached the impasse situation. The available experimental data for single component water adsorption is are at 303 K and up to bulk condensation pressure (see the later Chapters). However, for the reasons outlined above, validating the model against this experimental data becomes a separate and substantial challenge. On the other hand for the cases where the partial pressure of water is very low (post-combustion capture), the isotherms considered above predict essentially zero adsorption (except for the 6 Å) and really no integration over a PSD is needed. In the absence of any independent validation this result however is difficult to assert.

We would like to further make a note on purely computational challenges associated with simulation of water in slit pores. These challenges arise from the very slow equilibration processes. For example, a full adsorption/desorption isotherm in a 10 Å pore requires about 35 days of CPU time, not taking into account overheads associated with data management (which would increase this time to three months). This simulation is required for each adsorption width in the kernel (tens of isotherms) and each temperature requires a new kernel. We anticipate that for wider pores this time would increase, making this study computationally cumbersome and the model less attractive from an engineering point of view. Therefore, at this stage predictive studies of water adsorption in slit pores based on AIE/PSD have not been pursued any further.

More fundamental aspects related to the adsorption of water in high surface area activated carbons, including the role of the oxygenated groups, will be investigated in Chapter 5.

3.8. Conclusions

This chapter has considered three different types of slit pore models in application to Maxsorb activated carbon; we have tried to extract pore size distributions using simulated and experimental data for methane and carbon dioxide, both at 273 and 298 K. The extracted PSDs have then been used to make adsorption predictions.

For the fluids we have examined, the classical slit pore model gives quite accurate results when the PSD extracted from the data for CO_2 at 298 K is used. Data from CO_2 at 273 K, which in principle should give more accurate predictions, have not been used because of the technical challenges related to the capillary condensation shown by some of the isotherms in the kernel In general, a lower level of accuracy is characteristic for the predictions based on PSD from methane adsorption data. In the case of the single layer model we have observed an improvement in the predictions performed starting from the data for CO_2 at 298 K, and, as expected, a worsening in the case of pore size distributions obtained from the methane data. The introduction of groups and defects has in general lowered the predictive power of the resultant pore size distributions, at least in the absence of a re-calibration of the solid-fluid interaction parameters.

The observations above make sense if approached from the signal-to-noise point of view. Stronger interacting species (carbon dioxide) produce more robust and reliable PSD models, compared to weaker interacting species (methane). Reducing the number of carbon layers in the model and further introduction of defects weakens the solid-fluid interactions thus lowering the signal-to-noise ratio. One would hope that the addition of the surface groups would somehow counterbalance this trend (at least for polar species such as carbon dioxide) however it is clearly not the case here. The work by Liu and Wilcox (56) (who explored the pressure regime up to 1 Bar) and by Tenney and Lastoskie (42) actually showed a general increase in the CO_2 adsorption in the presence of oxygenated groups. A possible explanation for this discrepancy in the results can be searched into the differences in structure and composition of the models (including the number of graphitic sheets, the type and accessibility of the functional groups, the C/O ratios or the dimension of the structural defects), which also highlights the importance of a proper re-calibration of the parameters. Further comments on this aspect will be introduced in Chapter 4, which will present a more

systematic study on the role of different parameters, including the presence/absence of functional groups in a disordered model for high surface area activated carbons, their number and type.

For the models we have studied, the pore size distributions are in general different one from another, although they all tend to show more or less pronounced peaks around 10 and 20 Å. None of them exactly coincides with the PSD extracted by Otowa et al. using data for nitrogen at 77 K, but in some cases (especially for the classical slit pore model) the presence of the most intense peak at 20 Å of width indicates some agreement with the nitrogen sorption data. Having said this, it is important to emphasize that the PSD obtained by Otowa et al. also required an assumption of an independent slit pore structure and their analysis was based on Cranston and Inkley's pore analysis method (54), which itself is a subject of a number of assumptions.

From the analysis presented here it is clear that the obtained PSDs are not precise or rigorous properties, although they give some indication about the most relevant aspects of the porous structure.

In agreement with the previous studies by Sweatman and Quirke (5, 75, 76) , re-calibration of the solid fluid interactions for the individual species using a single reference experimental isotherm can substantially improve the scope and accuracy of the models. As such, for the adsorption of simple components (such as methane, carbon dioxide, hydrogen, nitrogen etc) and their mixtures at ambient and high temperatures and pressures, a classic slit pore model with calibrated solid-fluid interactions and a PSD obtained from fitting the carbon dioxide isotherm may still provide the most accurate route after all, even though the classic slit pore model is not compatible with the experimentally measured structural characteristics of Maxsorb MSC-30.

The greatest challenge to the slit pore models came in this study from the adsorption of water. A model based on a single layer of graphene featuring defects decorated with surface groups exhibited lower quality predictions in general compared to the classic slit pore model and, even after the re-calibration of the solid-fluid interaction for methane, which definitely improved the predictive capability of the model (making it comparable to the capability of the classic slit pore model for the prediction of methane and carbon dioxide) at the same time has

not achieved any particular promising water sorption characteristics expected from it. To some extent, as hinted before, this failure could be associated with the particular protocol to position the surface groups and more advanced approaches that take into account their accessibility must also be considered. As a result, the water isotherms in model slit pores feature essentially zero water adsorption loading prior to capillary condensation and a substantial hysteresis loop. This makes the probability of this model, if integrated over a PSD, to accurately reproduce experimental results highly unlikely, while generation of the kernel of water isotherms with correctly identified phase coexistence conditions presents a computationally tedious problem.

While not discarding the classic slit pore model within the realm where it works very well (simple adsorbing species at ambient conditions etc), peculiar structural features of Maxsorb MSC-30 and issues associated to water adsorption prompted us to explore other possible models. This will be the topic of the next two Chapters.

References

1. Harris PJF, Liu Z, Suenaga K. Imaging the atomic structure of activated carbon. J Phys: Condens Matter. 2008;20(36):362201-5.
2. Lillo-Ródenas MA, Cazorla-Amorós D, Linares-Solano A, Béguin F, Clinard C, Rouzaud JN. HRTEM study of activated carbons prepared by alkali hydroxide activation of anthracite. Carbon. 2004;42(7):1305-10.
3. Everett DH, Powl JC. Adsorption in slit-like and cylindrical micropores in the henry's law region. A model for the microporosity of carbons. Journal of the Chemical Society, Faraday Transactions 1: Physical Chemistry in Condensed Phases. 1976;72(0):619-36.
4. Seaton NA, Walton JPRB, quirke N. A new analysis method for the determination of the pore size distribution of porous carbons from nitrogen adsorption measurements. Carbon. 1989;27(6):853-61.
5. Sweatman MB, Quirke N. Characterization of Porous Materials by Gas Adsorption: Comparison of Nitrogen at 77 K and Carbon Dioxide at 298 K for Activated Carbon. Langmuir. 2001;17(16):5011-20.
6. Lastoskie C, Gubbins KE, Quirke N. Pore size distribution analysis of microporous carbons: a density functional theory approach. The Journal of Physical Chemistry. 1993;97(18):4786-96.
7. Sosin KA, Quinn DF. Using the high pressure methane isotherm for determination of pore size distribution of carbon adsorbents. J Porous Mater. 1995;1(1):111-9.
8. Scaife S, Kluson P, Quirke N. Characterization of Porous Materials by Gas Adsorption: Do Different Molecular Probes Give Different Pore Structures? The Journal of Physical Chemistry B. 2000;104(2):313-8.
9. Davies GM, Seaton NA. Development and Validation of Pore Structure Models for Adsorption in Activated Carbons. Langmuir. 1999;15(19):6263-76.
10. Davies GM, Seaton NA, Vassiliadis VS. Calculation of Pore Size Distributions of Activated Carbons from Adsorption Isotherms. Langmuir. 1999;15(23):8235-45.
11. Davies GM, Seaton NA. Predicting adsorption equilibrium using molecular simulation. AIChE Journal. 2000;46(9):1753-68.
12. Heuchel M, Davies GM, Buss E, Seaton NA. Adsorption of Carbon Dioxide and Methane and Their Mixtures on an Activated Carbon: Simulation and Experiment. Langmuir. 1999;15(25):8695-705.
13. Pérez-Mendoza M, Schumacher C, Suárez-García F, Almazán-Almazán MC, Domingo-García M, López-Garzón FJ, et al. Analysis of the microporous texture of a glassy carbon by adsorption measurements and Monte Carlo simulation. Evolution with chemical and physical activation. Carbon. 2006;44(4):638-45.
14. Pinto da Costa JMC, Cracknell RF, Seaton NA, Sarkisov L. Towards predictive molecular simulations of normal and branched alkane adsorption in carbonaceous engine deposits. Carbon. 2011;49(2):445-56.
15. Ravikovitch PI, Vishnyakov A, Russo R, Neimark AV. Unified Approach to Pore Size Characterization of Microporous Carbonaceous Materials from N2, Ar, and CO2 Adsorption Isotherms†. Langmuir. 2000;16(5):2311-20.
16. Wilson JD. Statistical approach to the solution of first-kind integral equations arising in the study of materials and their properties. Journal of Materials Science. 1992;27(14):3911-24.
17. Cai Q. Hybrid Molecular Dynamic Simulation/Pore Network Model of Diffusion in Nanoporous Carbons: The University of Edinburgh; 2007.
18. Vega LF. Chapter 5. In: Balbuena PB, J.M. S, editors. Nanomaterials: Design and Simulation: Elsevier; 2007. p. 101-26.
19. Jagiello J, Schwarz JA. Relationship between energetic and structural heterogeneity of microporous carbons determined on the basis of adsorption potentials in model micropores. Langmuir. 1993;9(10):2513-7.

20. Kaneko K, Cracknell RF, Nicholson D. Nitrogen Adsorption in Slit Pores at Ambient Temperatures: Comparison of Simulation and Experiment. Langmuir. 1994;10(12):4606-9.
21. Cracknell R, Nicholson D, Tennison S, Bromhead J. Adsorption and selectivity of carbon dioxide with methane and nitrogen in slit-shaped carbonaceous micropores: Simulation and experiment. Adsorption. 1996;2(3):193-203.
22. Samios S, Stubos AK, Kanellopoulos NK, Cracknell RF, Papadopoulos GK, Nicholson D. Determination of Micropore Size Distribution from Grand Canonical Monte Carlo Simulations and Experimental CO2 Isotherm Data. Langmuir. 1997;13(10):2795-802.
23. McCallum CL, Bandosz TJ, McGrother SC, Müller EA, Gubbins KE. A Molecular Model for Adsorption of Water on Activated Carbon: Comparison of Simulation and Experiment. Langmuir. 1998;15(2):533-44.
24. Ravikovitch PI, Vishnyakov A, Russo R, Neimark AV. Unified Approach to Pore Size Characterization of Microporous Carbonaceous Materials from N_2, Ar, and CO_2 Adsorption Isotherms Langmuir. 2000;16(5):2311-20.
25. Sweatman MB, Quirke N. Characterization of Porous Materials by Gas Adsorption: Comparison of Nitrogen at 77 K and Carbon Dioxide at 298 K for Activated Carbon. Langmuir. 2001;17(16):5011-20.
26. Yang Q, Zhong C. Computer Simulations of Adsorption Characteristics of Carbon Dioxide in Slit Graphite Pores. The Canadian Journal of Chemical Engineering. 2004;82(3):580-9.
27. Billemont P, Coasne B, De Weireld G. An Experimental and Molecular Simulation Study of the Adsorption of Carbon Dioxide and Methane in Nanoporous Carbons in the Presence of Water. Langmuir. 2011;27(3):1015-24.
28. Lithoxoos GP, Peristeras LD, Boulougouris GC, Economou IG. Monte Carlo simulation of carbon monoxide, carbon dioxide and methane adsorption on activated carbon. Molecular Physics. 2012;110(11-12):1153-60.
29. Silvestre-Albero J, Silvestre-Albero A, Rodríguez-Reinoso F, Thommes M. Physical characterization of activated carbons with narrow microporosity by nitrogen (77.4 K), carbon dioxide (273 K) and argon (87.3 K) adsorption in combination with immersion calorimetry. Carbon. 2012;50(9):3128-33.
30. Nicholson D. A Simulation Study of Energetic and Structural Heterogeneity in Slit-Shaped Pores. Langmuir. 1999;15(7):2508-15.
31. López-Ramón MV, Jagiełło J, Bandosz TJ, Seaton NA. Determination of the Pore Size Distribution and Network Connectivity in Microporous Solids by Adsorption Measurements and Monte Carlo Simulation. Langmuir. 1997;13(16):4435-45.
32. Jorge M, Schumacher C, Seaton NA. Simulation Study of the Effect of the Chemical Heterogeneity of Activated Carbon on Water Adsorption. Langmuir. 2002;18(24):9296-306.
33. Müller EA, Rull LF, Vega LF, Gubbins KE. Adsorption of Water on Activated Carbons: A Molecular Simulation Study. The Journal of Physical Chemistry. 1996;100(4):1189-96.
34. Müller EA, Gubbins KE. Molecular simulation study of hydrophilic and hydrophobic behavior of activated carbon surfaces. Carbon. 1998;36(10):1433-8.
35. Vishnyakov A, Piotrovskaya E, Brodskaya E. Capillary Condensation and Melting/Freezing Transitions for Methane in Slit Coal Pores. Adsorption. 1998;4(3-4):207-24.
36. Brennan JK, Thomson KT, Gubbins KE. Adsorption of Water in Activated Carbons: Effects of Pore Blocking and Connectivity. Langmuir. 2002;18(14):5438-47.
37. Jorge M, Seaton NA, F. Rodriguez-Reinoso BMJRaKU. Characterisation of the surface chemistry of activated carbon by molecular simulation of water adsorption. Studies in Surface Science and Catalysis. Volume 144: Elsevier; 2002. p. 131-8.
38. Jorge M, Seaton NA. Predicting adsorption of water/organic mixtures using molecular simulation. AIChE Journal. 2003;49(8):2059-70.

39. Do DD, Do HD. Modeling of Adsorption on Nongraphitized Carbon Surface: GCMC Simulation Studies and Comparison with Experimental Data. The Journal of Physical Chemistry B. 2006;110(35):17531-8.
40. Coasne B, Gubbins KE, Hung FR, Jain SK. Adsorption and structure of argon in activated porous carbons. Molecular Simulation. 2006;32(7):557-66.
41. Wongkoblap A, Do DD. The effects of energy sites on adsorption of Lennard-Jones fluids and phase transition in carbon slit pore of finite length a computer simulation study. Journal of Colloid and Interface Science. 2006;297(1):1-9.
42. Tenney CM, Lastoskie CM. Molecular simulation of carbon dioxide in chemically and structurally heterogeneous porous carbons. Environmental Progress. 2006;25(4):343.
43. Wongkoblap A, Do DD. Characterization of Cabot non-graphitized carbon blacks with a defective surface model: Adsorption of argon and nitrogen. Carbon. 2007;45(7):1527-34.
44. Jagiello J, Olivier JP. A Simple Two-Dimensional NLDFT Model of Gas Adsorption in Finite Carbon Pores. Application to Pore Structure Analysis. The Journal of Physical Chemistry C. 2009;113(45):19382-5.
45. Lucena SMP, Paiva CAS, Silvino PFG, Azevedo DCS, Cavalcante Jr ClL. The effect of heterogeneity in the randomly etched graphite model for carbon pore size characterization. Carbon. 2010;48(9):2554-65.
46. Liu Y, Wilcox J. Molecular simulation of CO_2 adsorption in micro- and mesoporous carbons with surface heterogeneity. International Journal of Coal Geology. 2012;104(0):83-95.
47. Kandagal VS, Pathak A, Ayappa KG, Punnathanam SN. Adsorption on Edge-Functionalized Bilayer Graphene Nanoribbons: Assessing the Role of Functional Groups in Methane Uptake. The Journal of Physical Chemistry C. 2012;116(44):23394-403.
48. Gotzias A, Tylianakis E, Froudakis G, Steriotis T. Theoretical study of hydrogen adsorption in oxygen functionalized carbon slit pores. Microporous and Mesoporous Materials. 2012;154(0):38-44.
49. Nguyen TX, Bhatia SK. Probing the Pore Wall Structure of Nanoporous Carbons Using Adsorption. Langmuir. 2004;20(9):3532-5.
50. Nguyen TX, Bhatia SK. Characterization of Pore Wall Heterogeneity in Nanoporous Carbons Using Adsorption: the Slit Pore Model Revisited. The Journal of Physical Chemistry B. 2004;108(37):14032-42.
51. Nguyen TX, Cohaut N, Bae J-S, Bhatia SK. New Method for Atomistic Modeling of the Microstructure of Activated Carbons Using Hybrid Reverse Monte Carlo Simulation. Langmuir. 2008;24(15):7912-22.
52. Pinto da Costa JMC, Cracknell RF, Sarkisov L, Seaton NA. Structural characterization of carbonaceous combustion-chamber deposits. Carbon. 2009;47(14):3322-31.
53. Otowa T, Tanibata R, Itoh M. Production and adsorption characteristics of MAXSORB: High-surface-area active carbon. Gas Separation & Purification. 1993;7(4):241-5.
54. Cranston RW, Inkley FA. 17 The Determination of Pore Structures from Nitrogen Adsorption Isotherms. In: Adalbert F, editor. Advances in Catalysis. Volume 9: Academic Press; 1957. p. 143-54.
55. Gregg SJ, Sing KSW. Adsorption, Surface Area and Porosity. New York: Academic Press; 1982.
56. Liu Y, Wilcox J. Effects of Surface Heterogeneity on the Adsorption of CO2 in Microporous Carbons. Environmental Science & Technology. 2012;46(3):1940-7.
57. Ewald PP. Die Berechnung optischer und elektrostatischer Gitterpotentiale. Annalen der Physik. 1921;369(3):253-87.
58. Fennel CJ, ; Gezelter, D. Is the Ewald summation still necessary? Peirwise alternatives to the accepted standard for long-range electrostatics. The Journal of Chemical Physics. 2006;124:234104.
59. Steele WA. The interaction of rare gas atoms with graphitized carbon black. The Journal of Physical Chemistry. 1978;82(7):817-21.
60. Weiner SJ, Kollman PA, Case DA, Singh UC, Ghio C, Alagona G, et al. A new force field for molecular mechanical simulation of nucleic acids and proteins. Journal of the American Chemical Society. 1984;106(3):765-84.

61. Jorgensen WL, Madura JD, Swenson CJ. Optimized intermolecular potential functions for liquid hydrocarbons. Journal of the American Chemical Society. 1984;106(22):6638-46.
62. Jorgensen WL, Maxwell DS, Tirado-Rives J. Development and Testing of the OPLS All-Atom Force Field on Conformational Energetics and Properties of Organic Liquids. Journal of the American Chemical Society. 1996;118(45):11225-36.
63. Freindorf M, Gao J. Optimization of the Lennard-Jones parameters for a combined ab initio quantum mechanical and molecular mechanical potential using the 3-21G basis set. Journal of Computational Chemistry. 1996;17(4):386-95.
64. Martin MG, Siepmann JI. Transferable Potentials for Phase Equilibria. 1. United-Atom Description of n-Alkanes. The Journal of Physical Chemistry B. 1998;102(14):2569-77.
65. Potoff JJ, Siepmann JI. Vapor–liquid equilibria of mixtures containing alkanes, carbon dioxide, and nitrogen. AIChE Journal. 2001;47(7):1676-82.
66. Gupta A, Chempath S, Sanborn MJ, Clark LA, Snurr RQ. Object-oriented Programming Paradigms for Molecular Modeling. Molecular Simulation. 2003;29(1):29-46.
67. Gusev VY, O'Brien JA, Seaton NA. A Self-Consistent Method for Characterization of Activated Carbons Using Supercritical Adsorption and Grand Canonical Monte Carlo Simulations. Langmuir. 1997;13(10):2815-21.
68. Davies GM, Seaton NA. The effect of the choice of pore model on the characterization of the internal structure of microporous carbons using pore size distributions. Carbon. 1998;36(10):1473-90.
69. Wahba G. Practical Approximate Solutions to Linear Operator Equations When the Data are Noisy. SIAM Journal on Numerical Analysis. 1977;14(4):651-67.
70. Gusev VY, O'Brien JA. Can Molecular Simulations Be Used To Predict Adsorption on Activated Carbons? Langmuir. 1997;13(10):2822-4.
71. Davies GM. Molecular Simulation of Adsorption Equilibrium in Microporous Solids: Model Development and Performance Prediction: University of Cambridge; 1999.
72. Yun J-H, Düren T, Keil FJ, Seaton NA. Adsorption of Methane, Ethane, and Their Binary Mixtures on MCM-41: Experimental Evaluation of Methods for the Prediction of Adsorption Equilibrium. Langmuir. 2002;18(7):2693-701.
73. Otowa T, Nojima Y, Miyazaki T. Development of KOH activated high surface area carbon and its application to drinking water purification. Carbon. 1997;35(9):1315-9.
74. Barton SS, Evans MJB, MacDonald JAF. Adsorption of Water Vapor on Nonporous Carbon. Langmuir. 1994;10(11):4250-2.
75. Sweatman MB, Quirke N. Gas Adsorption in Active Carbons and the Slit-Pore Model 1: Pure Gas Adsorption. The Journal of Physical Chemistry B. 2005;109(20):10381-8.
76. Sweatman MB, Quirke N. Modelling Gas Adsorption in Slit-Pores Using Monte Carlo Simulation. Molecular Simulation. 2001;27(5-6):295-321.
77. Liu JC, Monson PA. Does Water Condense in Carbon Pores?†. Langmuir. 2005;21(22):10219-25.
78. Striolo A, Chialvo AA, Cummings PT, Gubbins KE. Water Adsorption in Carbon-Slit Nanopores. Langmuir. 2003;19(20):8583-91.
79. Monson PA. Modeling Adsorption of Hydrogen - Bonded Molecules in Porous Structures. University of Massachusets Amherst, 2005.
80. Thommes M. Physical Adsorption Characterization of Nanoporous Materials. Chemie Ingenieur Technik. 2010;82(7):1059-73.
81. Gelb L, Gubbins KE, Radhakrishnan R, Sliwinska-Bartkowiak M. Phase separation in confined systems. Rep Prog Phys. 1999;62:1573–659.
82. Sarkisov L, Monson PA. Modeling of Adsorption and Desorption in Pores of Simple Geometry Using Molecular Dynamics. Langmuir. 2001;17(24):7600-4.
83. Page KS, Monson PA. Monte Carlo calculations of phase diagrams for a fluid confined in a disordered porous material. Physical Review E. 1996;54(6):6557-64.

84. Liu JC, Monson PA. Monte Carlo Simulation Study of Water Adsorption in Activated Carbon. Industrial & Engineering Chemistry Research. 2006;45(16):5649-56.

Chapter 4

Systematic development of a molecular model of high surface area activated carbons

4.1. Introduction

In Chapter 3 we have attempted to construct a predictive model for Maxsorb MSC-30 using three different variants of the slit pore representation: the classical slit pore model, the slit pore model with each wall made of a single carbon layer and the same model with additional groups and defects introduced in the structure. For each of the models we have generated several pore size distributions for Maxsorb using different sets of data and tested the ability of the models to predict adsorption of other species or at other conditions.

The classic slit pore model shows very good predictive capability, at least for simple gases such as methane and carbon dioxide. A model with additional surface groups and defects is also a promising route, although it requires some optimization of the solid-fluid potential for methane. The main advantage of the approache based on the slit pore model is that the construction of the PSD (and hence predictions) is instructed by ***all*** experimental points on the reference adsorption isotherm. Thus, we use this opportunity to acknowledge that slit pore models remain a powerful method for predictive models of gas adsorption in activated carbons.

Nonetheless, adsorption of water and in particular simulation of the kernel of adsorption isotherms proved to be challenging. Firstly, each adsorption isotherm required substantial computational time; secondly, presence of a significant adsorption hysteresis would require additional, more advanced methods to establish the location of the equilibrium transition.

Furthermore, as we mentioned in Chapter 3, surface area of Maxsorb MSC-30 (> 3000 m^2/g) is not compatible with a slit pore representation, as even a single layer graphite "wall" has lower surface area of 2622 m^2/g (1). These factors combined prompted us to explore an alternative set of models, based on a packing of structural elements, which are meant to capture more accurately accessible surface area of Maxsorb MSC-30 and which do not require generation of an adsorption kernel.

We now briefly review what has been done in the field of the disordered models of activated carbons.

A common description of the structure of activated carbons is based on the presence of graphitic microcrystallites. In particular, Oberlin and co-workers (2) introduced in 1980 the concept of basic structural unit (BSU), which they considered as the fundamental building block in the structure of activated carbons. A BSU is essentially a graphitic fragment and it was postulated that these BSU assemble to form regions of local molecular orientation (LMO). Finally it was assumed that the regions of LMO further assemble to form a complex structure. In this description the structure of activated carbons therefore appears to be hierarchical. These approaches were further reviewed by Ruthven in 1984 (3). From the modern perspectives, the concepts of crystallites, microcrystallites or graphitic fragments are probably oversimplified and somewhat outdated, however they are still a convenient starting point in the development of theoretical approaches.

It is now commonly accepted that the most realistic structure for carbon materials is a 3-D macromolecular network consisting of polyaromatic and substituted or heterocyclic aromatic units linked by covalent and noncovalent bonds (hydrogen bonds, van der Waals interactions, electrostatic interactions, and $\pi-\pi$ interactions). The presence of curved, fullerene-related elements due to the existence of non-hexagonal rings as in the model proposed by Harris et al. (4-7) is also widely accepted. In these respects, the models by Nguyen et al. (8), Palmer et

al. (9) and Kumar et al. (10), which aim to accurately reproduce the actual process of the activated carbon formation, are probably the most realistic that have so far been proposed.

In particular, Nguyen et al. (8) and Palmer et al. (9) have adopted two different types of Hybrid Reverse Monte Carlo (HRMC) procedures, which in general consist of adding particular constraints to the Reverse Monte Carlo (RMC) method (11). The RMC method was introduced by McGreevy et al. (11) to model the structure of disordered materials. The algorithm is similar in spirit to the Monte Carlo (MC) in canonical ensemble, however instead of differences in energy between a new and an old configurations, it is based on the differences between the experimental and the simulated structure factors of the material. Therefore, the application of this method requires x-ray diffraction (XRD) data. Starting from an arbitrary initial configuration, a new configuration is always accepted if the difference between the simulated and experimental structure factors is smaller than the initial value, otherwise it is accepted based on the Boltzmann probability distribution. A problem with the basic RMC method is that it is biased towards the production of unrealistic (highly strained) four- and three-member rings. Also, given that the algorithm starts from an arbitrary configuration, the computational time required for the convergence of the results can be very long. For this reason HRMC methods have been introduced. One of the first examples of HRMC was presented by Opletal et al. (12), who modelled an amorphous carbon structure adding to the basic RMC algorithm an additional constraint in the form of an inter-atomic energy term. Additional constraints could also concern the coordination number of the atoms or the potential cut-off. Nguyen et al. (8) generated their initial configuration for activated carbon fiber ACF-15 using the results from the interpretation of argon adsorption on the material, rather than starting from an arbitrary one, while Palmer et al. (9) produced a detailed model for BPL starting from the radial distribution function and the mean carbon density of the material. In summary, RMC methods require several complementary sources of experimental information (at least the XRD data, as mentioned before), which then provide constraints for the model.

Here the aim is to create a model for high surface area activated carbons which is as general as possible and therefore involves as little constraints and as little experimental data as possible. The constraint we are mostly interested in is the surface area, given its relevance in the adsorption properties of the different materials and given that it is always available for a sample of porous material, unlike other characteristics.

The notion of BSU can be combined with the well-established theoretical and simulation approaches, where disordered porous materials are represented as a collection of randomly distributed structural elements (13). One of the earlier examples of this approach is the model proposed by Segarra and Glandt (14). The basic element of this model is a platelet, or a rigid disk of cylindrical shape, representing a stack of several (between 1 and 3) fragments of a carbon layer. The thickness of the disks is therefore variable. A further assumption or approximation in the design of the model is that the carbon atoms of the surfaces are of uniform and continuous density.

Adsorbate-adsorbent interactions are described in this model by developing a potential function for a platelet of a limited size in a fashion similar to the procedure required for the Steele 10-4-3 potential (15). The complete model considers a random packing of these platelets, in which the final configuration is obtained using a canonical Monte Carlo program to move the relative positions of the disks until thermodynamic (minimum energy) equilibrium is obtained.

This model was employed in grand canonical Monte Carlo simulations of methane and ethane adsorption, and as well as adsorption of water vapour (14).

Liu and Monson further developed the model by Segarra and Glandt to accurately reflect specific structural characteristics of BPL carbon (16). In their model the size of the platelet (1.7 nm) and the porosity of the structure corresponded to the existing experimental values. The original work was based on the structureless platelets and effective potentials, similar to that of Segarra and Glandt, while in the second phase of the work carbonylic groups and Coulombic interactions associated with them were modelled explicitly (17). Figure 4.1 shows a computer visualization of the first version of the model by Liu and Monson:

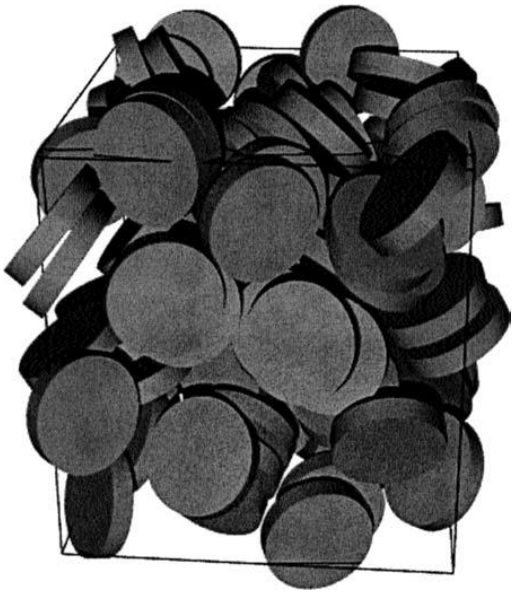

Figure 4.1. Computer visualization of the platelet model for activated carbon, as revised by Liu and Monson (17).

Many other realistic models, some of which feature curved, fullerene-related elements, have been developed over the years. In particular, Terzyk and co-authors have compared different methods for the determination of the PSD in a structure made of fragments of this type (18), while Kowalczyc and co-authors have studied the displacement of CH_4 by carbon dioxide on different types of Schwartzites (19). Kumar and co-authors have investigated the mixtures CH_4/H_2 and CH_4/N_2 in different models for microporous carbon, including a random arrangement of coronene graphitic basic units (20, 21).

A general problem with all disordered models of activated carbons is that it is difficult to generate a model capable of quantitatively accurate predictions, even when the construction of the model is instructed by the available experimental data. Yet, this is precisely what we strive to accomplish here. Our approach is described in the next section.

4.2. Methodology

Given the high level of disorder in the structure of Maxsorb, we use the platelet-based approach. As a building unit, we start with the simplest molecular structure compatible with the size of the graphitic fragments observed experimentally in activated carbons (>1nm) (4),

which is the molecule of coronene. It has been also recently shown that using coronene as a BSU, it is possible to create realistic disordered models of activated carbon with surface areas equal and exceeding that of Maxsorb MSC-30 (22).

Using random packings of rigid molecules of coronene (or its variants) as model porous materials, we systematically examine carbon dioxide and methane adsorption behaviour in these structures as a function of their surface area, pore volume, size of the molecular fragments, presence and nature of surface groups and fragment curvature.
Finally, using the insights from these studies and the experimental information about Maxsorb, we attempt to construct a predictive molecular model of this material and investigate its accuracy and performance. This final model for Maxsorb MSC-30 consists of a random arrangement of fullerene like elements, all formally equal to the molecule of corannulene, functionalized with hydroxylic groups.

The overall computational strategy is depicted in figure 4.2 and consists of the following stages. In the first stage, we consider a cubic simulation box and randomly pack it with rigid carbon fragments. In the second stage we use computational tools to characterize the resulting model structures in terms of their accessible surface area, pore volume, Henry's constants of adsorption with respect to carbon dioxide and methane. The structural characteristics can be further modulated by randomly removing some of the fragments. Finally, in the third step, we use these random packings as model structures in grand canonical Monte Carlo (GCMC) simulations of single component adsorption of carbon dioxide and other gases.

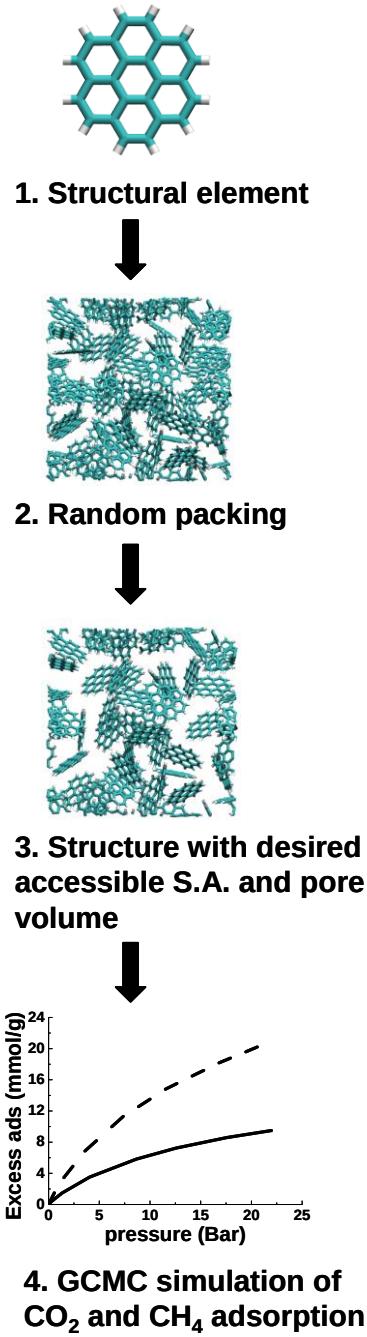

Figure 4.2. Schematic description of the model construction process.

In the final part of the work we focus on one particular model which can be considered as a good representation of Maxsorb in terms of disorder, surface area, pore volume, carbon/oxygen ratio. To validate the model, we simulate carbon dioxide and methane adsorption at 298 K and 323 K and compare the results with the reference experimental data. Where necessary the model is then further tuned to correctly reproduce the reference isotherms and once this objective is reached the model is applied to simulate adsorption of

nitrogen and hydrogen. Simulations of adsorption become more sensitive to the details of the forcefield and the accuracy of the structure representation at lower temperatures, and therefore, to test the robustness of the model, we apply it to predict adsorption of methane and carbon dioxide at 273 K, although this lower temperature is not directly relevant to any applications of interest. Below we describe specific methodology details associated with these steps.

4.2.1. Construction of the models

The computational protocol outlined above is fairly general, and for a specific implementation of this protocol we need to consider a number of options. They include the geometry and chemical nature of the rigid fragments (commonly called here platelets), their interactions with each other during the packing processes (the parameters of these interactions can be different from those employed in the adsorption studies), the algorithm for removing some of the platelets in order to adjust the final structure properties and so on.

For all these options, we first try the simplest solution possible. Specifically, we start with the simplest carbon fragment possible, which allows us to create model structures with high surface areas. This is the molecule of coronene shown in figure 4.3. Starting with this structure we also consider larger fragments, fragments decorated with different types of surface groups, curved platelets and so on.

During the packing process, the atoms of the platelets interact with each other via a hard-sphere potential with the collision diameters reported in table A1 in the Appendix. The choice of these parameters will be further discussed in Section 4.2.3.

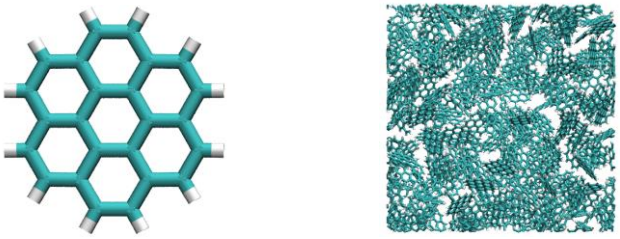

Figure 4.3. (a) The molecule of coronene. (b) Typical packing of coronene platelets in a simulation cell. The cubic cell shown has sides of 60Å and contains 228 platelets in periodic boundary conditions. Cyan: carbon, grey: hydrogen.

4.2.2. Characterization of the models

The models produced in the first stage are characterized using the package Poreblazer 1.2, which consists in a series of simulation tools developed by Sarkisov and Harrison using *Fortran 90* programming language (23).

In particular, the total accessible surface area for each model has been calculated as the sum of the individual accessible surface areas associated with each atom of the adsorbent, using a nitrogen atom as a probe; this procedure has allowed us to directly relate the calculated surface areas to those measured in the BET adsorption experiments. In the Appendix (section A9.4.1) we demonstrate that the BET surface area (either from experiments or simulations) is a property consistent with the accessible surface area for this type of materials.
Summary of the parameters involved in this calculation is provided in the Appendix (table A5).

Accessible pore volume is calculated using the Widom insertion method and helium atom as a probe in order to make this characteristic consistent with the results from the helium porosimetry measurements (24). For the parameters involved in this calculation the reader is referred to table A6 in the Appendix.

The experimental values of the micropore volume we use as the reference for Maxsorb MSC-30 have been obtained from the Dubinin – Radushkevich method (25) using nitrogen adsorption at 77.35 K. Applying the same method to the nitrogen isotherms at 77.35 K

simulated on the proposed models, we have found that the results for the micropore volume are consistent with the results obtained from the computational helium porosimetry. Some test cases with regards to this are reported in the Appendix (section A4). Given this consistency in the results and much lower computational cost of the method based on the Widom insertion, the latter approach was the methodology of choice for all subsequent studies.

Henry's constant of adsorption is calculated using a simple approach, recently proposed by Sarkisov, based on the lattice representation of the simulation cell (26). Summary of the parameters involved in this calculation is provided in the Appendix (table A7).

4.2.3. Simulation details

First, we provide the details of the intermolecular interactions. As we did in Chapter 3, for methane we use the united atom model (27), and for carbon dioxide we use the three center model from the TraPPE forcefield (28). In the final part of the work nitrogen is also modelled using the three centre model from the TraPPE forcefield (28) , while for hydrogen, following the work by Cracknell (29), the single-site model by Buch (30) is employed.

As a starting point for our study, for carbon fragments (again, as in Chapter 3) we use the parameters proposed by Tenney and Lastoskie (31). These parameters and charges are used for all the models described in the first part of this chapter, apart from the few cases in which it is explicitly stated, and the complete summary of parameters is provided in the Appendix (table A1).

In the last part of our work, which deals with the choice of one particular model to reproduce the behaviour of Maxsorb, the solid-fluid interaction for methane is slightly scaled to obtain a better agreement with the experimental isotherm. This kind of tuning is justified by the recent studies which show that the presence of curved surfaces, together with the presence of groups and defects in the structure of activated carbons, increases the solid-fluid interaction for some species, compared to what has been proposed for graphite (8, 9, 32). It is important to emphasise however that in the scaling described above several effects (i.e. curvature of fragments and presence of groups) are grouped together via a single scaling factor. Since in

our work functional groups and Coulombic interactions are explicitly modelled, it is only the effect of curvature we are trying to incorporate via the scaling factor and for species involving Coulombic interactions (carbon dioxide), we anticipate less tuning required. This will be discussed later in more detail.

Partial charges in our final model of Maxsorb are calculated using the B3LYP Density Functional Theory method (33), with 6-31g basis set and CHELPG (34) charge analysis with the Gaussian 09 software package (35).

Once a model with the desired features has been prepared, GCMC simulations are used to calculate adsorption isotherms. For each system, we consider cubic simulation cell with a side of 60Å in length, placed in periodic boundary conditions. Typically, a packing would contain more than 200 platelets, depending on the system. In the studies of disordered systems it is very important to assess variation of the adsorption properties as a function of structure realization and, if necessary, average the calculated adsorption properties over sufficient number of structure realizations. In the Appendix (section A7) we demonstrate that the system size here is sufficiently large to generate properties independent of a particular structure realization, and therefore all simulations presented here are performed using a single realization of the system. Further details of the GCMC simulations protocol adopted in this chapter are provided table A4 in the Appendix.

For a correct comparison with the experimental data all the simulated adsorption densities are converted into excess values following the procedure proposed by Talu and Myers (24) and described in Chapter 2.

4.3. Preliminary studies

In order to understand the motivation behind the extensive studies in the next section of this chapter and the selection of the final parameters for the molecular model of Maxsorb, it is instructive to revisit one of the first systems explored in this study.

Our original idea was to focus on just two characteristics of Maxsorb MSC-30, its high surface area and pore volume, which we believed were particularly important. For this we constructed a model structure based on a packing of the coronene (CR) platelets, with morphological features resembling Maxsorb MSC-30. Table 4.1 below shows characteristics of this model, whereas figure 4.4 compares experimental and simulated adsorption isotherms for methane and carbon dioxide at room temperature (298 K).

Table IV.1. Characteristics of the model structure based on coronene platelets (CR), compared to the experimentally measured properties of Maxsorb MSC-30 (MSC-30). In this table, S.A. is the surface area, V is the micropore volume, k_H is the Henry's constant of adsorption and C/O is the carbon to oxygen ratio (in weight) in the material.

SYSTEM	**S.A.** m^2/g	**V, 298 K** cm^3/g	**k_H CH_4, 298 K** mol/kg/Bar	**k_H CO_2, 298 K** mol/kg/Bar	**C/O**
CR	3428.8	1.24	0.51	2.00	-
MSC-30	3000 - 3500	1.3 – 1.7	1.3 – 1.9	2.4	7.8

Table IV.1 shows that for the surface area and micropore volume the model values are close to the ones typically found for Maxsorb MSC-30; nevertheless the surface area is closer to the upper bound of the experimentally observed values, while the micropore volume is slightly below the lower bound of the experimental values. As for the Henry's constants there is a clear under-prediction in the case of methane, while for CO_2 the agreement can be considered reasonable. The current model does not consider functional groups or any other moieties containing oxygen, as seen from the C/O parameter.

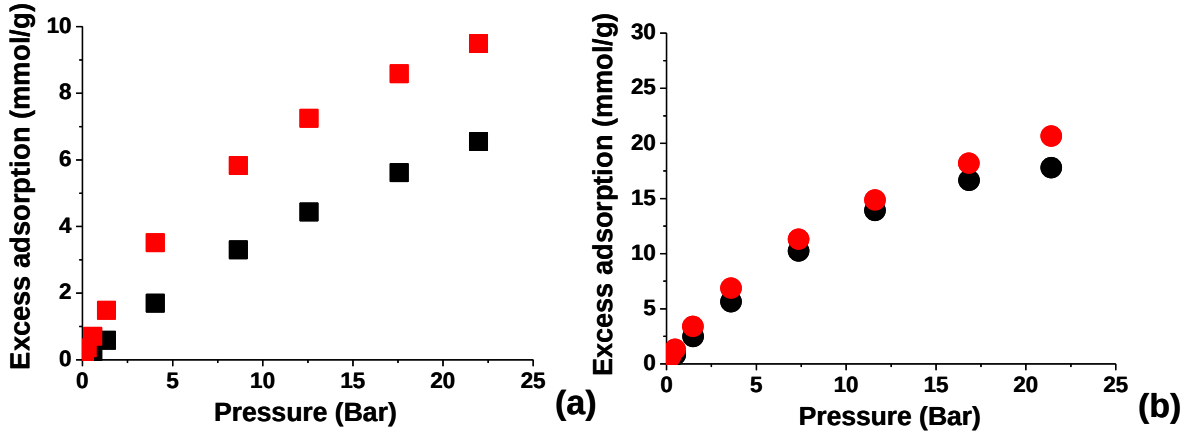

Figure 4.4. Experimental (red symbols) and simulated (black symbols) adsorption isotherms for CH_4 (a) and CO_2 (b) at 298 K for the model structure based on coronene platelets (CR).

Figure 4.4 shows adsorption isotherms for methane and carbon dioxide in CR model at 298 K. To give an indication on the statistical errors on the simulated adsorbed densities (in this work these errors are always determined calculating standard deviations with the method of block averaging, details of which can be found in the literature (36)) we precise that for CO_2 these have been calculated to be 7.3% and 0.32% at 0.1 Bar and 22 Bar respectively, while for CH_4 the simulation errors at the same pressures are 14.5% and 0.33%. These simulation errors are consistent with the simulation errors for all the isotherms presented in section 4.4, when a scaling of the solid-fluid interaction is not applied. Simulation errors for this latter case will be considered in section 4.5.

From figure 4.4, it seems that this model based on the realistic values of the surface area and pore volume of the target structure is reasonably accurate, at least for carbon dioxide adsorption. There are nevertheless clear deviations in the behaviour. Particularly, methane adsorption is underpredicted in the whole range of pressures, as can be also anticipated from the lower value of the Henry's constant, compared to the experiment (table IV.1). This preliminary result posed a number of questions. Can the differences in methane adsorption be reconciled by some variation of the properties of the platelets and their packings, and if so to what extent? Is the accurate prediction of carbon dioxide adsorption a result of some fortuitous cancellation of errors, and if so how shall the model be further refined? In order to answer these questions and produce some systematic approach to further development of the

model, we set to investigate its behaviour as a function of a number of parameters and this study is presented in the next section.

4.4. Systematic study of different platelet models

The models presented below explore how several variables can influence the simulated adsorption isotherms for methane and carbon dioxide at 298 K. In this section we present, in the order, the effect of the size of the platelets, presence of functional groups, type of groups, increasing surface area of the system, model of charges and platelet curvature.

4.4.1.Effect of platelet size

To study the effect that the size of the basic structural unit can have on adsorption isotherms we constructed three different models starting from platelets that correspond to coronene (CR), hexabenzocoronene (HCR) and circumcircumcoronene (CCR) molecules respectively, as shown in figure 4.5.

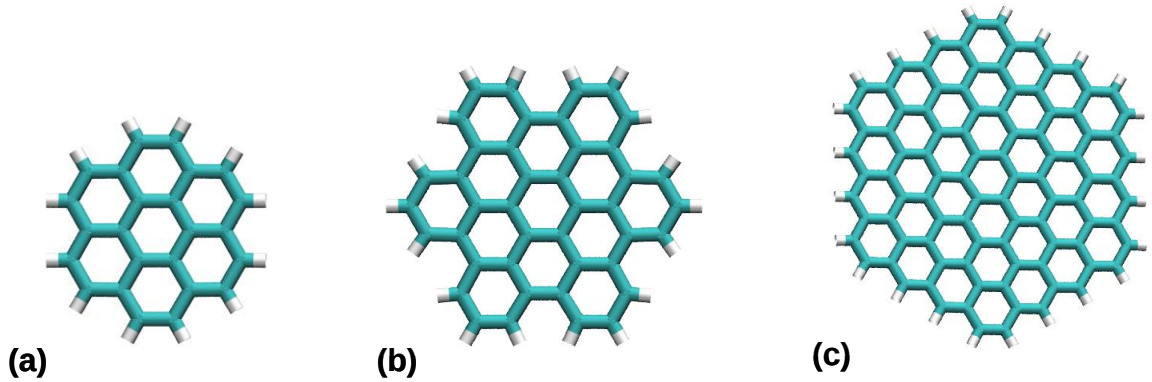

Figure 4.5. Molecular visualizations of platelets based on (a) Coronene (CR), (b) Hexabenzocoronene (HCR), (c) Circumcircumcoronene (CCR). Cyan: carbon, grey: hydrogen.

The properties of the systems are summarized in table IV.2. To study adsorption behaviour as a function of just one parameter at a time, the packings of various fragments are constructed in such a way (through the judicious addition and removal of fragments) so to have about the same surface area and pore volume, although as it is seen below the latter parameter is not a fully independent characteristic. It is difficult to achieve the value of the surface area corresponding to Maxsorb for large platelets, because, given the dimensions of the simulation box, they tend to pack very inefficiently, leading to sparse structures and higher surface areas. Hence, all three models here are compared to each other at somewhat higher value of the surface area, than that for Maxsorb.

Table IV.2. Properties of the systems under examination for the study of the effect of the size of the platelets. In this table, S.A. is the surface area, V is the micropore volume, k_H is the Henry's constant of adsorption, d is the size of the platelet (largest distance between two hydrogen atoms) and ρ is density.

SYSTEM	**S.A.** m^2/g	V_{He}, 298 K cm^3/g	k_H CH_4, 298 K mol/kg/Bar	k_H CO_2, 298 K mol/kg/Bar	**d** Å	**ρ** g/cm^3
CR	3919.1	1.40	0.49	1.83	9.45	0.49
HCR	3888.5	1.41	0.58	2.11	13.44	0.51
CCR	3900.0	1.57	0.71	2.37	19.15	0.50

For each system table IV.2 also shows the values of the apparent density (ρ) and the length of the longer dimension of the platelets (d).

The simulated CO_2 and CH_4 adsorption isotherms are shown in figure 4.6. From this figure it appears that when the size of the platelet increases there is also an increase in adsorption densities, either in the Henry's law region or at high pressures, although this effect is not as visible for carbon dioxide.

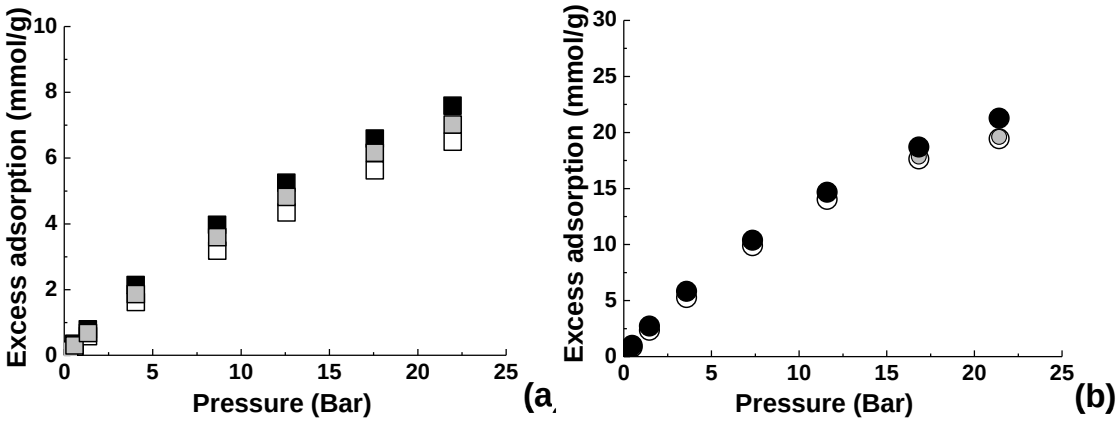

Figure 4.6. (a) Excess adsorption isotherms at 298 K for CH_4 in CR (open squares), HCR (grey squares) and CCR (black squares) models; (b) Excess adsorption isotherms at 298 K for CO_2 in CR (open circles), HCR (grey circles) and CCR (black circles) models.

At higher pressures this effect could be to some extent attributed to slightly higher porosities of the model porous materials based on the larger fragments. A more general reason for this is stronger solid-fluid interactions for larger platelets as suggested by the Henry's constants of adsorption for carbon dioxide and methane in table IV.2.

We further investigate these effects in figure 4.7 by plotting the ensemble average solid-fluid interaction energy as a function of pressure.

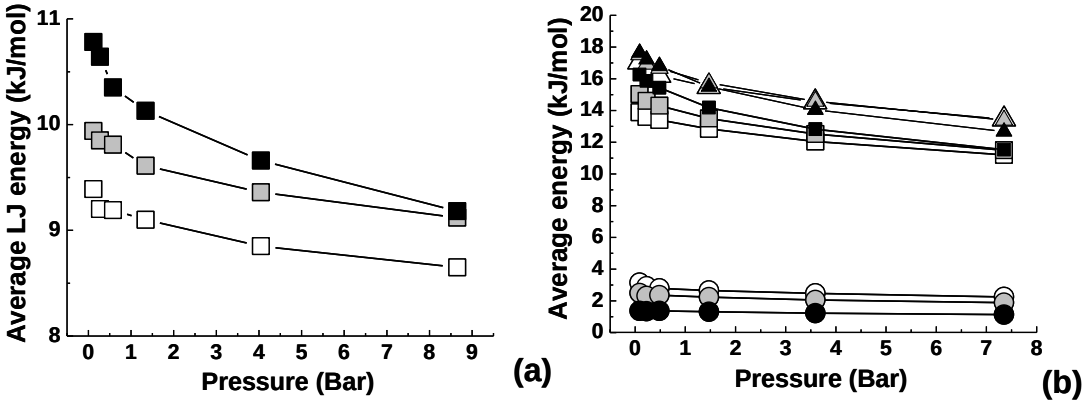

Figure 4.7. (a) Average CH_4-adsorbent interaction expressed in kJ per mol of adsorbate as a function of pressure. (b) Average CO_2-adsorbent Lennard-Jones (squares), Coulombic (circles), and total (triangles) interaction expressed in kJ per mol of adsorbate as a function of pressure. Open symbols are for the CR model, grey symbols are for the HCR model and black symbols are for the CCR model, respectively. Lines are for eye guidance only.

In the case of CH_4 only LJ interactions are included, and it is clear from the graph in figure 4.7(a) that an increase in the size of the platelets leads to an increase in the interaction energy. At low pressures this property is dominated by the adsorbate molecules located either in close vicinity or at the surface of the platelets. At higher pressures as the loading increases a greater proportion of the molecules occupy regions of porous space further away from the platelets, and as a result the average solid-fluid interaction energy decreases with pressure.

The average LJ energy between CO_2 and the platelets behaves in a similar way as for methane, and for larger platelets this interaction is stronger (figure 4.7(b)). However, the Coulombic contribution to the CO_2-platelet interaction follows the opposite trend and for larger platelets this contribution becomes smaller.

For the fragments in figure 4.5, the predominant contribution to solid-fluid Coulombic energy is the interaction between carbon dioxide and termini hydrogen atoms on the edges of the platelets. As the size of the platelet increases, the concentration of hydrogens per gram of material decreases (since the surface area grows proportionally to the square of the diameter of the platelet, while the number of hydrogen atoms increases linearly with the size). Specifically, the concentrations of termini hydrogens for CR, HCR and CCR fragments are respectively $4.0*10^{-2}$, $3.4*10^{-2}$ and $2.0*10^{-2}$ mol/g. As a result, the LJ interaction per molecule of adsorbate is stronger in the CCR system compared to CR, but the Coulombic interaction is weaker. The combination of the two opposite energy trends in case of CO_2 provides a plausible explanation for the lesser effect of platelet size on CO_2 adsorption isotherms, compared to methane. Both Lennard-Jones and Coulombic CO_2-adsorbent energies decrease with pressure following a trend similar to that of methane.

4.4.2. Effect of functional groups

We now turn our attention to the role of functional groups in the adsorption of carbon dioxide and methane.

Let us first briefly review what is known about the nature of functional groups and their concentration in Maxsorb. The article by Otowa et al. (37) describes the quantitative analysis of the surface functional groups that was performed on Maxsorb using the Bohem's titration method (37). For Maxsorb MSC-30 hydroxil, carboxyl and lactone groups were identified in the concentrations of 79, 46 and 36 meq/g, respectively. From the elemental composition the C/O ratio appeared to be 7.8. Clearly, the structure of the real material is quite complex, with some properties such as charge distribution and location of the groups being closely coupled. To isolate the effect of presence of the groups from their nature, we consider a simplified system, where all oxygen in the structure is present in the form of hydroxyl groups (the most abundant) only. This choice, which will be further discussed in the next section, is supported by previous studies which indicate that the adsorption behaviour of carbon materials is influenced mainly by the total amount of oxygen rather than by the type of groups themselves (38).

We use the coronene molecule as our reference system, and consider two variants of this structure modified with two and three hydroxilic groups respectively, (CR-$(OH)_2$ and CR-$(OH)_3$), as shown in figure 4.8. The C-O bonds lie on the plane of the platelet, which insures the maintenance of the sp^2 hybridization for the carbon atoms. The number of the groups is chosen to reflect the experimentally observed C/O ratios in Maxsorb (37), while the mutual positions of the groups are meant to minimize the cooperative effects between the groups (in other words, the groups are separated as far as possible from each other within a single platelet). Although this is not the only way to distribute the surface groups, for now we adhere to the simplest approach possible.

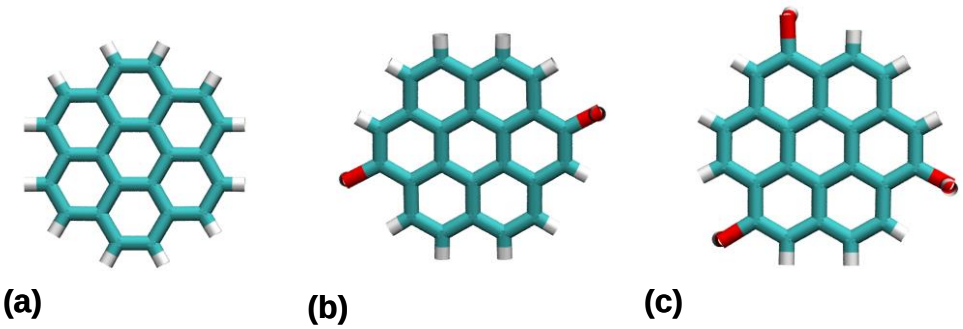

Figure 4.8. Molecular visualizations of platelets based on (a) Coronene (CR), (b) Coronene functionalized with two hydroxylic groups (CR-$(OH)_2$), and (c) Coronene functionalized with three hydroxilic groups (CR-$(OH)_3$). Cyan: carbon, grey: hydrogen, red: oxygen.

We prepare packings of these platelets, with characteristics shown in table IV.3. Similarly to the previous case, these packings feature very similar surface areas, pore volumes and densities and therefore the effect of the presence of surface groups can be isolated from other variables.

Table IV.3. Properties of the systems under examination for the study of the effect of functional groups. The properties in this table are defined in the same way as for tables IV.1 and IV.2.

SYSTEM	**S.A.** $\mathbf{m^2/g}$	**V, 298 K** $\mathbf{cm^3/g}$	$\mathbf{k_H}$ **$\mathbf{CH_4}$, 298 K** **mol/kg/Bar**	$\mathbf{k_H}$ **$\mathbf{CO_2}$, 298 K** **mol/kg/Bar**	**C/O**	**ρ** $\mathbf{g/cm^3}$
CR	3428.8	1.24	0.51	2.00	-	0.52
CR-$(OH)_2$	3410.5	1.23	0.52	2.26	9	0.54
CR- $(OH)_3$	3433.5	1.26	0.57	2.41	6	0.54

The CO_2 and CH_4 excess adsorption isotherms at 298 K for these systems are shown in figure 4.9.

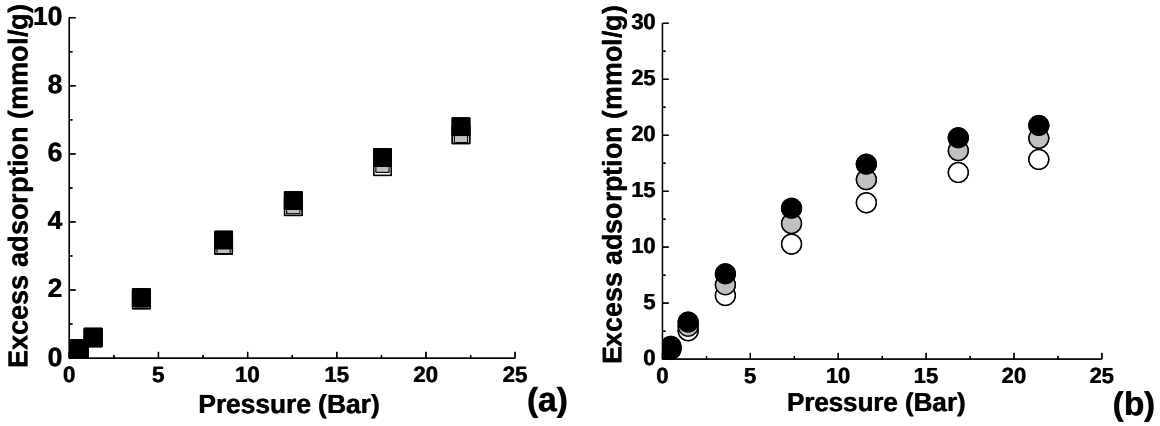

Figure 4.9. (a) Excess adsorption isotherms at 298 K for CH_4 in CR (open squares), CR-$(OH)_2$ (grey squares) and CR-$(OH)_3$ (black squares) systems, respectively. (b) Excess adsorption isotherms at 298 K for CO_2 in CR (open circles), CR-$(OH)_2$ (grey circles) and CR-$(OH)_3$ (black circles) systems, respectively.

Not surprisingly, presence of the groups has only a minor effect on the adsorption of methane, either at low or at high pressures, while the effect on the CO_2 adsorption is definitely stronger and proportional to the number of groups used to functionalize the platelets. These results can be explained by taking into account that only CO_2 molecules are engaged in the Coulombic interactions, which are obviously increased by the presence of the polar groups.

Table IV.3 shows how the Henry's constants for CH_4 and CO_2 vary with the presence of the groups: in both cases the higher the number of the groups the higher the Henry's constants. In agreement with what has been stated in Section 4.4.1, addition of functional groups can be seen as a general increase in the size of platelets and the number of interaction sites involved in each platelet thus leading to stronger adsorbate-adsorbent interactions even for species that are not involved in Coulombic interactions with the surface groups (methane). However, similarly to adsorption isotherms, for Henry's constants the effect of the functional groups is more pronounced for carbon dioxide rather than for methane due to polar nature of the groups.

4.4.3. Effect of the nature of functional groups

Now, when we established the overall influence of the presence of the polar functional groups on adsorption behaviour of carbon dioxide and methane, we can focus in more detail on the nature of these groups. Here we construct a model to test the observation, mentioned in the previous section, that the type of the oxygenated groups does not play a crucial role in influencing the extent of adsorption, which depends mostly on the total concentration of oxygen atoms at the surface (38). For this, we consider two systems, coronene functionalized with two hydroxylic groups and coronene functionalized with one carboxylic group (CR-COOH), as shown in figure 4.10.

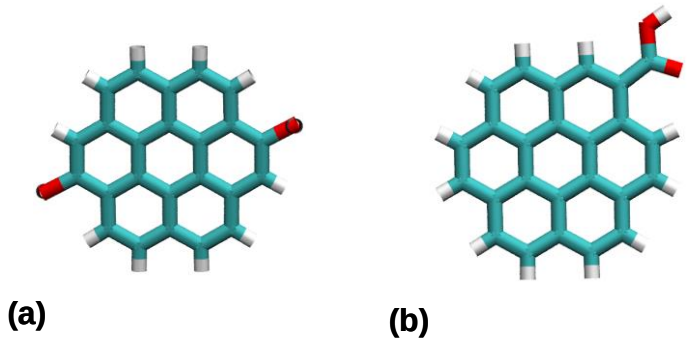

Figure 4.10. Molecular visualizations of platelets based on (a) coronene functionalized with two hydroxylic groups (CR-$(OH)_2$) and (b) coronene functionalized with one carboxylic group (CR-COOH). Cyan: carbon, grey: hydrogen, red: oxygen.

This arrangement allows us to keep the C/O ratio for two systems very close to each other, thus isolating the effect of the nature of the group from the effect of the total oxygen concentration in the system. Also, as seen from table IV.4, other morphological properties of the systems are maintained very close to each other.

Table IV.4. Properties of the systems under examination for the study of the effect of the nature of functional groups. The properties in this table are defined in the same way as for tables IV.1 and IV.2.

SYSTEM	S.A. m^2/g	V_{He}, 298 K cm^3/g	k_H CH_4, 298 K mol/kg/Bar	k_H CO_2, 298 K mol/kg/Bar	C/O	ρ g/cm^3
CR-$(OH)_2$	3410.5	1.23	0.52	2.26	9.00	0.54
CR-COOH	3428.1	1.27	0.54	2.37	9.38	0.53

The adsorption isotherms for these systems are provided in figure 4.11.

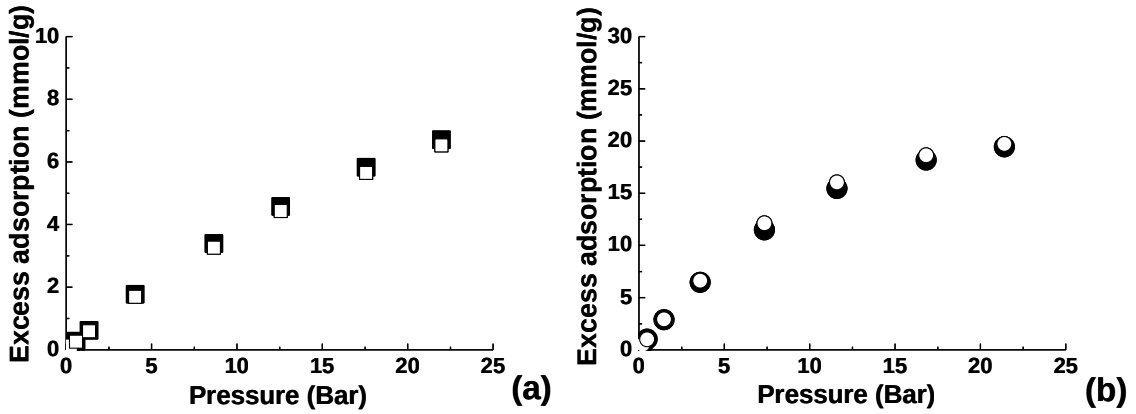

Figure 4.11. (a) Excess adsorption isotherms at 298 K for CH_4 in CR-$(OH)_2$ (open squares) and CR-COOH (black squares) systems, respectively. (b) Excess adsorption isotherms for CO_2 at 298 K in CR-$(OH)_2$ (open circles) and CR-COOH (black circles) systems, respectively.

Table IV.4 shows that the values of Henry's constants are very close to each other. This is in agreement with the adsorption isotherms, which show only minimal differences. These results seem to reinforce the idea that the most influential aspect in terms of adsorption is the total concentration of oxygen on the surfaces, rather than the nature of groups themselves.

4.4.4. Effect of the surface area

In this section we use coronene with three added hydroxylic groups ($CR\text{-}(OH)_3$) as a basic structural unit and consider six different structures with increasing surface area, each of them obtained by progressive removal of platelets from the initial denser structure. This naturally also leads to structures of higher porosity and therefore it is important to explore their properties in conjunction with both their surface area and porosity.

Figure 4.12 (a) shows the Henry's constants for CO_2 and CH_4 and porosity of the model structures as a function of the surface area. As the surface area increases the Henry's constants of adsorption decrease, both for CO_2 and methane, while the pore volume increases. These trends can be explained by considering that any increase in the accessible surface area is accompanied by a decrease in the number of interaction sites in the system, which becomes progressively less dense. Denser systems are characterized by energetically favourable regions of porous space, resulting from the interaction emanating from several platelets. As the system becomes progressively sparse, these regions disappear. The above mentioned effect appears to be more pronounced for CO_2 compared to methane.

Figure 4.12 (b) shows the excess amount adsorbed for both methane and carbon dioxide at the highest pressure explored (p_{max}=22 Bar) as a function of the surface area. The general trend appears to be as follows: the increase of the surface area is always accompanied by an increase in the accessible pore volume of the system and this determines an increase in the amount of fluid that can be adsorbed at high pressures. This effect can be observed particularly clearly for CO_2 up to the surface areas of around 5500 m^2/g. For CH_4 there is a smaller but still noticeable increase in the maximum excess amount adsorbed for the surface areas up to about 3800 m^2/g. As the systems become even sparser, there is a change in the trend. The density of the adsorbed phase starts to resemble the bulk phase, and with the excess amount being simply the difference between these two properties, it starts to decrease ultimately approaching zero.

The actual details of this trend depend not only on the porous material but also on the properties of the adsorbing species, and the location of the conditions under consideration on the bulk phase diagram. With methane (critical temperature -82.7˚C) being deep in the

supercritical region of the phase diagram compared to CO_2 (critical point 31.1˚C), bulk-like densities of the confined fluid are expected to be reached at lower values of porosity of model structures. We do not extend our study to surface areas higher than 6500 m^2/g, which has recently been shown to be the theoretical limit of surface area for carbon materials (22).

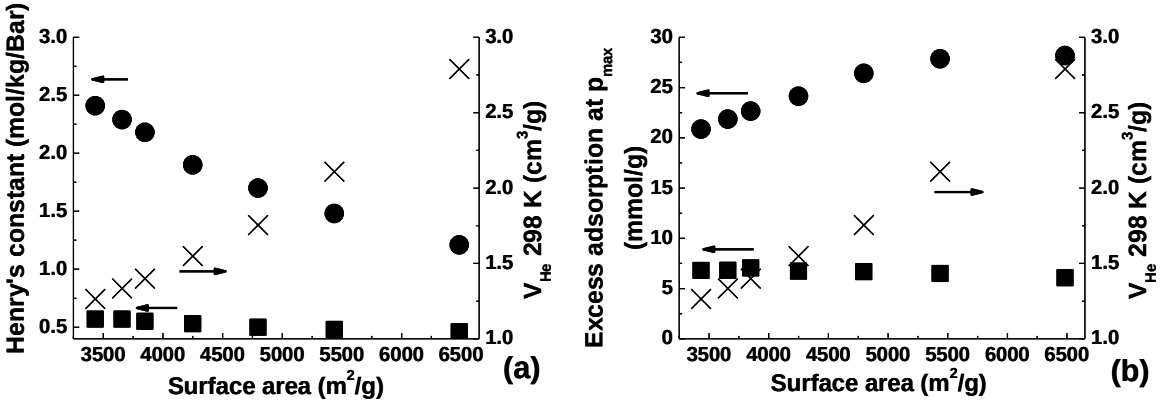

Figure 4.12. (a) Henry's constants of adsorption at 298 K for CH_4 (squares, left scale) and CO_2 (circles, left scale), pore volume (crosses, right scale) as a function of surface area. (b) Excess adsorption at p_{max} for CH_4 (squares, left scale) and CO_2 (circles, left scale), pore volume (crosses, right scale) as a function of surface area.

An overall observation that comes from the present section is that CO_2 adsorption is much more sensitive than methane to the differences in the surface area and porosity of the adsorbent under considered conditions.

4.4.5. Effect of the charge model

In this section we are interested in the effect of the method used to attribute partial charges on platelets on CO_2 adsorption isotherms (CH_4 adsorption is obviously not affected, given the model we are using).

We investigate two of the systems introduced in Section 4.4.2, coronene and coronene functionalized with two hydroxyl groups, and compare the behaviour of the same systems using the charges from Tenney and Lastoskie (obtained from *ab initio* calculations for

representative ~100 atom polycyclic aromatic hydrocarbons using the Hartree-Fock method, 6-31G(d,p) basis set and Mulliken population analysis) and the charges determined by us through B3LYP DFT method, 6-31G basis set and CHELPG population analysis (figure 4.13).

Summary of the actual charges assigned by both methods is provided tables A8 and A9 in the Appendix. The properties of the two systems under investigation have already been summarized in table IV.3.

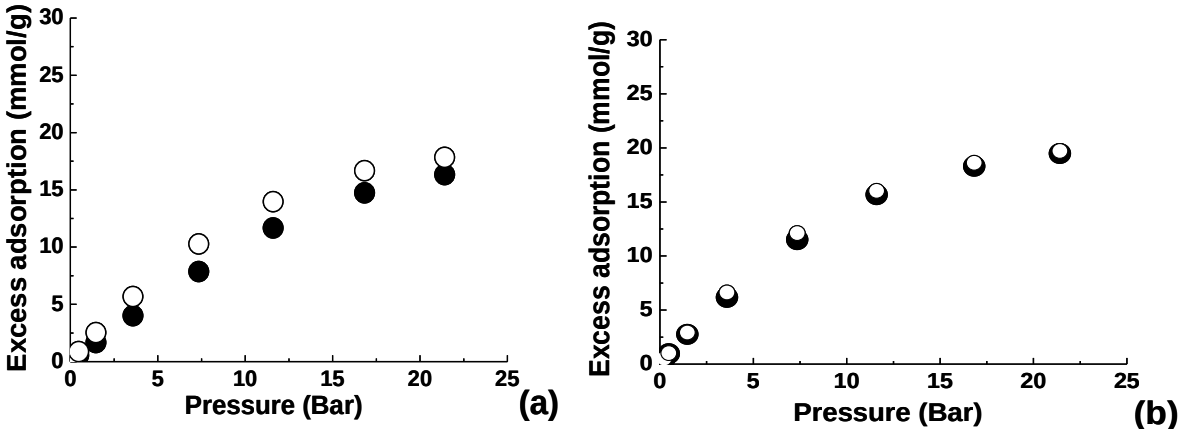

Figure 4.13. Excess adsorption isotherms for CO_2 at 298 K in (a)CR and (b) CR-$(OH)_2$ systems with different sets of charges. Open circles correspond to parameters from Tenney and Lastoskie; black circles correspond to the present work.

Interestingly, in the absence of functional groups (figure 4.13 (a)) the method used to attribute the charges makes a difference, and the charges calculated by us result in the lower loading and Henry's constant (2.0 mol/kg/Bar for Tenney and Lastoskie charge model compared to 1.2 mol/kg/Bar for our model). In the presence of the functional groups (figure 4.13 (b)) the differences in the adsorption behaviour become much smaller. The difference in the Henry's constant is also smaller, with the actual values being 2.26 mol/kg/Bar for Tenney and Lastoskie charge model and 2.10 mol/kg/Bar for our charge model, respectively. A detailed investigation of these differences is beyond the scope of this thesis. We note here that both values of the Henry's constant for the model featuring surface groups are reasonably close to the experimental value (2.4 mol/kg/Bar). Within the charge model of Tenney and Lastoskie, presence of the functional groups has lesser effect on the adsorption properties,

with k_H values being 2.0 and 2.26 mol/kg/Bar for systems with no groups and with groups, respectively. An alternative charge model proposed here suggests a more substantial role of functional polar groups. As we intend to consider a broader range of systems with some groups not considered in the original parameterization of Tenney and Lastoskie, we adopt a combination of B3LYP DFT and CHELPG methods for all subsequent more specialized models of Maxsorb, considered in Section 4.5.

4.4.6. Effect of the platelet curvature

As mentioned in the introduction the results of several recent studies suggest that the curved surfaces in the structure of activated carbons play a significant role in their adsorption behaviour. In this section we compare the adsorption isotherms simulated for the systems based on coronene, which has a flat geometry, figure 4.14 (a), and corannulene (CRNL), which is shown in figure 4.14 (b), (c) and is curved due to the presence of a five member ring (this can be considered as a fragment of a fullerene). As seen in table IV.5 we maintain surface area and pore volume of the systems as close to each other as possible to single out the effect of curvature only. In both cases the charges have been determined using B3LYP DFT and CHELPG methods.

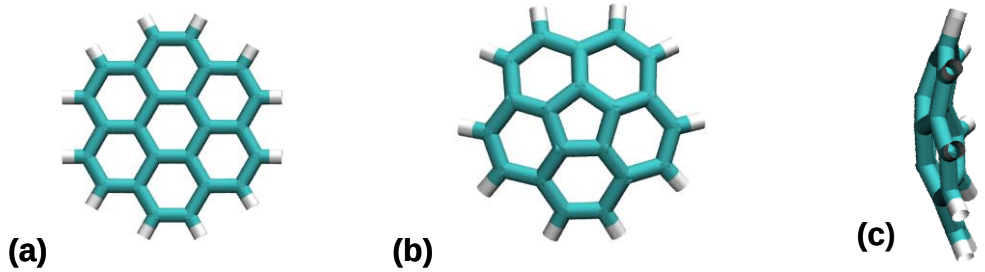

Figure 4.14. Molecular visualization of platelets based on coronene, CR (a) and curved corannulene, CRNL (b) and (c) fragments. (b): top view, (c): side view. Cyan: carbon, grey: hydrogen.

It has been shown for several adsorbates that the solid-fluid interaction with the graphitic carbon is stronger near curved surfaces, and this effect has often been attributed to the

intermediate hybridization of carbon between sp^2 and sp^3 within curved fragments, as opposed to sp^2 hybridization in planar graphite sheets (8, 9, 32).

Table IV.5. Properties of the systems under examination for the study of the effect of the platelet curvature. The properties in this table are defined in the same way as for tables 4.1 and 4.2.

SYSTEM	**S.A.** m^2/g	**V, 298 K** cm^3/g	k_H **CH_4, 298 K** mol/kg/Bar	k_H **CO_2, 298 K** mol/kg/Bar	**ρ** g/cm^3
CR	3428.8	1.24	0.51	1.20	0.52
CRNL (not scaled)	3427.6	1.25	0.43	1.01	0.51
CRNL (scaled)	3427.6	1.29	0.59	1.62	0.51

CRNL (not scaled) system in table IV.5 is based on the same Lennard-Jones interaction parameters as the reference CR system. For the system presented as CRNL (scaled), a scaling factor is applied to the depth of the potential well for all the LJ interactions between carbon atoms of the platelets and atoms of adsorbate molecules. We use scaling factor of 1.1, which is very close to what has been previously adopted to reproduce experimental data for adsorption of methane in BPL and ACF-15 carbons, without any further modification of parameters. (8, 9). We note that the most optimal scaling factor for Maxsorb MSC-30 does not necessarily have to be the same.

Having justified the scaling of the solid-fluid interaction based on the curvature of the adsorbent surface, it is also worth to note that the solid-fluid interaction parameters in this work are always calculated, as explained in Chapter 2, using the Lorentz-Berthelot combining rules. These rules are the most commonly adopted practice for the estimation of the Lennard-Jones parameters for interaction between the unlike species. However, the Lorentz-Berthelot rules are known to overestimate the potential well-depth and, in fact, are not the only choice for mixing rules (39, 40). Thus, a potential additional avenue of research for the model optimization would consider alternative mixing rules for solid-fluid interactions.

The simulated adsorption isotherms for the different systems are shown in figure 4.15.

.

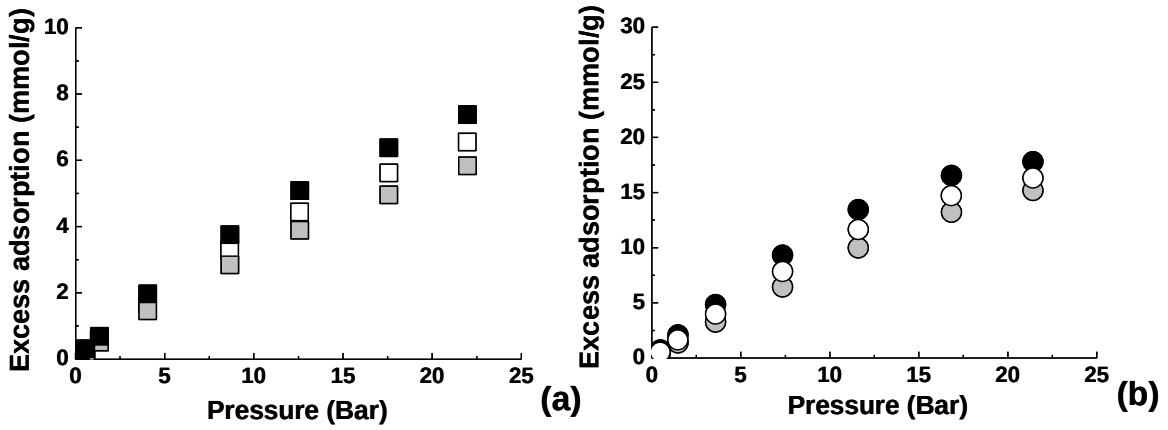

Figure 4.15. (a) Excess adsorption isotherms for CH_4 at 298 K in CR (empty squares), CRNL with no scaling (grey squares) and CRNL with scaling applied (black squares). (b) Excess adsorption isotherms for CO_2 at 298 K in CR (empty circles), CRNL with no scaling (grey circles) and CRNL with scaling applied (black circles).

Comparing the behaviour of CR and CRNL (not scaled) it is clear that the introduced platelet curvature itself leads to a decrease in the adsorption of both methane and carbon dioxide. This is true not only in the Henry's law region (table IV.5) but also at higher pressures (figure 4.15). We may speculate that this is related to packing effects of curved platelets. We further note that curved platelets are slightly smaller in size (lower number of carbon atoms), compared to the reference flat platelets, and this may also lead to a diminished adsorption as discussed earlier. Application of the scaling factor leads to a net increase in adsorption both at low and high pressures for both adsorbing species. From the last two rows of table IV.5, scaling has also a small effect on the accessible pore volume, which is expected as it is determined from the Widom insertion method and helium atom interacting via the LJ potential with the atoms of the structure.

4.5. Selection of a representative model of Maxsorb MSC-30

The results of the preliminary studies presented in Section 4.3 showed a reasonable agreement between the simulated and experimental CO_2 adsorption, while the adsorption of CH_4 was clearly under-estimated. Also, this model was not the most realistic, with many important details such as presence of functional groups and curvature ignored. The results presented in Section 4.4 allow us to state which parameters have a significant effect on the adsorption properties of the model with respect to CO_2 and CH_4 and which do not.

The presence of functional groups, the C/O ratio, the surface area (and consequently the pore volume), the scaling of the solid-fluid interaction performed to take into account the presence of curvature all have a noticeable impact on the adsorption isotherms, while the type of functional groups have only a minor effect. As for the dimension of the platelets this does have a substantial effect on the adsorption of methane. However, there is a substantial computational cost associated with generating the systems based on larger platelets, while maintaining the properties of the packings, such as surface area, close to the target ones of Maxsorb. Hence this strategy has been discarded. In principle, the method used to determine the charges may have an effect on the adsorption properties, depending on the chosen model of the platelet. This needs to be further investigated.

Although the observed trends are not sufficient to construct a unique model of Maxsorb, we believe they instruct us on how to construct a reasonable model. Specifically, we choose as a BSU a platelet corresponding to corannulene (so it is curved) functionalized with two hydroxylic groups (figure 4.16). The study of the actual chemical stability or reactivity of this species is beyond the scope of the present work.

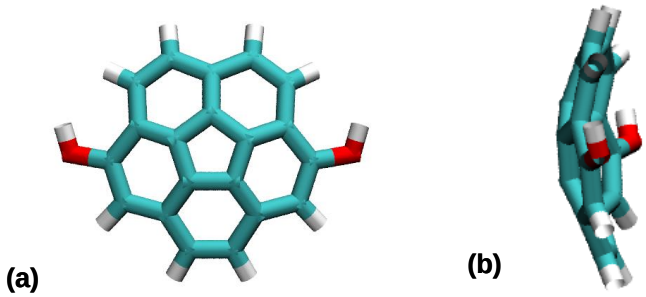

Figure 4.16. Computer visualization of a molecule of corannulene functionalized with two hydroxylic groups. (a): top view, (b): side view. Cyan: carbon, grey: hydrogen, red: oxygen.

Before proceeding to the random packing step (based simply on hard-sphere interactions) the structure is energy minimized and charges are calculated using the B3LYP/CHELPG set of methods with the Gaussian 09 software package (33-35). The packing properties are adjusted (through the removal of platelets from the most dense structure) to reproduce the surface area of Maxsorb as closely as possible. The characteristics of the final model are summarized in table IV.6 which also presents for comparison the typical characteristics of Maxsorb MSC-30.

Table IV.6. Characteristics of the final model constructed in this work compared with typical characteristics of Maxsorb MSC-30 activated carbon. The properties in this table are defined in the same way as for tables 4.1 and 4.2.

SYSTEM	**S.A.** m^2/g	**V, 298 K** cm^3/g	**k_H CH_4, 298 K** mol/kg/Bar	**k_H CO_2, 298 K** mol/kg/Bar	**C/O**
CRNL-$(OH)_2$	3236.64	1.28	1.03	1.96	7.5
MSC-30	3000 - 3500	1.3 – 1.7	1.3 – 1.9	2.4	7.8

It is also important to note here that despite being formally made by an arrangement of discrete elements, packings of platelets here form a self-sustained fully percolated network in three dimensions, as characterized using the package Poreblazer 1.2, which adds an additional element of realism to the model.

The model has been further characterized through the determination of the geometric pore size distribution, the calculation of Henry's constants for CO_2 and CH_4 at different temperatures and the determination of the differential enthalpies of adsorption at zero coverage for the same adsorbates. The details and results of the calculations are presented in Section A9 of the Appendix. Here we will limit ourselves to explain that the method to determine the geometric pore size distribution has been developed in our group starting from the idea proposed by Gelb and Gubbins (41). The main concept is that, given a molecular model representing the structure of an adsorbent, a randomly chosen point can be said to belong to a pore of radius *r* if it belongs to a sphere of radius *r* which does not overlap with the atom of the structure. For full details of the Monte Carlo procedure involved the reader is reminded to the publication by Sarkisov and Harrison (23).

As seen in figure A8 the geometric pore size distribution is centered around 7 Å. How does this compare to the PSDs obtained using slit pore models? Let us consider one specific case: a PSD obtained for the model with surface groups and defects starting from data for CO_2 at 298 K. We need to note that the peak of the geometric pore size distribution corresponds to a slit pore width of 10.4 Å, given that, as explained in Chapter 3, the width of a slit pore is calculated as the distance between the centres of the carbon atoms on opposite pore walls and does not take into account their collision diameters. Considering these values make the two pore size distributions comparable, given that in Chapter 3 the pore size distribution we show is centred around 10 Å. A comparison between the two pore size distributions made using this criterion is shown in figure 4.17, where the blue line represents the PSD extracted using the slit pore with groups and defects model, while the black line shows the PSD computed using the platelet model, but translated by 3.4 Å to the right to make the comparison consistent..

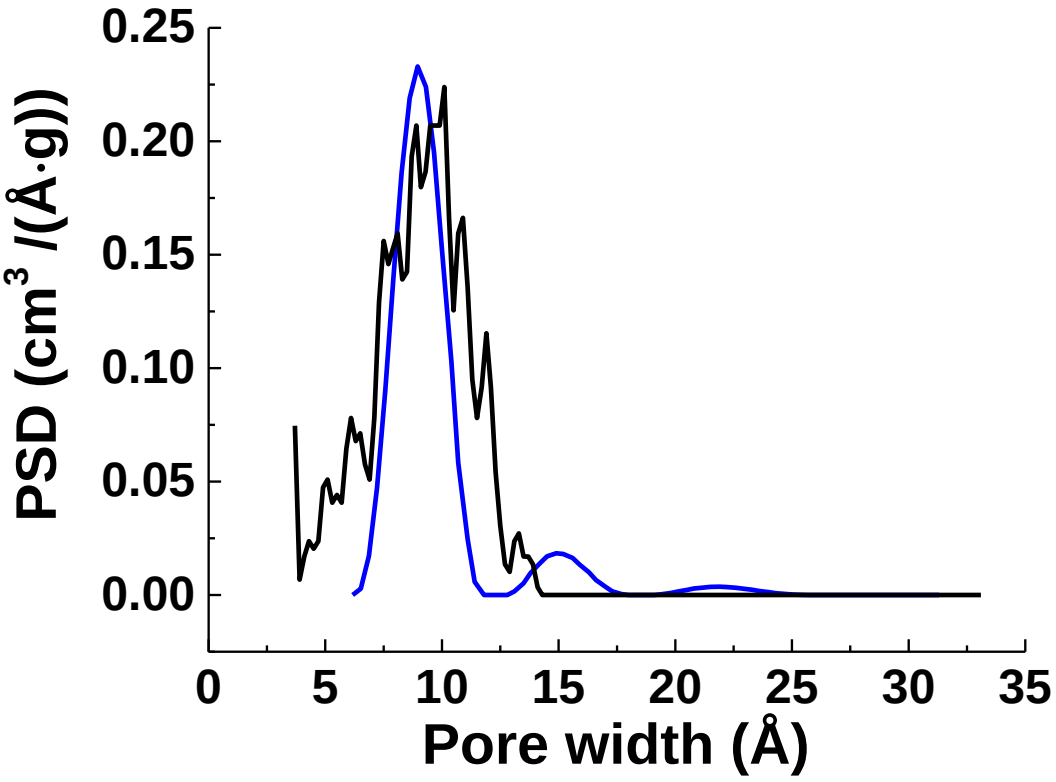

Figure 4.17. Comparison between PSDs extracted for Maxsorb MSC-30 using two different types of models. Blue line: slit pore with groups and defects model starting from data for CO_2 at 298 K; black line: geometric PSD translated by 3.34 Å to the right to make the comparison consistent.

From figure 4.17 it is clear that in the case of the slit pore model the PSD is much smoother than in the case of the platelet model. This could be a reflection of the higher level of disorder that characterizes the platelet model.

In simulation of adsorption isotherms and calculation of the Henry's constants, a scaling factor if 1.23 is applied for methane-platelet interactions to obtain better agreement with the experimental data. No scaling however is applied in case of carbon dioxide adsorption. Although this scaling is arbitrary to some extent and is simply a reflection of the intrinsic imperfections of the model, here we speculate on how this scaling can be justified. In our model the functional groups and the Coulombic interactions are explicitly represented and this has an important effect on CO_2 adsorption. This becomes particularly evident if we consider that for carbon dioxide adsorption Coulombic energy constitutes about 23% of the total solid-fluid interaction. To the best of our knowledge the previous studies involving curved surfaces did not include groups and Coulombic interactions in the models and the

scaling of solid-fluid interactions was applied to account for all the different types of heterogeneity and curvature effects (8, 9). It seems by modelling the polar groups explicitly we introduced a sufficient degree of heterogeneity to reproduce correctly adsorption of polar species. However, heterogeneity influencing adsorption of apolar species, such as methane, is not yet incorporated to full extent in the current model, and hence some scaling is still needed. This argument also suggests how the scaling should be consistently applied for species other than carbon dioxide and methane. Specifically, the same scaling factor determined for CH_4 is applied to hydrogen, as for both species Coulombic interactions have not been modelled explicitly; however in the case of nitrogen no scaling factor is applied, as in the three site model of nitrogen employed here the Coulombic interactions are included explicitly.

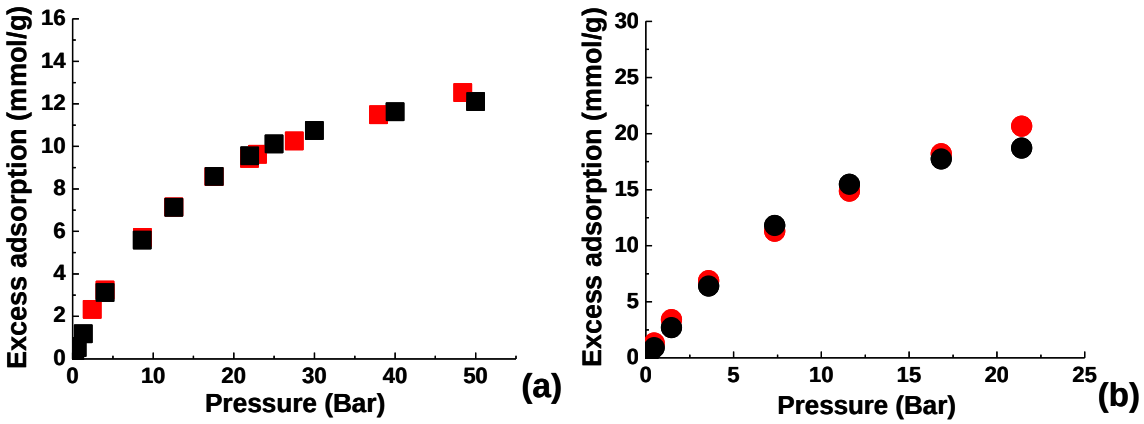

Figure 4.18. (a) Comparison between simulated (black squares) and experimental (red squares) adsorption isotherms for CH_4 at 298 K. (b) Comparison between simulated (black circles) and experimental (red circles) adsorption isotherms for CO_2 at 298 K.

In principle we could have used quantum mechanics to calculate the solid-fluid interaction for each adsorbate species, but the computational cost associated with this would have been much higher, especially given that the calculations would be required for each new species to be introduced in the mixtures considered in this study. Therefore, we have chosen to apply the scaling factor simply as a fitting parameter. One may argue that the scaling could have simply been applied to the non-curved platelets. However, it is the curvature of the surfaces that, as has been discussed above, leads to stronger interaction for certain species; therefore, unlike for flat platelets, adjustment of solid-fluid interactions for curved platelets is justified

on physical grounds, although it is not performed in quantitatively rigorous way. We believe that the presence of curvature gives a more correct representation of the microstructure of the material, which has an important effect when studying the structure of the adsorbed phase and may have an important role from the kinetic point of view: as we mentioned in Chapter 1 it is not only important to study the equilibrium adsorption properties, but also to take into account the kinetic aspects. This could be the subject of a future study with the use of molecular dynamics.

The final simulated adsorption isotherms at 298 K are shown in figure 4.18 in comparison with the experimental data. For methane (figure 4.18 (a)) the model shows an excellent agreement (which is not surprising given that some scaling was involved). For carbon dioxide (figure 4.18 (b)), the model performs very well up to pressures of about 20 Bar, but somewhat underpredicts adsorption density at higher pressures.

In this case the statistical errors on the simulated adsorbed densities for CO_2 have been calculated to be 8.7% and 0.3% at 0.1 Bar and 22 Bar respectively, while for methane the errors at the same pressures are 7.8% and 1.6%.

Any simulation model is valuable only if it is able to provide accurate predictions for a range of conditions and situations. To test the accuracy of the model we simulate CO_2 and CH_4 adsorption at 273 and 323 K. It is anticipated that at lower temperature the results become more sensitive to the details of the structure and the force field and hence the accuracy should deteriorate, while at higher temperatures the model should still remain accurate. The results are shown in figure 4.19 (isotherms at 273 K) and figure 4.20 (isotherms at 323 K). In the case of CH_4 and also for CO_2 at 323 K the chosen reference isotherms are the ones published by Himeno and co-authors (42).

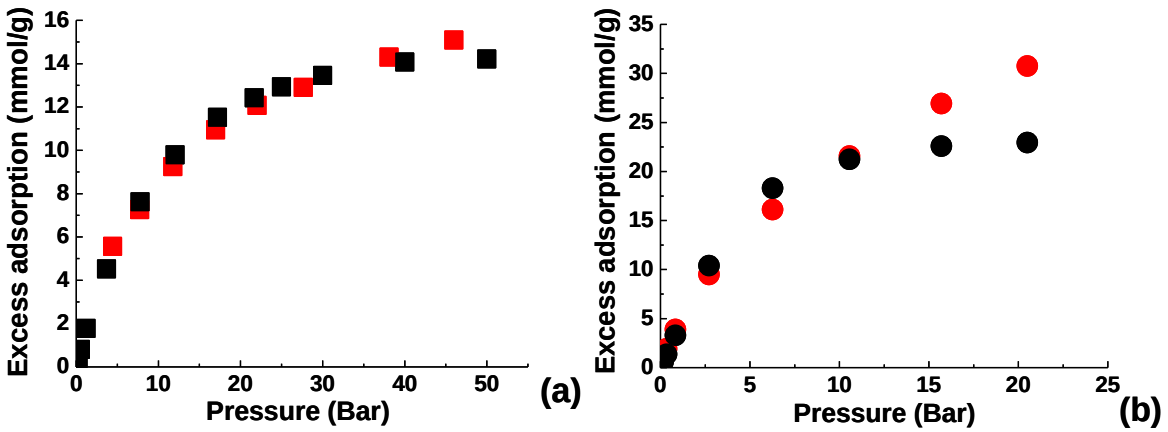

Figure 4.19. (a) Comparison between simulated (black squares) and experimental (red squares) adsorption isotherms for CH_4 at 273 K. (b) Comparison between simulated (black circles) and experimental (red circles) adsorption isotherms for CO_2 at 273 K.

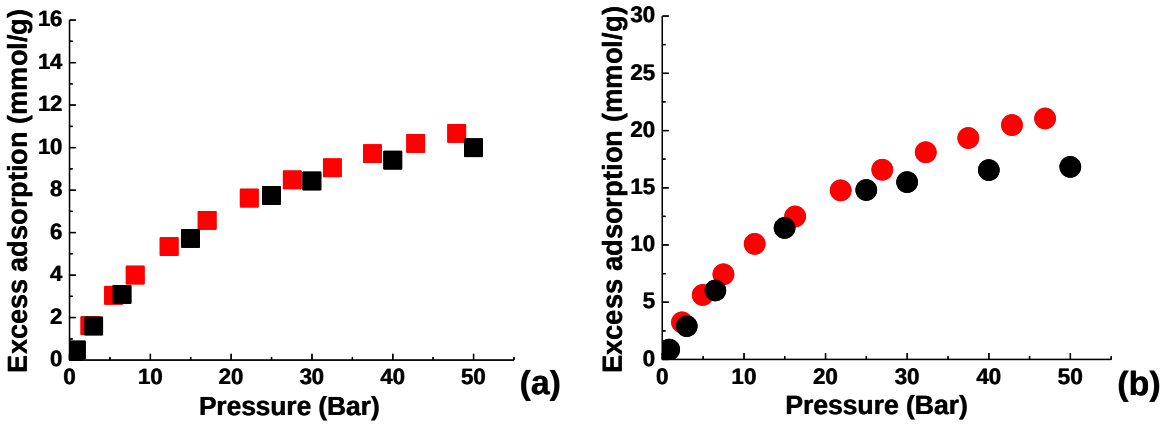

Figure 4.20. (a) Comparison between simulated (black squares) and experimental (red squares) adsorption isotherms for CH_4 at 323 K. (b) Comparison between simulated (black circles) and experimental (red circles) adsorption isotherms for CO_2 at 323 K.

It is quite clear that for methane the model seems to work really well over the range of temperatures 273-323 K in a broad range of pressures, from 0 to 50 Bar. In the case of CO_2 the model works well for temperatures between 273 and 323 K in a range of pressures that becomes broader the higher the temperature. In particular, at 273 K the results for CO_2 are reliable up to 10-12.5 Bar, while at 298 and 323 K the range of pressures where the model is still accurate (within 15% of reference adsorbed density) is shifted to 20-22.5 and 25 Bar respectively. At higher pressures (>25 Bar) the model underestimates CO_2 adsorption. Aside from the imperfections of the adsorbent model, another contribution to this trend may arise

from the tendency of TraPPE to underestimate density for CO_2 at high pressures (see Appendix, section A11).

For further validation of the model we need to put it in the context of a real application. Here we apply it to predict adsorption of nitrogen and hydrogen, which are the main components of the streams for the post and pre-combustion processes respectively. The comparison of the simulated adsorption isotherm for nitrogen at 373 K compared with the experimental measurements by Grande and co-authors (43), shown in figure 4.21 (a), suggests that the model should be applicable to the post-combustion streams.

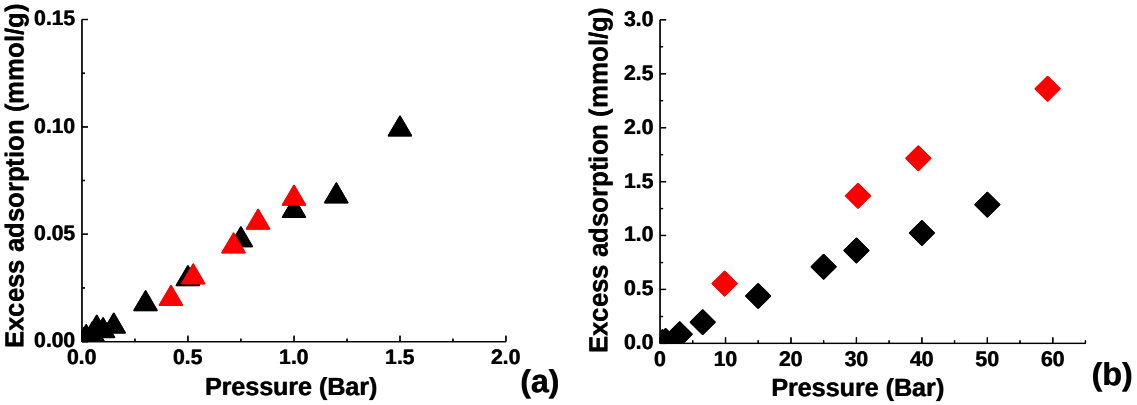

Figure 4.21 (a) Comparison between simulated (black triangles) and experimental (red triangles) adsorption isotherms for N_2 at 373 K. (b) Comparison between simulated (black diamonds) and experimental (red diamonds) adsorption isotherms for H_2 at 298 K.

For pre-combustion processes it is important, as a first step, to correctly predict adsorption of hydrogen and carbon dioxide. Comparison between our simulated isotherm for H_2 at 298 K and the measurement performed by Linares-Solano and co-workers (44) is shown in figure 4.21 (b). 298 K is not exactly the temperature of the pre-combustion stream (313 K) but this is the temperature at which our reference isotherm was measured.

Both simulations and experiments indicate that the amount of hydrogen adsorbed in Maxsorb is small even at relatively high pressures (up to 60 Bar). The simulations in general underestimate adsorbed density of hydrogen compared to the experimental isotherm. However, given the simplicity of the adopted model for hydrogen and the broad range of pressures under examination, the agreement can be considered as acceptable, especially given

that the mechanism of adsorption of hydrogen on carbon materials has not yet been fully understood, this implying the actual lack of accurate potential models (29). Several alternative models for hydrogen-carbon interaction are also explored in the Appendix (section A10).

The key characteristic of importance here is the high affinity that Maxsorb shows for carbon dioxide over hydrogen. Figure 4.22 shows the pure component adsorption isotherms (simulated and experimental) for both CO_2 and H_2. From the figure it is clear that the model correctly captures the higher affinity that Maxsorb shows for carbon dioxide over hydrogen; also, if the predictive capability for CO_2 is reasonably accurate only up to 20 – 22.5 Bar, for hydrogen the performance of the model is constant over a broader range of pressures.

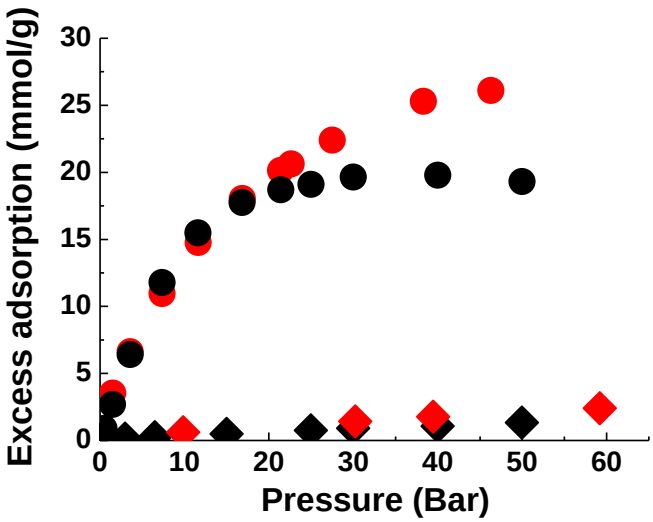

Figure 4.22. Comparison between simulated and experimental pure component adsorption isotherms for CO_2 (black and red circles, respectively) and H_2 (black and red diamonds, respectively).

The separation between hydrogen and carbon dioxide, including selectivity analysis, will be studied in more detail in Chapter 5.

4.6. Conclusions

The objective of the present chapter has been to develop a predictive model for high surface area activated carbon Maxsorb in application to industrial carbon capture and related adsorption separation processes.

Building on the ideas of Segarra and Glandt (14) and more recent studies of Kumar et al (20, 21), the proposed model is based on a random packing of small, symmetric fragments (platelets) of graphite sheet. This model has many essential features of activated carbons, such as high surface area, disorder and heterogeneity of the structure. At the same time it is sufficiently flexible to tune its parameters in a systematic way and introduce additional features to reflect specific properties of the material of interest. In application to carbon dioxide and methane adsorption in Maxsorb, we show that an encouraging correlation with the experimental data can be obtained simply by constructing a model with realistic values of the surface area and accessible pore volume. For a more accurate agreement with the experimental data, a better understanding of the role of different parameters was required and our study was undertaken with a focus on the effects of platelet size, surface area, concentration and nature of surface groups, charge model, geometry of platelets and other parameters. This strategy can be applied to the development of accurate models of other high surface area carbons, with Maxsorb being only one example.

Using insights from these studies we constructed a realistic (in terms of disorder and surface area) model of Maxsorb material with as few tuneable parameters as possible. The final model is given by a random packing of fullerene-like fragments functionalized with hydroxylic groups and having surface area, accessible pore volume and carbon/oxygen ratio consistent with the features of Maxsorb activated carbon. The models gives very reasonable predictions for a variety of species under a range of temperature conditions and up to pressures relevant for mixtures involved in carbon capture processes.

Having said this, the Henry's constants of adsorption for the adsorbate species under investigation and experimental adsorption points on a reference isotherm have not been used as a constraint in the construction of the model. Therefore, a possible criticism of this approach would be not utilizing all the experimental data available.

In contrast, the accuracy of the slit pore model in terms of single component predictions at least for light gases must in general be higher, given that in that case each point of the isotherm acts as a constraint to construct the pore size distribution, and given that the Henry's regime is also reproduced.

Therefore, an interesting research area would be to develop a method that constraints construction of the disordered model in a similar way that the PSD for the slit pore model is obtained, by using all the experimental adsorption points and by aiming to reproduce the Henry's law regime.

Nevertheless, in summary the disordered model we are proposing retains an acceptable level of accuracy (given a small number of arbitrary adjustments) for a number of species and conditions relevant to industrial carbon removal processes. And therefore we believe this model can be used to systematically optimize the use of Maxsorb in these processes, explore applicability of Maxsorb in other similar processes, or to develop completely new processes, where molecular insights on the behaviour of Maxsorb can be useful.

In the next chapter the model will be applied to the simulation of multicomponent mixtures involved in CC processes, using conditions as realistic as possible.

References

1. Gregg SJ, Sing KSW. Adsorption, Surface Area and Porosity. New York: Academic Press; 1982.
2. Oberlin A, Villey M, Combaz A. Influence of elemental composition on carbonization: Pyrolysis of kerosene shale and kuckersite. Carbon. 1980;18(5):347-53.
3. M. RD. Principles of Adsorption and Adsorption Processes: Wiley - Interscience; 1984.
4. Harris PJF, Tsang SC. High-resolution electron microscopy studies of non-graphitizing carbons. Philosophical Magazine A. 1997;76(3):667-77.
5. Harris PJF, Burian A, Duber S. High-resolution electron microscopy of a microporous carbon. Philosophical Magazine Letters. 2000;80(6):381-6.
6. Harris PJF. Fullerene-related structure of commercial glassy carbons. Philosophical Magazine. 2004;84(29):3159-67.
7. Harris PJF. New Perspectives on the Structure of Graphitic Carbons. Critical Reviews in Solid State and Materials Sciences. 2005;30(4):235-53.
8. Nguyen TX, Cohaut N, Bae J-S, Bhatia SK. New Method for Atomistic Modeling of the Microstructure of Activated Carbons Using Hybrid Reverse Monte Carlo Simulation. Langmuir. 2008;24(15):7912-22.
9. Palmer JC, Brennan JK, Hurley MM, Balboa A, Gubbins KE. Detailed structural models for activated carbons from molecular simulation. Carbon. 2009;47(12):2904-13.
10. Kumar A, Lobo RF, Wagner NJ. Grand canonical Monte Carlo simulation of adsorption of nitrogen and oxygen in realistic nanoporous carbon models. AIChE Journal. 2011;57(6):1496-505.
11. McGreevy RL, Pusztai L. Reverse Monte Carlo Simulation: A New Technique for the Determination of Disordered Structures. Molecular Simulation. 1988;1(6):359-67.
12. Opletal G, Petersen T, O'Malley B, Snook I, McCulloch DG, Marks NA, et al. Hybrid approach for generating realistic amorphous carbon structure using metropolis and reverse Monte Carlo. Molecular Simulation. 2002;28(10-11):927-38.
13. Gelb LD, Gubbins KE, Radhakrishnan R, Sliwinska-Bartkowiak M. Phase separation in confined systems. Reports on Progress in Physics. 1999;62:1573-659.
14. Segarra EI, Glandt ED. Model microporous carbons: microstructure, surface polarity and gas adsorption. Chemical Engineering Science. 1994;49(17):2953-65.
15. Steele WA. The interaction of rare gas atoms with graphitized carbon black. The Journal of Physical Chemistry. 1978;82(7):817-21.
16. Liu J-C, Monson PA. Molecular Modeling of Adsorption in Activated Carbon: Comparison of Monte Carlo Simulations with Experiment. Adsorption. 2005;11(1):5-13.
17. Liu JC, Monson PA. Monte Carlo Simulation Study of Water Adsorption in Activated Carbon. Industrial & Engineering Chemistry Research. 2006;45(16):5649-56.
18. Terzyk AP, Furmaniak S, Harris PJF, Gauden PA, Wloch J, Kowalczyk P, et al. How realistic is the pore size distribution calculated from adsorption isotherms if activated carbon is composed of fullerene-like fragments? Physical Chemistry Chemical Physics. 2007;9(44):5919-27.
19. Kowalczyk P, Gauden PA, Terzyk AP, Furmaniak S, Harris PJF. Displacement of Methane by Coadsorbed Carbon Dioxide Is Facilitated In Narrow Carbon Nanopores. The Journal of Physical Chemistry C. 2012;116(25):13640-9.
20. Kumar KV, Müller EA, Rodríguez-Reinoso F. Effect of Pore Morphology on the Adsorption of Methane/Hydrogen Mixtures on Carbon Micropores. The Journal of Physical Chemistry C. 2012;116(21):11820-9.
21. Kumar VK, Rodríguez-Reinoso F. Co-adsorption of N_2 in the presence of CH_4 within carbon nanospaces: evidence from molecular simulations. Nanotechnology. 2013;24(3):35401.
22. Sarkisov L. Accessible Surface Area of Porous Materials: Understanding Theoretical Limits. Advanced Materials. 2012;24(23):3130-3.
23. Sarkisov L, Harrison A. Computational structure characterisation tools in application to ordered and disordered porous materials. Molecular Simulation. 2011;37(15):1248-57.

24. Talu O, Myers AL. Molecular simulation of adsorption: Gibbs dividing surface and comparison with experiment. AIChE Journal. 2001;47(5):1160-8.
25. Dubinin MM, Radushkevich LV. Equation of the characteristic curve of activated charcoal. Proceedings of the Academy of Sciences, Physical Chemistry Section, USSR 55. 1947:331-3.
26. Sarkisov L. Toward Rational Design of Metal-Organic Frameworks for Sensing Applications: Efficient Calculation of Adsorption Characteristics in Zero Loading Regime. The Journal of Physical Chemistry C. 2012;116(4):3025-33.
27. Martin MG, Siepmann JI. Transferable Potentials for Phase Equilibria. 1. United-Atom Description of n-Alkanes. The Journal of Physical Chemistry B. 1998;102(14):2569-77.
28. Potoff JJ, Siepmann JI. Vapor–liquid equilibria of mixtures containing alkanes, carbon dioxide, and nitrogen. AIChE Journal. 2001;47(7):1676-82.
29. Cracknell RF. Molecular simulation of hydrogen adsorption in graphitic nanofibres. Physical Chemistry Chemical Physics. 2001;3(11):2091-7.
30. Buch V. Path integral simulations of mixed *para*-D_2 and *ortho*-D_2 clusters: The orientational effects. The Journal of Chemical Physics. 1994;100(10):7610-29.
31. Tenney CM, Lastoskie CM. Molecular simulation of carbon dioxide in chemically and structurally heterogeneous porous carbons. Environmental Progress. 2006;25(4):343.
32. Klauda JB, Jiang J, Sandler SI. An ab Initio Study on the Effect of Carbon Surface Curvature and Ring Structure on N2(O2)âˆ'Carbon Intermolecular Potentials. The Journal of Physical Chemistry B. 2004;108(28):9842-51.
33. Axel DB. A new mixing of Hartree--Fock and local density-functional theories. The Journal of Chemical Physics. 1993;98(2):1372-7.
34. Breneman CM, Wiberg KB. Determining atom-centered monopoles from molecular electrostatic potentials. The need for high sampling density in formamide conformational analysis. Journal of Computational Chemistry. 1990;11(3):361-73.
35. Frisch MJT, G. W.; Schlegel, H. B.; Scuseria, G. E.; Robb, M. A.; Cheeseman, J. R.; Scalmani, G.; Barone, V.; Mennucci, B.; Petersson, G. A.; Nakatsuji, H.; Caricato, M.; Li, X.; Hratchian, H. P.; Izmaylov, A. F.; Bloino, J.; Zheng, G.; Sonnenberg, J. L.; Hada, M.; Ehara, M.; Toyota, K.; Fukuda, R.; Hasegawa, J.; Ishida, M.; Nakajima, T.; Honda, Y.; Kitao, O.; Nakai, H.; Vreven, T.; Montgomery, Jr., J. A.; Peralta, J. E.; Ogliaro, F.; Bearpark, M.; Heyd, J. J.; Brothers, E.; Kudin, K. N.; Staroverov, V. N.; Kobayashi, R.; Normand, J.; Raghavachari, K.; Rendell, A.; Burant, J. C.; Iyengar, S. S.; Tomasi, J.; Cossi, M.; Rega, N.; Millam, J. M.; Klene, M.; Knox, J. E.; Cross, J. B.; Bakken, V.; Adamo, C.; Jaramillo, J.; Gomperts, R.; Stratmann, R. E.; Yazyev, O.; Austin, A. J.; Cammi, R.; Pomelli, C.; Ochterski, J. W.; Martin, R. L.; Morokuma, K.; Zakrzewski, V. G.; Voth, G. A.; Salvador, P.; Dannenberg, J. J.; Dapprich, S.; Daniels, A. D.; Farkas, Ö.; Foresman, J. B.; Ortiz, J. V.; Cioslowski, J.; Fox, D. J. . Gaussian 09, Revision A.1. 2009.
36. Earl DJ, Deem MW. Monte Carlo Simulations. In: Kukol A, editor. Methods in Molecular Biology. 443, Molecular Modeling of Proteins. Totowa, NJ: Humana Press; 2008. p. 25-36.
37. Otowa T, Nojima Y, Miyazaki T. Development of KOH activated high surface area carbon and its application to drinking water purification. Carbon. 1997;35(9):1315-9.
38. Jorge M, Schumacher C, Seaton NA. Simulation Study of the Effect of the Chemical Heterogeneity of Activated Carbon on Water Adsorption. Langmuir. 2002;18(24):9296-306.
39. Al-Matar AK, Rockstraw DA. Assessment of the Effect of Mixing Rules on Predicting the Second Virial Coefficient and a Further Evidence of the Inadequacy of the Lorentz-Berthelot Rules. Dirasat, Engineering Sciences. 2006;33(1):27-36.
40. Delhommelle J, Millié P. Inadequacy of the Lorentz-Berthelot combining rules for accurate predictions of equilibrium properties by molecular simulation. Mol Phys. 2001;99(8):619-25.
41. Gelb LD, Gubbins KE. Pore Size Distributions in Porous Glasses: A Computer Simulation Study. Langmuir. 1999;15(2):305-8.
42. Himeno S, Komatsu T, Fujita S. High-Pressure Adsorption Equilibria of Methane and Carbon Dioxide on Several Activated Carbons. Journal of Chemical & Engineering Data. 2005;50(2):369-76.

43. Grande CA, Cavenati S, Rodrigues AE, editors. Pressure swing adsorption for carbon dioxide sequestration. 2nd Mercosur Congress on chemical Engineering; 4th Mercosur Congress on Process systems Engineering; 2005; Costa Verde Do Brasil.
44. Jordá-Beneyto M, Suárez-García F, Lozano-Castelló D, Cazorla-Amorós D, Linares-Solano A. Hydrogen storage on chemically activated carbons and carbon nanomaterials at high pressures. Carbon. 2007;45(2):293-303.

Chapter 5

Application of the platelet based model to CO_2 capture processes

5.1. Introduction

In Chapter 4 we have developed a realistic molecular model for Maxsorb MSC-30. The model is based on representing the structure of Maxsorb as a random packing of corannulene-like elements, functionalized with hydroxylic groups. Chemical composition of the model, including the amount of oxygen present, and its structural characteristics, such as surface area and pore volume, have been tuned to closely reflect these parameters for Maxsorb. The developed model has been calibrated and tested through the comparison to the experimental single component isotherms for carbon dioxide, methane and some of the main components of the streams involved in carbon capture processes.

In this chapter we apply this model to explore Maxsorb behaviour with respect to multi-component mixtures, representative of different carbon capture processes under realistic conditions, including presence of water vapour in the streams.

5.1.1. Study of CO_2 capture separations

As we mentioned in Chapter 1, there are broadly three different types of CO_2 capture processes that could possibly be applied to fossil-fuel power plants. They are post-combustion capture, pre-combustion capture and oxyfuel combustion processes (1). Various features of these processes, including conditions, energy requirements, stream compositions, as well as comparative advantages and disadvantages, have been comprehensively reviewed in the literature (1-9). In this chapter we will focus on pre and post combustion capture and we will also explore the process of sweetening of sour natural gas which, although not directly related to the power plant operation, is still associated with carbon capture (6). The general characteristics of these processes have been introduced in Chapter 1, in which we have also briefly presented typical operational temperatures and pressures, together with average compositions of the streams (table I.1).

Previous studies on carbonaceous materials and CO_2 adsorption from mixtures mainly involve only binary (CO_2/CH_4) and ternary ($CO_2/CH_4/N_2$) systems in the absence of water vapour (10-14). An exception is the work by Wu et al., which reports experimental measurements and predictions for the quaternary mixture $H_2/N_2/CH_4/CO_2$ (15).

Studies based on single component isotherms have also been used to predict the behaviour of the mixtures; an example is given by the work of Herm et al. (16), in which the authors apply the Ideal Adsorbed Solution Theory (IAST) (17) to the data published in the comprehensive work by Sircar (18) to predict the behaviour of CO_2/H_2 mixtures in BPL activated carbon and provide a comparison with the behaviour of several metal-organic frameworks. Equally, the work by Himeno et al. (19), which reports CO_2 and CH_4 pure component isotherms for several activated carbons, could be used for a similar purpose.

Simulation studies include the works by Cracknell et al. (20), by Kluson and Scaife (21) on CO_2/N_2 and CO_2/CH_4 mixtures and the work by Cao and Wu (22) on CO_2/H_2 mixtures. In all these studies the slit pore model was used to represent the carbon structure. More recent simulation studies considered CO_2/CH_4 mixtures using more realistic models of activated carbons (23, 24). In particular, Furmaniak and co-workers systematically explored how the efficiency of the separation depends on the surface oxidation and on the pore size in virtual porous carbons (VPC) (24). Further examples of binary mixtures in disordered models (even

if not necessarily related to CO_2 capture) include the studies by Kumar and co-workers (25, 26).

One general consideration is that not many studies so far have considered conditions representing operational temperatures, pressures or compositions of the streams associated with the actual CO_2 capture processes. In the majority of the cases the studies have involved pure component isotherms or equimolar binary mixtures at 298 K, and the presence of minor components has rarely been considered. The effect of humidity, which is crucial for the efficiency of gas separations, has been essentially ignored. The next sub-section will focus exactly on this aspect.

5.1.2. Adsorption of water in activated carbons and effect of humidity on CO_2 capture separations

All multi-component streams involved in the CO_2 capture processes subject of this study are prone to contain water in various amounts, depending on the process, and therefore it is important to include water into consideration.

Adsorption of water on activated carbons has been a long standing problem. An important and comprehensive review on the experimental and computational studies in the field has been published by Brennan et al. (27). In particular, the authors summarize substantial developments in our understanding of the role of polar surface groups on water adsorption in activated carbons, arising from a number of important contributions (28-33). Brennan and co-workers further investigated the problem in a study in which the structure of an activated carbon is represented through a realistic model, featuring variable number of functional groups (34). More recently, Liu and Monson (35), Horikawa et al. (36) and Wang et al. (37) studied the effect of structural and surface chemical characteristics on water adsorption and desorption in activated carbons. In particular, as mentioned in Chapter 4, Liu and Monson simulated the adsorption of water on a model consisting of a random packing of platelet shaped elements featuring functional groups, developed from the model first proposed by Segarra and Glandt (38). Horikawa and co-workers (36) focused on the effect of surface

nitrogen in nitrogen-doped porous carbons, while Wang and co-workers (37) also considered the effect of acidic surface groups.

Do and co-workers have made an important contribution to the understanding of the mechanism of water adsorption in activated carbons (39-42). The models they formulated, called DD model (39) and HD model (42), have been validated against experimental evidence and have been subject of further modifications and studies (41, 43-46). The two models describe the mechanism of water adsorption respectively in micro and in mesopores, as we will introduce below.

To summarize substantial number of observations, accumulated from both computer simulations and experiments, water shows a very peculiar behaviour when adsorbed on activated carbon. The surface of activated carbons is in general hydrophobic, but it does contain heteroatoms (most commonly oxygen, nitrogen and sulphur), often in the form of polar groups. It is precisely in the proximity of these hydrophilic centres where the adsorption of water is believed to start. The first molecules adsorbed around the hydrophilic centres through hydrogen bonding then function as nuclei around which water clusters can grow.
In particular, it has been shown that the higher the concentration of functional groups in carbon is, the higher the extent of water adsorption at low pressure is; moreover, an increase in the number of functional groups can lead to transition of an adsorption isotherm from type V to type III (27-33).

It has also been shown that for highly oxidized activated carbons the differential enthalpy of adsorption calculated for values of p/p° approximately around 0.1 can reach values as high as the latent heat of bulk water condensation (45 kJ/mol) (27, 47-49). This indicates that the formation of water clusters around primary sites must occur at very low pressures.

As explained in detail by the DD and the HD models, once the clusters reach a certain critical size α_1 they start filling the micropores, and when they further grow up to a critical size α_2 they start filling the mesopores. This would explain the “two steps shape” typical of water adsorption in carbons characterized by micropores and mesopores with non-overlapping pore size distributions (41, 42).

Given enormous interest in water adsorption on activated carbons, the number of studies on the impact of humidity on adsorption of other species is surprisingly modest. The effect of water presence on carbon dioxide adsorption from mixtures and under conditions resembling real industrial cases has been investigated to an even lesser extent.

The majority of the work which has been published so far is experimental. Several studies in this context explore adsorption of carbon dioxide, methane and other gases on humid activated carbon or coal. For example, comparative pure component adsorption of CH_4 and CO_2 on coal in the presence of water was investigated by Kroos et al. (50). A similar study on activated carbons has been carried out by Wang et al. (51). Sun et al. (52) assessed the effect of humidity on the pure component adsorption of CO_2 on activated carbon.

Sun and co-workers (53) also investigated adsorption of CO_2/CH_4 mixture on activated carbon in the presence of water. Billemont and co-workers employed both experiments and grand canonical Monte Carlo simulations to explore single component and binary mixture adsorption for carbon dioxide and methane on humid porous carbons (54, 55). As a model of the carbon structure they considered both the classical slit pore model and a more realistic disordered structure. In the case of the disordered structure they studied two systems, one featuring and one not featuring any functional groups.

Other experimental studies include the work by Fitzgerald et al. (56) on the ternary mixture of carbon dioxide, methane and nitrogen, adsorbing on humid Tiffany coal. Xu and co-workers (57, 58) investigated the realistic case of the effect of water on CO_2 capture from the model flue gas using vacuum swing adsorption (VSA) process on activated carbon. Their study involved quaternary $N_2/CO_2/O_2/H_2O$ mixture.

What in general emerges from all these studies is the fact that small amounts of humidity in the mixtures do not change the shape of the adsorption isotherms and do not influence the pore filling mechanism, but they do have an effect in decreasing the adsorption, to an extent proportional to the amount of water. The decrease in the adsorption may actually be hardly noticeable, if the amount of water is very small.

It has also been shown that species forming hydrates under conditions of interest may be preferentially adsorbed (53).

5.2. Methodology

5.2.1. Simulation details

As we did for the results reported in Chapters 3 and 4, for all our simulations we use the energy biased grand canonical Monte Carlo method (GCMC), as implemented in the MuSiC simulation package (59). The details of the GCMC simulations protocol adopted in this chapter are the same as for the studies reported in Chapter 4, and they are provided in the Appendix of the thesis (Section A2). Whenever variations to the protocol are applied, this is mentioned in the chapter as needed.

All the simulated adsorption densities are converted into excess values following the procedure proposed by Talu and Myers (60); we note that the density of the bulk adsorbate, required for this conversion, is calculated performing a separate, bulk GCMC simulation, using a simulation cell with the volume equal to the Helium pore volume of the Maxsorb model. The choice to determine the density of the bulk adsorbate directly from GCMC simulations, rather than using an appropriate equation of state, aims to minimize the error intrinsically associated with the differences in fluid properties as predicted from the force-field models and from the EOS methods. This is particularly important for high pressure multi-component mixtures.

The Lennard-Jones parameters and charges associated with the model structure for the adsorbent are the same as determined in Chapter 4 for the final model of Maxsorb, and they are reported in the Appendix of the thesis (table A1).

As for the fluids involved in the simulations, the species which have already been simulated when developing and testing the model for Maxsorb are represented using the same models as in Chapter 4. In general, TraPPE models (61-64) are used where available; hydrogen is represented using the spherical model by Buch (65) and carbon monoxide is modeled using the two centre model with partial charges by Sweatman and Quirke (66). For water the tip4p model has been adopted (67).

A table with the bond lengths and bond angles for the non-spherical models (all models are non-spherical apart from hydrogen and methane) and a table with the full set of LJ parameters and charges are reported in the Appendix of the thesis (table A2 and table A3). We note here that all adsorbing species are treated as rigid molecules.

As introduced in Chapter 4 the LJ solid-fluid interaction parameters have in general been calculated using the standard Lorentz-Berthelot mixing rules, but a scaling factor of 1.23 has been applied to the graphitic carbon-fluid LJ interaction for species with molecular models featuring no explicit charges, such as methane and hydrogen.
Fluid-fluid Coulombic interactions between partial charges have been calculated using the Fennell-Gezelter method (68) based on a spherically truncated summation, while in the solid-fluid case Ewald summation (69) has been applied.

5.2.2. Carbon capture separations analysis

As mentioned in the introduction we consider separation processes related to post combustion capture, pre combustion capture and sweetening of sour natural gas. In all cases we show some exemplary adsorption isotherms, accompanied by the analysis of selectivities (separation factors) for the main separations, calculated as:

$$S_{i/j} = \frac{x_i/x_j}{y_i/y_j} \tag{V.1}$$

where $S_{i/j}$ is the selectivity for component *i* over component *j*; x_i, x_j are the molar fractions of components *i* and *j* in the adsorbed phase (calculated form absolute adsorption); y_i, y_j are the molar fractions of components *i* and *j* in the bulk phase.

For the same mixtures we also predict selectivities in the Henry's law regime using the formula:

$$S_{i/j}^{H} = \frac{K_{H,i}}{K_{H,j}} \quad \text{(V.2)}$$

where $S_{i/j}^{H}$ is the selectivity for component *i* over component *j* in the Henry's law region, while $K_{H,i}$ and $K_{H,j}$ are the Henry's constants for components *i* and *j*, respectively.

Selectivity as a parameter can give a good indication on how efficient the separation of the components in a mixture can be, but nevertheless it is not the only criterion that needs to be taken into account for the assessment of CO_2 capture materials: for example high values of selectivity do not only imply high efficiency in a certain separation, but they may also imply very high affinity of the adsorbent for a certain component in the mixture and therefore high costs associated with its regeneration. Hence, a complete analysis must be based on selectivity in conjunction with other characteristics such as high working capacity, affordable cost of material, stability to water and so on. In general, the most comprehensive assessment of a material should come from a process simulation (70-72).

In this work we compare the values of selectivity calculated for Maxsorb using simulations for multi-component mixtures with the data available for other materials. In the majority of cases in the literature selectivities have been estimated using single component isotherms. The values obtained following this procedure do not necessarily correspond to the actual selectivities, but most likely they tend to underestimate them, especially in the case of materials with strong polarizing sites. Nonetheless, they can be used to indicate the trends and compare materials to each other.

Only few studies report selectivities evaluated using IAST; data on selectivities calculated from experimental or simulated adsorption isotherms for mixtures is limited. In many cases, also, selectivities have been reported for separations at ambient temperature.When possible we try to compare our results either with the data obtained from direct simulation or

experiments for mixtures, or evaluated using IAST; also, we try to make our comparisons with the selectivities under the conditions as close as possible to the realistic industrial cases.

For all binary mixture separations we also apply IAST. The results are shown and discussed in the Section 5.5.

5.3. Water adsorption in Maxsorb MSC-30

As has been already discussed, adsorption of water in activated carbons is an important problem from the fundamental perspective and it should be also carefully considered when designing an actual adsorption separation process. Hence, in this section we concentrate on the simulation of water adsorption on Maxsorb MSC-30. First of all we explore single component adsorption at different temperatures; we then concentrate on adsorption at 298 K and investigate the role of functional groups in the adsorption process.

5.3.1.Water adsorption on Maxsorb: single component case

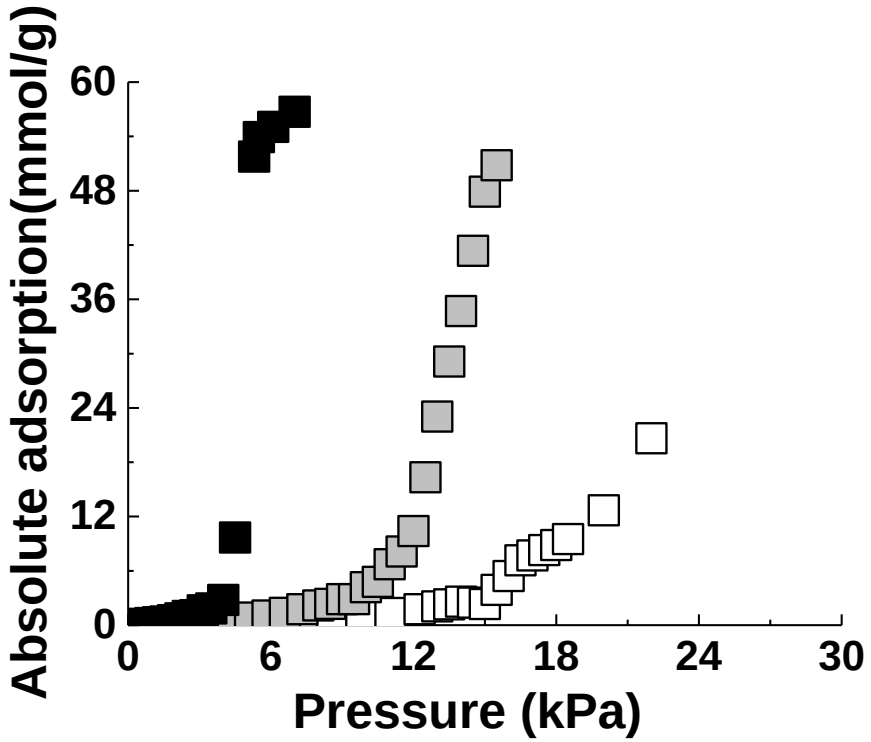

Figure 5.1. Absolute adsorption isotherms for water simulated on the model for Maxsorb MSC-30 at 298 K (black symbols), 313 K (grey symbols) and 323 K (white symbols).

Figure 5.1 shows single component water adsorption isotherms (absolute) at three different temperatures. The isotherm at 298 K has been calculated using 300 to 900 million iterations per point, while for the isotherms at 313 and 323 K 40 million iterations have been used. All the isotherms correspond to Type V, with the current Maxsorb model behaving as a hydrophobic material, despite the high concentration of functional groups.

This point is further illustrated in figure 5.2, which plots the isotherm for 298K (black symbols for adsorption and red symbols from desorption) in reduced pressure units p/p°, where p° is the bulk water condensation pressure. For tip4p it is 4.5 kPa at 298K (73). The simulated isotherm shows a broad hysteresis loop. The graph also compares simulated results (black filled symbols) with the available experimental data: grey symbols represent the results by Carlile et al. (74), which have been obtained using the gravimetric method at 303 K, while the white symbols represent the data by Iiyama et al. (75), with the SAC31 material in their work corresponding to a sample of Maxsorb material (as confirmed through a personal communication with Prof. Kaneko). In the absence of clarification we assume the

experimental isotherms to be showing absolute adsorption values, with the difference between excess and absolute adsorption being minor in the conditions under consideration. The substantial difference between the two sets of experimental data suggests that consistent measurement of water adsorption on activated carbons still presents a substantial challenge.

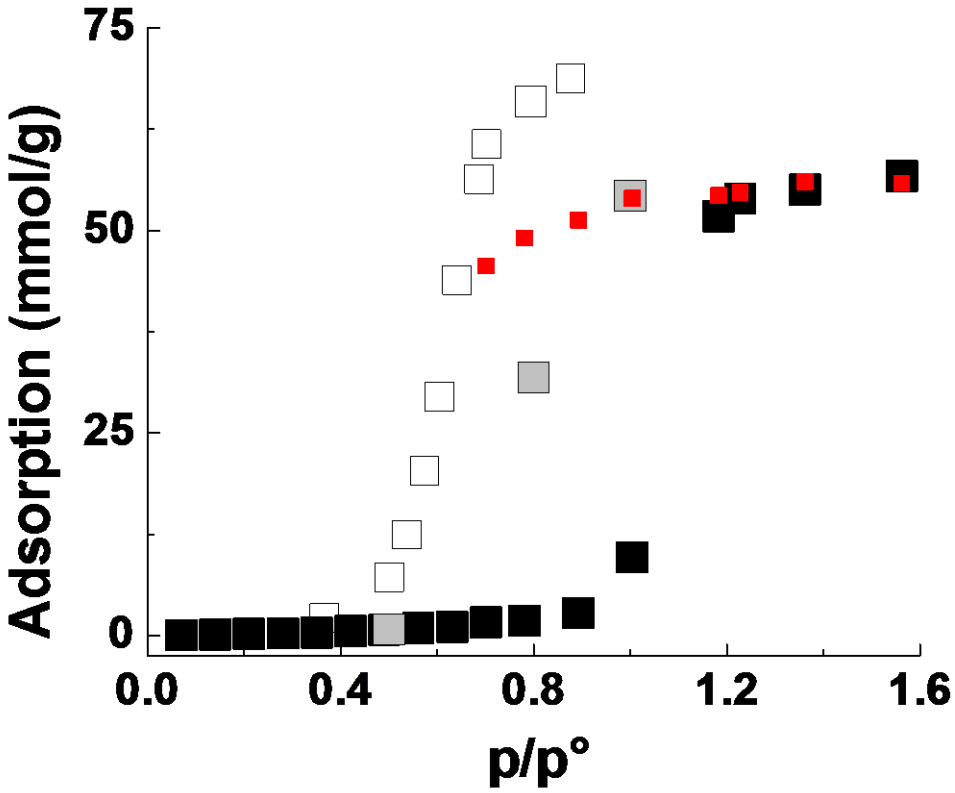

Figure 5.2. Water adsorption isotherms on Maxsorb at 298 K. Black symbols: simulation results (adsorption), filled red symbols: simulation results (desorption), grey symbols: data by Carlile et al. (74), white symbols: data by Iiyama et al. (75)

A careful inspection of figure 5.2 reveals that in the very low pressure regime the adsorption, as expected, is negligible; as the pressure increases the simulated adsorption capacity becomes instead very high (close to 60 mmol/g at the highest relative pressure under examination) and actually comparable to the adsorption reported by Carlile et al. (74), although the isotherm does not appear to be fully leveled out. In the disordered systems, such as the current model of Maxsorb, the hysteresis can be seen as an outline of a region of a large number of metastable states, which further complicates location of the confined vapour-

liquid coexistence or studies of the phase behavior in general (in fact, multiple transitions and phase envelopes are possible in the disordered systems (76, 77)). We argue that the simulated isotherm shows sufficient, even semi-quantitative, agreement with the experimental data, as the adsorption capacities are comparable. Analysis of the adsorption branch only would also lead to the conclusion that complete filling of the material with water occurs at pressures exceeding bulk condensation pressures. This type of phenomena has been observed in qualitative studies of porous systems with unfavorable solid-fluid interactions (78).

A comparison with the data by Iiyama et al. (75), instead, shows a much higher adsorption for the experimental results and shows that in this case the model actually overestimates the hydrophobicity of the material. Again, the lack of consistency between experimental data underlines the challenge brought by the measurement of water adsorption on activated carbons. .

Apart from this second comparison, an adsorption of 60 mmol/g can in general be considered high in the context of water adsorption in activated carbons: this becomes clear if we compare it to the experimental measurements on BPL (maximum adsorption capacity is between 20 and 25-26 mmol/g) (74) (79) or on some oxidized activated carbons: in the data presented by Stoeckly et al. (33), for example, all samples show at 293 K maximum adsorption capacities just below 30 mmol/g. Similar capacities have been presented by Talu and Meunier (80). In their study only one material, activated carbon AX21, shows saturation capacity between 50 and 55 mmol/g, which is well above the average for other materials. Even in the work by Carlile et al. (74) the adsorption capacity of Maxsorb definitely exceeds typical results for other activated carbons.

From this point on, our analysis will focus just on the adsorption branch of the water adsorption isotherm. From figure 5.1 adsorption of water decreases as the temperature increases, in agreement with the expected physical adsorption behavior of other fluids. Interestingly, according to the studies of Horikawa et al. (41), in mesoporous carbons at temperatures lower than 298 K water adsorption can also decrease with decreasing temperature. The authors proposed a mechanism of water uptake explaining this effect. In this mechanism, water adsorption crucially depends on the formation of water clusters of an appropriate size within hydrophobic mesoporous space of the material. Formation of these clusters is a kinetically controlled process, facilitated by higher temperatures. Here, the

temperatures are 298 K or higher, and the model porous structure does not feature any mesopores, so the effects investigated by Horikawa and co-workers are not observed in this study.

It has been widely accepted that the surface groups play an important role in the water uptake process. To illustrate this, we contrast the behavior of the original model for Maxsorb with that of the model featuring no surface groups. To make this comparison consistent and isolate the effect of surface groups from other factors we consider a system, based on non-functionalized corannulene elements, with structural characteristics (such as surface area, pore volume and density) very similar to the original model of Maxsorb. Structural characteristics of the two models are compared in table V.1.

Table V.1. Characteristics of the model structures based on corannulene elements functionalized with hydroxyl groups (CRNL-$(OH)_2$), and on non-functionalized corannulene elements (CRNL). In this table, S.A. is the surface area, V is the micropore volume and ρ is the density.

SYSTEM	**S.A.** $\mathbf{m^2/g}$	**V, 298 K** $\mathbf{cm^3/g}$	**P** $\mathbf{g/cm^3}$
CRNL-$(OH)_2$	3236.64	1.28	0.54
CRNL	3241.72	1.30	0.52

In figure 5.3 we show absolute water adsorption isotherms simulated at 298 K on the model of Maxsorb MSC-30 (black symbols), compared to the isotherms simulated on the model without functional groups (with properties reported in table V.1). White and grey symbols correspond to two slightly different variants of the second model: in the case of white symbols the model still features partial charges on the edges of the platelets associated with the termini hydrogen atoms, while in the case of the grey symbols no solid-fluid Coulombic interactions are taken into account. All isotherms have been calculated using 300 million iterations per point.

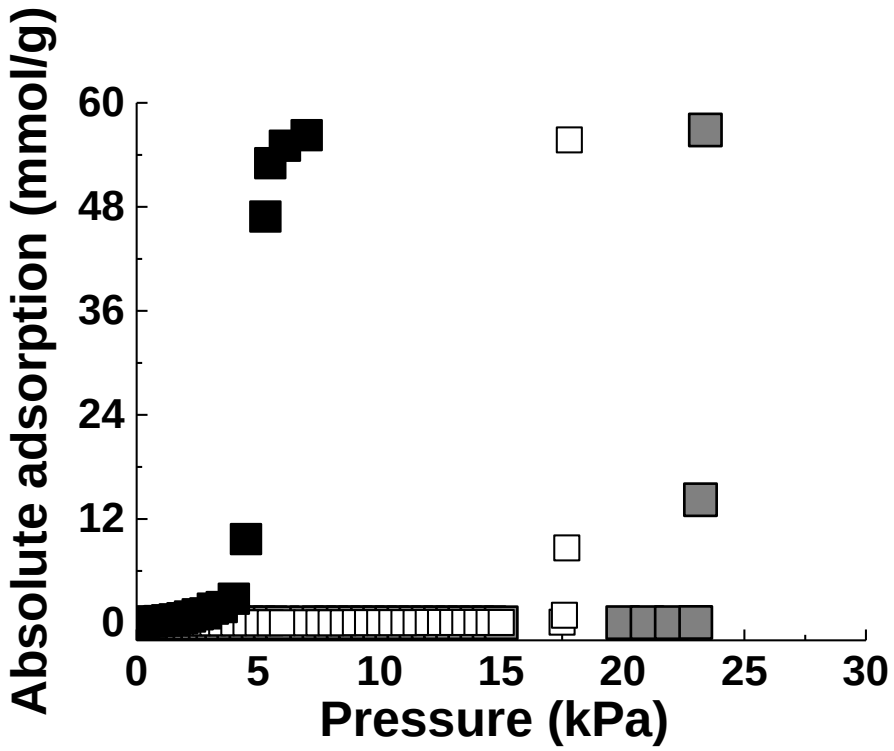

Figure 5.3. Water absolute adsorption isotherms simulated on model for Maxsorb MSC-30. Black symbols correspond to the reference Maxsorb model. White symbols are for the system with no functional groups. The system still features partial charges associated with the carbon atoms of the platelets and termini hydrogens. Grey symbols correspond to the system with no functional groups and no Coulombic interactions between the platelets and water molecules.

It is clear that the presence of the functional groups substantially changes the adsorption behavior of water. Firstly, the isotherms in the models featuring no functional groups are shifted to much higher pressures, and this is in agreement with the results by Billemont and co-authors (55), which show that the presence of oxygenated groups in a sparse model for activated carbon determines an increase in the amount of adsorbed water at a given pressure. Similar results were also shown in the work by Brennan and co-workers (34), in which the adsorption of water was found to be proportional to the amount of functional groups on the structure of the carbon. Secondly, n the material with functional groups, the isotherm a relatively smooth S-shape, with a number of intermediate points, before the final adsorption capacity is reached. For the models with no functional groups, water adsorption isotherms feature abrupt condensation step, and lower degree of polarity (induced by not considering solid-fluid Coulombic interactions), shifts the position of this step to higher pressures.

Let us consider in more detail processes on molecular level associated with the formation and growth of the water clusters in the model structure. First, we need to define a cluster. Two water molecules are considered to be connected if the distance between their oxygen atoms is less than 3.5Å (this distance corresponds to the first minimum in oxygen-oxygen radial distribution function for the bulk liquid water at ambient conditions). A pathway, consisting of these pairwise connections can be constructed for any two water molecules within a cluster. In the system with functional groups, formation of a cluster starts with association of a water molecule with one of the groups. In figure 5.4 we show a system involving one platelet and one molecule of water in the lowest potential energy configuration, whereas table V.2 summarizes contributions of Lennard-Jones and Coulombic terms to the total potential energy. As can be seen from the figure the water molecule forms a hydrogen bond with the surface group. This association is predominantly governed by the Coulombic interaction (table V.2).

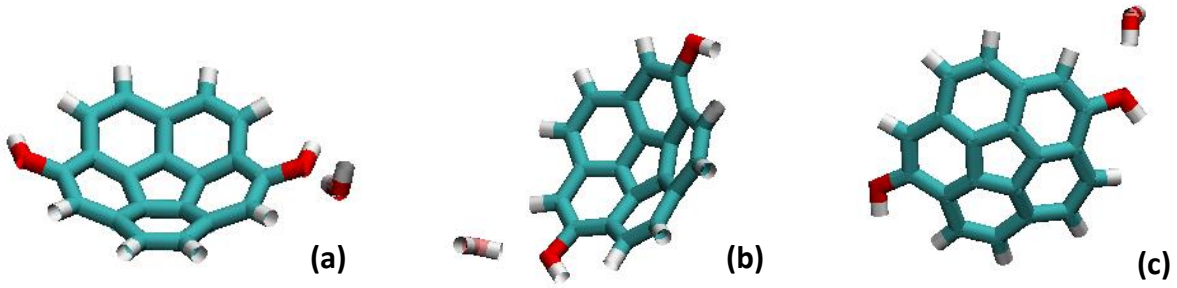

Figure 5.4. Computer visualization of the minimum potential energy configuration of a single water molecule and one platelet. The snapshots correspond to different view angles of the same configuration.

Table V.2. Contributions to the total solid-fluid interaction energy for a system of a single platelet and a water molecule in the minimum potential energy configuration. Energies are expressed in kJ/mol.

H_2O global energy minimum	
LJ	4.39
Coulombic	-29.42
Total	-25.03

In the system with functional groups, clusters form and grow around the surface groups. This is illustrated in figure 5.5, where we show the water clusters respectively for the system with groups (top panel) and the system without groups but still bearing charges on carbon atoms and termini hydrogens (bottom panel). In all cases what is actually shown are the oxygen atoms in each cluster, with different colours corresponding to different clusters.

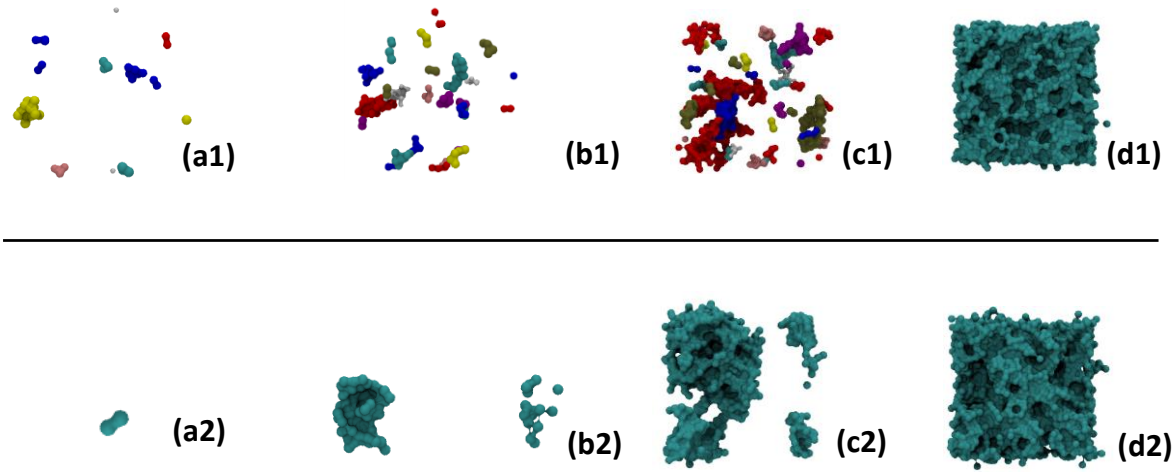

Figure 5.5. Visualizations of oxygen atoms in water clusters formed during simulation on the model featuring functional groups (top panel) and the model featuring no functional groups (bottom panel) at different pressures. In the top panel (a1): 2.20 kPa, (b1): 3.5 kPa, (c1): 4.5 kPa, (d1): 7 kPa; different colours correspond to different clusters. In the bottom panel (a2): 17.5 kPa, (b2): 17.6 kPa, (c2): 17.7

kPa, (d2): 17.8 kPa; at all pressures only one cluster is present, eventually shown in periodic boundary conditions.

Again, the behaviour is very different in two cases. In the model of Maxsorb, featuring functional groups, condensation starts at very low pressure (the lowest pressure shown in figure 5.5 (a) is 2.2 kPa, however the clusters actually start to appear at about 0.63 kPa). Several small clusters form around functional groups, and as the simulation progresses these clusters grow in size, until one percolated cluster spanning the whole system forms. This is in agreement with a similar cluster analysis presented by Brennan and co-workers (34) in their work about the influence that the functional groups on the structure of the carbon exert on the adsorption of water.

In the case of the material with no functional groups the onset of cluster formation is delayed to much higher pressures (17.5 kPa), and the following process corresponds to gradual growth of one cluster, as opposed to many clusters developing in parallel as in the first case. The process, as described by the snapshots in the bottom panel of figure 5.5, occurs within a very narrow pressure range between 17.5 kPa and 17.8 kPa, thus corresponding to an abrupt condensation.

5.3.2. Effect of water on carbon dioxide adsorption in Maxsorb MSC-30

Before we turn our attention to more complex, multi-component systems, first, it is important to explore in more detail co-adsorption of carbon dioxide and water under different conditions.

Table V.3. Henry's constants of adsorption calculated for water and carbon dioxide at three different temperatures.

T (K)	K_H(mol/kg/Bar)	
	CO_2	H_2O
298	1.96	23.49
313	1.34	10.68
323	1.07	6.72

It is illustrative to begin this section by comparing the Henry's constants of adsorption in zero loading regime for pure component carbon dioxide and water at three different temperatures (298, 313 and 323 K). These constants, summarized in table V.3, indicate much stronger interaction of water molecules with the porous structure (or to be more precise with the functional groups), which can explain stronger adsorption of water compared to other gases as will be seen in the next section.

Nevertheless, from the appearance of the water isotherms, Maxsorb behaves as a typical hydrophobic material. This is a result of even stronger interaction between molecules of water itself, compared to the interaction with the porous material, particularly once the polar groups on the structure of the carbon, already saturated with water molecules, become unavailable.

The zero loading (this is the regime reflecting the most favorable interactions) isosteric heat of adsorption (calculated using the zero loading Henry constants above) is estimated to be 40.13 kJ/mol, which is comparable to the latent heat of condensation for water (45 kJ/mol). This result, in line with the data reported in literature (27, 47-49), is consistent with the fact that the formation of water clusters starts at very low pressures.

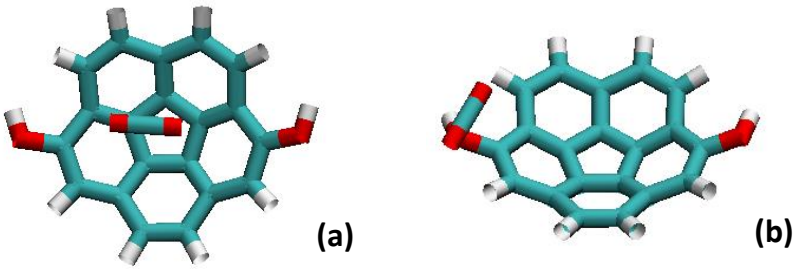

Figure 5.6. Minimum potential energy configurations for a single carbon dioxide molecule in the presence of a single platelet. Panel (a) shows global energy minimim, panel (b) shows local energy minimum in the vicinity of the surface group.

In figure 5.6 (a) and (b) we show the locations corresponding to the energy minima of a single carbon dioxide molecule interacting with a single platelet. Panel (a) corresponds to the global minimum and the location of this minimum is not on the edges but at the core of the structural element. Panel (b) shows instead an example of local energy minimum for carbon dioxide in the vicinity of a hydroxyl group. Comparisons of the energy contributions for the two cases, provided in table V.4, shows that the global energy minimum is dominated by the Lennard-Jones contribution, emanating from the carbon atoms of the platelet. In the vicinity of the surface group, Coulombic term increases substantially (about eight times), but this is not enough to compensate for the weaker LJ interactions at the edge of the platelet.

Table V.4. Solid-fluid interaction energies calculated for preferential positions of water and carbon dioxide molecules in the proximity of one platelet. Energies are expressed in kJ/mol.

CO_2 global energy minimum		**CO_2 local energy minimum**	
LJ	-15.03	**LJ**	-4.6
Coulombic	-0.92	**Coulombic**	-7.21
Total	-15.95	**Total**	-11.81

The global energy minimum for carbon dioxide is significantly lower (in a sense that is the interaction is weaker) compared to the water molecule.

We now consider binary mixtures with different molar content of water at 313 K, with the aim of studying the effect of small amounts of water in pre-combustion conditions.
As we specified before, in the case of pre combustion the total pressure of the streams ranges between 30 and 55 Bar at 313 K and the water molar percentages range on average between 0.2 and 1% (5, 6).

When considering the effect of water we must take into account that when water reaches its saturation pressure (7.33 kPa at 313 K) the vapour in the stream condenses: each molar percentage of water in the stream can therefore be associated to a threshold value of the total pressure, which must not be reached in order not to have condensation. If we make the approximation of considering the mixture as ideal, the threshold values of the total pressure for different molar percentages of water are reported in table V.5.

Table V.5. Threshold values of the total pressure to avoid water condensation in streams containing different molar percentages of water at 313 K.

Water molar %	**Threshold pressure of mixture (Bar) at 313 K**
0.1	73.3
0.2	36.6
0.5	14.6
0.75	9.8
1	7.3

As can be seen from the table, for molar percentages of water equal to 0.5 and higher the total pressure of the mixture is definitely lower than the pressures that normally should be involved in the pre combustion CO_2 capture process. This suggests that in these cases the water vapor might need to be removed in a preliminary stage. If the water content is 0.1%, instead, no condensation in the stream should occur during the pre-combustion phase; if the

concentration of water reaches 0.2% the total pressure of the stream should be kept under 36.6 Bar.

The upper pressure limit for the isotherms shown in figure 5.7 does not exceed the corresponding threshold value for a particular water content; therefore for water molar percentages higher than 0.5 no isotherms will be shown.

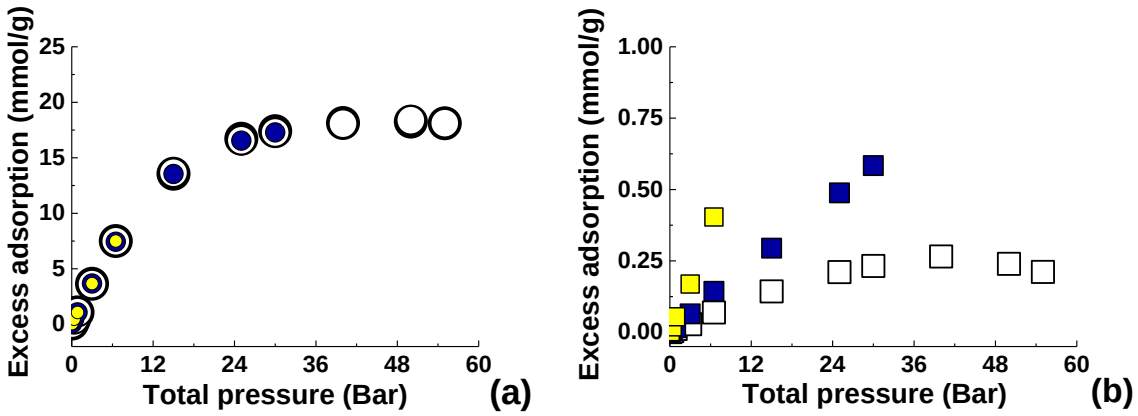

Figure 5.7. CO_2 (graph (a)) and H_2O (graph (b)) excess adsorption isotherms for the CO_2/H_2O mixture at different contents of water. Black symbols are for 0%; white symbols are for 0.1%; blue symbols are for 0.2%; yellow symbols are for 0.5%.

From figure 5.7 (a), water does not seem to have a particularly big impact on the adsorption of carbon dioxide in the ranges of pressure our consideration.The isotherms in graph (b) confirm the results shown in graph (a); the amount of water adsorbed remains insignificant under the conditions of interest and the preferentially adsorbed species is CO_2. This is predominantly due to the overwhelming excess of carbon dioxide in the binary mixture. When the molar content of water is as low as 0.1% the shape of the isotherm indicates that at the higher pressures carbon dioxide even displaces the adsorbed water molecules.

In section 5.3.1 we have investigated the tendency of water to cluster during the pure component adsorption on Maxsorb, and we have shown that clusters start to appear from very low pressures (at about 0.63 kPa). This behavior is consistent with the results previously

reported in the literature (27, 34, 39, 42) and can be attributed to the presence of the surface functional groups.

We now intend to show that water keeps the tendency to cluster even when it is a minor component in a binary mixture, mainly composed of carbon dioxide. For this we consider an example of a binary mixture with the molar composition CO_2/H_2O=99/1 at 313K. The range of pressures we consider exceeds the specified threshold in table V.5 and therefore this case is not relevant for practical process design. Absolute adsorption isotherms for carbon dioxide and water in this mixture up to total pressure of 55 Bar are shown in figure 5.8.

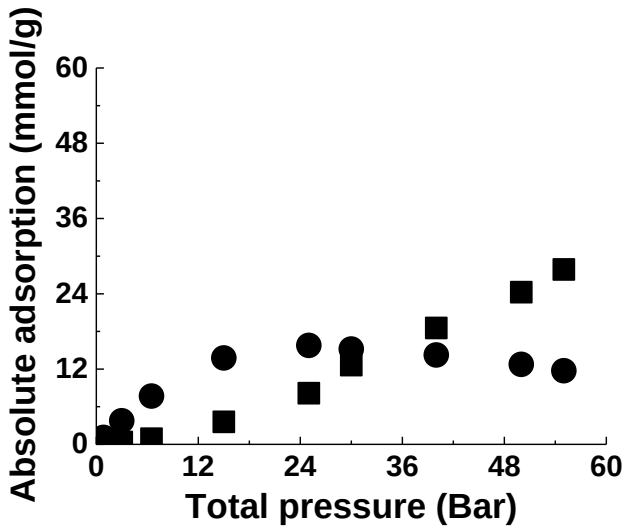

Figure 5.8. Absolute adsorption isotherms for the binary mixtures CO_2/H_2O containing 1% of water. Circles are for CO_2, square symbols are for H_2O.

Given the range of pressure under consideration and given the higher content of water, the situation presented above is very different from the situation shown in figure 5.7: as the pressure increases, water starts to condense in the pores of the material and to compete with carbon dioxide. Above 30 bar water becomes the preferentially adsorbed species, while the amount of adsorbed carbon dioxide starts to decrease.

In figure 5.9 we show the radial distribution functions (RDFs) for water (graph (a)) and carbon dioxide (graph (b)) for different pressure points in the isotherms simulated at 313 K. In the case of water we show the O-O RDF, while for carbon dioxide we show the C-C RDF.

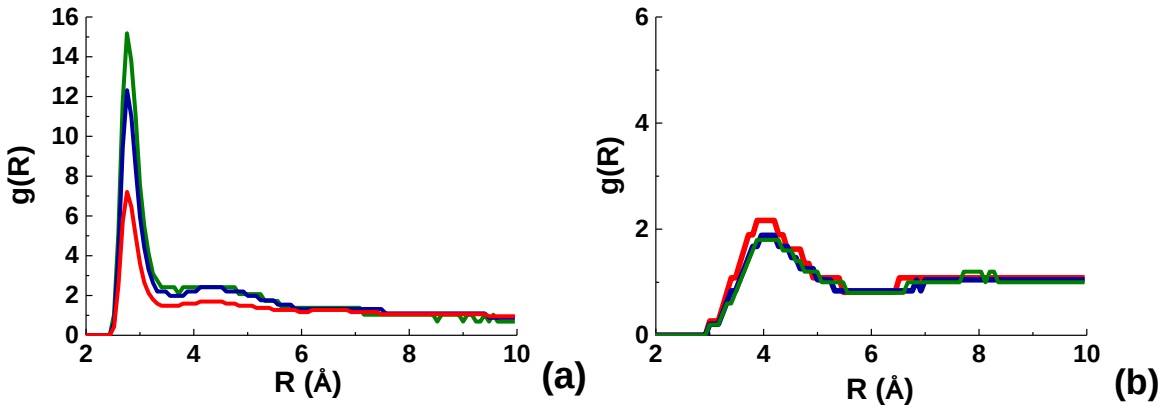

Figure 5.9. (a): radial distribution function for water (O-O RDF); (b): radial distribution function for carbon dioxide (C-C RDF) in CO_2/H_2O=99/1 mixture at 313 K. Green lines correspond to the total pressure of the system of 25 Bar, blue lines correspond to 30 Bar and red lines correspond to 55 Bar, respectively.

In the case of H_2O the peaks in the RDFs appear similar in shape to those reported for bulk water (including the tip4p model) at intermediate densities (81, 82). The pronounced first peak can be seen simply as a manifestation of strong water-water interactions. We also note that even at the lowest water concentration (green line), the RDF for water starts to develop a second peak, indicating onset of more of a liquid-like structure. Carbon dioxide exhibits RDFs typical of low density gas and consistent with the results reported in the literature for supercritical CO_2, (83, 84).

The visualizations for the water clusters in the mixture, reported in figure 5.10, show that the water molecules start to cluster at a total pressure of 3 Bar, which corresponds approximately to the partial pressure of 3 kPa.

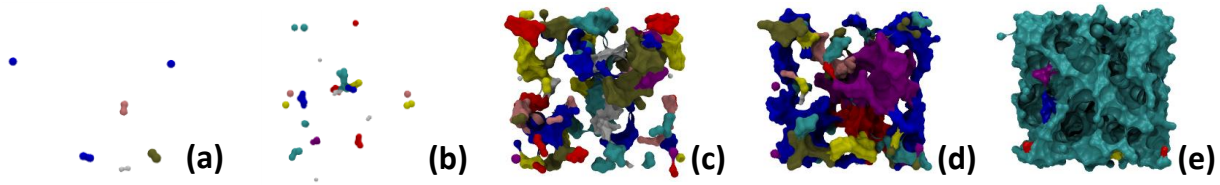

Figure 5.10. Visualizations for water clusters in the mixture CO_2/H_2O=99/1 simulated at 313 K and corresponding to the total pressure of the system of 3 (a), 6.5 (b), 25 (c), 30 (d) and 55 (e) Bar. Colours correspond to different clusters, based on the positions of oxygen atoms of water molecules.

Similar to the pure-component case, condensation is a consequence of formation and growth of different clusters, which eventually merge into a single one.

The results shown so far suggest that water and carbon dioxide might preferentially occupy different sub regions in the porous space; as we mentioned before it is now accepted that the adsorption of water in activated carbons starts with the formation of clusters in the proximity of heteroatoms or, more in general, of polar centres. At the same time, at low pressures carbon dioxide prefers the curved surface of the platelet, as shown by the energy minimization analysis. Therefore, at least at lower pressures two species may co-adsorb without much influence on each other.

To validate our hypothesis we calculated solid-fluid radial distribution functions for the same CO_2/H_2O mixture considered above, both for water and carbon dioxide. For the adsorbate species, the RDFs were calculated considering the same atoms as for the fluid-fluid RDFs before, while for the adsorbent we used oxygen atom belonging to the hydroxyl group. The results are presented in figure 5.11, which shows the solid-water RDF in graph (a) and the solid-carbon dioxide RDF in graph (b). In both cases the pressures of 25 (green lines) and 55 Bar (red lines) are considered. These are not realistic pressures as under these conditions the bulk water should condense, however we use these pressure values simply to create systems with high loading of water, with the structural properties being of primary interest.

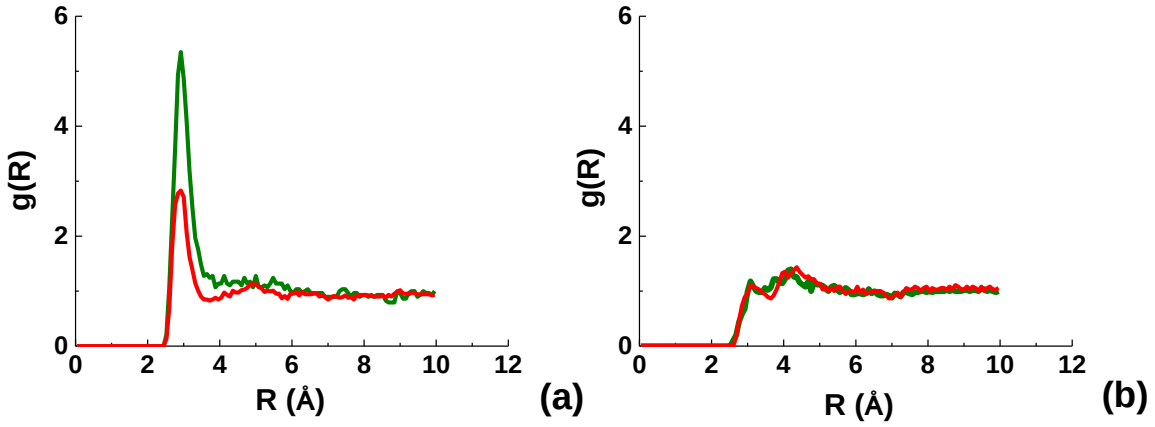

Figure 5.11. Solid-fluid radial distribution functions for adsorbed water (graph (a)) and carbon dioxide (graph (b)) in the system with CO_2/H_2O=99/1 composition at 313K. The functions were calculated considering oxygen atom for water, carbon atom for carbon dioxide and oxygen atom belonging to the hydroxilic group for the adsorbent. Green lines are for 25 Bar total system pressure and red symbols are for 50 Bar total system pressure.

From the figure above we can clearly notice pronounced peaks for the solid-water RDFs at distances below 3.5 Å (left side panel), with the effect being more pronounced at the lower pressure; RDFs for carbon dioxide do not feature any pronounced peaks, indicating essentially no density variations around hydroxyl groups of platelets. The difference in pressure does not seem to have an important effect for carbon dioxide either. These results reinforce the idea that water and carbon dioxide preferentially occupy different sub-regions in the porous space; indeed, water molecules prefer proximity of heteroatoms or, more in general, of polar centres, whereas carbon dioxide prefers the curved surface of the platelet, as shown by the energy minimization analysis. Therefore, under conditions of interest two species may co-adsorb without much influence on each other. At very low pressures, the last statement is a result of simply very low number of molecules present (we will comment on this later); the RDF analysis here however is performed on systems containing substantial number of molecules of each species. To better clarify our statement, in table V.6 we show, for both the systems to which figure 5.11 is referred, the number of molecules for each adsorbed species per unit cell, together with the solid-fluid and fluid-fluid interaction energies, expressed in kJ per mol of adsorbed species. Green rows correspond to the 25 Bar system (green lines in figure 5.11), while red rows correspond to the 50 Bar system (red lines in figure 5.11).

Table V.6. Number of molecules, fluid-fluid and solid-fluid interaction energies for the systems described in figure 5.11. Energies are in kJ per mole of adsorbed species, green rows refer to the 25 Bar system (green lines in figure 5.11) and red rows correspond to the 50 Bar system (red lines in figure 5.11).

H_2O MOLEC	H_2O-H_2O COUL	H_2O-H_2O LJ	H_2O-ADS COUL	H_2O-ADS LJ
889.52	-30.41	5.4	-10.46	-2.28
1964.89	-34.1	6	-8.51	-2.49
CO_2 MOLEC	CO_2-CO_2 COUL	CO_2-CO_2 LJ	CO_2-ADS COUL	CO_2-ADS LJ
1070.51	-1	-3.1	-2.09	-11.08
826.54	-0.9	-2.7	-1.2	-11.66

In both cases we can notice that the fluid-fluid interaction energies are higher (much higher in the case of Coulombic interactions) for water compared to CO_2, which is responsible for the tendency of water to cluster; also, as observed before, in the case of the solid-fluid interaction the Coulombic contribution definitely prevails over the Lennard-Jones contribution for water, while the trend is reversed for CO_2. This suggests that the presence of oxygen containing polar groups, their concentration and location, will have a much more profound effect on the adsorption of water than on the adsorption of CO_2. This statement however needs to be revisited for the case of amine-type surface groups.

5.4. Simulation of Carbon Capture separation processes

5.4.1. Post combustion Carbon Capture

The main separation we will investigate in this case is between N_2 and CO_2. After consideration of the equimolar mixture case we will shift to a mixture of molar composition CO_2/N_2=10/90, more closely reflecting industrially relevant conditions, and then we will progressively add other, minor components to the system, to study ternary mixtures of CO_2, N_2 and O_2 (15/80/5) and quaternary mixtures of CO_2, N_2, O_2 and H_2O (15/75/5/5) with molar percentages of the components given in the brackets. All the simulations are at 323 K, as this temperature can be considered representative for the post-combustion processes. To make

presentation more compact, we will predominantly focus on CO_2/N_2 selectivity in various systems, while the actual isotherms will be shown for illustration purposes for several selected cases only. The full set of adsorption isotherms for the systems under considerations is shown in section A12 in the Appendix, which also includes an indication on the statistical error on the simulations. The same criterion will be followed for the pre-combustion and sweetening of natural gas cases.

An example of excess adsorption isotherms for a ternary mixture is shown on the left of figure 5.12, while on the right we summarize selectivity behavior for binary and ternary systems as a function of pressure. The lowest value of pressure considered in figure 5.12 (b) is 0.1 Bar, as pressures around 0.1-0.15 Bar have been recognized as a reasonable lower limit for the desorption processes involving flue gas separations (3, 85, 86).

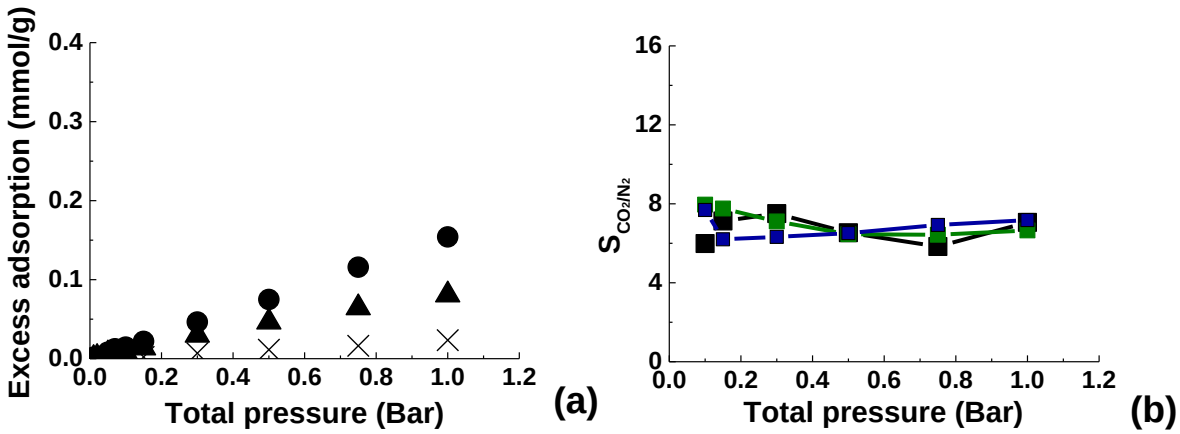

Figure 5.12. (a): Excess adsorption isotherms for the mixture $CO_2/N_2/O_2$=15/80/5. Circles are for CO_2, triangles are for N_2, crosses are for O_2. (b): carbon dioxide/nitrogen selectivities as a function of pressure for binary mixture CO_2/N_2=50/50 (black squares), binary mixture CO_2/N_2=10/90 (green squares) and ternary mixture $CO_2/N_2/O_2$=15/80/5 (blue squares). Lines are for eye guidance only.

In general, all systems in the figure exhibit selectivity values between 6 and 8. In particular, we notice that for the binary mixture (black and green lines and symbols, respectively) a change in the molar composition has almost no effect on the selectivity. Addition of oxygen to the mixture also seems to have minor effect on the overall CO_2/N_2 selectivity.

Zero loading, intrinsic CO_2/N_2 selectivity, obtained using equation *V.2* is 6.59 at 323 K; this value seems to be consistent with the values calculated on average for all the post combustion mixtures.

We now compare the selectivities we have calculated with the data reported in literature for other materials in the context of the same separation and in similar conditions.

As expected, zeolites tend to show much higher values of selectivity for carbon dioxide, given the presence of ionic centres in their structure: for example the values of CO_2/N_2 selectivity evaluated by Bae et al. (87) using IAST for a mixture containing 0.15 Bar of CO_2 and 0.75 Bar of N_2 at 313 K are respectively 250 and 310 for zeolites Ca-A and Na-X. Also, selectivities estimated for zeolite 5A and for zeolite 13X from pure component isotherms at ambient temperature are respectively 61.8 and 86.2 (85, 88, 89). These zeolites have indeed been considered among the top candidates for CO_2 capture from flue gas in the assessment recently made by Bae and Snurr (85), based on consideration of different parameters.

In the case of the MOFs which have been considered applicable for CO_2 capture from flue gas the values of selectivity calculated using IAST all tend to be higher than 20 at room temperature (6, 90) (with $[Zn_2(bttb)(py\text{-}CF_3)_2]$ reaching the value of 41 at 17.5 Bar (91), for example); this is confirmed also in the work by Bae and Snurr (85), who identified among the most promising candidates ZIF-79 and Co-carborane MOF-4b (with estimated CO_2/N_2 selectivities of 21.3 and 154 respectively (92, 93)).

As for other activated carbons, the values of selectivity are generally lower compared to MOFs and zeolites. For example, the selectivity reported for activated carbon AX21 with respect to the equimolar mixture at 293.1 K up to 1 Bar ranges approximately between 6 and 7, as calculated by Kluson and Scaife (21) by applying IAST to the pure component experimental isotherms. For Norit R1-extra the selectivity estimated from the experimental pure component isotherms for the mixture CO_2/N_2=10/90 at 298 K and total pressure of 1 Bar is 10.7 (85).

Broadly speaking, the selectivities we have calculated seem to be in line with the values reported in the literature for different activated carbons, and given that our simulations have been run at higher temperature we can expect Maxsorb to be more selective than AX21 when

the two materials are considered under the same conditions. This result is consistent with the higher concentration of oxygenated groups present in Maxsorb.

Besides performing calculations based on the experimental data, in the same work Kluson and Scaife have also predicted CO_2/N_2 selectivity under the same conditions using a slit pore model and non-local density functional theory. Before making a comparison between the results of our simulations and these reference data we note that, as shown in the Appendix (figure A8), the geometric pore size distribution for the Maxsorb model shows that the most relevant pores have dimension between 0.5 and0.75 nm, which correspond to the slit pore widths of 0.85-1.10 nm as measured between the centers of the atoms of the walls.

The average selectivity calculated by Kluson and Scaife was enhanced in pores of 0.8 to 1 nm wide, ranging between 8 and 10. These values are higher than the corresponding experimental values for AX21. A similar study was presented by Cracknell et al. (20), which considered competitive adsorption of CO_2/N_2 and CO_2/CH_4 equimolar mixtures at 313.15 K and up to about 50 Bar, using GCMC simulations in carbon slit pores with widths ranging between 0.8 and 1.2 nm. The selectivities they calculated ranged between about 8.4 and 12.5 at pressures approximately between 0.1 and 0.8 Bar for the 0.8 nm pore, while they ranged approximately between 3.8 and 4.9 for pressures of about 0.1 and 0.6 Bar in the 1.2 nm pore. Overall, the selectivities we calculated seem consistent with the selectivities reported in both simulation studies.

From figure 5.12, the values of selectivity remain relatively independent of the composition of the mixture and pressure; some variation at low pressure is expected as the number of nitrogen molecules adsorbed is small and selectivity becomes subject of large fluctuations and statistical error. For example, at the total pressure of 0.1 Bar for the CO_2/N_2 equimolar mixture the error in selectivity reaches 44.6 %, while at 1 Bar the error is approximately 12.8%. In the work by Kluson and Scaife selectivity for the same species as a function of pressure also remained constant after an initial increase (21).

Figure 5.13 shows the effect of a relatively small amount of water (5%) on co-adsorption of carbon dioxide, nitrogen and oxygen. Water saturation pressure at 323 K is 12.26 kPa and the total pressure of the mixture, at which water should start to condense (2.45 Bar) is outside of the pressure range considered here. In panel (a) on the left we report the excess adsorption

isotherms for the mixture with the composition $CO_2/N_2/O_2/H_2O$=15/75/5/5, while in panel (b) on the right the CO_2/N_2 selectivities are shown as a function of pressure for the same mixture (red symbols and lines) in addition to the selectivities previously shown in figure 5.11(b).

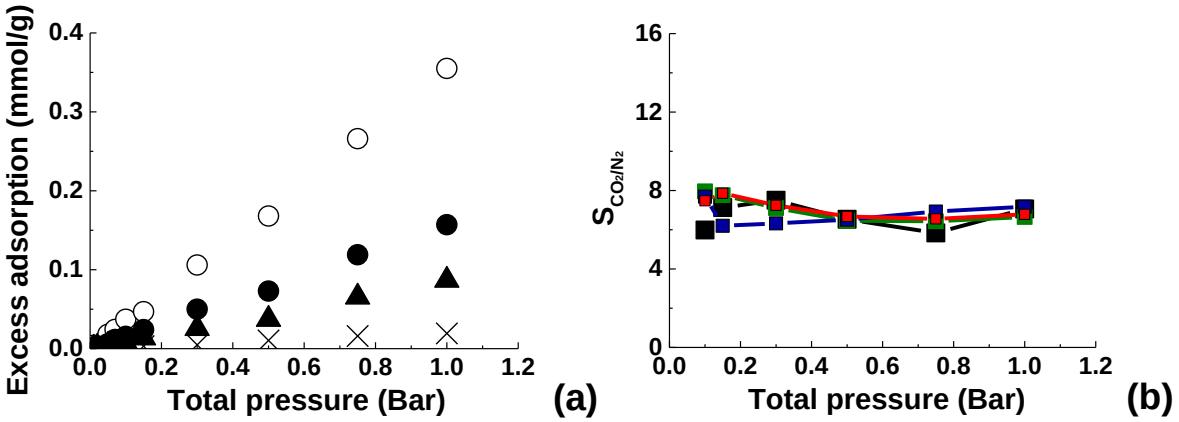

Figure 5.13. (a): Excess adsorption isotherms for the mixture $CO_2/N_2/O_2/H_2O$=15/75/5/5. Filled circles are for CO_2, triangles are for N_2, cross shaped symbols are for O_2, empty circles are for H_2O. (b): carbon dioxide/nitrogen selectivities as a function of pressure for binary mixture CO_2/N_2=50/50 (black squares), binary mixture CO_2/N_2=10/90 (green squares), ternary mixture $CO_2/N_2/O_2$=15/80/5 (blue squares) and quaternary mixture $CO_2/N_2/O_2/H_2O$=15/75/5/5 (red squares). Lines are for eye guidance only.

The effect of water on the CO_2/N_2 separation appears on average quite small, in the sense that the adsorbed amounts of carbon dioxide, nitrogen and oxygen shown in figure 5.13 (a) have not changed significantly, compared to the result shown in figure 5.12 (a). The effect of water is minimal also on the CO_2/N_2 selectivities, as shown in figure 5.13 (b). It is clear that the amount of adsorbed water exceeds all the other adsorbed species, so that water becomes the preferentially adsorbed species.

These results altogether suggest that none of the species present in the mixture must compete with water for the occupancy of sub-regions of the porous space; as has been elucidated in the previous section, water molecules fill the regions in the neighborhood of the functional groups, while the other species actually prefer other regions of porous space.

Nonetheless, we must consider that in the system in figure 5.13 the number of adsorbed molecules is very small: at the total pressure of 1 Bar the system contains 25 molecules of

water and 12 molecules of carbon dioxide per unit cell; given that the number of functional groups per cell is 500 (much higher than the number of adsorbed molecules for each species), this means that, at this total pressure, one fluid is not likely to have any influence on the other, as there will be no competition for the occupation of the space around the functional groups for example. This case is different from the cases described in table V.6, in which the numbers of adsorbed molecules for each species are higher than the number of functional groups, which means that, despite preferentially occupying different positions, the molecules of one species do have an effect on the molecules of other, in the sense that they end up competing for the occupation of the porous space. This is clearly not the case for the system in figure 5.13, and this is also why water does not show any influence on the other adsorbed species.

Overall, in terms of CO_2/N_2 selectivity Maxsorb does not come across as the best candidate for CO_2 capture from flue gas, especially because key advantages of this material, such as high adsorption capacity at high pressures cannot be exploited in this context.
As for the humidity in the stream, however, given the low adsorbed densities for all the species involved, this does not affect adsorption of carbon dioxide and carbon dioxide-nitrogen separation factors under conditions of interest.

5.4.2. Pre-combustion Carbon Capture

In this case the main separation is between carbon dioxide and hydrogen. CO_2 capture from pre combustion streams can probably be considered as an easier problem compared with the separation of post combustion streams. This is due to the much higher concentration of carbon dioxide, much higher pressures involved and weak adsorption of hydrogen, compared to carbon dioxide, leading to high selectivity under a variety of conditions.

All simulations have been run at the temperature of 313 K. We consider equimolar binary mixture of carbon dioxide and hydrogen, CO_2/H_2=40/60 case, and multi-component mixtures, which include small amounts of H_2S and CO, specifically ternary mixture $CO_2/H_2/H_2S$=39/60/1 and quaternary mixture $CO_2/H_2/H_2S$/CO=38/60/1/1, respectively.

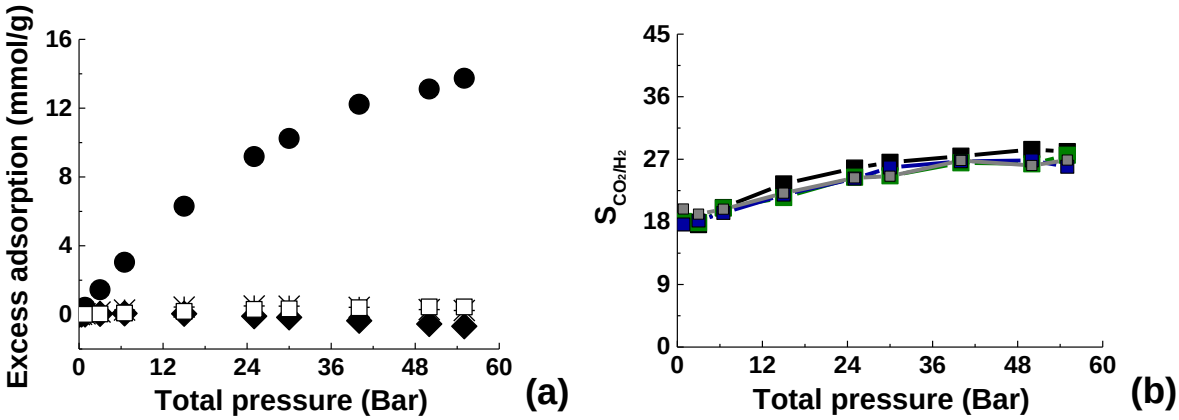

Figure 5.14. (a): Excess adsorption isotherms for the mixture $CO_2/H_2/CO/H_2S$=38/60/1/1. Filled circles are for CO_2, diamonds are for H_2, stars are for CO, and empty squares are for H_2S. (b): carbon dioxide/hydrogen selectivities as a function of pressure for binary mixture CO_2/H_2=50/50 (black squares), binary mixture CO_2/H_2=40/60 (green squares), ternary mixture $CO_2/H_2/H_2S$=39/60/1 (blue squares) and quaternary mixture $CO_2/H_2/H_2S/CO$=38/60/1/1 (grey squares). Lines are for eye guidance only.

These results are summarized in figure 5.14. Firstly, as an example, panel (a) shows adsorption isotherms for the quaternary mixture $CO_2/H_2/CO/H_2S$ case. The excess adsorption for hydrogen appears to be negative, and this has been observed in all mixtures under consideration in this section, starting from the binary equimolar case (all isotherms are reported in section A12 in the Appendix file). This effect, as shown in the Appendix (section A10.1), is not related to the particular model adopted for hydrogen and means that the presence of Maxsorb favours carbon dioxide so much that the density of hydrogen adsorbed is lower than what would be present in the bulk mixture. It is quite clear that the separation CO_2/H_2 should be reasonably efficient and not particularly affected by the presence of carbon monoxide and hydrogen sulfide.

The efficiency of the carbon dioxide separation is confirmed by the results in figure 5.14 (b), which shows carbon dioxide-hydrogen selectivities as a function of pressure for all cases. The lowest pressure considered is 0.85 Bar, which is consistent with the lower bound of 1-1.5 Bar generally reported for the PSA processes involving high pressures (85, 94). Similarly to the post combustion case the selectivities are not particularly affected by the composition of the

mixture, and the presence of the minor components in the stream does not have a major effect either.

Also, the general tendency is a slow increase in the separation factors with pressures up to a more or less pronounced plateau. This can be contrasted by literature studies showing variation in selectivity trends depending on the materials and conditions. For example, an increase in CO_2/H_2 selectivity with pressure has been attributed to the cooperative CO_2-CO_2 interactions becoming predominant (86, 95), while a decrease in selectivity at even higher pressures has been attributed to an entropic effect, which favours adsorption of smaller hydrogen molecules (86, 96). A substantial decrease in selectivity at low pressures has instead been attributed to the strongest adsorbing sites becoming unavailable as the loading of CO_2 increases (86, 95).

In all cases presented in figure 5.14 (b) the selectivities start from values around 18 and reach values over 25 (over 27 for the equimolar mixture); these results are consistent with the zero loading selectivity in the Henry's law regime, for which a value of 17.82 was obtained.

We also notice that, apart from the lowest pressure range, the selectivities tend to be much more stable, showing lower degree of scattering, compared to the results for the post combustion separations; this is consistent with the error analysis for the selectivities in this case: for the mixture CO_2/H_2=40/60 error in selectivity is estimated at 14.4% at 0.85 Bar, 4.49% at 6.5 Bar and 2.7% at 55 Bar.

For comparison with the data reported in the literature we refer to the recent studies by Herm et al. (16) and by Cao and Wu (22): in the former, experimental study, the authors consider binary CO_2/H_2 mixture with compositions and under conditions relevant to the pre combustion capture and use IAST to compare the behavior of selected MOFs to the behavior of some zeolites and activated carbons considered as benchmark materials; the latter study employs GCMC simulations of CO_2/H_2 binary mixtures at different temperatures in carbon slit pores of different sizes.

In agreement with the results reported for the post-combustion case, in the study by Herm et al. the highest selectivities for the CO_2/H_2=40/60 mixture at 313 K up to 40 Bar is observed for zeolites and MOFs with exposed metal cation sites. Specifically, zeolite 13X and metal-organic framework Mg_2(dobdc) show selectivities respectively between 200 and 300 and between 300 and 600. These values of selectivities, however, appear to be well above the

typical values for other materials; for example metal-organic framework Cu-BTTri, which also shows exposed cation metal sites, has selectivity approximately between 25 and 37.5, while all other MOFs considered in the publication exhibit selectivities lower than 20 and, in some cases, lower than 10.

As for the activated carbons presented in the study, JX101 shows quite a high selectivity (approximately between 50 and 100) (15, 16), while the selectivity of BPL is approximately between 20 and 37.5 at 303 K (16, 18). Interestingly, in all cases reported by Herm et al. the selectivities tend to decrease or to remain constant with increasing pressure; this behavior differs from the trends we present in figure 5.13 and suggests that in our case the cooperative effect between carbon dioxide molecules seems to prevail, while in the reference cases mentioned above the effect of the strongly adsorbing sites becoming unavailable dominates or, at least, counterbalances the increased CO_2-CO_2 interaction, in particular for the materials featuring exposed metal sites.
Also, the selectivities we have calculated for Maxsorb are lower than the data reported for JX101, while they are similar with the values calculated for BPL.

From the work by Cao and Wu we consider as an example the CO_2/H_2 selectivities calculated for a mixture of composition CO_2/H_2=1/2 at 298 K between 10 and 55 Bar; the values range approximately between 12 and 27.5 in a pore of 0.89 nm in width. Given the differences in temperature of the systems, we conclude that our results are in a reasonable agreement with those from Cao and Wu.

We now consider the effect of small amounts of water on the adsorption of a quaternary mixture. Figure 5.15 (a) shows excess adsorption isotherms, while figure 5.15 (b) shows CO_2/H_2 selectivities for the quinary system $CO_2/H_2/CO/H_2S/H_2O$=38.8/59/1/1/0.2, together with the selectivities already shown in figure 5.14. The upper limit of the pressure we have now chosen is consistent with the threshold value reported in table V.5 for a mixture containing 0.2% of water (36.6 Bar).

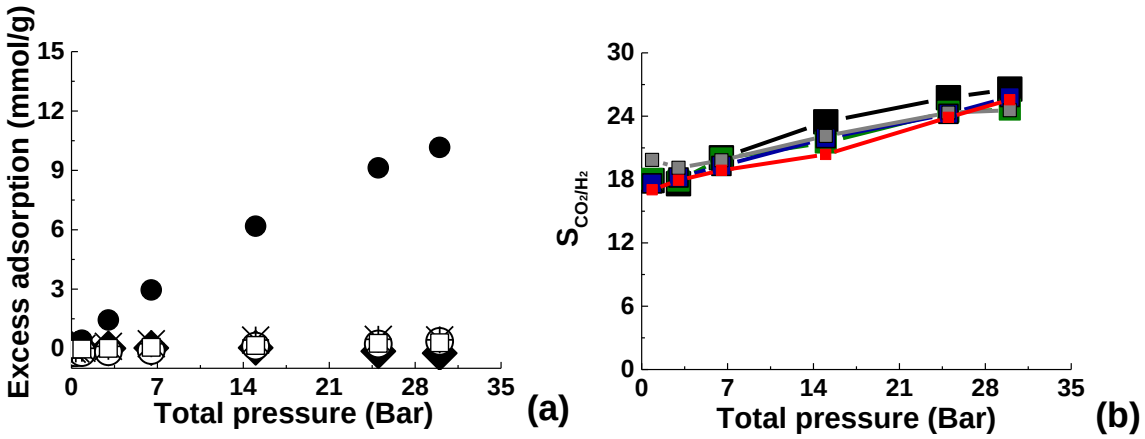

Figure 5.15. (a): excess adsorption isotherms for the mixture $CO_2/H_2/CO/H_2S/H_2O$=38.8/59/1/1/0.2 at 313 K. Filled circles are for CO_2, diamonds are for H_2, stars are for CO, empty squares are for H_2S, empty circles are for H_2O. (b): carbon dioxide/hydrogen selectivities as a function of pressure for binary mixture CO_2/H_2=50/50 (black squares), binary mixture CO_2/H_2=40/60 (green squares), ternary mixture $CO_2/H_2/H_2S$=39/60/1 (blue squares), quaternary mixture $CO_2/H_2/H_2S/CO$=38/60/1/1 (grey squares), quinary mixture $CO_2/H_2/CO/H_2S/H_2O$=38.8/59/1/1/0.2 (filled red squares, solid red line). Lines are for eye guidance only.

In the range of pressure we are considering water does not affect adsorption of other species. This is clear not only from figure 5.15 (a), in which the isotherms are almost identical to the ones shown in figure 5.14 (a), but also from figure 5.15 (b), in which the selectivities follow the general trend presented in figure 5.14 (b).

The results shown in this section suggest that Maxsorb, despite not being the most selective among the materials presented in literature, is worth further investigation for applications in pre combustion capture using adsorption. Again, selectivity is not the only parameter that needs to be considered in the development of an adsorption application. Other criteria such as high capacity at high pressure and the regenerability also need to be taken into account when assessing suitable materials. Maxsorb (and activated carbons in general) satisfies these criteria very well.

5.4.3. Sweetening of sour natural gas

In sweetening of sour natural gas the composition of the mixture and properties of the stream can vary substantially depending on the source of the fossil fuel. As a typical example we can consider a stream with molar percentage of CO_2 around 10–15% at temperatures between 10 and 40°C and pressures of about 68–75 Bar (7, 8).

In this case we will limit ourselves to the main separation between carbon dioxide and methane and therefore binary mixtures only.
Equimolar mixture of carbon dioxide and methane and a more realistic case of CO_2/CH_4=15/85 composition are considered at a temperature of 288 K and pressures up to 75 Bar.

Figure 5.16 (a) shows excess adsorption isotherms for the mixture CO_2/CH_4=15/85, while figure 5.16 (b) shows selectivities for both mixtures as a function of pressure. In this case the number of iterations per simulation point has been 60 million.

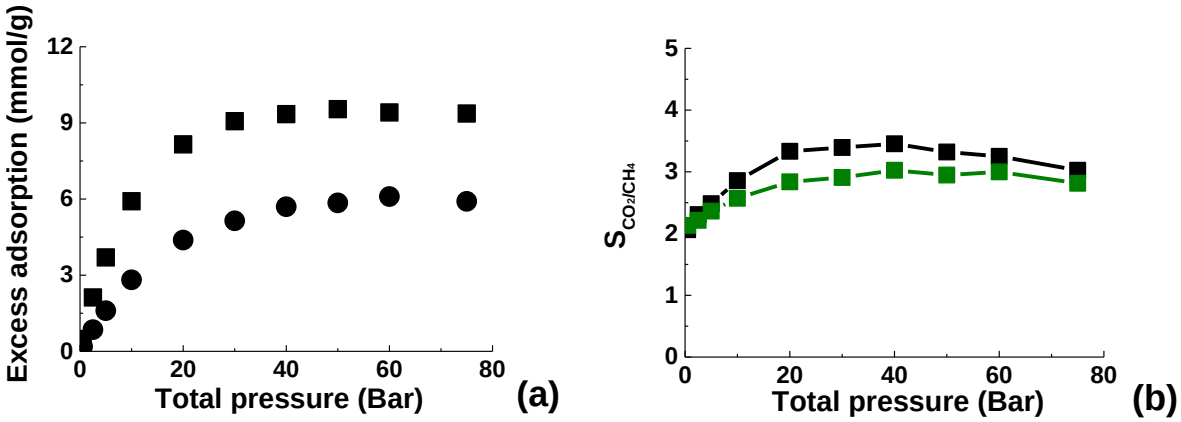

Figure 5.16. (a): Excess adsorption isotherms for the mixture CO_2/CH_4=15/85 at 288 K. Circles are for CO_2, squares are for CH_4. (b): carbon dioxide/methane selectivities as a function of pressure for binary mixture CO_2/CH_4=50/50 (black squares) and binary mixture CO_2/CH_4=15/85 (green squares). Lines are for eye guidance only.

From this figure, Maxsorb is selective towards CO_2, however the values of selectivity seem to be rather modest, between about 2 at lower pressures and not exceeding 4 at the maximum. In addition, selectivities for 15/85 mixture are uniformly shifted to somewhat lower values

compared to the equimolar case. Zero loading selectivity in the Henry's law regime is calculated to be 2.04, consistent with the results shown in figure 5.15 (b). The trend in the curves is similar to the trend observed in the case of pre combustion, and the error in the selectivities ranges from 23% at 0.5 Bar, to 4.65% at 10 Bar, and down to 2.3% at 75 Bar.

From the literature survey, many metal-organic frameworks have selectivities close to 5 for the CO_2/CH_4 equimolar mixture at ambient temperature (90). MOFs considered to be good candidates for this separation process exhibit selectivity values in the range between 4.5 and 30 (6), with the highest value (30) corresponding to $[Zn_2(bpdc)_2(dpni)]$ at 296 K and 18 Bar (97-99).

Selectivities estimated from pure component isotherms for 5A and 13X zeolites for CO_2/CH_4=10/90 mixture at ambient temperature at the pressure of 5 Bar are respectively 20 and 18.9 (85, 88, 89). For activated carbon Norit R1-Extra under the same conditions the estimated value is 4.75 (13, 85).

On average, then, Maxsorb is not the most selective among the materials reported in literature, but its selectivity appears to be within the range characteristic of many other adsorbents.In the studies by Cracknell et al. (20) and later by Kluson and Scaife (21) on carbon materials using slit pore model selectivities appear to be quite low: in the first case they span from 1.5 to 2.5 between 0 and 35 Bar in the whole range of pore sizes, while in the second study the average selectivity is approximately 2.

Interestingly, a comparison with the study by Furmaniak and co-authors (24) shows that the selectivities we have predicted for Maxsorb correspond to the lower limit of the selectivities they calculated for oxidized virtual porous carbons. This aspect might need further investigation.

5.5. Application of Ideal Adsorbed Solution Theory on the binary mixtures

Ideal Adsorbed Solution Theory (IAST) is a simple technique introduced by Myers and Prausnitz (17) to calculate the adsorption equilibria for components in a gaseous mixture, using only data for the pure component adsorption equilibria at the same temperature and on the same adsorbent. Here we recollect only the main aspects of the technique, and for an exhaustive description the reader is referred to the original publication (17). IAST is based upon the assumptions that the same surface area is available to all adsorbates, that the adsorbent is inert, and that the multicomponent mixture behaves as an ideal solution (such that the mean strength of interaction is equal between all molecules of the solution) at constant spreading pressure and temperature. At the heart of IAST there is the following equation, analogous to Raoult's law for vapour-liquid equilibrium:

$$p_{TOT} y_i = p_i^0 x_i \qquad \text{(V.3)}$$

where p_{TOT} is the total pressure of the mixture, y_i is the molar fraction of component *i* in the bulk phase, p_i^0 is the hypothetical pressure that the component *i* would exert as a pure adsorbed component at the same temperature and spreading pressure as those of the mixture and x_i is the molar fraction of component i in the adsorbed phase.

At adsorption equilibrium, all components in the mixture must have the same spreading pressure, which can be expressed as:

$$\frac{\pi_i}{RT} = \int_0^{p_i^0} \frac{n_i^0(p)}{p}\, dp \qquad i = 1, 2, \ldots, N \qquad \text{(V.4)}$$

where π_i is the spreading pressure of component *i*, T is the temperature, $n_i^0(p)$ describes the pure component equilibrium capacity as a function of pressure and p_i^0 is described as for equation (V.3) .

The function $n_i^0(p)$ must be specified by fitting a continuous function to a discrete set of adsorption data obtained over a finite range of pressures. As mentioned in Chapter 2, in this work Toth equation (100, 101) has been applied for the fitting of the high pressure simulated isotherms (pre combustion and sweetening of sour natural gas conditions), while for the low pressure data (post combustion conditions) the use of Henry's type isotherms has been sufficient.

Solution of equation (V.4) allows the calculation of p_i^0 and this allows the calculation of the molar fraction x_i through equation (V.3). By assuming ideal mixing at constant spreading pressure and temperature, the total amount adsorbed, n_T, is related to the molar fractions x_i of the single components in the adsorbed phase and to the amounts of pure components $n_i^0(p_i^0)$ that would be adsorbed at the pressures p_i^0 by the equation (calculated according to the functions that describe the pure component isotherms):

$$\frac{1}{n_T} = \sum_{i=1}^{N} \left[\frac{x_i}{n_i^0(p_i^0)} \right] \tag{V.5}$$

with the constraint:

$$\sum_{i=1}^{N} x_i = 1 \tag{V.6}$$

This allows the calculation of the actual number of moles n_i adsorbed of each component in the mixture, given that

$$n_i = x_i n_T \tag{V.7}$$

We now present the results of the application of IAST to the main separations involved in the CO_2 capture processes we have examined in the previous sections and compare them with the results of the direct simulation of the mixtures. In all cases the results of IAST are

represented using empty symbols, while the results of the direct simulations are shown as filled symbols.

Figure 5.17 shows data for the equimolar binary mixture CO_2/N_2 (graph (a)) and for the mixture of molar composition 10/90 (graph (b)), both in post combustion conditions. Figures 5.18 and 5.19 show results for pre-combustion and sweetening of sour natural gas conditions respectively. Similarly to figure 5.17, in both cases graphs (a) show results for the equimolar mixture, while graphs (b) show results for a more realistic composition: for figure 5.18 this is CO_2/H_2 = 40/60 and for figure 5.19 this is CO_2/CH_4 = 15/85.

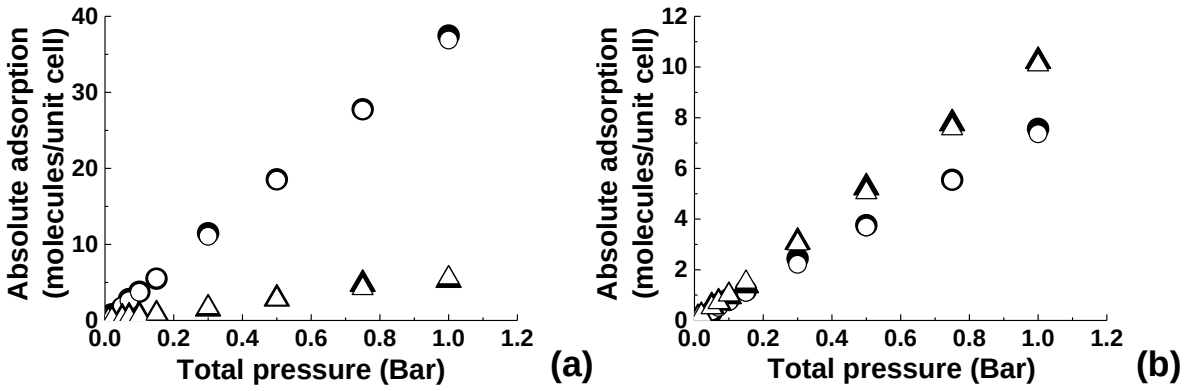

Figure 5.17. Comparison between the results of IAST (empty symbols) and the results of the direct simulation (filled symbols) of the binary mixtures CO_2/N_2=50/50 (graph (a)) and CO_2/N_2 = 10/90 (graph (b)) at 323 K. Circles represent carbon dioxide and triangles represent nitrogen.

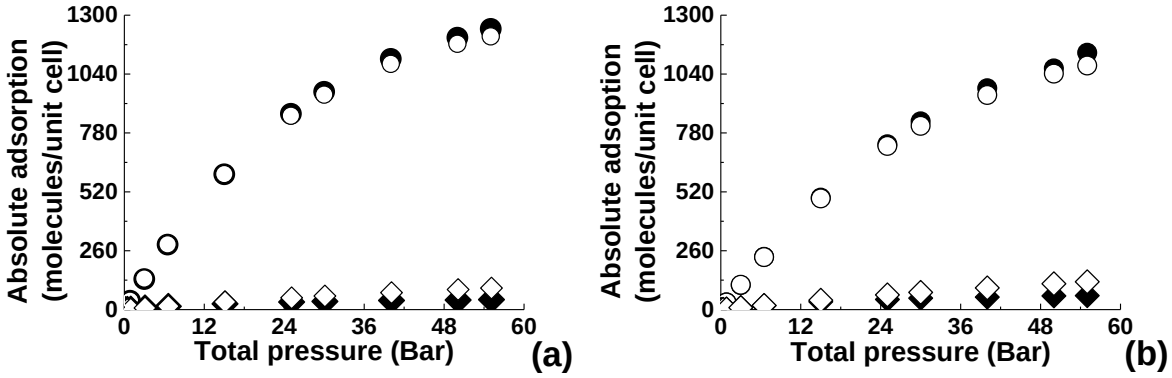

Figure 5.18. Comparison between the results of IAST (empty symbols) and the results of the direct simulation (filled symbols) of the binary mixtures CO_2/H_2=50/50 (graph (a)) and CO_2/H_2 = 40/60 (graph (b)) at 313 K. Circles represent carbon dioxide and diamonds represent hydrogen.

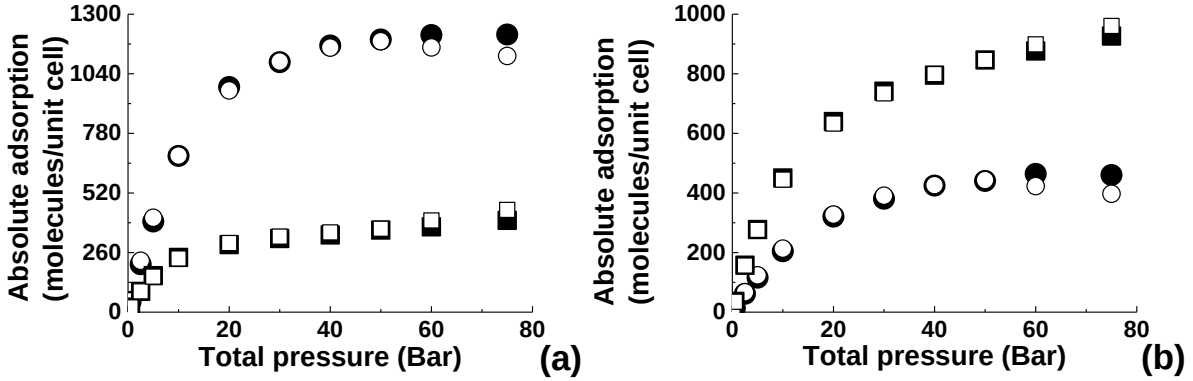

Figure 5.19. Comparison between the results of IAST (empty symbols) and the results of the direct simulation (filled symbols) of the binary mixtures CO_2/CH_4=50/50 (graph (a)) and CO_2/CH_4 = 15/85 (graph (b)) at 288 K. Circles represent carbon dioxide and squares represent methane.

From the figures above it is clear that for the separations under consideration IAST agrees very well with the direct simulations of the mixtures. We can only notice a slight deterioration in the accuracy at the highest pressures, at which the dissimilarities of the adsorbate molecules may have a more important effect.

In the case of the binary mixtures containing water IAST cannot be successfully applied, because in the ranges of pressure under consideration water as a single component would condense.

5.6. Conclusions

The purpose of this chapter was to investigate the behaviour of high surface area activated carbons as adsorbents in CO_2 capture separations, using the model developed in Chapter 4. In particular, we have used GCMC simulations to study separation of multi-component mixtures involved in the pre and post combustion processes and in sweetening of sour natural gas, using realistic temperature and pressure conditions. For the cases of pre and post combustion we have also considered the presence of minor components in the mixture. These aspects are particularly important, since multi-component adsorption data is scarce and difficult to obtain experimentally.

Our approach is mostly based on the analysis of the simulated isotherms and focuses on the selectivity shown by the adsorbent for CO_2 over the other main component of each mixture. We are aware that more aspects should be considered for the evaluation of adsorbents in the context of CO_2 capture, but nonetheless selectivity gives a good indication of the efficiency of the separations.

Another aspect we take into account is the effect of water on the separations under consideration, given that humidity may have a great impact on the efficiency and the cost of the processes.

Our results for high surface area activated carbons predict selectivities below the average established for most of the other materials in the case of post combustion separation; in the case of sweetening of sour natural gas the predicted selectivities are also quite low but in line with the average for activated carbons in general. In the case of pre combustion Maxsorb shows a reasonable selectivity performance, even though it is not the highest reported in literature. This result suggests that high surface area activated carbons are worth further

investigation for this type of separation, especially given that other parameters such as material cost and adsorption capacity would rank Maxsorb very favorably.

The efficiency in both pre- and post-combustion separations does not appear to be affected by the concentration of water vapours in the stream, as long as the total pressure is kept below the threshold value, after which water condensation would occur in the bulk stream. In the case of post combustion this lack of influence on behalf of water is also due to the low number of adsorbed molecules for each species, which implies a lack of competition for occupation of the porous space.

We also looked in more detail into the behavior of water as an adsorptive, both as a pure component and as a minor component in the presence of carbon dioxide. In either case the model predicts the peculiar behavior of water in activated carbons, i.e. the tendency to cluster and to interact with polar centers through hydrogen bonds. The tendency to form hydrogen bonds is confirmed by the energy minimization studies. These studies also revealed preferential locations of carbon dioxide and water molecules on a single platelet: while CO_2 molecules locate in the regions of greatest Lennard-Jones interaction, the H_2O molecules prefer the regions where the Coulombic interaction prevails. This behavior also explains why, up to a certain concentration, water does not seem to have a significant effect on the adsorption of carbon dioxide, given that the two species do not compete for the same sub-regions of the porous space.

As in most of the cases shown in Chapter 3, simulation of water as a pure component has shown hysteresis. This aspect opens a window in terms of further investigation for the determination of the phase behavior of water under confinement in disordered models of activated carbons. Nonetheless, for the cases of practical interest here, the pressures involved are always lower than the pressures at which water condensation would occur, therefore the results we have obtained would not be affected by the hysteresis phenomena.

Another aspect which has been considered is the effect that the polar groups on the structure of the adsorbent exert on the adsorption of water; in particular we show that their presence greatly affects the extent of water adsorption at low pressure and it also influences the extension of the pressure range in which condensation occurs: when the functional groups are present condensation happens more gradually than when they are absent. This is because in the first case small clusters start to appear in the proximity of the groups at very low pressure,

and eventually they merge into one cluster percolating the whole structure; in the second case condensation happens much more abruptly and at higher pressures, as it is determined by the growth of one single cluster.

When possible all binary separations have also been studied applying the Ideal Adsorbed Solution Theory; for mixtures containing no water the results are in excellent agreement with the GCMC simulations, but for binary mixtures containing water IAST cannot be successfully applied, due to the condensation of water as a single component. This implies that for the study of CO_2 capture processes in realistic conditions the direct simulation of the mixtures involved is essential.

References

1. Metz B, Davidson O, de Coninck H, Loos M, Meyer L. IPCC special report on carbon dioxide capture and storage. 2005.
2. Aaron D, Tsouris C. Separation of CO_2 from Flue Gas: A Review. Separation Science and Technology. 2005;40(1-3):321-48.
3. Grande CA, Cavenati S, Rodrigues AE, editors. Pressure swing adsorption for carbon dioxide sequestration. 2nd Mercosur Congress on chemical Engineering; 4th Mercosur Congress on Process systems Engineering; 2005; Costa Verde Do Brasil.
4. Chaffee AL, Knowles GP, Liang Z, Zhang J, Xiao P, Webley PA. CO_2 capture by adsorption: Materials and process development. International Journal of Greenhouse Gas Control. 2007;1(1):11-8.
5. DOE/NETL-2007/1281. Cost and Performance Baseline for Fossil Energy Plants Volume 1: bituminous Coal and Natural Gas to Electricity Rev.12007.
6. D'Alessandro DM, Smit B, Long JR. Carbon Dioxide Capture: Prospects for New Materials. Angewandte Chemie International Edition. 2010;49(35):6058-82.
7. Alonso TV, editor High efficiency on CO_2 removal in natural gas with UCARSOL™ solvents Rio Oil & Gas Expo and Conference; 2010; Rio de Janeiro, Brazil.
8. Gudmundsson JSN, A.; Ismailpour, A.; Saleem, F.; Idrees, M.U., Zaidy, S.A.H. Natural Gas Sweetening & Effect of Declining Pressure. Department of Petroleum Engineering & Applied Geophysics - Norwegian University of Science & Technology, Trondheim, Norway, 2011.
9. Boot-Handford ME, Abanades JC, Anthony EJ, Blunt MJ, Brandani S, Mac Dowell N, et al. Carbon capture and storage update. Energy & Environmental Science. 2013.
10. Busch A, Gensterblum Y, Krooss BM. Methane and CO2 sorption and desorption measurements on dry Argonne premium coals: pure components and mixtures. International Journal of Coal Geology. 2003;55(2–4):205-24.
11. Ottiger S, Pini R, Storti G, Mazzotti M. Competitive adsorption equilibria of CO2 and CH4 on a dry coal. Adsorption. 2008;14(4-5):539-56.
12. Sudibandriyo M, Pan Z, Fitzgerald JE, Robinson RL, Gasem KAM. Adsorption of Methane, Nitrogen, Carbon Dioxide, and Their Binary Mixtures on Dry Activated Carbon at 318.2 K and Pressures up to 13.6 MPa. Langmuir. 2003;19(13):5323-31.
13. Dreisbach F, Staudt R, Keller JU. High Pressure Adsorption Data of Methane, Nitrogen, Carbon Dioxide and their Binary and Ternary Mixtures on Activated Carbon. Adsorption. 1999;5(3):215-27.
14. Ottiger S, Pini R, Storti G, Mazzotti M. Measuring and Modeling the Competitive Adsorption of CO2, CH4, and N2 on a Dry Coal. Langmuir. 2008;24(17):9531-40.
15. Wu J, Zhou L, Sun Y, Su W, Zhou Y. Measurement and prediction of adsorption equilibrium for a H2/N2/CH4/CO2 mixture. AIChE Journal. 2007;53(5):1178-91.
16. Herm ZR, Swisher JA, Smit B, Krishna R, Long JR. Metal−Organic Frameworks as Adsorbents for Hydrogen Purification and Precombustion Carbon Dioxide Capture. Journal of the American Chemical Society. 2011;133(15):5664-7.
17. Myers AL, Prausnitz JM. Thermodynamics of mixed-gas adsorption. AIChE Journal. 1965;11(1):121-7.
18. Sircar S, Golden TC, Rao MB. Activated carbon for gas separation and storage. Carbon. 1996;34(1):1-12.
19. Himeno S, Komatsu T, Fujita S. High-Pressure Adsorption Equilibria of Methane and Carbon Dioxide on Several Activated Carbons. Journal of Chemical & Engineering Data. 2005;50(2):369-76.
20. Cracknell R, Nicholson D, Tennison S, Bromhead J. Adsorption and selectivity of carbon dioxide with methane and nitrogen in slit-shaped carbonaceous micropores: Simulation and experiment. Adsorption. 1996;2(3):193-203.
21. Kluson P, Scaife SJ. Microporous Adsorbents for a Selective Separation of Carbon Dioxide from Mixtures with Methane and Nitrogen. Chem Biochem Eng Q. 2002;16(3):97-103.

22. Cao D, Wu J. Modeling the selectivity of activated carbons for efficient separation of hydrogen and carbon dioxide. Carbon. 2005;43(7):1364-70.
23. Kowalczyk P, Gauden PA, Terzyk AP, Furmaniak S, Harris PJF. Displacement of Methane by Coadsorbed Carbon Dioxide Is Facilitated In Narrow Carbon Nanopores. The Journal of Physical Chemistry C. 2012;116(25):13640-9.
24. Furmaniak S, Kowalczyk P, Terzyk AP, Gauden PA, Harris PJF. Synergetic effect of carbon nanopore size and surface oxidation on CO2 capture from CO2/CH4 mixtures. Journal of Colloid and Interface Science. 2013;397(0):144-53.
25. Kumar KV, Müller EA, Rodríguez-Reinoso F. Effect of Pore Morphology on the Adsorption of Methane/Hydrogen Mixtures on Carbon Micropores. The Journal of Physical Chemistry C. 2012;116(21):11820-9.
26. Kumar VK, Rodríguez-Reinoso F. Co-adsorption of N_2 in the presence of CH_4 within carbon nanospaces: evidence from molecular simulations. Nanotechnology. 2013;24(3):35401.
27. Brennan JK, Bandosz TJ, Thomson KT, Gubbins KE. Water in porous carbons. Colloids and Surfaces A: Physicochemical and Engineering Aspects. 2001;187–188(0):539-68.
28. Choma J, Burakiewicz-Mortka W, Jaroniec M, Li Z, Klinik J. Monitoring Changes in Surface and Structural Properties of Porous Carbons Modified by Different Oxidizing Agents. Journal of Colloid and Interface Science. 1999;214(2):438-46.
29. Müller EA, Rull LF, Vega LF, Gubbins KE. Adsorption of Water on Activated Carbons: A Molecular Simulation Study. The Journal of Physical Chemistry. 1996;100(4):1189-96.
30. Salame II, Bagreev A, Bandosz TJ. Revisiting the Effect of Surface Chemistry on Adsorption of Water on Activated Carbons. The Journal of Physical Chemistry B. 1999;103(19):3877-84.
31. Salame II, Bandosz TJ. Experimental Study of Water Adsorption on Activated Carbons. Langmuir. 1998;15(2):587-93.
32. Salame II, Bandosz TJ. Study of Water Adsorption on Activated Carbons with Different Degrees of Surface Oxidation. Journal of Colloid and Interface Science. 1999;210(2):367-74.
33. Stoeckli HF, Kraehenbuehl F, Morel D. The adsorption of water by active carbons, in relation to the enthalpy of immersion. Carbon. 1983;21(6):589-91.
34. Brennan JK, Thomson KT, Gubbins KE. Adsorption of Water in Activated Carbons: Effects of Pore Blocking and Connectivity. Langmuir. 2002;18(14):5438-47.
35. Liu JC, Monson PA. Monte Carlo Simulation Study of Water Adsorption in Activated Carbon. Industrial & Engineering Chemistry Research. 2006;45(16):5649-56.
36. Horikawa T, Sakao N, Hayashi J, Do DD, Katoh M, Sotowa KI. Preparation of nitrogen-doped porous carbon and its water adsorption behaviour. Adsorption Science and Technology. 2013;31(2-3):135-44.
37. Wang R, Amano Y, Machida M. Surface properties and water vapor adsorption-desorption characteristics of bamboo-based activated carbon. Journal of Analytical and Applied Pyrolysis. 2013;104:667-74.
38. Segarra EI, Glandt ED. Model microporous carbons: microstructure, surface polarity and gas adsorption. Chemical Engineering Science. 1994;49(17):2953-65.
39. Do DD, Do HD. A model for water adsorption in activated carbon. Carbon. 2000;38(5):767-73.
40. Do DD, Junpirom S, Do HD. A new adsorption–desorption model for water adsorption in activated carbon. Carbon. 2009;47(6):1466-73.
41. Horikawa T, Sakao N, Do DD. Effects of temperature on water adsorption on controlled microporous and mesoporous carbonaceous solids. Carbon. 2013;56:183-92.
42. Horikawa T, Sekida T, Hayashi Ji, Katoh M, Do DD. A new adsorption–desorption model for water adsorption in porous carbons. Carbon. 2011;49(2):416-24.
43. Cossarutto L, Zimny T, Kaczmarczyk J, Siemieniewska T, Bimer J, Weber JV. Transport and sorption of water vapour in activated carbons. Carbon. 2001;39(15):2339-46.

44. Furmaniak S, Gauden PA, Terzyk AP, Rychlicki G, Wesołowski RP, Kowalczyk P. Heterogeneous Do–Do model of water adsorption on carbons. Journal of Colloid and Interface Science. 2005;290(1):1-13.
45. Lagorsse S, Campo MC, Magalhães FD, Mendes A. Water adsorption on carbon molecular sieve membranes: Experimental data and isotherm model. Carbon. 2005;43(13):2769-79.
46. Neitsch M, Heschel W, Suckow M. Water vapor adsorption by activated carbon: a modification to the isotherm model of Do and Do. Carbon. 2001;39(9):1437-8.
47. Avgul NN, Dzhigit OM, Kiselev AV, Shcherbakova KD. AN SSSR. 1953;92.
48. Avgul NN, Dzhigit OM, Kiselev AV, Shcherbakova KD. AN SSSR. 1955;101.
49. Hassan NM, Ghosh TK, Hines AL, Loyalka SK. Adsorption of water vapor on BPL activated carbon. Carbon. 1991;29(4–5):681-3.
50. Krooss BM, van Bergen F, Gensterblum Y, Siemons N, Pagnier HJM, David P. High-pressure methane and carbon dioxide adsorption on dry and moisture-equilibrated Pennsylvanian coals. International Journal of Coal Geology. 2002;51(2):69-92.
51. Wang Y, Zhou Y, Liu C, Zhou L. Comparative studies of CO2 and CH4 sorption on activated carbon in presence of water. Colloids and Surfaces A: Physicochemical and Engineering Aspects. 2008;322(1–3):14-8.
52. Sun Y, Wang Y, Zhang Y, Zhou Y, Zhou L. CO2 sorption in activated carbon in the presence of water. Chemical Physics Letters. 2007;437(1–3):14-6.
53. Sun Y, Xue Q, Zhou Y, Zhou L. Sorption equilibria of CO2/CH4 mixture on activated carbon in presence of water. Journal of Colloid and Interface Science. 2008;322(1):22-6.
54. Billemont P, Coasne B, De Weireld G. An Experimental and Molecular Simulation Study of the Adsorption of Carbon Dioxide and Methane in Nanoporous Carbons in the Presence of Water. Langmuir. 2010;27(3):1015-24.
55. Billemont P, Coasne B, De Weireld G. Adsorption of Carbon Dioxide, Methane, and Their Mixtures in Porous Carbons: Effect of Surface Chemistry, Water Content, and Pore Disorder. Langmuir. 2013;29(10):3328-38.
56. Fitzgerald JE, Pan Z, Sudibandriyo M, Robinson JRL, Gasem KAM, Reeves S. Adsorption of methane, nitrogen, carbon dioxide and their mixtures on wet Tiffany coal. Fuel. 2005;84(18):2351-63.
57. Xu D, Xiao P, Zhang J, Li G, Xiao G, Webley PA, et al. Effects of water vapour on CO2 capture with vacuum swing adsorption using activated carbon. Chemical Engineering Journal. 2013;230(0):64-72.
58. Xu D, Zhang J, Li G, Xiao P, Webley P, Zhai Y-c. Effect of water vapor from power station flue gas on CO2 capture by vacuum swing adsorption with activated carbon. Journal of Fuel Chemistry and Technology. 2011;39(3):169-74.
59. Gupta A, Chempath S, Sanborn MJ, Clark LA, Snurr RQ. Object-oriented Programming Paradigms for Molecular Modeling. Molecular Simulation. 2003;29(1):29-46.
60. Talu O, Myers AL. Molecular simulation of adsorption: Gibbs dividing surface and comparison with experiment. AIChE Journal. 2001;47(5):1160-8.
61. Martin MG, Siepmann JI. Transferable Potentials for Phase Equilibria. 1. United-Atom Description of n-Alkanes. The Journal of Physical Chemistry B. 1998;102(14):2569-77.
62. Potoff JJ, Siepmann JI. Vapor–liquid equilibria of mixtures containing alkanes, carbon dioxide, and nitrogen. AIChE Journal. 2001;47(7):1676-82.
63. Zhang L, Siepmann JI. Direct calculation of Henry's law constants from Gibbs ensemble Monte Carlo simulations: nitrogen, oxygen, carbon dioxide and methane in ethanol. Theor Chem Acc. 2006;115(5):391-7.
64. Kamath G, Lubna N, Potoff JJ. Effect of partial charge parametrization on the fluid phase behavior of hydrogen sulfide. The Journal of Chemical Physics. 2005;123(12):124505-7.
65. Buch V. Path integral simulations of mixed *para*-D_2 and *ortho*-D_2 clusters: The orientational effects. The Journal of Chemical Physics. 1994;100(10):7610-29.

66. Sweatman MB, Quirke N. Modelling Gas Adsorption in Slit-Pores Using Monte Carlo Simulation. Molecular Simulation. 2001;27(5-6):295-321.
67. Jorgensen WL, Chandrasekhar J, Madura JD, Impey RW, Klein ML. Comparison of simple potential functions for simulating liquid water. The Journal of Chemical Physics. 1983;79(2):926-35.
68. Fennel CJ, ; Gezelter, D. Is the Ewald summation still necessary? Peirwise alternatives to the accepted standard for long-range electrostatics. The Journal of Chemical Physics. 2006;124:234104.
69. Ewald PP. Die Berechnung optischer und elektrostatischer Gitterpotentiale. Annalen der Physik. 1921;369(3):253-87.
70. Banu A-M, Friedrich D, Brandani S, Düren T. A Multiscale Study of MOFs as Adsorbents in H2 PSA Purification. Industrial & Engineering Chemistry Research. 2013;52(29):9946-57.
71. Hasan MMF, Baliban RC, Elia JA, Floudas CA. Modeling, Simulation, and Optimization of Postcombustion CO_2 Capture for Variable Feed Concentration and Flow Rate. 2. Pressure Swing Adsorption and Vacuum Swing Adsorption Processes. Industrial & Engineering Chemistry Research. 2012;51(48):15665-82.
72. Hasan MMF, Baliban RC, Elia JA, Floudas CA. Modeling, Simulation, and Optimization of Postcombustion CO_2 Capture for Variable Feed Concentration and Flow Rate. 1. Chemical Absorption and Membrane Processes. Industrial & Engineering Chemistry Research. 2012;51(48):15642-64.
73. Cracknell RF, Nicholson D, Parsonage NG, Evans H. Rotational insertion bias: a novel method for simulating dense phases of structured particles, with particular application to water. Molecular Physics. 1990;71(5):931-43.
74. Carlile DL, Friday DK, Chemical Research D, Center E. 1,1,2-trichloro, 1,2,2-trifluoroethane (CFC-113) and Water Isotherm Measurements on Impregnated and Unimpregnated Activated Carbons: Chemical Research, Development & Engineering Center; 1992.
75. Iiyama T, Nishikawa K, Otowa T, Kaneko K. An Ordered Water Molecular Assembly Structure in a Slit-Shaped Carbon Nanospace. The Journal of Physical Chemistry. 1995;99(25):10075-6.
76. Sarkisov L, Monson PA. Lattice model of adsorption in disordered porous materials: Mean-field density functional theory and Monte Carlo simulations. Physical Review E. 2001;65(1):011202.
77. Sarkisov L, Monson PA. Computer simulations of phase equilibrium for a fluid confined in a disordered porous structure. Physical Review E. 2000;61(6):7231-4.
78. Page KS, Monson PA. Monte Carlo calculations of phase diagrams for a fluid confined in a disordered porous material. Physical Review E. 1996;54(6):6557-64.
79. Rudisill EN, Hacskaylo JJ, LeVan MD. Coadsorption of hydrocarbons and water on BPL activated carbon. Industrial & Engineering Chemistry Research. 1992;31(4):1122-30.
80. Talu O, Meunier F. Adsorption of associating molecules in micropores and application to water on carbon. AIChE Journal. 1996;42(3):809-19.
81. Soper AK. The radial distribution functions of water and ice from 220 to 673 K and at pressures up to 400 MPa. Chemical Physics. 2000;258(2–3):121-37.
82. Vega C, McBride C, Sanz E, Abascal JLF. Radial distribution functions and densities for the SPC/E, TIP4P and TIP5P models for liquid water and ices I, I, II, III, IV, V, VI, VII, VIII, IX, XI and XII. Physical Chemistry Chemical Physics. 2005;7(7):1450-6.
83. Ishii R, Okazaki S, Okada I, Furusaka M, Watanabe N, Misawa M, et al. Density dependence of structure of supercritical carbon dioxide along an isotherm. The Journal of Chemical Physics. 1996;105(16):7011-21.
84. Zhu A, Zhang X, Liu Q, Zhang Q. A Fully Flexible Potential Model for Carbon Dioxide. Chinese Journal of Chemical Engineering. 2009;17(2):268-72.
85. Bae Y-S, Snurr RQ. Development and Evaluation of Porous Materials for Carbon Dioxide Separation and Capture. Angewandte Chemie International Edition. 2011;50(49):11586-96.
86. Sumida K, Rogow DL, Mason JA, McDonald TM, Bloch ED, Herm ZR, et al. Carbon Dioxide Capture in Metal–Organic Frameworks. Chemical Reviews. 2012;112(2):724-81.

87. Bae T-H, Hudson MR, Mason JA, Queen WL, Dutton JJ, Sumida K, et al. Evaluation of cation-exchanged zeolite adsorbents for post-combustion carbon dioxide capture. Energy & Environmental Science. 2013;6(1):128-38.
88. Park J-H, Kim J-N, Cho S-H, Kim J-D, Yang RT. Adsorber dynamics and optimal design of layered beds for multicomponent gas adsorption. Chemical Engineering Science. 1998;53(23):3951-63.
89. Cavenati S, Grande CA, Rodrigues AE. Adsorption Equilibrium of Methane, Carbon Dioxide, and Nitrogen on Zeolite 13X at High Pressures. Journal of Chemical & Engineering Data. 2004;49(4):1095-101.
90. Li J-R, Ma Y, McCarthy MC, Sculley J, Yu J, Jeong H-K, et al. Carbon dioxide capture-related gas adsorption and separation in metal-organic frameworks. Coordination Chemistry Reviews. 2011;255(15–16):1791-823.
91. Bae Y-S, Farha OK, Hupp JT, Snurr RQ. Enhancement of CO2/N2 selectivity in a metal-organic framework by cavity modification. Journal of Materials Chemistry. 2009;19(15):2131-4.
92. Banerjee R, Furukawa H, Britt D, Knobler C, O'Keeffe M, Yaghi OM. Control of Pore Size and Functionality in Isoreticular Zeolitic Imidazolate Frameworks and their Carbon Dioxide Selective Capture Properties. Journal of the American Chemical Society. 2009;131(11):3875-7.
93. Bae Y-S, Spokoyny AM, Farha OK, Snurr RQ, Hupp JT, Mirkin CA. Separation of gas mixtures using Co(ii) carborane-based porous coordination polymers. Chemical Communications. 2010;46(20):3478-80.
94. Espinal L, Poster DL, Wong-Ng W, Allen AJ, Green ML. Measurement, Standards, and Data Needs for CO2 Capture Materials: A Critical Review. Environmental Science & Technology. 2013;47(21):11960-75.
95. Babarao R, Jiang JW. Cation Characterization and CO2 Capture in Li+-Exchanged Metal−Organic Frameworks: From First-Principles Modeling to Molecular Simulation†. Industrial & Engineering Chemistry Research. 2010;50(1):62-8.
96. Van Tassel PR, Davis HT, McCormick AV. Adsorption Simulations of Small Molecules and Their Mixtures in a Zeolite Micropore. Langmuir. 1994;10(4):1257-67.
97. Ma B-Q, Mulfort KL, Hupp JT. Microporous Pillared Paddle-Wheel Frameworks Based on Mixed-Ligand Coordination of Zinc Ions. Inorganic Chemistry. 2005;44(14):4912-4.
98. Mulfort KL, Hupp JT. Chemical Reduction of Metal−Organic Framework Materials as a Method to Enhance Gas Uptake and Binding. Journal of the American Chemical Society. 2007;129(31):9604-5.
99. Bae Y-S, Mulfort KL, Frost H, Ryan P, Punnathanam S, Broadbelt LJ, et al. Separation of CO2 from CH4 Using Mixed-Ligand Metal−Organic Frameworks. Langmuir. 2008;24(16):8592-8.
100. Tóth J. Uniform interpretation of gas/solid adsorption. Advances in Colloid and Interface Science. 1995;55(0):1-239.
101. Toth J. Adsorption. Theory, modeling, and analysis.: Taylor & Francis; 2002.

Chapter 6

General Conclusions & Future Work

The main objective of this thesis has been the development of realistic, predictive models of high surface area activated carbons to explore the adsorption behaviour of these materials in the context of carbon capture processes.

As a representative of the category we focused on Maxsorb MSC-30, produced by The Kansai Coke and Chemicals, and featuring surface area in excess of 3000 m^2/g.

The processes we have considered are pre and post combustion separations and sweetening of sour natural gas, using as realistic conditions as possible. In particular, we have considered not only realistic pressures and temperatures, but we have also taken into account presence of minor components in gas streams, including water.

Despite activated carbons not showing the highest selectivities towards carbon dioxide, the choice of these materials is motivated by several advantages such as versatility, commercial availability, relatively low cost, general easiness of regeneration, generally fast kinetics and, for the high surface area materials, high adsorption capacity.

The main tools we have applied during our research are molecular simulations and experimental measurements of adsorption. Molecular simulations are a particularly useful tool when adsorption of mixtures at high pressures is concerned, as the experimental measurements on these systems are difficult.

The challenge associated with activated carbons is their complex structure: for many decades researchers have confronted the problem of describing it using various molecular models, but no comprehensive model has, as yet, emerged. In fact, different models with different levels of accuracy can be considered more or less useful according to the type of study they are involved in.

The models we applied in this project essentially belong to two broad classes: the first is represented by the slit pore models (1), and the second is represented by more sparse structures as in the platelet model introduced by Segarra and Glandt (2). All these models have been applied to the simulation of methane and carbon dioxide adsorption; this has produced a good test on their reliability, given that we have been able to compare the simulated results with the experimental measurements performed in our group or in different groups.

Application of the slit pore models has allowed us to extract pore size distributions for the activated carbon and to employ them for the prediction of adsorption isotherms, which have been compared with the experimental data.

In this context we started with the simplest representation as possible, which is the classic slit pore model (1); this model has shown good accuracy for the prediction of simple species like methane and carbon dioxide. Despite this success, there is a philosophical concern whether the extracted pore size distributions, aside from their predictive value, have correct physical significance in the sense that, for materials as sparse as Maxsorb, it is unlikely they reflect the actual spatial organization of the material and therefore they become purely abstract functions effectively masking the imperfections of the slit pore model altogether. Another concern was associated with how this model would perform with respect to presence of water in the gas streams of interest. Following the wealth of previous studies (Jorge and Seaton) (3, 4), it seemed it was necessary to explicitly model surface groups to capture water behaviour.

Therefore, starting from the classic slit pore model, we progressively added elements of realism, such as finite number of sheets in each pore wall, structural defects and functional surface groups. The addition of these elements of realism has required some re-calibration of the solid-fluid interaction parameters in the case of methane in order to maintain the accuracy of the model. However, this model applied to water encountered a number of challenges associated with very long equilibration times for adsorption isotherms in individual pores and adsorption hysteresis. The later issue implies that prediction of water adsorption isotherm using adsorption integral equation and pore size distribution would require additional tools and methods to establish the location of the true vapour-liquid equilibrium for water in each pore. This aspect, together with the long computational times involved (at least 35 days per isotherm, with a kernel of isotherms needing to be simulated) has encouraged us to explore a different avenue based on the models with structural disorder, with the idea to investigate whether these models would be more attractive for practical applications such as the routine (and therefore relatively quick) screening of CO_2 capture materials.

Inspired by the studies by Segarra and Glandt (2), and more recent works by Kumar and co-workers (5, 6) we constructed several models of activated carbons based on random packings of structural elements (mostly circular-like fragments of a carbon sheet).

In particular, we have studied the effect that variables such as dimension of the structural elements, presence or absence of polar groups, type of polar groups, accessible surface area of the model, method adopted to calculate partial charges, presence or absence of curvature on the structure of the element on the simulated adsorption isotherms.

Based on our results and observations, we have chosen as a reasonable representation of Maxsorb a model constructed using a random packing of corannulene-like elements (therefore curved), all featuring hydroxilic groups. The accessible surface area and pore volume and the carbon/oxygen ratio in the structure are as close as possible to the experimental values typically reported for Maxsorb MSC-30.

Validation and testing of the model have shown reasonable accuracy in the prediction of the adsorption of the main species involved in the CO_2 capture processes. Therefore the model has been applied to simulate the streams involved in pre and post combustion and in the

sweetening of sour natural gas. This has allowed us to evaluate the behaviour of Maxsorb as a physisorbent in these contexts, particularly in terms of selectivity towards carbon dioxide.

Our results suggest that high surface area activated carbons are worth further investigation for applications in pre combustion separations; this is due to the reasonable selectivities we have calculated, together with the high adsorption capacity at high pressures.

Another important aspect we have considered is the presence of water. We started with the simulation of water single component isotherms and then continued with the study of CO_2/H_2O binary mixtures, with water present as a minor component. Even if our model overpredicts the hydrophobicity of Maxsorb, it captures the peculiar behaviour of water molecules in activated carbons, i.e. the tendency to cluster, starting from the proximity of the polar centres. Also, in agreement with previous studies (7), the model highlights the importance of the functional groups on the structure of the adsorbent, given that in their absence the adsorption behaviour changes profoundly.

Energy minimization studies have also allowed us to establish the different preferential position of carbon dioxide and water molecules on the structure of the adsorbent, showing that the two species might occupy different sub-regions of the porous space.

This is in agreement with the results obtained when we studied the effect of small concentrations of water vapour in the streams: in the range of pressures we have considered (all chosen such as to avoid water condensation in the bulk stream) the adsorption of water has determined almost negligible changes to the adsorption of carbon dioxide, even when water has become the preferential adsorption species (in the post-combustion case this is actually due to the low number of adsorbed molecules for each species, so that there is actually no competition for the occupation of the different regions of the porous space.

It is important to mention that in the case of the platelet model the simulation of water as a single component has also shown adsorption hysteresis and has required long computational time. Nonetheless, it is also important to point out that in the case of the platelet model the generation of a kernel is not required: in few words, simulation of adsorption of a single species or a mixture requires one simulation only.

This last observation is a good starting point for a critical comparison between the two classes of models, considered in this thesis:

1) Computational cost: in the case of the slit pore with groups and defects model, once the structure representative of a specific type of activated carbon has been constructed, the prediction of adsorption for a particular gas at a particular temperature always requires generation of a kernel of isotherms to be used within the AIE; in the case of the platelet model, instead, once the structure is ready, one prediction simply requires generation of one isotherm. To give an idea about the difference in computational time we can make the following comparison. Consider one case of CO_2 adsorption at 298 K up to 20 Bar. To generate an adsorption isotherm using slit pore model requires 18 isotherms constituting the kernel with each isotherm requiring about 11 hours. Preliminary calculations of the potential maps may require between 30 and 60 hours per isotherm. Therefore, the total computational cost is between 528 and 858 hours. For the platelet model, generation of the potential maps is required only once (30-60 hours) and once the model is constructed one simulation is needed for the whole isotherm (about 21 hours). Therefore the total cost is 51-81 hours. Of course, the hidden cost is associated with the variation of the model during the construction to get the structural characteristics right. For example, if we had to repeat the process for ten different variants of the platelet model, the cost would become comparable to the slit pore model and kernel calculations.

   It is true that in the case of the classic slit pore model once a kernel of isotherms has been generated it is possible to use it for predictions and characterization involving different types of activated carbons, this meaning that all the simulation work can be done "up-front"; this is not a possibility for the platelet models, because they are calibrated for specific activated carbons. Nonetheless, when using the slit pore with groups and defects model the advantage of the work made up-front is not that evident anymore, because activated carbons with different C/O ratios do require different models and therefore the generation of new kernels;

2) Accuracy in terms of predictions: the slit pore models are in general bound to be more accurate than the platelet models, given that the former are calibrated using all the experimental points, and therefore they preserve their accuracy even at high pressures

and in the Henry's region. Particularly, the slit pore models are very accurate for the prediction of simple gases and mixtures in carbon materials, which over the years has been shown in a significant amount of literature (8-15). The platelet models are in general calibrated according to a smaller number of parameters (2, 5) and the ones we have constructed, for example, are not calibrated to exactly reproduce the Henry's constants and in general lose accuracy at high pressures. Nonetheless, we consider their accuracy to be sufficient for the systems and conditions object of this study, especially given the low number of constraints (accessible surface area and pore volume, C/O ratio) we have used to build them;

3) Similarity to the structure of the real materials: the platelet models can correctly reproduce the disordered nature of the different materials and because of their versatility they can be easily adjusted to reproduce other important features such as accessible surface area and pore volume; the slit pore model is clearly a simplification of the structures, given that it does not consider structural disorder or other characteristics such as accessible pore volume or accessible surface area (especially given that all the space is accessible) or pore connectivity. We do believe that both models can give an indication of which pore sizes play the most relevant role in the adsorption properties, particularly given the similarities we have obtained between the geometric pore size distribution (as calculated from the platelet model for Maxsorb) and the pore size distribution extracted using the slit pore with groups and defects model starting from data for CO_2 at 298 K.

4) Simulation of mixtures: in this work we have not simulated any mixtures using the slit pore model, but this has been shown to be a promising tool (15) (14); particularly, Sweatman and Quirke (14) have used slit-pore model approach to predict the behaviour of mixtures using the IAST and its variants. These variants address the ideal mixture assumptions: EMAST (equal mixing adsorbed solution theory) implies that the interactions between the adsorptive molecules are the same both in the bulk and in the adsorbed phase, but without requiring the mixture to be ideal; IMAST approximates the mixture to be ideal, but does not use the ideal gas approximation (as IAST does).

The authors also predicted the behaviour of mixtures using Density Functional Theory (DFT), and their results show that DFT is superior to the IAST (and its variants) approach at high pressures.

In this work we have predicted the behaviour of mixtures using the platelet model both with direct simulation and IAST, obtaining very similar results; we believe that the direct simulation is a more straightforward method, given that one prediction simply requires one simulation, without the need for the pure component isotherms and without the necessity to further process the results. Moreover, IAST cannot be applied for the simulation of mixtures containing water.

Given the discussion above we conclude that for high surface area activated carbons the slit pore model (even in its classic version) is a very accurate and powerful tool, especially for the prediction of simple gases and, even for mixtures, in combination with DFT (although we have not investigated the latter aspect ourselves); therefore it should certainly be used when a high level of accuracy is required, particularly in wide pressure ranges and in fundamental studies involving the testing of different simulation methods, for example. The platelet models are also a powerful tool because of their versatility, which allows them to be employed for predictions concerning a relatively broad range of conditions for different species (including water). Moreover, their ability to reproduce important structural features of the materials allows a detailed study of the adsorbed phase even in terms of molecular arrangement and will allow the models to be used for the study of adsorption also from the kinetics point of view (using molecular dynamics, for example).

We cannot neglect that the platelet models lose accuracy at very low and high pressures, but their versatility and easiness of use makes them a very useful tool for the routine screening of capture materials, this meaning that once the promising materials have been identified they can and have to be submitted to further and more accurate investigation. For the same reason even in the case of mixtures we believe that the direct simulation using the sparse model is a powerful tool, which makes their use preferable to experimental measurements (especially in the presence of water). With this, again, we do not mean to deny the power of the slit pore models, especially in conjunction to DFT.

Further development of our study in terms of screening of capture materials should involve a more comprehensive assessment of high surface area activated carbons through a process simulation. This would require the coupling of the molecular simulation tools we use with a full-scale pressure swing adsorption system modelling and with molecular dynamics, thus allowing us to evaluate also different characteristics, including the working capacities of the materials and the kinetics of the process. A similar study has been recently published by Banu et al. (16) in the context of hydrogen purification using metal-organic frameworks as adsorbents.

Another possible future research direction is the study of high surface area activated carbons as substrates for more complex materials, with the aim of improving their CO_2 capture ability even at low pressure, and therefore even in post-combustion processes.

An interesting possibility could be the study of pressure swing wetting layer adsorption: the idea, proposed by Sweatman (17, 18), is to combine the high surface area of porous materials with the high affinity for carbon dioxide of liquid solvents. This is achieved by creating a composite porous material, with a surface wetted by a suitable solvent.

The idea could be applied using room temperature ionic liquids (RTIL) as solvents, given that they have been recently considered as promising for carbon dioxide capture and other power cycle related separations, due to their negligible vapour pressures, reasonable thermal stability, strong dissolubility, wide liquid range and tunability of structure and properties (19, 20).

From the point of view of the development of molecular models of high surface area activated carbons two directions should be followed, especially bearing in mind the results we have obtained with water: in the case of the platelet model it would be important to try to use different polar groups (carboxylic, for example) to observe what effect they have in terms of hydrophobicity of the material, while in the case of the slit pore model it would be important to explore different protocols for the addition of functional groups, possibly with the aim of maximizing their accessibility. Finally, even the results we have already obtained could become a starting point for more fundamental studies concerning the simulation of water adsorption (especially hysteresis), both in slit pore and platelet models.

References

1. Everett DH, Powl JC. Adsorption in slit-like and cylindrical micropores in the henry's law region. A model for the microporosity of carbons. Journal of the Chemical Society, Faraday Transactions 1: Physical Chemistry in Condensed Phases. 1976;72(0):619-36.
2. Segarra EI, Glandt ED. Model microporous carbons: microstructure, surface polarity and gas adsorption. Chemical Engineering Science. 1994;49(17):2953-65.
3. Jorge M, Schumacher C, Seaton NA. Simulation Study of the Effect of the Chemical Heterogeneity of Activated Carbon on Water Adsorption. Langmuir. 2002;18(24):9296-306.
4. Jorge M, Seaton NA, F. Rodriguez-Reinoso BMJRaKU. Characterisation of the surface chemistry of activated carbon by molecular simulation of water adsorption. Studies in Surface Science and Catalysis. Volume 144: Elsevier; 2002. p. 131-8.
5. Kumar KV, Müller EA, Rodríguez-Reinoso F. Effect of Pore Morphology on the Adsorption of Methane/Hydrogen Mixtures on Carbon Micropores. The Journal of Physical Chemistry C. 2012;116(21):11820-9.
6. Kumar VK, Rodríguez-Reinoso F. Co-adsorption of N_2 in the presence of CH_4 within carbon nanospaces: evidence from molecular simulations. Nanotechnology. 2013;24(3):35401.
7. Billemont P, Coasne B, De Weireld G. Adsorption of Carbon Dioxide, Methane, and Their Mixtures in Porous Carbons: Effect of Surface Chemistry, Water Content, and Pore Disorder. Langmuir. 2013;29(10):3328-38.
8. Davies GM, Seaton NA. Development and Validation of Pore Structure Models for Adsorption in Activated Carbons. Langmuir. 1999;15(19):6263-76.
9. Gusev VY, O'Brien JA, Seaton NA. A Self-Consistent Method for Characterization of Activated Carbons Using Supercritical Adsorption and Grand Canonical Monte Carlo Simulations. Langmuir. 1997;13(10):2815-21.
10. Davies GM, Seaton NA. Predicting adsorption equilibrium using molecular simulation. AIChE Journal. 2000;46(9):1753-68.
11. Nguyen TX, Bhatia SK. Characterization of Pore Wall Heterogeneity in Nanoporous Carbons Using Adsorption: the Slit Pore Model Revisited. The Journal of Physical Chemistry B. 2004;108(37):14032-42.
12. Pinto da Costa JMC, Cracknell RF, Seaton NA, Sarkisov L. Towards predictive molecular simulations of normal and branched alkane adsorption in carbonaceous engine deposits. Carbon. 2011;49(2):445-56.
13. Sweatman MB, Quirke N. Gas Adsorption in Active Carbons and the Slit-Pore Model 1: Pure Gas Adsorption. The Journal of Physical Chemistry B. 2005;109(20):10381-8.
14. Sweatman MB, Quirke N. Gas Adsorption in Active Carbons and the Slit-Pore Model 2: Mixture Adsorption Prediction with DFT and IAST. The Journal of Physical Chemistry B. 2005;109(20):10389-94.
15. Heuchel M, Davies GM, Buss E, Seaton NA. Adsorption of Carbon Dioxide and Methane and Their Mixtures on an Activated Carbon: Simulation and Experiment. Langmuir. 1999;15(25):8695-705.
16. Banu A-M, Friedrich D, Brandani S, Düren T. A Multiscale Study of MOFs as Adsorbents in H2 PSA Purification. Industrial & Engineering Chemistry Research. 2013;52(29):9946-57.
17. Sweatman MB. Equilibrium behaviour of a novel gas separation process, with application to carbon capture. Chem Eng Sci. 2010;65(13):3907-13.
18. Sweatman MB. Improving the equilibrium performance of active carbons for separation processes by co-adsorption with low pressure solvent: application to carbon capture. Adsorption-Journal of the International Adsorption Society. 2011;17(4):723-37.
19. Bara JE, Carlisle TK, Gabriel CJ, Camper D, Finotello A, Gin DL, et al. Guide to CO2 Separations in Imidazolium-Based Room-Temperature Ionic Liquids. Industrial & Engineering Chemistry Research. 2009;48(6):2739-51.

20. Bara JE, Camper DE, Gin DL, Noble RD. Room-Temperature Ionic Liquids and Composite Materials: Platform Technologies for CO2 Capture. Accounts of Chemical Research. 2010;43(1):152-9.

Appendix

Supplemental Data

A1. Forcefield parameters

The Lennard-Jones parameters summarized in table A1 have been used for the construction and characterization of all the models in the present work, excluding only the cases, specified in Chapters 4 and 5, in which a scaling of the ε parameter of the Lennard-Jones (LJ) potential has been applied. The charges reported in table A1 have been applied for all the models presented in Chapter 3 and in Sections 4.3 and 4.4 of Chapter 4, apart from the cases (specified in Section 4.4.5 and in Section 4.4.6), in which charges have been calculated using the B3LYP Density Functional Theory method, with 6-31g basis set and CHELPG charge analysis with the Gaussian 09 software package (1-3).

Table A1. Parameters for LJ interaction and charges. All the parameters come from the work by Tenney and Lastoskie (4), apart from the LJ parameters for the groups CH_2 and CH_3, which come from the OPLS force field (5). The charge of 0.30 on the CH_2 groups (always connected to OH groups) has been attributed to insure electroneutrality.

ATOM	**σ (Å)**	**ε/k_B (K)**	**CHARGE (e)**
C (aromatic)	3.4	28.0	0.00
C (aromatic, C-H)	3.4	28.0	-0.16
C (aromatic, C-OH)	3.4	28.0	0.30
C (aromatic, C-COOH)	3.4	28.0	-0.06
H (H-C)	2.4	12.0	0.16
O (hydroxylic)	3.1	79.0	-0.60
H (hydroxylic)	1.3	30.0	0.30
C (carboxylic)	3.4	28.0	0.75
O (carboxylic, C=O)	3.1	79.0	-0.50
O (carboxylic, OH)	3.1	79.0	-0.55
H (carboxylic, OH)	1.3	30.0	0.36
CH_2	3.905	59.4	0.30
CH_3	3.905	88.1	0.00

Table A2 reports the LJ interaction parameters for all the adsorptive fluids studied in this work, while table A3 reports the features of the non-spherical models only.

Table A2. Lennard-Jones parameters and charges associated to the models chosen for the different fluids (6-12) .

Site	σ (Å)	ε/k_B (K)	Charge (e)
C (CO_2)	2.800	27.00	0.7000
O (CO_2)	3.050	79.00	-0.3500
CH_4	3.730	148.00	0.0000
N (N_2)	3.310	36.00	-0.4820
COM (N_2)	0.000	0.00	0.9640
H_2	2.960	34.20	0.0000
O (O_2)	3.020	49.00	-0.1130
COM (O_2)	0.000	0.00	0.2260
S (H_2S)	3.720	232.00	-0.3800
H (H_2S)	0.000	0.00	0.1900
C (CO)	3.490	22.80	0.0203
O (CO)	3.130	63.50	-0.0203
O (H_2O)	3.154	78.00	0.0000
H (H_2O)	0.000	0.00	0.5200
A (H_2O)	0.000	0.00	-1.0400

Table A3. Bond lengths and bond angles for the non-spherical molecular models used in this work. (6-12)

Molecule	Bond length (Å)	Bond angle (°)
CO_2	1.16	180
N_2	1.1	180
O_2	1.21	180
H_2S	1.34	92.5
CO	1.12	180
H_2O	0.9572	104.52

A2. Simulation details

GCMC simulations were carried using the MuSiC simulation package (13). LJ interactions between different atoms were evaluated through the standard Lorentz-Berthelot mixing rules. Coulombic interactions between partial charges were calculated using the Fennell-Gezelter (FG) method based on a spherically truncated summation (14) in the case of the fluid-fluid interaction, while for the solid-fluid interaction Ewald (15) summation was used. Further details are summarized in table A4.

Table A4. Details of the GCMC simulations.

Iterations	20000000
Cutoff (Å)	13
Type of moves	Insertion, deletion, translation, rotation
Weight of each type of move	0.25, 0.25, 0.25, 0.25
Iterations used for equilibration	50%
Iterations used for statistical sampling	50%
α and shield parameters for FG electrostatic potential	0.1, 1.0
KMAX, KAPPA and LOCUT for Ewald	15, 6.7, 1E-10
xyz dimensions of the unit cell in the classic slit pore model (Å)	28.06, 27.69, varies with pore width
xyz dimensions of the unit cell in the single layer models (Å)	34.08, 34.43, varies with pore width
xyz dimensions of the unit cell in the platelet models (Å)	60.0, 60.0, 60.0
Angles of the unit cell (º)	90.0, 90.0, 90.0

A3. Structural characterization of the models: parameters

Table A5. Parameters involved in the determination of the accessible surface area of the models.

Collision diameters for the adsorbent (σ)	As in table A1
Probe size (Å)	3.314
Number of insertions per atom of structure	500

Table A6. Parameters involved in the determination of the accessible pore volume of the models.

Collision diameters for the adsorbent (σ)	As in table A1
Depths of the potential wells (ε)	As in table A1
Number of trial insertions	15000
Temperature [(1)]	298.0
σ (Å), ε (K) of the probe (He)	2.58 , 10.22
Cutoff (Å)	20.0

[(1)] For the isotherms simulated at different temperatures the accessible pore volume used for the determination of the excess adsorption has been determined at the same temperature used for the simulation.

Table A7. Parameters involved in the determination of the Henry's constants for different adsorbate species in the models.

Collision diameters for the adsorbent (σ)	As in table A1
Depths of the potential wells for the adsorbent (ε)	As in table A1
Lattice grid size (Å)	0.5
Cutoff (Å)	13.0
α and shield parameters for Fennell-Gezelter (FG) electrostatic potential	0.1, 1.0

A4. Consistency between different methods of measurement of the micropore volume for the platelet models

In this section we present two test cases to show the consistency of two different approaches for the measurement of the micropore volume in the platelet models: the method which uses He as a probe (described in Chapter 4 – Section 4.2.2) and Dubinin – Radushkevich (DR) method (16), which is applied to the isotherms simulated for nitrogen at 77.35 K. The systems we are now considering are based on packings of respectively coronene (CR) platelets and corannulene elements featuring two hydroxilic groups ($CRNL(OH)_2$). Their features are summarized in Chapter 4 in tables 4.1 and 4.6 respectively.

These systems are here considered as representative of all systems based on non-curved platelets and systems based on structural elements featuring curvature respectively.

Figure A1 shows the DR plots for CR (graph (a)) and CRNL $(OH)_2$ (graph (b)).

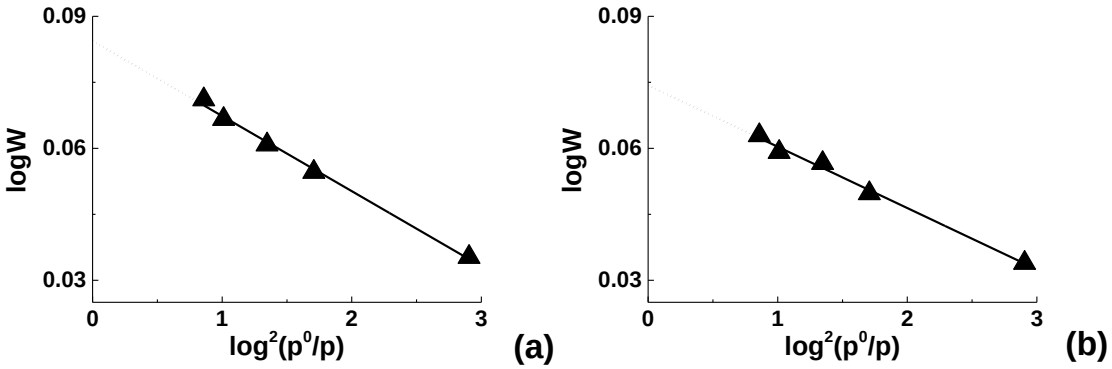

Figure A1. DR plots for the systems (a): CR and (b): CRNL-$(OH)_2$

In the case of CR the application of DR method gives a value of micropore volume of 1.21 cm^3/g, which is very close to the value of 1.24 cm^3/g, calculated using He as a probe.

In the case of $CRNL(OH)_2$ the micropore volume calculated using DR method is 1.19 cm^3/g, while using He as a probe the volume is 1.28 cm^3/g. In this case, given the curvature of the elements, the graphitic carbon-He ε parameter has been scaled by a factor 1.23, coherently with the protocol adopted for all non-polar adsorptive species when simulating adsorption using $CRNL(OH)_2$ model (as described in Section 4.5). The agreement between the two

values of micropore volume can still be considered good; we anyway decide to also make a comparison with the volume that would result without applying any scaling factor to the solid-fluid interaction. Interestingly, the result becomes 1.18 cm^3/g, which is much closer to the value calculated using DR method. One may argue, therefore, that in the case of He a scaling factor may not be required. Nevertheless the problem would need to be further investigated and for the moment we simply decide to remain coherent with the general rule adopted in this work. Also, the difference between the two different values calculated for the micropore volume has proved not to be sufficient to cause any noticeable difference in the calculation of the excess adsorption for the isotherms we have simulated.

A5. Simulation of carbon dioxide in a classic slit pore: comparison between results obtained using Steele potential and results obtained using an atomistic representation of the adsorbent

As stated in Chapter 3 at the beginning of our project we have simulated carbon dioxide adsorption in activated carbon using the classic slit pore model. In particular, we have compared the results obtained using the Steele potential (17) to the results obtained using an atomistic representation of the pores, with walls made of at least three graphitic sheets.

Figure A2 shows the results of this comparison, for simulations run at 300 K in a pore of 10 Å width, and xy dimensions of the unit cell respectively 25.62 and 36.21 Å. All the other parameters coincide with the ones reported in table A4, apart from the cutoff, which in this case is 12.5 Å.

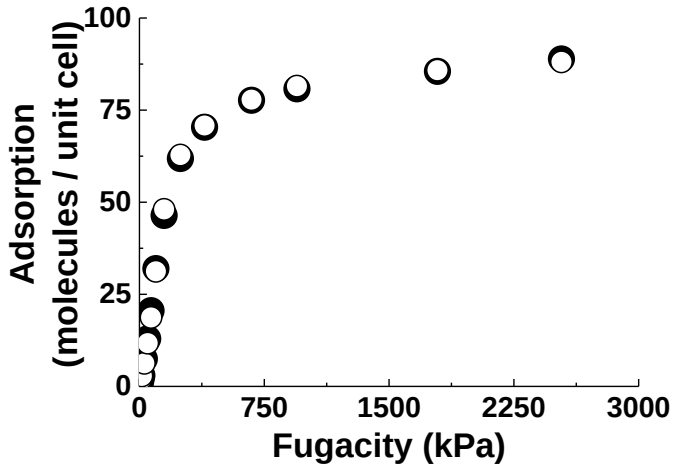

Figure A2. Comparison between carbon dioxide simulation in a slit pore obtained using Steele potential (white symbols) and results obtained using an atomistic representation of the adsorbent (black symbols).

The two different representations of the pore clearly produce almost identical results.

A6. Kernels of adsorption isotherms simulated using the slit pore models

Figures A3, A4 and A5 show the kernels of adsorption isotherms we have simulated for carbon dioxide and methane in the classic slit pore model, in the single layer model and in the single layer with groups and defects model respectively. The pore widths in Angstrom are reported in the legends.

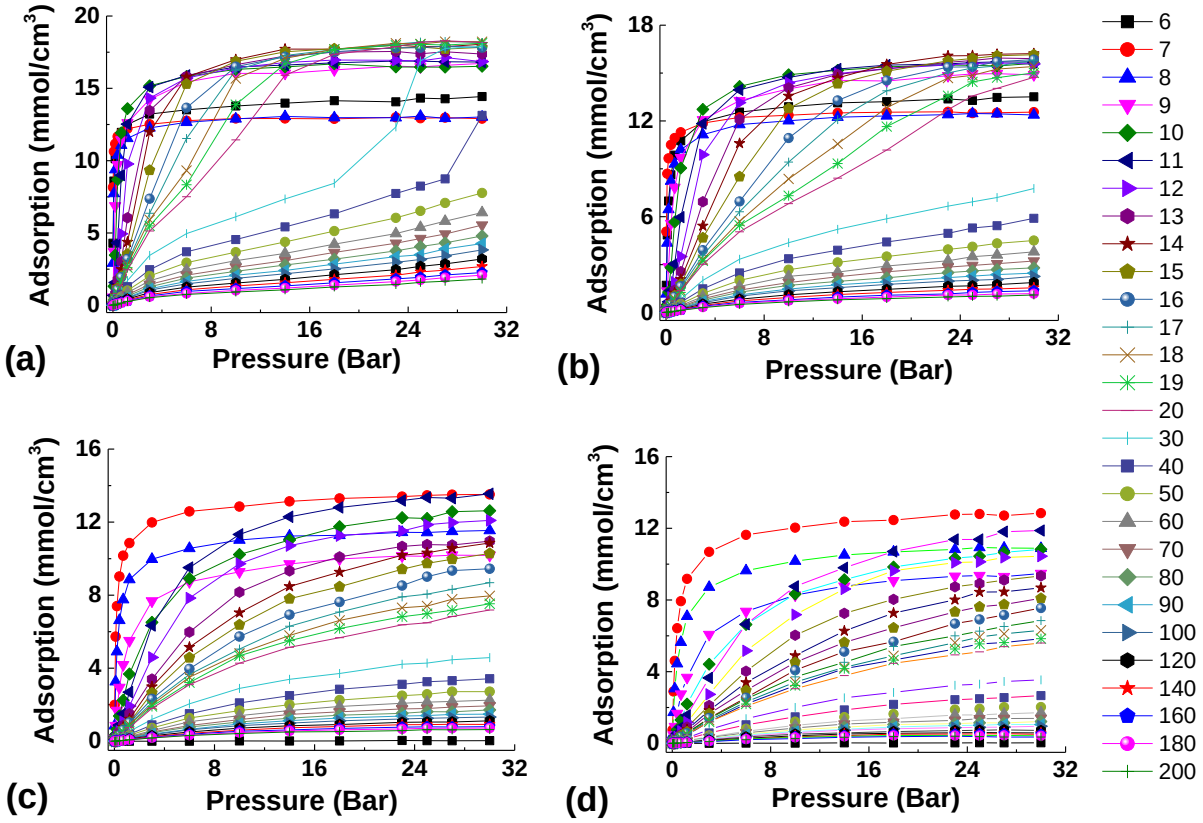

Figure A3. Kernels of adsorption isotherms simulated in the classic slit pore model for (a): CO_2 at 273 K, (b): CO_2 at 298 K, (c): CH_4 at 273 K, (d): CH_4 at 298 K. Pore widths (legend on the right side of the picture) are reported in Å.

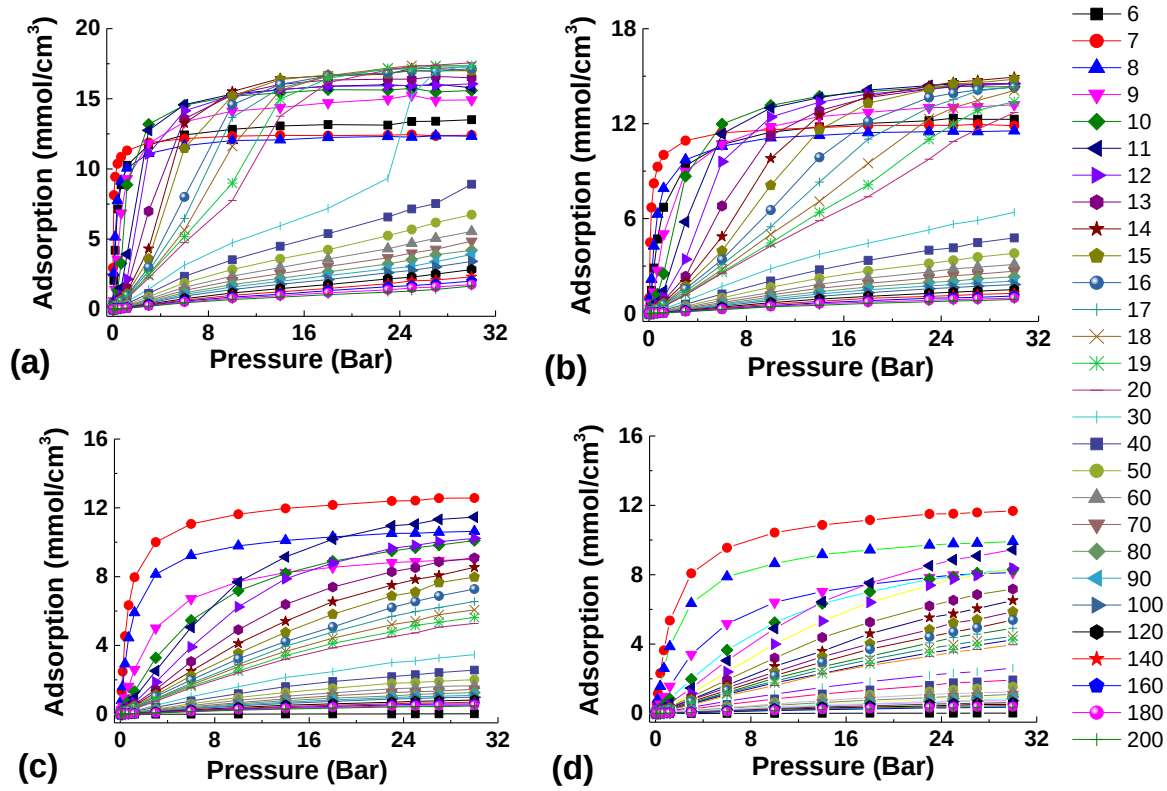

Figure A4. Kernels of adsorption isotherms simulated in the single layer model for (a): CO_2 at 273 K, (b): CO_2 at 298 K, (c): CH_4 at 273 K, (d): CH_4 at 298 K. Pore widths (legend on the right side of the picture) are reported in Å.

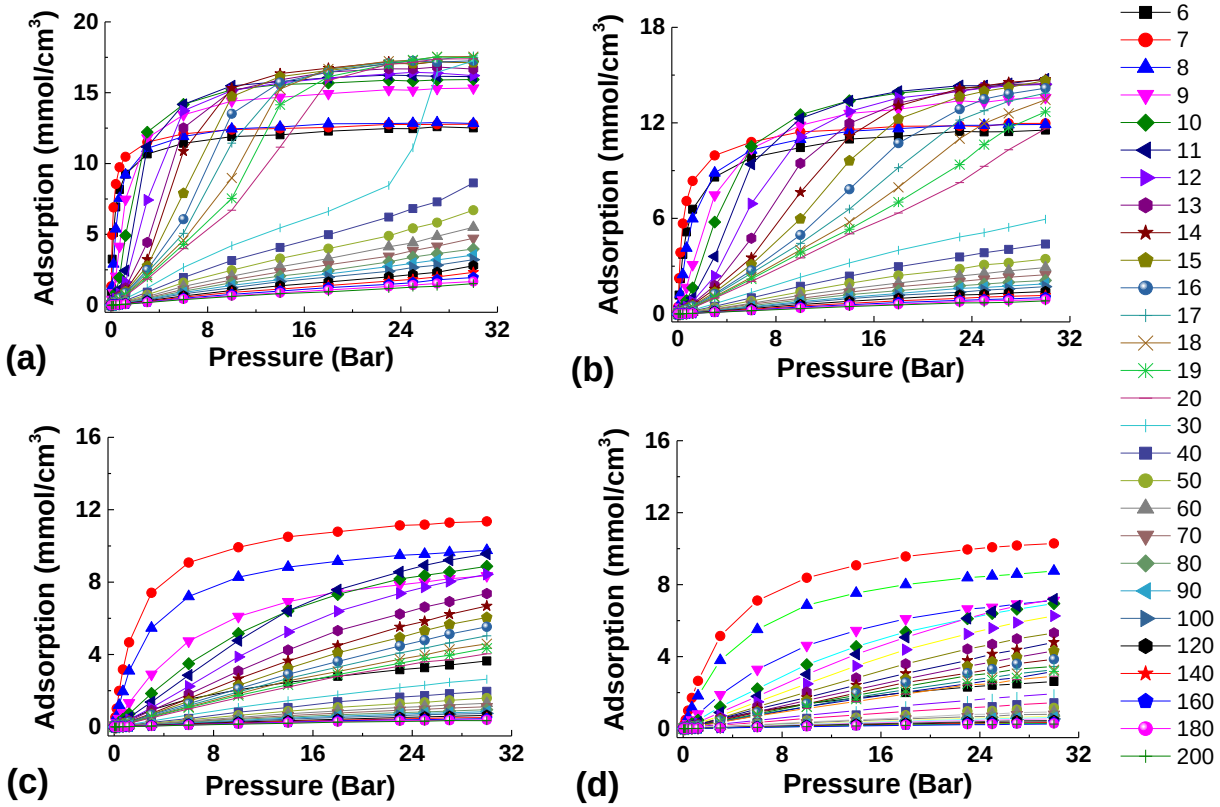

Figure A5. Kernels of adsorption isotherms simulated in the single layer with groups and defects model for (a): CO_2 at 273 K, (b): CO_2 at 298 K, (c): CH_4 at 273 K, (d): CH_4 at 298 K. Pore widths (legend on the right side of the picture) are reported in Å.

A7. Test on the effect of a specific realization of the platelet model on the simulated adsorption isotherms

For each activated carbon platelet model only one realization has been used for the simulation of the adsorption isotherms. This choice has been justified by a test performed on a sample case, in which three different realizations of the same model have been used. The basal element in this case has been a platelet made of 84 carbon atoms and functionalized with 8 hydroxylic groups ($C84\text{-}(OH)_8$ as shown in figure A6.

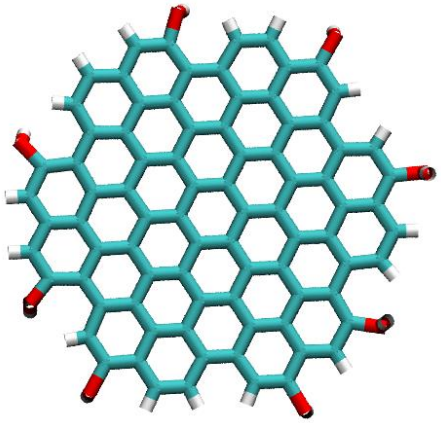

Figure A6. Structural element $C84\text{-}(OH)_8$

Figure A7 shows methane and carbon dioxide adsorption isotherms simulated on three different realizations of the same model. These realizations, all with surface area ~ 3800 m^2/g and micropore volume ~ 1.6 cm^3/g, have been constructed simply varying the random number seed for the packing of the platelets with hard sphere potential.

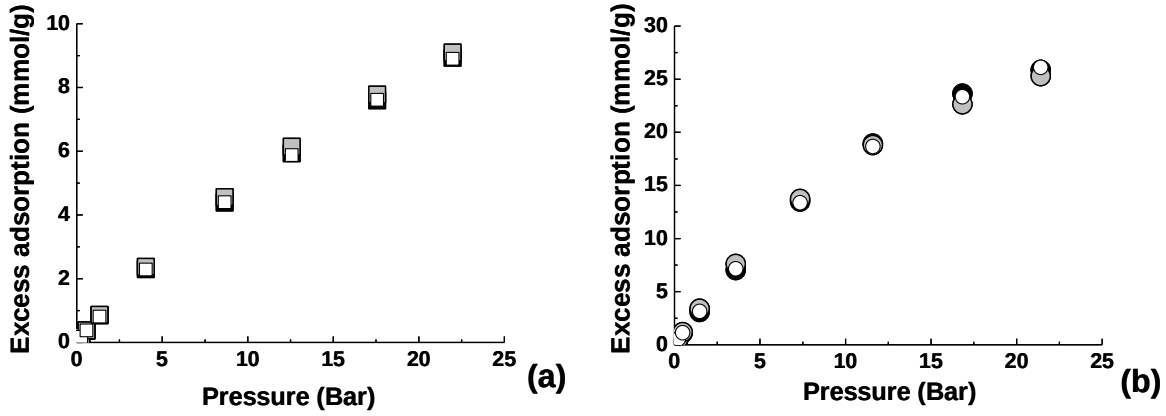

Figure A7. Simulated CH_4 (a) and CO_2 (b) adsorption isotherms on three different realizations of the same model of C84-$(OH)_8$

It is clear from figure A7 that the effect of the specific realization of the model on the simulated adsorption isotherms is minor. Therefore, the choice to consider only one realization in each case is justified.

A8. Summary of the partial atomic charges involved in the calculations

Table A8. Atomic coordinates and charges involved in the simulations described in Section 4.4.5 of the thesis for the coronene-like platelet.

ATOM	CARTESIAN COORDINATES (Å)			CHARGE A[(2)] (e)	CHARGE B[(3)] (e)
	x	y	z		
C (aromatic)	-2.5030	-1.2492	-0.5016	0.0000	0.1348
	-0.3824	-2.7356	0.6692	0.0000	0.1410
	-0.1911	-1.3671	0.3344	0.0000	-0.0151
	-1.2509	-0.6243	-0.2507	0.0000	-0.0189
	-1.0598	0.7428	-0.5851	0.0000	0.0185
	1.0598	-0.7428	0.5851	0.0000	0.0185
	1.2509	0.6243	0.2507	0.0000	-0.0189
	0.1911	1.3671	-0.3344	0.0000	-0.0151
	0.3824	2.7356	-0.6692	0.0000	0.1410
	2.5030	1.2492	0.5016	0.0000	0.1348
	-2.1207	1.4864	-1.1708	0.0000	0.1066
	2.1207	-1.4864	1.1708	0.0000	0.1066
C (aromatic, C-H)	-2.6801	-2.6086	-0.1646	-0.1600	-0.1748
	-1.6305	-3.3443	0.4149	-0.1600	-0.1945
	2.6801	2.6086	0.1646	-0.1600	-0.1748
	1.6305	3.3443	-0.4149	-0.1600	-0.1945
	-1.9178	2.8445	-1.4985	-0.1600	-0.1534
	-0.6790	3.4628	-1.2503	-0.1600	-0.2016
	-3.3591	0.8541	-1.4149	-0.1600	-0.1749
	-3.5483	-0.4998	-1.0837	-0.1600	-0.1981
	0.6790	-3.4628	1.2503	-0.1600	-0.2016
	1.9178	-2.8445	1.4985	-0.1600	-0.1534
	3.3591	-0.8541	1.4149	-0.1600	-0.1749
	3.5483	0.4998	1.0837	-0.1600	-0.1981
H (H-C)	-3.5765	-3.0723	-0.3395	0.1600	0.1190
	-1.7831	-4.3293	0.6507	0.1600	0.1256
	3.5765	3.0723	0.3395	0.1600	0.1190
	1.7831	4.3293	-0.6507	0.1600	0.1256
	-2.6728	3.3929	-1.9210	0.1600	0.1120
	-0.5560	4.4493	-1.4967	0.1600	0.1246

	-4.1326	1.3770	-1.8362	0.1600	0.1222
	-4.4559	-0.9364	-1.2703	0.1600	0.1270
	0.5560	-4.4493	1.4968	0.1600	0.1246
	2.6728	-3.3929	1.9210	0.1600	0.1120
	4.1325	-1.3770	1.8362	0.1600	0.1222
	4.4559	0.9364	1.2703	0.1600	0.1270

Table A9. Atomic coordinates and charges involved in the simulations described in Section 4.4.5 of the thesis for the coronene-like platelet functionalized with two hydroxyl groups.

ATOM	**CARTESIAN COORDINATES (Å)**			**CHARGE A$^{(2)}$ (e)**	**CHARGE B$^{(2)}$ (e)**
	x	**y**	**z**		
C (aromatic)	23.9670	10.8830	19.0540	0.0000	0.1896
	24.8300	9.8300	19.4630	0.0000	0.0165
	24.3670	8.8550	20.3880	0.0000	0.0320
	23.0430	8.9310	20.9050	0.0000	-0.0859
	25.2330	7.8040	20.7950	0.0000	-0.0817
	24.7750	6.8270	21.7210	0.0000	0.1647
	26.5550	7.7300	20.2820	0.0000	0.0221
	27.4190	6.6790	20.6940	0.0000	0.1864
	26.1510	9.7550	18.9480	0.0000	-0.0764
	27.0170	8.7050	19.3560	0.0000	0.0270
	26.6090	10.7330	18.0230	0.0000	0.1628
	28.3420	8.6320	18.8420	0.0000	-0.0839
C (aromatic, C-H)	22.2000	9.9830	20.4830	-0.1600	-0.0508
	22.6560	10.9470	19.5700	-0.1600	-0.2705
	23.4620	6.9120	22.2280	-0.1600	-0.3607
	26.9520	5.7160	21.6120	-0.1600	-0.2340
	25.6430	5.7880	22.1200	-0.1600	-0.1515
	24.4340	11.8470	18.1350	-0.1600	-0.2357
	25.7410	11.7730	17.6250	-0.1600	-0.1508
	27.9240	10.6520	17.5210	-0.1600	-0.3599
	29.1850	7.5770	19.2610	-0.1600	-0.0530
	28.7290	6.6140	20.1760	-0.1600	-0.2683
C (aromatic, C-OH)	22.6060	7.9530	21.8290	0.3000	0.3783
	28.7840	9.6170	17.9280	0.3000	0.3777

H (H-C)	21.2430	10.0630	20.8380	0.1600	0.0987
	22.0210	11.6980	19.2870	0.1600	0.1400
	23.1180	6.2130	22.8930	0.1600	0.1699
	27.5600	4.9510	21.9180	0.1600	0.1391
	25.3320	5.0760	22.7860	0.1600	0.1156
	23.8250	12.6110	17.8290	0.1600	0.1397
	26.0540	12.4860	16.9610	0.1600	0.1156
	28.2670	11.3480	16.8520	0.1600	0.1698
	30.1420	7.4990	18.9080	0.1600	0.0991
	29.3650	5.8650	20.4610	0.1600	0.1396
O (hydroxylic)	21.3560	7.9820	22.3510	-0.6000	-0.6089
	30.0360	9.5920	17.4110	-0.6000	-0.6086
H (hydroxylic)	20.8030	7.5300	21.6810	0.3000	0.3980
	29.9720	8.9780	16.6500	0.3000	0.3979

(2) Tenney and Lastoskie (Hartree-Fock method, 6-31G(d,p) basis set and Mulliken population analysis for representative ~ 100 atom polycyclic aromatic hydrocarbons).

(3) Present work (B3LYP DFT method, 6-31G basis set and CHELPG population analysis).

A9. Characterization of the model for Maxsorb MSC-30 activated carbon

The final model for Maxsorb MSC-30 activated carbon has been characterized through the determination of the geometric pore size distribution, through the determination of the Henry's constants for methane and carbon dioxide at different temperatures and through the application of the BET equation to the simulated N_2 adsorption isotherm at 77.35 K. The Henry's constants have been then used to calculate the differential enthalpies of adsorption at zero coverage.

A9.1 Geometric pore size distribution

The geometric pore size distribution has been determined using the package Poreblazer 1.2 (18). The parameters involved in the calculation are presented in Table S9.

Table A10. Parameters involved in the determination of the geometric pore size distribution.

Number of trials	1000
Number of tests per trial	1000000
Smallest probe diameter (Å)	0.2
Probe diameter increment (Å)	0.2
Maximum probe diameter (Å)	30.0

The geometric pore size distribution determined for the final model for Maxsorb developed in this work is presented in figure A8.

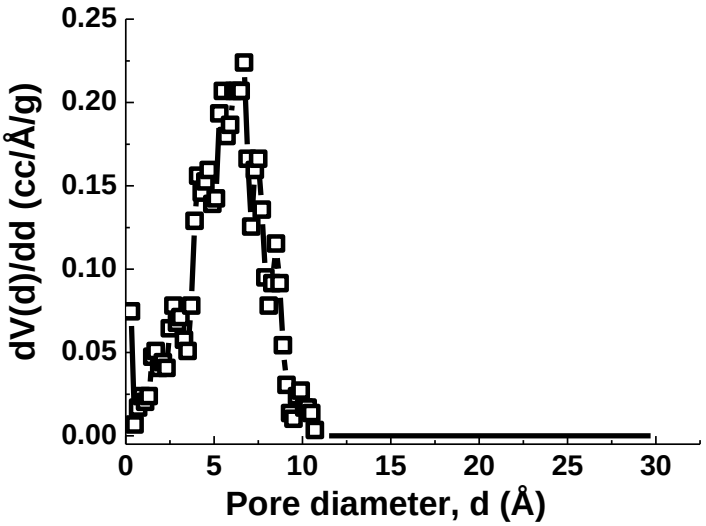

Figure A8. Geometric pore size distribution for the model for Maxsorb MSC-30 activated carbon developed in the present work.

The pore size distribution appears to consist of pore diameters of about 5 – 7.5 Å (which, to be compared consistently with the pore widths as defined for the slit pore model, as explained in Section 4.5 of the thesis, correspond to widths of 8.4–11 Å) . These values are smaller than the typical values of ~20 Å experimentally determined through the adsorption of nitrogen at 77 K (19), (20).

This result is not surprising as the model developed in this work does not take into account the mesoporosity of the sample. In principle, the model can be further modified to introduce the actual mesopores in the structure. One way of doing it would be to enlarge the system in one dimension without adding any graphitic fragments in the extra space. In periodic boundary conditions, this would introduce slit-like pores of certain width in the model, and this may result in the reconciliation of the pore size distributions. Preliminary calculations have shown that this would have only a minor effect on the simulated adsorption isotherms for methane and carbon dioxide at ambient temperatures.

A9.2. Henry's constants of adsorption

Using the variables shown in Table A7 the Henry's constants for methane and carbon dioxide have been calculated at 273, 298 and 323 K. The results have been compared to the values determined by Himeno *et al*. (21) using the experimental data (Table A11).

Table A11. Comparison between Henry's constants calculated for methane and carbon dioxide in the present work (CH_4(sim) and CO_2(sim), respectively) and from the experimental data by Himeno *et al.* (18) (CH_4(exp) and CO_2(exp), respectively).

T (K)	**K_H(mol/kg/Bar)**			
	CH_4 (sim)	**CH_4 (exp)**	**CO_2 (sim)**	**CO_2 (exp)**
273	1.8	2.32	4.14	4.68
298	1.03	1.31	1.96	2.44
323	0.64	0.76	1.07	1.55

In all the cases presented in table A11, the simulated Henry's constants show reasonable agreement with the experimental values, but in general they underestimate them.

A9.3. Differential enthalpies of adsorption at zero coverage

The values of the Henry's constants at different temperatures have been used to calculate the differential enthalpies of adsorption at zero coverage for methane and carbon dioxide according to the equation:

$$\Delta H = -R \left[\partial \ln K_H / \partial (1/T)\right]_N$$

where N represents the amount adsorbed, R is the gas constant, and ΔH is the differential enthalpy of adsorption. The results are compared to the values calculated from the experimental data by Himeno *et al*. (21) in table A12.

Table A12. Differential enthalpies of adsorption at zero coverage for methane and carbon dioxide. Sim: present work, exp: Himeno *et al*. (21).

Fluid	**ΔH (kJ/mol)**	
	sim	**exp**
CH_4	15.06	16.3
CO_2	19.87	16.2

The results presented in the table show reasonable agreement; nevertheless our model slightly under-estimates the differential enthalpy of adsorption at zero coverage for methane, while in the case of CO_2 there is an over-prediction.

A9.4. Nitrogen adsorption at 77.35 K and calculation of the BET surface area

The model developed for Maxsorb MSC-30 has been further characterized through the simulation of nitrogen adsorption at 77.35 K. A comparison between the simulated and the experimental isotherm, measured using a Quantachrome Autosorb apparatus (as described in Chapter 2) is presented in figure A9.

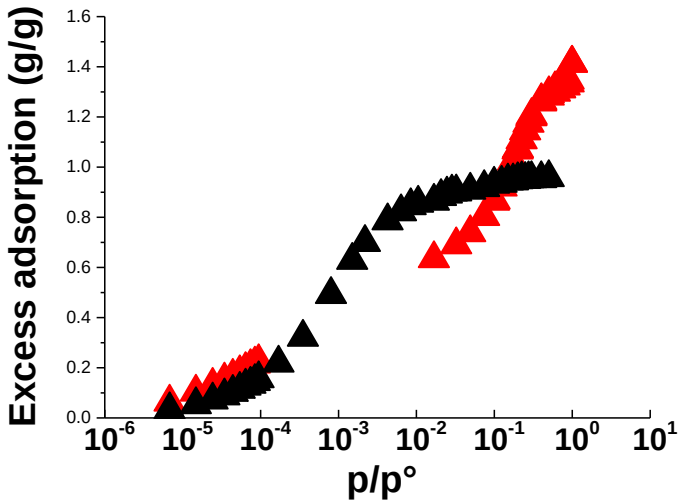

Figure A9. Experimental (red symbols) and simulated (black symbols) isotherms for N_2 adsorption at 77.35 K on Maxsorb MSC-30.

Although the isotherms are in reasonable agreement with each other at low pressures, there are clear differences at higher pressures. Again, this result is not surprising as the model does not capture some of the larger pores present in Maxsorb. Similar differences have been observed in other studies attempting to reproduce the microstructure of activated carbons.

In both cases the adsorption isotherms have been used to determine the BET surface area through the application of the criteria established by Rouquerol, Llewellyn and Rouquerol (22).

A9.4.1. Criteria by Rouquerol, Llewellyn and Rouquerol for the applicability of the BET equation to microporous materials

These criteria represent instruct on which linear portion of the BET plot should be chosen for the determination of the surface area, to make sure that the BET equation is applicable even to microporous adsorbents. These have been used in a number of studies (22- 24).
The criteria state the following:

1) The selected linear portion of the BET plot should have a positive intercept;
2) The term W*(p°-p), where W represents the mass adsorbed at a certain pressure p, should continuously increase together with p/p°; if not the pressure range should be narrowed;
3) The calculate BET monolayer capacity (W_m), when reported on the adsorption isotherm, should correspond to a relative pressure p/p° located within the range selected for the calculation.

Figure A10 and figure A11 show the plots involved in the BET studies for the experimental and simulated isotherms respectively. In these graphs the units are: excess amount adsorbed g/g for W and Torr for all pressure terms. In both cases the graph (a) gives a clear indication of what the upper limit of the interval of p/p° should satisfy of criterion number 2, while graph (b) is simply the linear portion of the BET plot that has been chosen for the calculation of the surface area.

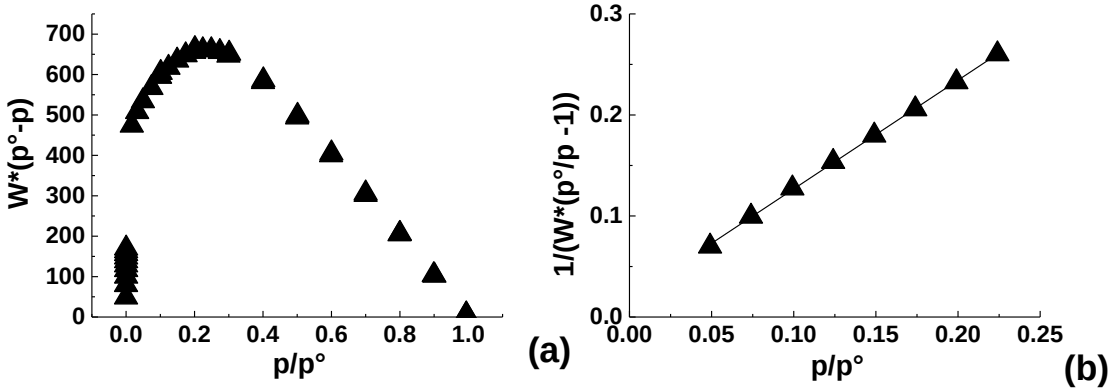

Figure A10. BET studies on the experimental adsorption isotherm of N_2 at 77.35 K on Maxsorb MSC-30. Graph (a) represents a plot of W*(p°-p) as a function of relative pressure (W is the mass adsorbed at a certain pressure p per gram of adsorbent), while graph (b) is the BET plot.

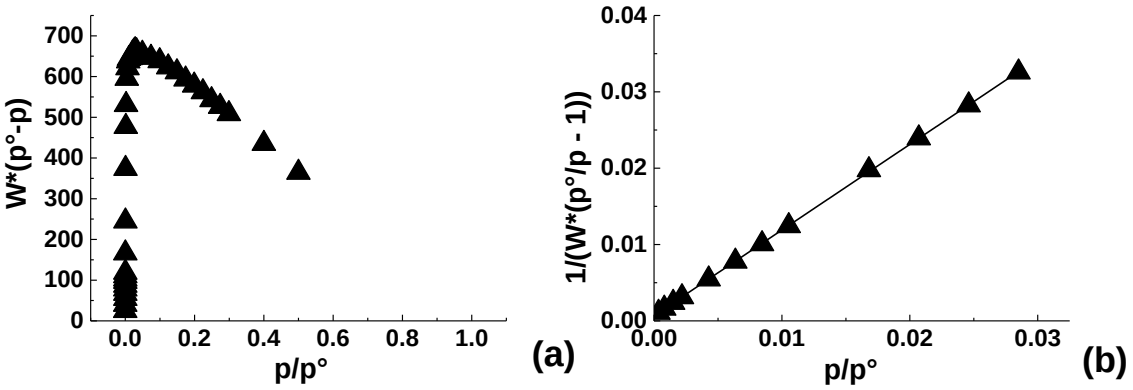

Figure A11. BET studies on the simulated adsorption isotherm of N2 at 77.35 K on the model for Maxsorb MSC-30. Graph (a) and graph (b) are defined as for figure A10.

For both cases presented in figure A10 and figure A11 the range of p/p° has been chosen so that criterion number 2 is satisfied. The results are summarized in table A13.

Table A13. Parameters determined from the BET plot for both the experimental and simulated N_2 isotherms at 77.35 K.

	Slope	**Intercept**	**W_m [g/g]**	**BET S.A. m^2/g**
Experiment	1.0763	0.0191	0.912909	3179.241
Simulation	1.1214	0.0007	0.891186	3103.592

Looking at the data reported in table A13 it is clear that even criteria 1 and 3 are satisfied: in both cases the intercept is positive (although quite different) and the values of W_m, if reported on the adsorption isotherms (figure A9), lie within the interval of p/p° that has been selected.

The value of the surface area of 3103.6 m^2/g calculated for the simulated isotherm is in a good agreement with the value of the accessible surface area (3236.64 m^2/g) justifying the model construction strategy adopted in the article.

A10. Application of alternative carbon-hydrogen potentials

It has been established that the standard solid-solid ε (epsilon) parameter for carbon, commonly used to derive solid-fluid interaction parameters for gases such as methane, leads to the underestimated strength of hydrogen interaction with carbon surfaces (25-28). Furthermore, inclusion of the curvature effects alone may not be sufficient to reconcile this.

Following the work by Nguyen *et al*. (29) we explore three different types of interaction potential for hydrogen.

Potential 1: this is the potential applied in Chapters 4 and 5. Hydrogen is represented using the spherical model by Buch (8), while for graphitic carbon the parameters listed in table A1 are applied. The solid-fluid ε (epsilon) calculated using the standard Lorentz-Berthelot mixing rules is scaled by the factor 1.23 adopted in the present work.

Potential 2: hydrogen is represented using a spherical model with the Lennard-Jones parameters taken from Levesque *et al*. (σ_{H-H} = 2.958 Å and ε_{H-H}/k_B = 36.7 K) (29), which provide excellent agreement between the simulated bulk isotherms and corresponding reference data at or above 77 K. The LJ carbon-carbon interaction parameters are taken from those obtained by Frankland and Brenner (26) based on the Raman shift of isolated H_2 inside carbon nanotubes. These parameters already take into account the presence of curvature. The carbon-hydrogen interaction has been determined using the standard Lorentz-Berthelot mixing rules.

Potential 3: hydrogen is represented using the same model and LJ parameters as in the case of Potential 2. The carbon-hydrogen interaction is estimated from the solid-fluid parameters determined by Wang *et al*. (25) for the graphite-H_2 interaction (σ_{C-H} = 2.97 Å and ε_{c-H}/k_B = 42.75 K) based on the fit of the theoretical quantum mechanical energy spectrum of hydrogen on graphite with its experimental counterpart measured by scattering methods. Nguyen *et al*. further scale this epsilon by 1.134 (and the same scaling is applied to all other solid-fluid epsilon parameters to take the curvature of surfaces into account) (30). We scale the parameters of Wang *et al*. by 1.23 adopted throughout this work. A list of the carbon-hydrogen parameters used for the three different types of potential is presented in table A14.

Table A14. Parameters for carbon-hydrogen LJ interaction used in the present study.

σ_{C-H} (Å)	ε_{C-H}/kB (K)	Type of potential
3.18	38.06	Potential 1
3.154	43.35	Potential 2
2.97	52.58	Potential 3

Figure A12 shows a comparison between the experimental isotherm taken as a reference (31) and the isotherms simulated in the present work using the parameters listed in table A14.

It is clear that both potential 2 and potential 3 produce results much closer to the experimental data compared to potential 1. This suggests that in case of hydrogen the presence of the surface curvature is not the only element to be taken into account when calculating the solid-fluid well depth. The special nature of hydrogen-carbon interactions should be incorporated as well.

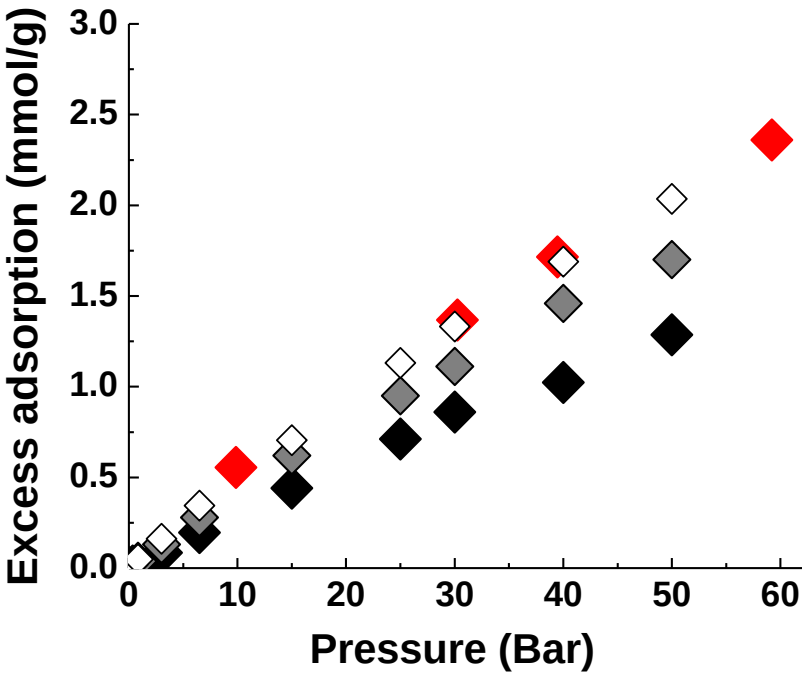

Figure A12. Experimental and simulated H_2 adsorption hydrogen on the model for Maxsorb MSC-30. Red symbols: experimental data (30), black symbols: Potential 1; grey symbols: Potential 2; white symbols: Potential 3.

A10.1 Application of alternative carbon-hydrogen potentials to the simulation of the binary mixture CO_2/H_2

Following the results presented Section A10 we now apply Potential 1 and Potential 3 (also described in Section A10) to the simulation of the carbon dioxide/hydrogen mixture with molar composition 40/60 at 313 K and pressures up to 55 Bar (pre combustion conditions). The results are presented in figure A13.

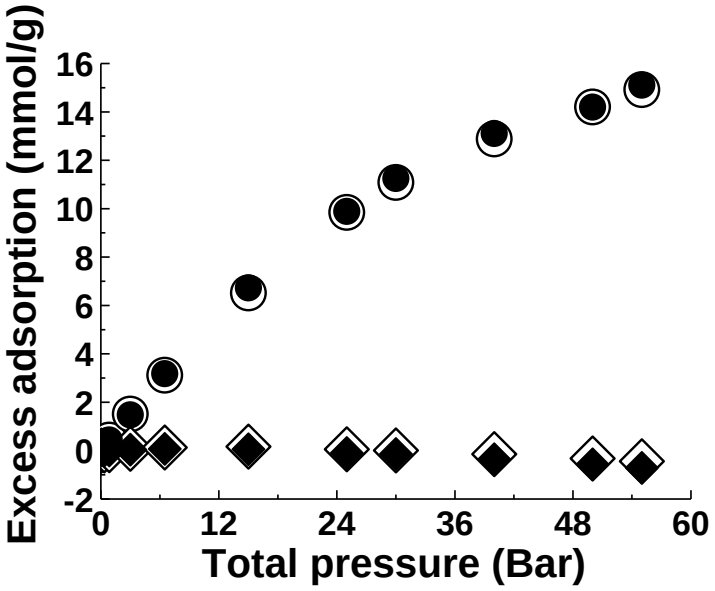

Figure A13. Simulated adsorption isotherms for the binary mixture of molar composition CO_2/H_2=40/60 at 313 K (pre combustion conditions) on the model for Maxsorb MSC-30. The solid-fluid potentials which have been applied are described in Section A10 and are respectively Potential 1 (black symbols) and Potential 3 (white symbols).

It is clear from the figure above that the two different solid-fluid potentials give very similar results. In particular, negative adsorption for hydrogen is observed in both cases, and therefore it is not related to the particular model adopted for hydrogen.

A11. Accuracy of the TraPPE model in prediction of carbon dioxide properties

In figure A14 we test the validity of the TraPPE model for carbon dioxide (6) by comparing the bulk isotherms simulated at 273, 298 and 323 K with the reference data at the same temperatures (32).

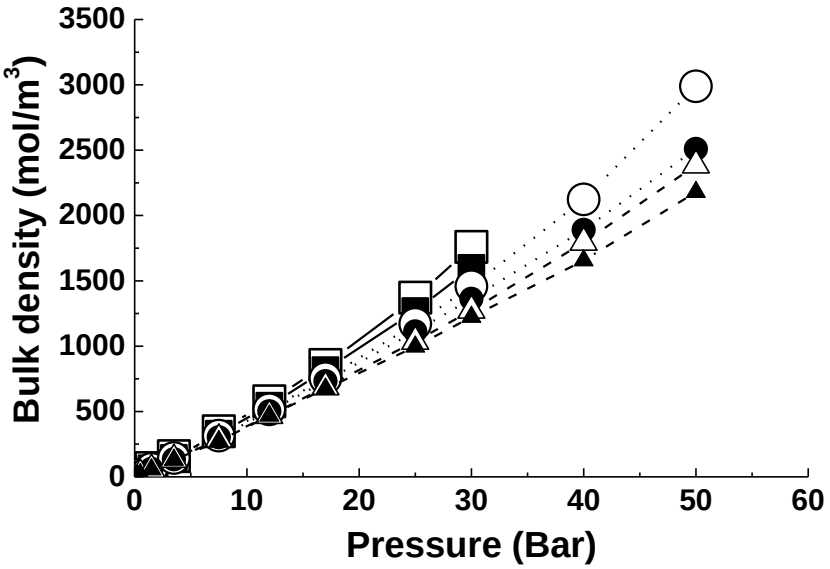

Figure A14. Experimental (empty symbols) (32) and simulated (filled symbols) bulk densities for CO_2 at 273 (squares), 298 (circles) and 323 (triangles) K.

The results presented in figure A14 show that TraPPE model for carbon dioxide agrees reasonably well with the experimental data at the temperatures under examination. In all cases the agreement can be considered very good for pressures up to ~25 Bar. At the temperature of 298 K the agreement is still reasonable up to 40 Bar, while around 50 Bar the difference between the simulation and the experimental data starts to be more pronounced. At 323 K the agreement is still reasonable up to 50 Bar.

Apart from the general observation that the TraPPE model for CO_2 performs reasonably well at the conditions of interest it is possible to notice a general improvement of the performance with the increase in temperature. This is in line with what has been observed for carbon

dioxide simulations, suggesting that the discrepancies between the simulated CO_2 isotherms and the experimental data could be partly due to the performance of the TraPPE model.

A12. Full sets of isotherms for all the separations not involving water presented in the work

In this section we present the full set of adsorption isotherms involved in the CO_2 separation from the mixtures examined in this thesis and not containing water.

Post combustion separations:

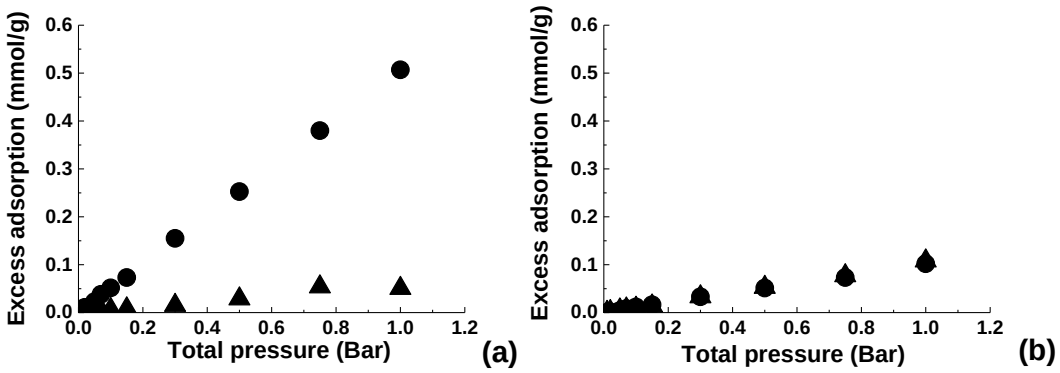

Figure A15. Simulated adsorption isotherms for the binary mixtures of molar composition CO_2/N_2=50/50 (graph (a)) and CO_2/N_2=10/90 (graph (b)) at 323 K. Circles: carbon dioxide, triangles: nitrogen.

For the equimolar mixture in graph (a) the statistical errors on the adsorbed densities for CO_2 are between 4.7% and 1.26% at the total pressures of 0.1 Bar and 1 Bar respectively, while for N_2 the errors at the same pressures are 12% and 4.24%.

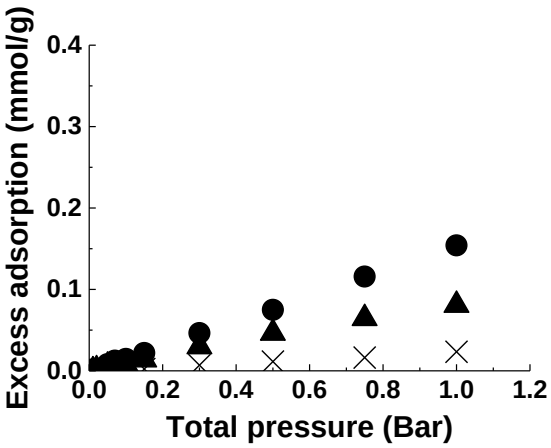

Figure A16. Simulated adsorption isotherms for the ternary mixture of molar composition $CO_2/N_2/O_2$=15/80/5 at 323 K. Circles: carbon dioxide, triangles: nitrogen, crosses: oxygen.

Pre combustion separations:

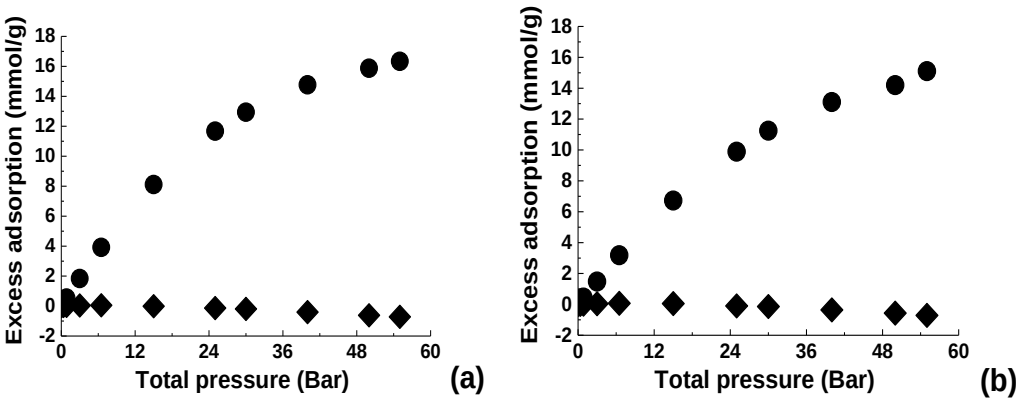

Figure A17. Simulated adsorption isotherms for the binary mixtures of molar composition CO_2/H_2=50/50 (graph (a)) and CO_2/H_2=40/60 (graph (b)) at 313 K. Circles: carbon dioxide, diamonds: hydrogen.

For the equimolar mixture in graph (a) the statistical errors on the adsorbed densities for CO_2 are 2.13%, 0.73% and 0.44% at the total pressures of 0.85 Bar, 6.5 Bar and 55 Bar respectively, while for H_2 the errors at the same pressures are 5.6%, 2.3% and 1.76%.

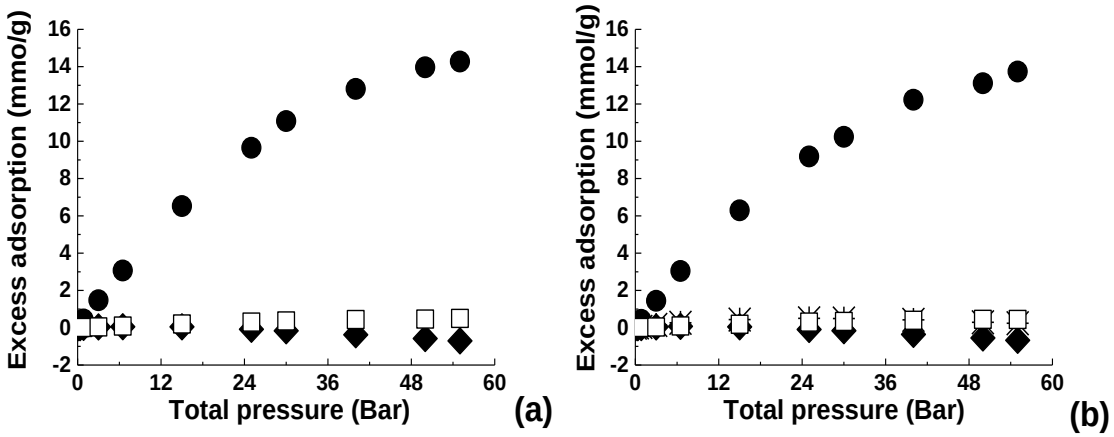

Figure A18. Simulated adsorption isotherms for the ternary mixture of molar composition $CO_2/H_2/H_2S$=39/60/1 (graph (a)) and $CO_2/H_2/H_2S$/CO=38/60/1/1 at 313 K. Circles: carbon dioxide, diamonds: hydrogen, empty squares: hydrogen sulfide, stars: carbon monoxide.

Sweetening of sour natural gas:

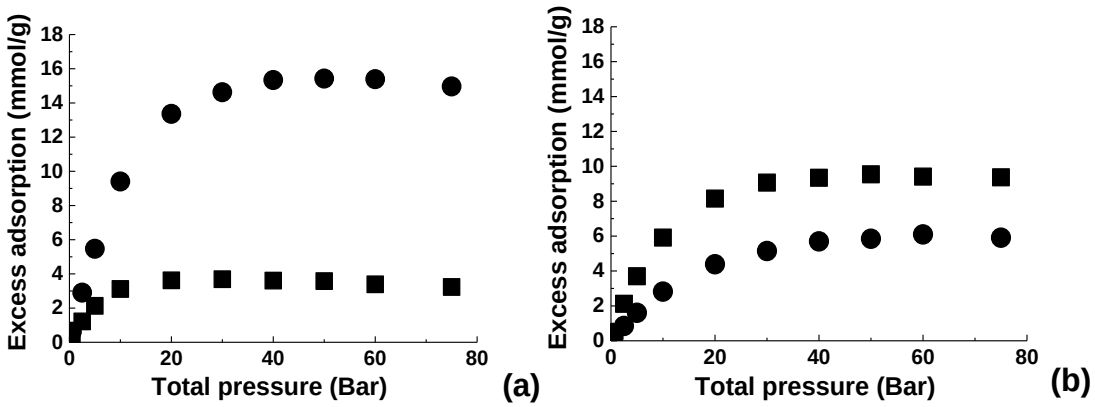

Figure A19. Simulated adsorption isotherms for the binary mixtures of molar composition CO_2/CH_4=50/50 (graph (a)) and CO_2/CH_4=15/85 (graph (b)) at 288 K. Circles: carbon dioxide, squares: methane.

For the mixture in graph (b) the statistical errors on the adsorbed densities for CO_2 are 2.4%, 0.63% and 0.6% at the total pressures of 0.5 Bar, 10 Bar and 75 Bar respectively, while for CH_4 the errors at the same pressures are 1.9%, 0.57% and 0.25%.

References

1. Axel DB. A new mixing of Hartree--Fock and local density-functional theories. The Journal of Chemical Physics. 1993;98(2):1372-7.
2. Breneman CM, Wiberg KB. Determining atom-centered monopoles from molecular electrostatic potentials. The need for high sampling density in formamide conformational analysis. Journal of Computational Chemistry. 1990;11(3):361-73.
3. Frisch MJT, G. W.; Schlegel, H. B.; Scuseria, G. E.; Robb, M. A.; Cheeseman, J. R.; Scalmani, G.; Barone, V.; Mennucci, B.; Petersson, G. A.; Nakatsuji, H.; Caricato, M.; Li, X.; Hratchian, H. P.; Izmaylov, A. F.; Bloino, J.; Zheng, G.; Sonnenberg, J. L.; Hada, M.; Ehara, M.; Toyota, K.; Fukuda, R.; Hasegawa, J.; Ishida, M.; Nakajima, T.; Honda, Y.; Kitao, O.; Nakai, H.; Vreven, T.; Montgomery, Jr., J. A.; Peralta, J. E.; Ogliaro, F.; Bearpark, M.; Heyd, J. J.; Brothers, E.; Kudin, K. N.; Staroverov, V. N.; Kobayashi, R.; Normand, J.; Raghavachari, K.; Rendell, A.; Burant, J. C.; Iyengar, S. S.; Tomasi, J.; Cossi, M.; Rega, N.; Millam, J. M.; Klene, M.; Knox, J. E.; Cross, J. B.; Bakken, V.; Adamo, C.; Jaramillo, J.; Gomperts, R.; Stratmann, R. E.; Yazyev, O.; Austin, A. J.; Cammi, R.; Pomelli, C.; Ochterski, J. W.; Martin, R. L.; Morokuma, K.; Zakrzewski, V. G.; Voth, G. A.; Salvador, P.; Dannenberg, J. J.; Dapprich, S.; Daniels, A. D.; Farkas, Ö.; Foresman, J. B.; Ortiz, J. V.; Cioslowski, J.; Fox, D. J. . Gaussian 09, Revision A.1. 2009.
4. Tenney CM, Lastoskie CM. Molecular simulation of carbon dioxide in chemically and structurally heterogeneous porous carbons. Environmental Progress. 2006;25(4):343.
5. Jorgensen WL, Madura JD, Swenson CJ. Optimized intermolecular potential functions for liquid hydrocarbons. Journal of the American Chemical Society. 1984; 106(22): 6638-46.
6. Potoff JJ, Siepmann JI. Vapor–liquid equilibria of mixtures containing alkanes, carbon dioxide, and nitrogen. AIChE Journal. 2001;47(7):1676-82.
7. Martin MG, Siepmann JI. Transferable Potentials for Phase Equilibria. 1. United-Atom Description of n-Alkanes. The Journal of Physical Chemistry B. 1998;102(14):2569-77.
8. Buch V. Path integral simulations of mixed *para*-D_2 and *ortho*-D_2 clusters: The orientational effects. The Journal of Chemical Physics. 1994;100(10):7610-29.
9. Zhang L, Siepmann JI. Direct calculation of Henry's law constants from Gibbs ensemble Monte Carlo simulations: nitrogen, oxygen, carbon dioxide and methane in ethanol. Theor Chem Acc. 2006;115(5):391-7.
10. Kamath G, Lubna N, Potoff JJ. Effect of partial charge parametrization on the fluid phase behavior of hydrogen sulfide. The Journal of Chemical Physics. 2005;123(12):124505-7.
11. Sweatman MB, Quirke N. Modelling Gas Adsorption in Slit-Pores Using Monte Carlo Simulation. Molecular Simulation. 2001;27(5-6):295-321.
12. Jorgensen WL, Chandrasekhar J, Madura JD, Impey RW, Klein ML. Comparison of simple potential functions for simulating liquid water. The Journal of Chemical Physics. 1983;79(2):926-35.
13. Gupta A, Chempath S, Sanborn MJ, Clark LA, Snurr RQ. Object-oriented Programming Paradigms for Molecular Modeling. Molecular Simulation. 2003;29(1):29-46.
14. Fennel CJ, ; Gezelter, D. Is the Ewald summation still necessary? Peirwise alternatives to the accepted standard for long-range electrostatics. The Journal of Chemical Physics. 2006;124:234104.
15. Ewald PP. Die Berechnung optischer und elektrostatischer Gitterpotentiale. Annalen der Physik. 1921;369(3):253-87.
16. Dubinin MM, Radushkevich LV. Equation of the characteristic curve of activated charcoal. Proceedings of the Academy of Sciences, Physical Chemistry Section, USSR 55. 1947:331-3.
17. Steele WA. The interaction of rare gas atoms with graphitized carbon black. The Journal of Physical Chemistry. 1978;82(7):817-21.
18. Sarkisov L, Harrison A. Computational structure characterisation tools in application to ordered and disordered porous materials. Molecular Simulation. 2011;37(15):1248-57.
19. Otowa T, Tanibata R, Itoh M. Production and adsorption characteristics of MAXSORB: High-surface-area active carbon. Gas Separation & Purification. 1993;7(4):241-5.

20. Wen ZB, Qu QT, Gao Q, Zheng XW, Hu ZH, Wu YP, *et al*. An activated carbon with high capacitance from carbonization of a resorcinol-formaldehyde resin. Electrochemistry Communications. 2009;11(3):715-8.
21. Himeno S, Komatsu T, Fujita S. High-Pressure Adsorption Equilibria of Methane and Carbon Dioxide on Several Activated Carbons. Journal of Chemical & Engineering Data. 2005;50(2):369-76.
22. Rouquerol J, Llewellyn P, Rouquerol F. Is the BET equation applicable to microporous adsorbents? In: Llewellyn PL, Rodriguez-Reinoso F, Rouquerol J, Seaton N, editors. Studies in SurfaceScience and Catalysis Elsevier; 2007. p. 49-56.
23. Coasne B, Gubbins KE, Pellenq RJM. A Grand Canonical Monte Carlo Study of Adsorption and Capillary Phenomena in Nanopores of Various Morphologies and Topologies: Testing the BET and BJH Characterization Methods. Particle & Particle Systems Characterization. 2004;21(2):149-60.
24. Bae Y-S, Yazaydın AÖ, Snurr RQ. Evaluation of the BET Method for Determining Surface Areas of MOFs and Zeolites that Contain Ultra-Micropores. Langmuir. 2010;26(8):5475-83.
25. Wang SC, Senbetu L, Woo C. Superlattice of Parahydrogen Physisorbed on Graphite Surface. Journal of Low Temperature Physics. 1980;41(5/6):611-28.
26. Frankland SJV, Brenner DW. Hydrogen Raman shifts in carbon nanotubes from molecular dynamics simulation. Chemical Physics Letters. 2001;334(1–3):18-23.
27. Kim H-Y, Lueking AD, Gatica SM, Karl Johnson J, Cole MW. A corresponding states principle for physisorption and deviations for quantum fluids. Molecular Physics. 2008;106(12-13):1579-85.
28. Nguyen TX, Bae JS, Wang Y, Bhatia SK. On the Strength of the Hydrogen−Carbon Interaction as Deduced from Physisorption. Langmuir. 2009;25(8):4314-9.
29. Levesque D, Gicquel A, Lamari Darkrim F. Monte Carlo simulations of hydrogen storage in carbon nanotubes. Journal of Physics: Condensed Matter 2002;14(40):9285-93.
30. Nguyen TX, Cohaut N, Bae J-S, Bhatia SK. New Method for Atomistic Modeling of the Microstructure of Activated Carbons Using Hybrid Reverse Monte Carlo Simulation. Langmuir. 2008;24(15):7912-22.
31. Jordá-Beneyto M, Suárez-García F, Lozano-Castelló D, Cazorla-Amorós D, Linares-Solano A. Hydrogen storage on chemically activated carbons and carbon nanomaterials at high pressures. Carbon. 2007;45(2):293-303.
32. Span R, Wagner W. A New Equation of State for Carbon Dioxide Covering the Fluid Region from the Triple-Point Temperature to 1100 K at Pressures up to 800 MPa. Journal of Physical and Chemical Reference Data. 1996;25(6):1509-96.